

**Optical *in situ* characterization of lab-scale and pilot-scale burners  
for nanoparticle synthesis**

Von der Fakultät für Ingenieurwissenschaften,  
Abteilung Maschinenbau und Verfahrenstechnik der  
Universität Duisburg-Essen

zur Erlangung des akademischen Grades  
eines  
Doktors der Ingenieurwissenschaften

Dr.-Ing.

genehmigte Dissertation

von

Florian Schneider  
aus  
Solingen

Gutachter: Prof. Dr. Christof Schulz  
Prof. Dr. Sebastian Kaiser

Tag der mündlichen Prüfung: 27.8.2020



Für Johanna

## Acknowledgement

This dissertation was created during my work as a research associate at the Institute for Combustion and Gas Dynamics – Reactive Fluids (IVG-RF). I would like to thank Prof. Dr. Christof Schulz for all his continuous support, the many inspiring discussions, and his strategic focus that guided me a lot when tasks piled up. Thank you, Christof, for all the opportunities you offered me over the past five years. I wish you all the best.

I would like to thank Prof. Dr. Thomas Dreier – the supervisor of the laser-diagnostics group – for his tireless support in the laboratory and in laser adjustment. Thank you for the many educational discussions and all your support during my doctoral studies. I had the privilege to be one of your last PhD students and I wish you healthiness and a wonderful new chapter in your life.

For all the work that has been done behind the scenes and for all their constant support, I would like to thank the IVG core-team: Natascha Schlösser, Beate Endres, Birgit Nelius, Barbara Graf, Barbara Nota, Dr. Erdal Alkyldiz, Sebastian Rosendahl, Jörg Albrecht, and Ludger Jerig. Many thanks also to Steffi Nickol for her support in organizing the Summer School and our nuanced conversations. You all helped me a lot to move forward and make progress – thank you.

I would like to thank Tim Hülser, Dr. Sophie Marie Schnurre, Frank Krumpolt, Mathias Spree, and Frederik Kunze for all their support during the challenging tasks at the IUTA nanoparticle pilot-scale facility. Thank you for your marvellous cooperation – I enjoyed every day we've spend together.

Moreover, I would like to thank all my colleagues from the IVG and the SPP1980, who have proven that a doctorate does not have to be a competition but can be a symbiotic cooperation. We have always supported each other and relaxed our – often quite stressful and overloaded – everyday business with some jokes and some sweets. Special thanks to Jasmina Kovachevic, Sebastian Kluge, Lin Shi, Paul Sela, Philip Niegemann, Matthias Beuting, Marc Lubnov, Andreas Rittler, Johannes Sellmann, E.B., Muhammad Asif, Sadrollah Karaminejad, Muhammad Ali Shabaz, Abbas El Moussawi, Baris Alkan, Stefan Kilian, Stefan Kuns, Sascha Apazeller, Carsten Brocksieper, Patrick Kranz, Ming Zhao, Stanislav Musikhin, Sebastian Peukert, Niklas Jüngst, Adrian Münzer, Markus Prenting, Alexander Tarasov, Raphael Mansmann, Torsten Endres, Irenäus Wlokas, Hartmut Wiggers, Jan Menser, Rongchao Pan, and Samer Suleiman. Thank you, guys!

Finally, I would like to express my gratitude to my parents. Thank you, for all your support and the possibilities you offered me. All this was possible thanks to the fundament you provided.

In the end, I'd like to thank my wife Johanna Paula. Thank you so much for motivating me, for your tireless support, and our countless discussions at dinner – where we reflected the events of the day and where you always gave good advice and opened-up new perspectives.

## Abstract

Nanoparticle-based materials enable devices and systems that can be used for improved or even new technologies for instance in the fields of health, mobility, energy conversion and energy storage. Continuous synthesis of high-purity oxidic nanoparticles with tailored properties is commonly applied in (spray) flames and requires detailed process engineering. Comprehensive experiments and numerical simulation provide deeper insight into the fundamentals of combustion-based nanoparticle synthesis as well as for up-scaling towards industrial production rates. Laser-based *in situ* temperature and velocity measurements are of particular importance since they provide crucial boundary conditions for computational fluid dynamics (CFD) simulations and allow for determining the temperature–time history of volume elements on their path through the reactor that is highly relevant for the property of the final product.

In this work, these quantities were investigated for lab-scale and pilot-scale (spray-flame) burners using multiple optical diagnostics in non-reacting (cold) flows as well as in un-doped and precursor-laden (spray) flames with tungsten hexafluoride ( $\text{WF}_6$ ), titanium isopropoxide (TTIP), iron pentacarbonyl ( $\text{Fe}(\text{CO})_5$ ), or iron(III) nitrate ( $\text{Fe}(\text{NO}_3)_3$ ) as precursors. For a lab-scale premixed flat flame burner, the surface temperature of the porous bronze burner matrix was investigated with infrared pyrometry during operation at commonly used synthesis conditions. Inhomogeneities in the surface temperature distribution were correlated with *in situ* gas-phase temperature measurements performed with multiline NO laser-induced fluorescence (LIF) thermometry and the observed influence of the  $\text{WF}_6$  and  $\text{Fe}(\text{CO})_5$  precursor concentration on the flame temperature was investigated. For a pilot-scale non-premixed gas burner, the gas-phase velocity was measured using particle image velocimetry (PIV). Multiple non-reacting operating parameter sets were investigated and suggestions for improved parameters were provided. A correction for spatial variation in laser-sheet attenuation during multiline NO-LIF thermometry was developed that is discussed in the context of pilot-scale nanoparticle synthesis of titania particles.

For the SpraySyn burner, an optical flame imaging benchmark was developed that ensures correct operation of the standardized lab-scale spray burner across laboratories. Using phase Doppler anemometry (PDA), droplet velocities and sizes were determined in non-reacting sprays of acetone, 1-butanol, ethanol, and n-hexane as well as in the ethanol spray flame. Characteristic nozzle curves for the two-fluid nozzle of the SpraySyn burner were determined. For a pilot-scale spray burner, gas-phase velocity fields were measured by PIV and the droplet velocity was investigated with multi-pulse shadowgraphic red/green/blue illumination and particle-tracking velocimetry (PTV) that was successfully validated with droplet velocities determined by PIV. Spatially resolved temperature fields of the ethanol spray flame (doped with iron(III) nitrate) were acquired with multiline NO-LIF thermometry in combination with laser sheet attenuation correction analyzing how the oxygen content in the dispersion gas influences the iron-atom concentration (determined with Fe LIF) as well as the corresponding flame temperature.

Besides providing boundary conditions for CFD simulations for all investigated burners, the presented results supported the development of a reaction mechanism for iron(III) nitrate and (simulation-aided) improvements on operating conditions and burner designs that are mandatory prerequisites for advancement in up-scaling of (spray) flame synthesis of tailored nanoparticles.

## Zusammenfassung

Nanopartikel-basierte Materialien ermöglichen die Entwicklung verbesserter oder sogar neuer Technologien beispielsweise in den Bereichen Gesundheit, Mobilität, Energiekonversion und -speicherung. Die kontinuierliche Synthese hochreiner oxidischer Nanopartikel mit maßgeschneiderten Eigenschaften wird üblicherweise in (Spray-) Flammen durchgeführt und erfordert ein detailliertes Prozessverständnis. Einander ergänzende Experimente und numerische Simulationen bieten ein großes Potential, um weitreichende Einblicke in die Grundlagen der verbrennungsbasierten Nanopartikelsynthese sowie das Hochskalieren hin zu industriellen Produktionsraten zu erlangen. Laserbasierte In-situ-Temperatur- und -Geschwindigkeitsmessungen liefern die Randbedingungen für CFD-Simulationen und ermöglichen die Bestimmung der Temperatur–Zeit-Historie reagierender Volumenelemente auf dem Weg durch den Reaktor, die die Eigenschaften des finalen Produkts bestimmt.

Diese Größen werden in der vorliegenden Arbeit an labor- und pilotskaligen (Spray-) Brennern mit mehreren optischen Messtechniken in nicht-reaktivem (kaltem) Betrieb sowie in Flammen dotiert mit Wolframhexafluorid ( $\text{WF}_6$ ), Tetraisopropylorthotitanat (TTIP), Eisenpentacarbonyl ( $\text{Fe}(\text{CO})_5$ ) oder Eisennitrat ( $\text{Fe}(\text{NO}_3)_3$ ) untersucht. Für einen laborskaligen Flachflammenbrenner wurde die Oberflächentemperatur der porösen Matrix mit Infrarotpyrometrie untersucht und Inhomogenitäten der Oberflächentemperaturverteilung mit abbildenden In-situ-Gasphasentemperaturmessungen korreliert, die durch Multilinien-NO-LIF Thermometrie (laserinduzierte Fluoreszenz) gemessen wurden. Basierend darauf wird der Einfluss der  $\text{WF}_6$ - und  $\text{Fe}(\text{CO})_5$ -Prekursorkonzentration auf die Flammentemperatur untersucht. An einem pilotskaligen Gasbrenner wurde die Gasphasengeschwindigkeit mit Particle Image Velocimetry (PIV) an einer Vielzahl nicht-reaktiver Betriebspunkte untersucht, woraus Vorschläge für optimierte Betriebsbedingungen abgeleitet wurden. Außerdem wurde ein Verfahren entwickelt, mit dem die Abschwächung der Energie des Laserlichtblatts während der NO-LIF-Thermometrie räumlich korrigiert werden kann, was im Kontext der Synthese von  $\text{TiO}_2$  vorgestellt wird.

Für den SpraySyn-Brenner wurde ein optisches Referenzmessverfahren entwickelt, wodurch ein einheitlicher Betrieb des standardisierten Spraybrenners laborübergreifend sichergestellt wird. Mithilfe von Phasen-Doppler-Anemometrie (PDA) wurden für den laborskaligen Brenner Tropfengeschwindigkeiten und -größen in nicht-reagierenden Aceton-, 1-Butanol-, Ethanol- und n-Hexan-Sprays sowie in einer Ethanol-sprayflamme ermittelt, woraus charakteristische Kennlinien für die Zweistoffdüse des SpraySyn-Brenners abgeleitet wurden. Für einen pilotskaligen Spraybrenner wurden Gasphasengeschwindigkeitsfelder mit PIV gemessen während Tropfengeschwindigkeiten durch Schattenwurf einer Folge rot/grün/blauer Lichtpulse und anschließender Particle-Tracking-Velocimetry (PTV) bestimmt wurden, die erfolgreich anhand von PIV-Tropfengeschwindigkeiten validiert werden konnten. Räumlich aufgelöste Temperaturfelder (eisennitratdotierter) Sprayflammen wurden durch NO-LIF-Thermometrie unter Anwendung Laserlichtblatt-Absorptionskorrektur gemessen, sodass der Einfluss des Sauerstoffgehalts im Dispersionsgas auf die Eisenatomkonzentration (ermittelt mit Fe-LIF) und die resultierende Flammentemperatur analysiert werden konnte.

Neben der Bereitstellung von Randbedingungen für CFD-Simulationen für alle untersuchten Brenner, können die vorgestellten Ergebnisse für die Entwicklung eines Reaktionsmechanismus für Eisen(III)-nitrat sowie (simulationsgestützte) Optimierungen von Betriebsbedingungen und Brennerkonstruktionen genutzt werden, die notwendige Voraussetzungen für Fortschritte beim Hochskalieren der Flammensynthese von maßgeschneiderten Nanopartikeln sind.

## Content

1	Introduction.....	13
2	Background.....	16
2.1	Combustion Synthesis of Functional Nanomaterials.....	16
2.2	Optical diagnostics of non-reacting and reacting flows related to nanoparticle synthesis	19
2.2.1	IR pyrometry.....	20
2.2.2	Gas-Phase Thermometry via Multiline Laser-induced Fluorescence Imaging .....	23
2.2.3	Particle Image Velocimetry.....	25
2.2.4	Laser Doppler and Phase Doppler Anemometry.....	27
2.2.5	Multi-pulse RGB shadowgraphy for Particle Tracking Velocimetry .....	30
3	Lab-scale premixed gas burner for nanoparticle synthesis.....	33
3.1	Porous-bronze flat-flame burner.....	33
3.2	Experimental.....	35
3.2.1	IR pyrometry.....	35
3.2.2	Multiline NO-LIF thermometry.....	36
3.3	Results .....	38
3.3.1	Pyrometric imaging of the porous plug.....	38
3.3.2	Temperature imaging during nanoparticle synthesis.....	41
3.4	Outlook.....	45
4	Pilot-scale non-premixed gas burner for nanoparticle synthesis.....	46
4.1	Concentric multi-tube gas burner .....	46
4.2	Experiment .....	48
4.2.1	Particle Image Velocimetry.....	48
4.2.2	Multiline NO-LIF thermometry.....	49
4.3	Results .....	51
4.3.1	Gas-phase velocity measurements under non-reacting conditions.....	51
4.3.2	Temperature imaging with laser sheet correction during nanoparticle synthesis .....	56
4.4	Outlook.....	61
5	Lab-scale spray burner for nanoparticle synthesis.....	63
5.1	SpraySyn burner .....	63
5.2	Experiment .....	66
5.2.1	Standardized experiment for imaging flame characterization.....	66
5.2.2	Phase Doppler Anemometry .....	67
5.3	Results .....	69
5.3.1	Characterization of the SpraySyn reference flames.....	69
5.3.2	Droplet size and velocity measurements in non-reacting sprays.....	72
5.3.3	Droplet size and velocity measurements in the ethanol spray flame .....	82
5.3.4	Comparison of reacting and non-reacting operation.....	84
5.3.5	Characterization of the two-fluid nozzle .....	89
5.4	Outlook.....	92
6	Pilot-scale spray burner for nanoparticle synthesis .....	93
6.1	IUTA spray burner.....	93
6.2	Experiment .....	95

6.2.1	Particle Image Velocimetry.....	95
6.2.2	Multi-pulse RGB shadowgraphy for Particle Tracking Velocimetry .....	96
6.2.3	Multiline NO-LIF thermometry and Fe-LIF.....	98
6.3	Results .....	98
6.3.1	Gas-phase and droplet velocity measurements in the non-reacting ethanol spray ...	98
6.3.2	Temperature imaging with laser sheet correction during nanoparticle synthesis ...	105
6.3.3	Relative iron concentration during nanoparticle synthesis from iron(III) nitrate .....	112
6.4	Outlook.....	114
7	Conclusions.....	116
	References.....	118
	Appendix.....	133
A1	Influence of the refractive index on the PDA droplet-size measurement .....	133
A2	Details of the experimental setup for multiline NO-LIF thermometry.....	133
A3	Allocation of raw data and post processing to the presented figures .....	136
A3.1	Lab-scale gas burner .....	136
A3.1.1	IR thermography.....	136
A3.1.2	Multiline NO-LIF thermometry.....	137
A3.2	Pilot-scale gas burner .....	138
A3.2.1	Particle Image Velocimetry.....	138
A3.2.2	Multiline NO-LIF thermometry.....	140
A3.3	Lab-scale spray burner .....	141
A3.3.1	Imaging spray-flame characterization .....	141
A3.3.2	Phase Doppler Anemometry .....	141
A3.4	Pilot-scale spray burner.....	144
A3.4.1	Particle Image Velocimetry.....	144
A3.4.2	Multi-pulse RGB shadowgraphy for Particle Tracking Velocimetry .....	145
A3.4.3	Multiline NO-LIF-Thermometry .....	145
A4	List of utilized software .....	146
A4.1	Proprietary software .....	146
A4.2	DiskGrab makro .....	147
A4.3	LIFSim.....	149
A4.4	Matlab codes .....	149
	Publications .....	156
	Peer-reviewed journal articles .....	156
	Conference proceedings.....	156
	Conference presentations .....	156
	Student supervision.....	157

## Nomenclature

### Latin symbols

$A_{21}$	Einstein coefficient describing the fluorescence rate of a photon from an excited state while the system relaxes to the ground state	1/s
A, B, C	Signal outputs of the pulse generator	-
$b_1, b_2, b_3$	Exponents used for the empirical equation of the Sauter Mean Diameter of the SpraySyn burners two-fluid nozzle	-
$b_{12}$	Absorption rate of an incident laser photon that excites a molecule from the ground state to the excited state	1/s
$C_{br}$	Color ratio of the blue and red color channel	-
$d$	Diameter	m
$d_0$	Inner diameter of the capillary	m
$d_i$	Inner diameter of the gas nozzle (i.e., outer diameter of the capillary)	m
$d_a$	Outer diameter of the gas nozzle	m
$dt$	Time delay	s
$\dot{E}$	Radiation power	W/m <sup>2</sup>
$f_B$	Boltzmann population of the ground state	-
$I_{LIF}$	Fluorescence intensity	W/m <sup>2</sup>
$\dot{m}_G$	Gas mass-flow rate	kg/s
$\dot{m}_L$	Liquid mass-flow rate	kg/s
$N$	Number density	1/m <sup>3</sup>
Oh	Ohnesorg number	-
$Q_{21}$	Quenching rate	1/s
$QE$	Quantum efficiency	-
$r$	Radius	m
$T$	Temperature	K
$t_0$	Time of the Initial trigger pulse	s
$t_1, t_2, t_3$	Time delays used in the trigger schemes	s
$u$	Axial (droplet) velocity component	m/s
$U_{1,2}$	Phase factor of the vertically aligned PDA detector pair	°/m
$u_{mag}$	Velocity magnitude	m/s
$v$	Radial (droplet) velocity component	m/s
$V_{1,2}$	Phase factor of the horizontally aligned PDA detector pair	°/m
$x$	Axis pointing towards the PDA laser (the droplet velocity component along this axis is inaccessible with the utilized PDA setup)	m

### Greek symbols

$\Delta_R, \Delta_G, \Delta_B$	Pulse widths used for the red/green/blue LEDs	s
$\Delta v$	Velocity difference	m/s
$\Delta v_{rel}$	Relative velocity difference	%
$\varepsilon$	Emissivity	-
$\phi$	Equivalence ratio	-
$\Phi_{1,2}$	Phase difference measured by the PDA	°
$\gamma$	Detection angle	°
$\Gamma$	Dimensionless overlap between the spectral profile of the incident laser beam and the absorption line	-

$\lambda$	Wavelength	m
$\eta_G$	Dynamic gas viscosity	kg/(m s)
$\eta_L$	Dynamic liquid viscosity	kg/(m s)
$\rho_G$	Gas density	kg/m <sup>3</sup>
$\rho_L$	Liquid density	kg/m <sup>3</sup>
$\sigma$	Standard deviation (chapter 5.3.1)	-
$\sigma_L$	Surface tension	kg/s <sup>2</sup>

### Constants

$b$	Wien constant	2897.7685 $\mu\text{m K}$
$\pi$	Archimedes constant	Approx. 3.14159
$\sigma$	Stefan-Boltzmann constant (chapter 2.2.1)	$5.6704 \times 10^{-8} \text{ W}/(\text{m}^2\text{K}^4)$

### Acronyms

Note: Digital file formats (e.g., TIFF for *Tagged Image File Format*), company/product names (e.g., TSI Inc. for *Thermo-Systems Engineering Incorporated*), operating parameter sets (e.g., SF1 for *spray flame 1*), as well as the hardware identifiers (e.g., EM for *Energy Monitor*) used in the chapters presenting the experimental setups are not listed here.

1D	One dimensional
2D	Two dimensional
3D	Three dimensional
BET	Brunauer-Emmett-Teller
C1	Cooling configuration 1 of the flat flame burner investigated in this work
C2	Cooling configuration 2 of the flat flame burner investigated in this work
CARS	Coherent anti-stokes Raman scattering
CCD	Charge coupled device
CFD	Computed fluid dynamics
CRDS	Cavity-ring-down absorption spectroscopy
D10	Number mean diameter
D20	Area mean diameter
D32	Sauter mean diameter (similar to SMD)
DBI	Diffuse back illumination
DCM	Laser dye 4-(Dicyanomethylene)-2-methyl-6-(4-dimethylaminostyryl)-4H-pyran
DEHS	Seeding oil Di(2-ethylhexyl) sebacate
DFG	German Research Foundation (Deutsche Forschungsgemeinschaft)
DIH	Digital in-line holography
DSC	Differential scanning calorimetry
DSLIR	Digital single-lens reflex (camera)
ECN	Engine combustion network
EDS	Energy-dispersive X-ray spectroscopy
FPS	Focal plane array
FRS	Filtered Rayleigh scattering
FSP	Flame spray pyrolysis
FTIR	Fourier-transform infrared spectroscopy
FWHM	Full width half maximum

GLR	Gas-to-liquid (mass) ratio
GUI	Graphical user interface
HAB	Height above burner
IC	Internal combustion
ICLAS	Intra-cavity laser absorption spectroscopy
ILIDS	Interferometric laser imaging droplet sizing
IR	Infrared
IUTA	Institute of Energy and Environmental Technology, Duisburg
IVG-RF	Institute for Combustion and Gas Dynamics – reactive fluids, University of Duisburg-Essen
Laser	Light amplification by stimulated emission of radiation
LD	Laser diffractometry
LDA	Laser Doppler anemometry
LDV	Laser Doppler velocimetry
LED	Light-emitting diode
LIF	Laser-induced fluorescence
MFC	Mass flow controller
MTV	Molecular tagging velocimetry
Nd:YAG	Neodymium-doped yttrium aluminum garnet ( $\text{Nd:Y}_3\text{Al}_5\text{O}_{12}$ )
PDA	Phase Doppler anemometry
PDI	Phase Doppler interferometry
PIV	Particle image velocimetry
PMMA	Poly(methyl methacrylate)
PMS	Particle mass spectrometry
PSV	Particle shadow velocimetry
PTU	Programmable timing unit
PTV	Particle tracking velocimetry
PVC	Probe volume correction
QCM	Quartz crystal microbalance
RGB	Red/green/blue color model
ROI	Region of interest
sCMOS	Scientific complementary metal-oxide semiconductor
SD	Secure digital
SEM	Scanning electron microscopy
SFM	Sum frequency mixing
SMD	Sauter mean diameter (similar to D32)
SMPS	Scanning mobility particle sizer
SNR	Signal-to-noise ratio
TDLAS	Tunable diode laser absorption spectroscopy
TGA	Thermogravimetric analysis
TNF	Turbulent non-premixed flame
TOF-MS	Time-of-flight mass spectrometry
TTIP	Titanium tetraisopropoxide
UV	Ultraviolet
VIS	Visible spectrum
WALS	Wide angle light scattering
XPS	X-ray photoelectron spectroscopy
XRD	X-ray diffraction



## 1 Introduction

Nanotechnology is one of the key technologies that enables creating new materials, devices, and systems [1] in multidisciplinary research to overcome current challenges in health, mobility, and energy [2, 3]. In nanotechnology, properties and phenomena are exploited that occur only in the regime with length scales between those of atomistic structures and continuous macroscopic structures (i.e., bulk material) [4]. In this regime with dimensions below 100 nm [4], particles have a very high specific surface. For example, a 10 nm particle that consists of around 30,000 atoms exhibits 20% of all its atoms at the surface, while 80% of all atoms are located in the outermost 2-nm layer [4]. This provides not only an extreme reactivity, e.g. valuable for catalysis, but also leads to a variation of materials properties such as melting point, light-matter interaction, and electronic and magnetic properties [4]. Varying the particle size of a respective material on the nano-scale opens an additional dimension of modifying materials properties beyond a compositional variation. In catalysis and sensors, in energy technology (batteries, fuel cells, solar cells), and in many other industries (medicine, cosmetics, food) nanoparticles enable a wealth of new or improved applications [5-7].

However, the controlled synthesis of nanoparticles with tailored materials properties is complex and requires detailed process engineering. In general, nanoparticles can be produced either by top-down or bottom-up pathways [8]. The former can be achieved for instance by milling of bulk material and is attributed with certain drawbacks regarding the final product (e.g., wide particle-size distributions, uncontrollable particle morphology, and impurities) [4]. In contrast, bottom-up pathways are based on molecular self-assembly from atoms and molecules and enable well-controlled product composition and quality [4, 9]. While most nanomaterials are generated by precipitation from the wet phase, gas-phase synthesis (chapter 2.1) that uses chemical compounds (precursors) containing the species of the desired material, is often used for the continuous synthesis of tailored, high-purity nanoparticles, especially of large materials quantities [7, 9]. Figure 1.1 illustrates important questions that need to be addressed when intending to synthesize high-purity nanoparticles with tailored materials properties for instance in a spray flame. Some of these questions need to be investigated in isolated experiments, e.g., in shock tubes for determining reaction kinetics [10, 11] and laminar flame speeds [12], or they are investigated during synthesis in complementary experiments and numerical simulations [13].

For nanoparticle synthesis in flames, *in situ* temperature and velocity measurements are of particular importance since they allow for estimating the temperature-time history of a particle, which is one of the most significant parameters for tuning the final product [14-16]. For that, a wide range of measurement technology is available like for instance thermocouples that are commonly used in practice to measure temperatures. However, they require contact with the system of interest and they measure at a single point, only. This invasive technique disturbs the investigated system [17], e.g., by introducing a heat capacity into the examined system and by physical disturbance of the flow field. In addition, the temperature probe itself is exposed to the investigated system. In a reactive process environment, a chemical reaction (oxidation) or surface contamination on the probe may falsify the measurement result. At high temperatures – such as in flames – the upper temperature limit of the probe material is quickly reached, so that measurements in multiple flames used for nanoparticle

synthesis are not accessible. Furthermore, rapid temperature fluctuations can only be detected insufficiently as thermocouples imply thermal inertia. Therefore, optical diagnostics became indispensable for *in situ* measurements in flames, e.g., for online process monitoring [18], for investigations in internal combustions engines (i.e., in-cylinder imaging) [19], and in nanoparticle synthesis [20].



Figure 1.1: A selection of central questions whose answers provide the key to (spray) flame synthesis of nanoparticles with tailored materials properties. The photo shows a spray flame (mixture of ethanol and ethylhexanoic acid) doped with iron(III) nitrate precursor operated in a flame reactor at 940 mbar.

The present work aims on deepening the process understanding of nanoparticle synthesis in flames. By the use of multiple optical measurement techniques (chapter 2.2), the non-reacting and reacting gaseous flow of four different nanoparticle-synthesis burners (Figure 2.1) is investigated. Thereby, detailed insights into relevant quantities such as gas-phase and liquid-phase velocities, gas-phase temperatures, and concentration-fields of intermediate species during synthesis are obtained, which are necessary prerequisites, e.g., for optimizing the process design, development of reaction mechanisms, and for the determination of boundary conditions for computational fluid dynamics (CFD) simulations. This framework between experimental results and validated simulations facilitates synergies that enables the simulation of entire synthesis reactors [21] and identifies key parameters for tailoring nanoparticle properties for industrial applications.

For the comparison of experiment and simulation, it is important to define the boundary conditions of the experiment. Therefore, in this thesis the temperature distribution across the porous bronze plug of a lab-scale flat flame gas burner (chapter 3.1) is investigated by infrared pyrometry (chapter 3.3) while the gas-phase temperature is measured during nanoparticle synthesis by multiline NO-LIF thermometry (chapter 3.3.2). For the lab-scale spray burner (chapter 5.1), droplet velocities and droplet sizes are characterized in the spray (flame) using Laser Doppler and Phase Doppler Anemometry (chapters 5.3.2–5.3.5). Moreover, an optical setup and a standardized post processing is developed that ensures uniform burner operation in different laboratories to promote establishing the burner as the first reference experiment for nanoparticle synthesis in spray flames (chapter 5.3.1).

For the pilot-scale burners (chapters 4.1 and 6.1), the gas-phase velocity of the non-reacting flow is examined using Particle Image Velocimetry (chapter 2.2.3) to enable first computational fluid dynamics (CFD) simulations of both burners. Additional essential boundary conditions are provided by PIV and by diffuse multi-pulse shadowgraphy (chapter 2.2.5) of the spray determining droplet velocities.

To characterize the reacting flow, imaging temperature measurements are performed for which the conventionally utilized setup for multiline NO-LIF thermometry needs to be optimized since experiences from a previous work [22] show that increased particle deposition on the optical ports of the pilot-scale reactor (kg/h) causes overall lower signal-to-noise ratios further decreasing during experiment. Moreover, the spatial iron-atom distribution during synthesis of iron-oxide nanoparticles should be investigated since the results are required for the development of a reaction mechanism for the iron(III) nitrate precursor.

This thesis is organized as follows: In chapter 2, background on combustion synthesis of nanoparticles and the utilized optical measurement techniques is presented. The results presented in this work are subdivided according to the investigated burner into four equally structured main chapters (3–6). In chapter 3 and 4, the lab-scale and pilot-scale gas burners are investigated while in chapter 5 and 6 the lab-scale and pilot-scale spray burners are examined. In each chapter, the investigated burner is introduced in the first subchapter. All presented burners were designed at the Institute for Combustion and Gas Dynamics (IVG) and are successfully utilized for nanoparticle synthesis in flames for many years at the IVG as well as at the Institute for Energy and Environmental Technology (IUTA) in Duisburg. The motivation of each burner design, its history, and *status quo* regarding available flow-field characterization is summarized. Subsequently, the experimental setups are described and the most relevant results of the flow characterization are discussed. At the end of each main chapter, an outlook suggesting future investigations is provided. In the conclusions (chapter 7), the impact of the achieved results is highlighted. In the appendix, a direct link between the raw data and the presented figures is provided (appendix A3), listing the software and scripts used for data acquisition and post-processing (appendix A4) to enable reproducibility for future publications.

## 2 Background

### 2.1 Combustion Synthesis of Functional Nanomaterials

Flame-assisted nanoparticle synthesis from the gas-phase is complex and requires detailed knowledge for instance in molecular chemistry, reaction kinetics, thermodynamics, and materials science. However, the underlying reactive particle-formation sequence can be described by four steps [23, 24]:

1. A precursor is added into a reactor where it decomposes at high temperature leading to the formation of a variety of gas-phase species
2. Condensable species nucleate in a super-saturated environment and create first clusters and particles
3. Surface-growth as well as coalescence lead to the formation of larger entities
4. Coagulation and aggregation can lead to the formation of larger structures composed from individual primary particles

To provide the necessary energy for the process, hot-wall and plasma reactors but also other energy sources such as electric arcs and lasers are suitable [9, 25]. However, well-established industrial processes exploit the energy of exothermic combustion reactions for cost-effective synthesis of  $\text{SiO}_2$ ,  $\text{TiO}_2$ , and  $\text{Al}_2\text{O}_3$  nanoparticles on the million-tons-per-year scale [23, 24]. These flame reactors can be designed for a wide range of operating-parameters and require either gaseous or liquid precursors [23, 24].

For situations where the process gases are premixed before entering the reactor, the precursor needs to be gaseous at environmental condition or it needs to be vaporizable and mixable with the burner gases [26]. Suitable precursors are often expensive and/or toxic, they are only available for a limited number of elements, and the precursor-supply often requires complex periphery [26]. On the other hand, premixed gas-phase processes are ideal for experimental and numerical research to investigate fundamentals like precursor decomposition, interaction of precursor-flame chemistry, and particle formation [7]. For processes with liquid precursor supply, the precursor (liquid or solid) is dissolved, e.g., in a combustible solvent and injected into a (pilot) flame as finely atomized droplets. In the spray flame, rapid evaporation of solvent and precursor lead to the same starting point of the particle-formation sequence as described for gas-phase synthesis (see “step 1” in the list above) [24]. Spray-flame synthesis requires less complex periphery, enables the use of almost all elements (including salts), and allows easy mixing of two or more precursors to adjust the composition of multinary oxides [26]. On the other hand, experimental and numerical investigations of multi-phase flows are more complex and spray-flame synthesis raises a number of additional questions such as details about reactions that already occur in the liquid phase before spray evaporation, the transfer of precursor into the gas phase, and explosive droplet evaporation [7, 27]. A profound description on nanoparticle synthesis from the gas-phase is given in literature, e.g., in Refs. [9] and [28] while more details on spray-flame synthesis can be found in Refs. [29] and [30].

In industry, operating parameters and burner designs are mostly intellectual-property (IP) protected and highly individual for each specific application. Although in the scientific community of *combustion synthesis of nanoparticles*, the burner designs (and operating parameters) are usually described in publications, historically, a large spectrum of different burners has grown that offer individual pros

and contras. In the following, a brief overview of common nanoparticle-synthesis burners is given and the burners utilized in this work are introduced.

In general, nearly all types of flames (burner-stabilized premixed flat flames, stagnation point premixed flames, coflow flames, counter flow flames, and multi-diffusion flames) are suitable for nanoparticle synthesis [9]. Commonly, the precursor is injected through the burner into the flame. In this work, a burner with gaseous precursor feed is denoted *gas burner* while a burner with liquid precursor supply is called *spray burner*. Gas burners frequently used for nanoparticle synthesis are:

- McKenna-type burner where a cooled, porous sintered metal plug is used to achieve a flat flame from a premixed fuel/air mixture [31-34]
- Hencken burner, which is a non-premixed flat-flame burner where multiple small-diameter fuel-supply tubes are (each) surrounded by a honeycomb mesh that provides air generating a surface mixing flame [35-37]
- Coflow non-premixed burners like the Santoro burner [38] or the Gülder burner [39] where fuel is provided through a central tube and air is promoted through a surrounding co-annular tube with ten times higher diameter that contains elements like glass beads to ensure uniform exit-flow profiles
- Concentric multi-tube burners (sometimes also called coflow burners [40]) like those presented in Refs. [41-43]) where three or more tubes with increasing diameter form co-annular ring gaps to separately provide fuel, oxidizing gases, and inert diffusion-barrier flows that allow adjusting the flame geometry

On the other hand, well-known spray burners for nanoparticle synthesis are:

- Ultrasonic-assisted burners comparable with the burner utilized for the first reported spray-flame synthesis of  $\text{Al}_2\text{O}_3$  nanoparticles, where ultrasonic-atomized,  $\mu\text{m}$ -size precursor/solvent droplets were carried by an oxygen flow through a central tube into a hydrogen-oxygen flame [44]
- Concentric multi-tube burners similar to the gas-burner type [41] described above, where a co-axial high-speed gas flow (e.g., hydrogen) is used to atomize a liquid precursor/solvent mixture fed through the center tube [45-47]
- Spray-flame burner as introduced by Mädler et al. [48], that is often referred to as Flame-Spray Pyrolysis (FSP) where a liquid precursor solution is atomized by a two-fluid nozzle and ignited either by six [48] or eighteen [49] surrounding pilot flames, by a non-premixed methane/oxygen flame originating from two co-annular ring gaps [50], or by a single premixed pilot flame originating from a narrow (150–200  $\mu\text{m}$ ) co-annular ring gap [51-53]
- SpraySyn burner [26] that was recently introduced as a variant of the previous one, which was introduced as the first standardized experiment for coordinated research on materials synthesis in spray flames. Its design meets the demands of various related sub-fields, e.g., by offering an alignment-capability for adjusting symmetrical flames and by providing easy-to-calculate boundary conditions for numerical simulations [7, 54-56]

Further insights about those and other synthesis-burners are given in Refs. [7, 23, 30, 40].

To investigate the fundamentals of the process chain of (spray) flame synthesis experimentally and numerically, burner (and flame) geometry should be as simple as possible to reduce complexity. However, even with simplified experiments, every research group needs to investigate the whole process chain of nanoparticle synthesis based on their individual burner designs (e.g., finding suitable operating conditions, analyzing the synthesized materials, and characterizing the flow). Besides being time

consuming and inefficient, the achieved results are hard to reproduce by other groups or hard to compare with the findings derived from another experiment [26].

The coordinated use of wide-spread or standardized experiments enables bundling scientific results from various research communities and efficiently promotes research progress as demonstrated for instance by “Sandia Flame D” [57] of the TNF workshop [58] or “Spray G” of the Engine Combustion Network (ECN) [59]. Therefore, in this work, a well-established flat-flame gas burner is investigated (Figure 2.1a) that is frequently used at the IVG for nanoparticle synthesis [60] and for developing optical diagnostics [61]. In addition, the SpraySyn burner is investigated (Figure 2.1b) that was recently introduced as a standard experiment [26] to provide a first characterization of its flow field since commissioning in 2018.

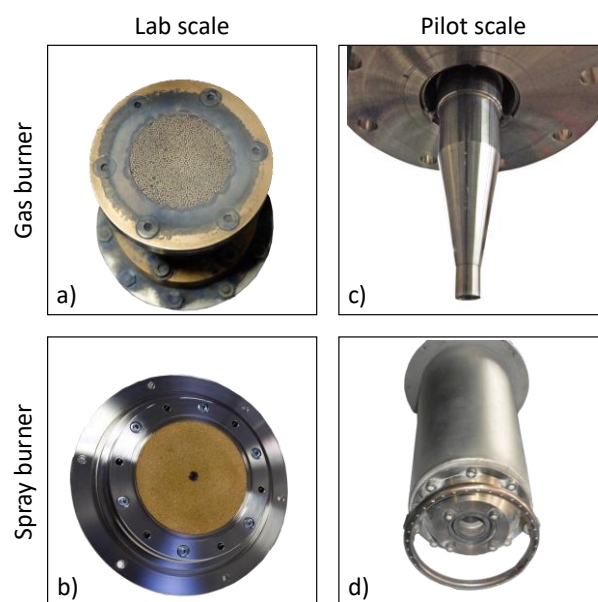


Figure 2.1: Lab-scale and pilot-scale burners for nanoparticle synthesis investigated in this work by optical non-intrusive *in situ* diagnostics. Depending on the phase in which the precursor is fed to the flame (gaseous or liquid) it is distinguished between gas and spray burners while the achievable nanoparticle production rate classifies the burners into lab-scale (few g/h) and pilot-scale (several hundred g/h) burners.

However, while for fundamental research on nanoparticle synthesis in flames, low production rates (a few g/h) are sufficient (and often even required), industrial applications demand thousands or even millions of tons per year claiming kg/h-production rates [62]. Since nanoparticle synthesis in flames is not fully understood yet [7, 63], up-scaling remains highly individual based on often IP-protected industrial developments (e.g., by Evonik, Cabot, and Dupont [64]) or based on the experience of individual research groups [62, 64-66]. Gröhn et al. provides an overview of nanoparticles synthesized on the pilot-scale (> 100 g/h) highlighting that only few compositions have been produced on the pilot-scale preserving the nanoparticle characteristics as synthesized on the lab-scale [66]. Among these are the pilot-scale gas burner (Figure 2.1c) and the pilot-scale spray burner (Figure 2.1d) utilized for nanoparticle synthesis at the IUTA [67, 68] that are investigated in the present thesis.

To characterize nanoparticles during and after synthesis, a multitude of different measurement techniques is required. For particle analysis, common tools are listed in the following whereby those suitable for *in situ* characterization are marked with a (\*):

- Scanning Mobility Particle Sizer (SMPS)\* and Particle Mass Spectrometer (PMS)\* to determine particle size in the gas phase

- Scanning Electron Microscopy (SEM) and Transmission Electron Microscopy (TEM) for particle size and morphology in the solid phase
- Gas adsorption according to Brunauer-Emmett-Teller (BET) to measure the specific surface area of a (porous) micro structure
- X-ray diffraction (XRD), Fourier-Transform Infrared (FTIR) Spectroscopy, and Scanning Auger Microscopy (SAM) to determine phase composition and chemical composition,
- Energy-dispersive X-ray spectroscopy (EDS) and X-ray photoelectron spectroscopy (XPS) for analyzing the surface contamination (i.e., elemental surface composition), and
- Differential Scanning Calorimetry (DSC) and Thermogravimetric Analysis (TGA) to obtain for instance heat capacities, thermal decomposition rates, and phase transition phenomena (glass transition, crystallization, melting).

This enables the investigation of many important materials properties of the synthesized nanoparticles. However, the reaction process itself needs to be characterized to understand why which particle properties have developed and by which process parameters the final product can be optimized for a given application. To improve or modify the final product, e.g., smaller size distributions, shift of reaction towards a specific phase or morphology, synthesis of core-shell materials or composites [29], and to enable higher production rates while preserving the desired product quality, detailed knowledge of a burners flow field is required.

## 2.2 Optical diagnostics of non-reacting and reacting flows related to nanoparticle synthesis

A large number of measurement techniques is available for the characterization of flows. Inexpensive and therefore frequently used instruments are for example thermocouples (for temperature measurement) or hot-wire anemometers (for measuring gas-phase velocities and mass flows). While the disturbances caused by such probes are irrelevant for many applications, their introduction into processes like flame synthesis of nanoparticles results in a drastic change in the local environment to which a nanoparticle-loaded flow is exposed there. Consequently, the results obtained do not reflect the state that would prevail at the respective location without the interference caused by the measuring instrument. This is why optical diagnostics are used to characterize flows related to nanoparticle synthesis. Among their merits are the ability of being non-intrusive, instantaneous, spatially and temporally-resolved, and capable of detecting several quantities simultaneously [69, 70]. One of the best-known examples is infrared pyrometry (chapter 2.2.1) that can be used to measure the surface temperature of objects without contact.

Table 2.1 gives an overview of common optical diagnostics for flow characterization whereby the techniques utilized in this thesis are highlighted in bold type. Some of the listed techniques are capable of detecting multiple quantities (simultaneously) that are not considered in this overview. More detailed insights as well as further optical diagnostics can be found, for instance, in the reviews by Aldén et al. [71], Tropea [72], Fansler et al. [73], Dreier et al. [21], and Xu et al. [74].

Table 2.1: Optical diagnostics for quantitative characterization of (reacting) gas-phase and multi-phase flows. Those commonly applied in flames to investigate the corresponding target quantity are marked with \*. The measurement techniques used in this thesis are highlighted in bold type.

Target quantity	Measurement technique
Gas-phase temperature	Coherent anti-stokes Raman scattering (CARS)* [75-77]
	<b>Laser-induced fluorescence (LIF)*</b> [78, 79]
	Filtered Rayleigh scattering (FRS)* [80, 81]
Gas-phase velocity	Tunable diode laser absorption spectroscopy (TDLAS)* [82-84]
	Filtered Rayleigh scattering (FRS) [85-87]
	Laser Doppler anemometry (LDA)* [88, 89]
Droplet velocity	Molecular tagging velocimetry (MTV)* [90-92]
	<b>Particle image velocimetry (PIV)*</b> [93, 94]
	<b>Diffuse back illumination (DBI) / multi-pulse RGB shadowgraphy</b> [95-97]
Droplet size	Digital in-line holography (DIH) [98-100]
	<b>Laser Doppler anemometry (LDA)*</b> [101, 102]
	<b>Particle image velocimetry (PIV)*</b> [103, 104]
Intermediate species concentrations	Interferometric laser imaging droplet sizing (ILIDS)* [105-107]
	Laser diffractometry (LD) [50, 108, 109]
	<b>Phase Doppler anemometry (PDA)*</b> [110, 111]
Intermediate species concentrations	Wide angle light scattering (WALS)* [112-114]
	Cavity-ring-down absorption spectroscopy (CRDS)* [115, 116]
	Fourier-transform infrared spectroscopy (FTIR)* [117-119]
Intermediate species concentrations	Intra-cavity laser absorption spectroscopy (ICLAS)* [120-122]
	<b>Laser-induced fluorescence (LIF)*</b> [60, 123]

All measuring techniques utilized in this work have in common that they investigate physical quantities (e.g., temperature or velocity) of the measuring object (e.g., burner surface or flow field) optically. For that, the diagnostic tools exploit the physical principles of light-matter interaction like absorption, emission, and scattering. Fundamentals on optics [124-127], quantum physics [128-130], spectroscopy [131-134], lasers [135-138], detectors [124, 134, 139, 140], and many more (e.g., electronics and data processing) are needed to fully describe the diagnostics presented in the following. Since the objective of the present work is to characterize the flow field of nanoparticle synthesis burners, these broad and interdisciplinary-linked topics are narrowed down to keep the focus of this work on the results achieved. Therefore, the applied optical diagnostics are described briefly in the following. For more in-depth details, please refer to the given references.

### 2.2.1 IR pyrometry

Infrared pyrometry is a non-intrusive optical technique for quantitative measurement of surface temperatures. They enable quantitative *in situ* measurements at high temporal and spatial resolution [141] in a broad field of applications, e.g., in medicine [142, 143], the building sector [144] and many more [145]. Compact and robust systems enable measurements in harsh environments for instance

in robot-assisted inspections of large industrial plants [146] or in aerospace investigations [147]. A variety of commercial vendors such as IRCAM, Jenoptik, FLIR Systems, Fluke, Telops, and Princeton Instruments offer turn-key applications comprising all required hardware and software. In the following, the background knowledge required to understand the underlying measuring principle is outlined before the operation of thermographic cameras is introduced.

Every physical object with a temperature above the absolute zero point emits electromagnetic radiation or light that is called thermal radiation. Kirchhoff found that the more radiation a body absorbs, the more it emits [148]. In literature, the model of an ideal temperature radiator (blackbody or blackbody radiator) is used. The blackbody radiator completely absorbs all light of all wavelengths hitting its surface and emits light depending on its temperature, only [149]. Planck's radiation law [149] describes the relationship between the emitted light intensity, the wavelength of the emitted light and the temperature of the black body. As the temperature rises, the intensity of the emitted radiation increases and the spectrum shifts to shorter wavelengths (Figure 2.2).

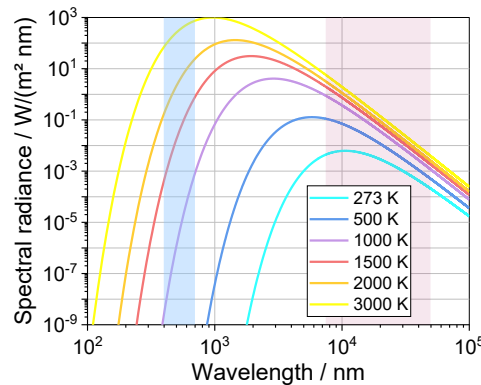


Figure 2.2: Spectral radiance of a blackbody radiator calculated according to Planck's law [148]. The spectral region visible to the human eye is highlighted in blue while the spectral region detectable by common infrared cameras using micro-bolometers [150] is highlighted in red following Ref. [151].

A direct relationship between the peak of the emission-spectrum of a blackbody radiator and its temperature is described by Wien's displacement law (eq. 2.1). It can be regarded as a limit case of Planck's law for small wavelengths [152]. From eq. 2.1, it can be seen that, for example, doubling the temperature of the blackbody radiator halves the emitted wavelength.

$$\lambda_{\max} / \mu\text{m} = \frac{b / \mu\text{mK}}{T / \text{K}} \quad 2.1$$

Here,  $b = 2897.7685 \mu\text{m K}$  is called Wien constant. Through integration of Planck's law over the entire wavelength range the Stefan-Boltzmann law can be derived (eq. 2.2), according to which the radiation power of a blackbody radiator is independent of the wavelength and increases with the fourth power of temperature.

$$\dot{E} = \sigma T^4 \quad 2.2$$

Here,  $\sigma = 5.6704 \times 10^{-8} \text{ Wm}^{-2}\text{K}^{-4}$  is called Stefan-Boltzmann constant. With that, the relation between wavelength, temperature and radiation power is described for an ideal blackbody radiator. To approximate the surface temperature of non-ideal (i.e., real physical) objects like the burner investigated in the present thesis more closely, the theoretical expressions need to be modified.

A commonly used approximation is the model of the graybody radiator. Like the blackbody radiator, the graybody radiator emits an isotropic continuous spectrum [149]. Its overall radiation intensity is reduced compared to an ideal blackbody radiator by a wavelength-independent proportionality factor called emissivity  $\varepsilon$ . The emissivity is defined as the ratio between the thermal radiation of a real surface to the thermal radiation of a blackbody radiator at the same temperature [153]. By that, it takes values in the range of  $0 < \varepsilon < 1$ , while  $\varepsilon = 1$  is synonymous for the blackbody radiator. However, real physical surfaces (also called selective radiators) require more complex approximations since the spectrum of thermal radiation of a selective radiator differs from the model of the gray body. Instead of a single proportionality factor  $\varepsilon$ , selective radiators emit spectra showing wavelength-dependent intensity fluctuations [149]. There is no common theory for describing the thermal radiation of real objects, so for detailed investigations calibration measurements are needed to determine the wavelength-dependence of the emissivity of each individual object [154]. For more-detailed insights on the radiation of real surfaces, see Ref. [154].

The contact-free measurement of temperature via thermal radiation emitted by an object is called pyrometry. In contrast, thermography denotes spatially resolved pyrometry that is most commonly achieved by the use of infrared cameras. The core components of these cameras are IR-transmissive lenses (e.g., calcium fluoride, germanium, or zinc selenide) and IR sensitive detectors. With regard to the detectors, a distinction must be made between two physical quantities that are being utilized: Photons or thermal energy [155]. Photon-based detectors are made of Indium Gallium Arsenide (InGaAs), Indium Antimonide (InSb), or Cadmium Mercury Telluride (MCT) used as direct bandgap semiconductors [156] or (InAs/GaAs) quantum dots [157-159]. Photonic detectors provide high sensitivity (approx. 25 mK at 30°C object temperature) but need to be cooled to reduce noise, which causes high equipment and operating costs [151]. Besides higher temperature sensitivity, their reaction time is faster compared to thermal detectors [155].

Thermal detectors are lower in cost and are made of vanadium oxide or amorphous silicon, e.g., applied in thermopiles and (micro-) bolometers [151, 159]. They are temperature stabilized at (or close to) ambient temperature, e.g., by a Peltier element [145]. The electronic signal is generated by the change in temperature that occurs when the IR radiation is absorbed by the detector surface [150]. Compared to photonic detectors, thermal detectors provide a lower sensitivity (approx. 80 mK at 30°C object temperature) and slower reaction times. However, in contrast to photodetectors, the sensitivity of thermal detectors is almost wavelength-independent. More details can be found in the work of Rogalski [159].

In post processing, the recorded raw data can be corrected, e.g., by specifying the emissivity of the examined object or the transmittance of a window between object and camera [150]. The false-color assignment can then be adjusted individually so that conclusive two-dimensional temperature fields (called thermograms) can be produced (e.g., Figure 3.7). In the experimental section (chapter 3.2.1), the most important parameters and settings used for data acquisition and evaluation of the results presented in this thesis are listed. Moreover, the digital raw data (cf., chapter A3.1.1) contain all parameters used.

### 2.2.2 Gas-Phase Thermometry via Multiline Laser-induced Fluorescence Imaging

Multiline NO-LIF thermometry is an optical technique for non-intrusive measurement of the gas phase temperature. It enables *in situ* imaging measurements at high spatial resolution even in reactive processes like nanoparticle synthesis in plasma [79] and (spray-) flame reactors [60, 160]. In contrast to two-line techniques [161, 162], multiline NO-LIF thermometry is calibration-free and is applicable to systems where background signals cannot be avoided [160]. So far, no commercial providers are offering this technology as a turnkey application with all necessary hardware and software.

The technique uses gaseous species such as OH [163, 164], NO [160, 165], or SiO [61, 166], that are exploited as target for spectroscopic temperature measurements. In the present thesis, nitric oxide (NO) is used because it can be easily added to the gas flow (typically from a gas mixture diluted in Argon) and does not decompose in the entire area of interest allowing measurements at (high) flame temperatures as well as at (low) temperatures of the surrounding gas inside the reactor [78]. Often, NO is artificially added to the flame in low concentrations (typically 100–2000 ppm) [78, 167], but the technique also works without additional NO-seeding in systems where NO is naturally formed at sufficient concentrations [168].

To record a two-dimensional (2D)-temperature field, a pulsed laser beam is expanded to a laser sheet by the use of lenses (e.g., Galilean telescope arrangement [169]) before crossing the flame (Figure 3.5). Subsequently, the laser is spectrally scanned over a specifically selected wavelength range (i.e., a suitable absorption band of the NO molecule) for which excimer lasers or dye lasers are frequently used [78, 170]. For multiline NO-LIF thermometry, the A-X(0,0) vibrational electronic absorption band at 225 nm is widely used [14, 167, 168]. For alternative applications like NO concentration measurements in flames the D-X(0,1) band at 193 nm [171, 172] and the A-X(0,2) band at 247 nm is suitable [173] while at high pressure above ten atmospheres the A-X(0,1) band at 236 nm can be employed [174, 175].

By scanning the laser wavelength through absorption transitions (i.e., lines), multiple rotational ground state energy levels of the NO molecule are probed (hence, “multiline”) measuring the induced fluorescence intensity [78, 176]. Every line has a specific fractional population  $f_b$  resulting from the Boltzman distribution that mainly depends on the temperature of the molecule [177]. Assuming thermal equilibrium in the investigated flames, the molecules (vibrational and rotational) temperatures are equal and the same as the (translational) flame temperature. The photon energy absorbed by the NO molecule [178] causes a transition to an electronically excited state (explained in detail in books such as [131] and [179]). However, the electronically excited state is not stable so the system returns to its ground state after a certain time (several nanoseconds) by radiative (fluorescence) and non-radiative processes (e.g., inter-molecular collisions, called quenching). The fluorescence emitted by the NO molecules (i.e., the NO-LIF signal) is detected spectrally integrated with an intensified CCD camera (ICCD) positioned perpendicular to the laser sheet (Figure 3.5). Since the fluorescence intensity  $I_{\text{LIF}}$  emitted by the excited molecules is typically not detected over the entire room angle  $4\pi$ , the signal detected by a camera for the limited detection angle  $\gamma$  and the limited quantum efficiency  $QE$  can be described for low laser intensities (i.e., the linear regime, where the fluorescence is proportional to the laser intensity) as follows [180]:

$$I_{\text{LIF}} \propto b_{12} N f_b \Gamma I_{\text{Laser}} \frac{A_{21}}{A_{21} + Q_{21}} \frac{\gamma}{4\pi} QE \quad 2.3$$

Here,  $I_{\text{LIF}}$  is the fluorescence intensity ( $\text{W}/\text{m}^2$ );  $b_{12}$  is the absorption rate ( $\text{s}^{-1}$ ) of an incident laser photon that excites a molecule from the ground state to the excited state;  $N$  describes the number density ( $\text{m}^{-3}$ ) of the probed NO molecules;  $f_b$  is the Boltzmann population of the ground state;  $\Gamma$  is the dimensionless overlap fraction between the spectral profile of the incident laser beam and the absorption line;  $A_{21}$  is the Einstein coefficient describing the fluorescence rate ( $\text{s}^{-1}$ ) of a photon from an excited state while the system relaxes to the ground state;  $Q_{21}$  is the quenching rate ( $\text{s}^{-1}$ ) [180, 181]. For a comprehensive explanation of laser-induced fluorescence see, for instance, [17] and [182].

Figure 2.3 shows exemplary excitation spectra for the scan range employed in this work that was extensively investigated in previous studies [78, 170, 183] to assure high temperature sensitivity between 250–2500 K [14]. The five “peaks” shown in the diagram consist of a total of twelve partly overlapping absorption transitions, each of which possesses individual ground state energies [176]. Depending on the absorption band used for NO excitation, the fluorescence can be detected blue or red shifted [181, 184]. Therefore, bandpass filters (e.g., dielectric reflection bandpass filters [181]) are commonly used to suppress the laser wavelength and enable detection of the fluorescence light whose intensity is several orders of magnitude weaker compared to the exciting laser light.

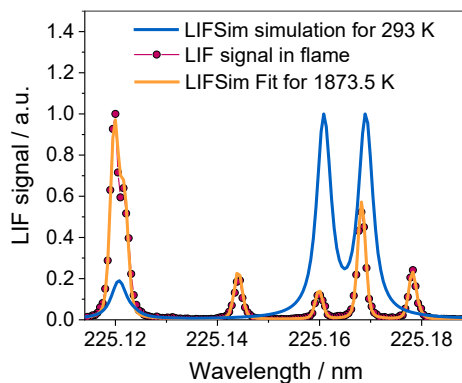


Figure 2.3: Background subtracted experimental (symbols) and fitted excitation spectra (orange line) when scanning the laser wavelength over the rotational lines between 225.114–225.19 nm (i.e., 44407–44422  $\text{cm}^{-1}$ ) in the NO A-X(0,0) band at 900 mbar. To illustrate the temperature dependence of the NO spectrum, an excitation spectrum for room temperature (293 K, 900 mbar) is plotted (simulated with LIFSim Desktop, cf., chapter A4.3).

At each laser spectral position, multiple NO-LIF images are recorded using an ICCD camera. The number of recorded images per wavelength position (generally between 10 and 50 images) is mostly determined by the necessary signal-to-noise (SNR) ratio to achieve a certain temperature precision [183]. When the spectral position of the laser is not resonant with the transitions of the NO molecule (e.g., at 225.135 nm, cf. Figure 2.3) only noise background can be detected (“baseline”), while at the specific NO absorption lines (e.g., 225.12 nm) a LIF signal can be detected that is proportional to the temperature-dependent Boltzmann fraction and the line strength (cf., equation 2.3) [174].

To obtain a temperature field from the camera images, a software (LIFSim) is used that is introduced in [78, 185]. Based on spectroscopic data (of the NO molecule) and the model for calculating LIF signals implemented in LIFSim, NO-LIF spectra can be simulated. In the post processing, the simulated spectrum is fitted to the experimental excitation spectrum extracted from each pixel of the NO-LIF images (an exemplary NO-LIF image from the image stack is presented in Figure 6.8).

For spectra fitting, initial values are predefined that are iteratively adjusted with a least-squares solver to minimize the residual between experimental and simulated data. The spectral position of the

measured peaks and the Gaussian and Lorentzian contributions to the Voigt profiles (used to model the absorption lines and the laser's spectral distribution) are crucial for achieving good fit results [185]. The result of the LIFSim fit is a single, unambiguous temperature that corresponds to the simulated spectrum [14], e.g., the corresponding temperature of the simulated spectrum shown in Figure 2.3 is 1873.5 K). This way, the temperature is determined for each pixel of the NO-LIF images, resulting in a time-averaged 2D-temperature map (e.g., Figure 6.11). The most significant parameters and settings for data acquisition and post processing of the results presented in this thesis are documented in the respective experimental sections (chapters 3.2.2, 4.2.2, and 6.2.3). In addition, all parameters used are provided together with the digital raw data (cf., chapter A3).

### 2.2.3 Particle Image Velocimetry

Particle Image Velocimetry (PIV) is an optical technique for non-intrusive measurement of gas-phase and liquid-phase velocities. Due to its scalability, PIV enables imaging *in situ* measurements at high spatial resolution for instance in macro-flows of (industrial) burners [186, 187], around full-scale cars [188], behind airplane wings in a wind tunnel [189], in micro-flows [190] (e.g., to investigate the flow inside a sub-millimeter size droplet [191]), and many more applications [192]. Multiple commercial vendors like TSI, Dantec Dynamics, ILA, Oxford Lasers, and LaVision offer turn-key applications including all required hardware and software.

Some basic features of the technique are known from everyday life, e.g., when small dust particles are swirled-up while getting illuminated by sunlight. Those dust particles make the air flow indirectly "visible" and the observer can draw qualitative conclusions about the direction of air movement and recognize potential vortices. Likewise, PIV uses  $\mu\text{m}$ -size particles or droplets ("seeding") that are laterally illuminated by an intense light source ("illumination") to measure the flow velocity magnitude and direction (Figure 4.3). For illumination, pulsed Nd:YAG solid-state lasers that emit monochromatic light at high energy densities are most commonly used [193] whereby intensive scattered light is generated at the seeding-droplets. A key principle of PIV is based on the ability that two laser pulses can be emitted shortly after each other with a precisely definable time interval (usually  $\mu\text{s}$ -scale). To this end, generally two individual Nd:YAG lasers are employed whose beam paths are superimposed enabling the time interval between both lasers getting accurately triggered, e.g., by a pulse-delay generator [194].

For the seeding of liquid flows, particles (e.g., glass spheres, baby powder, or titanium dioxide) are utilized while for seeding gas-phase flows, liquid droplets (e.g., from cooking oil, di(2-ethylhexyl) sebacate (DEHS), or silicon oil) are used [195]. An overview of different seeding materials is provided in [193, 196]. The choice of proper seeding must be individually adapted to the investigated flow field, however, cooking oil or DEHS are suitable for seeding gases in most applications [197]. Since PIV is applied in the present thesis to characterize gas-phase flows, the term "seeding-droplets" is used in the following. The seeding droplets have to satisfy two (contradictory) requirements, since they (1) need to be able to follow the flow and (2) need to scatter enough light to be clearly distinguishable from the background on the camera images.

The ability of droplets to follow the flow (1) can be estimated according to [198] for stationary flows and low Reynolds numbers. Another method to determine the velocity lag (or "slip velocity") is described by [193] and [196]. Accordingly, the decisive variables are the droplet diameter, the density

difference between the seeding droplets and the surrounding medium, and the viscosity of the surrounding medium. Since the medium is frequently subject of the investigation (and therefore not exchangeable) and the density difference between liquids and gases cannot be reduced arbitrarily, the droplet diameter must be as small as possible to be able to follow a flow optimally. Detailed calculations for DEHS in air (the system investigated in the present thesis) are provided by Engel, where, for example, the stopping-distance of the particles as well as the maximum fluctuation frequency of a flow are analyzed depending on the droplet diameter to check the suitability of the seeding in radial turbomachinery [199].

To calculate the intensity of the scattered light (2), Mie theory can be used that applies to (spherical) droplets whose diameter is larger than the wavelength of the incident light [182]. According to Mie theory, the intensity of the scattered light depends on the observation angle, the refractive index of the medium, the droplet size, and the wavelength and polarization of the incident light. In literature, diagrams are available for common drop sizes and seeding materials that quantify the complex spatial distribution of the scattered light at different drop diameters, as shown for example for DEHS in air by Engel [199]. Since the observation angle cannot be varied arbitrarily for imaging techniques, it is crucial that seeding droplets are as large as possible to achieve highest scattered-light intensity. Thus, a compromise needs to be made in the experiment, where the seeding droplets are small enough to follow the flow accurately, but large enough to scatter light sufficiently. To atomize the seeding liquids, commercial suppliers offer aerosol generators (“seeder”) that assure generation of droplet sizes around 1  $\mu\text{m}$  for a certain atomization-gas mass-flow range [200, 201].

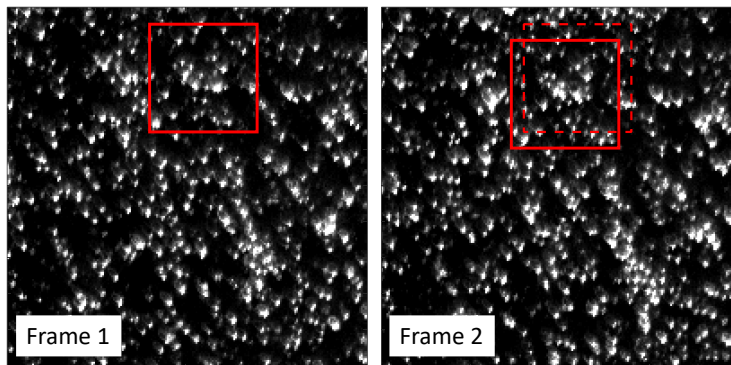


Figure 2.4: Cutout region of a PIV double-frame highlighting an arbitrarily selected interrogation area of 60×60 pixels (red) that is shifted 7 pixels to the left and 11 pixels downwards between frame 1 and frame 2. Together with the time delay between both frames, a vector can be derived indicating the (in-plane) velocity magnitude and direction.

To record a 2D-velocity field, the pulsed laser beam is expanded to a laser sheet and guided through the flow field. The light scattered by the seeding-droplets at the first laser pulse is detected by a camera positioned perpendicular to the laser sheet (Figure 5.3). After a defined time interval, the second laser pulse (from the second Nd:YAG laser) is emitted that – again – causes straylight on the seeding droplets. Both straylight pulses can either be detected on a single camera image (double-exposure, single-frame systems) or on two separate image frames (single-exposure, double-frame systems) [202]. Since double-frame detection is applied in the present thesis, exemplarily signals detected on each camera frame are presented in Figure 2.4.

In the experiment, the seeding density must be optimized, which requires experience of the experimenter, so that neither too few nor too many spots are visible on the camera images [193]. On the

other hand, the time interval between both laser pulses (called “delay time” or “ $dt$ ” in the following) needs to be adjusted so that a spatial displacement between the scattered spots detected on both frames can be recognized. In general, 5 pixel displacement is aimed for most applications [193]. Commercial vendors like LaVision provide integrated tools for software-aided optimization of the delay times (e.g., DaVis “ $dt$ -optimizer” dialog [203]).

The double frames generated that way contain all information required to calculate the velocity field. For evaluation, the first frame is divided into a predefined grid (after optional pre-processing), so that the entire image area now consists of several subfields (“interrogation areas”) [193, 203]). The choice of the subfield size determines the maximum number of vectors in the evaluated velocity field and is selected by the user along with many other parameters. Detailed explanations of the parameters required for acquisition and evaluation of PIV images are comprehensively provided in the book by Raffel et al. [193]. In each interrogation area, a unique spot distribution (spot pattern) can be found that is comparable to a fingerprint within the evaluated image. During evaluation, each spot pattern of frame one is searched in frame two. For double-frame image acquisition, a cross-correlation algorithm determines the direction and distance by which the interrogation areas of both frames (red rectangles in Figure 2.4) are shifted relative to each other [104]. Since the time interval between both frames (i.e., both laser pulses) is known, the velocity can be calculated by the determined spatial distance. Thus, the velocity and direction for each interrogation area of the PIV image is determined composing an instantaneous 2D vector field.

Depending on the selected evaluation software, various options are available for further post processing [193, 203]), enabling for instance sophisticated vector validation [204, 205] and quantification of uncertainties [206, 207]. By averaging a series of evaluated double-frame images, conclusive two-dimensional velocity fields can be obtained (e.g., Figure 4.5). The most significant parameters and settings for data acquisition and post processing of the results presented in this thesis are documented in the respective Experimental sections (chapters 4.2.1 and 6.2.1). In addition, all parameters used are provided together with the digital raw data (cf., chapter A3) as DaVis SET-files.

#### 2.2.4 Laser Doppler and Phase Doppler Anemometry

Laser Doppler Anemometry (LDA) or Laser Doppler Velocimetry (LDV) is an optical pointwise technique enabling non-intrusive measurement of droplet velocities [208]. LDA can also be used to measure gas-phase velocities [88] by artificial particle seeding to the flow (similar to PIV, cf. chapter 2.2.3). However, since liquid sprays are examined with this diagnostics method in the present work, the functioning principle will be explained by the example of droplets. Phase Doppler Anemometry (PDA) is an optical technique for non-intrusive droplet-size measurements that has a strong technical overlap to LDA [209]. In literature, the technique is also designated as an extension of LDA [210], which is why authors frequently only use the term PDA or Phase Doppler Interferometry (PDI) even though – besides droplet sizes – also droplet velocities are measured [110, 111, 211]. LDA and PDA enable *in situ* measurements at high temporal resolution ( $> 100$  kHz for individual events) for instance for the characterization of atomizer nozzles under non-reacting conditions [212] and in (nanoparticle synthesizing) spray flames [102, 111, 213]. They enable measurements in high-pressure atmospheres like for instance inside the combustion chamber of IC engines [214-216] and are applicable in harsh environments, e.g., for dust and cloud analysis in aircraft-based measurements [217, 218]. Multiple commercial vendors like LaVision (Phase Doppler Interferometer), TSI (Phase Doppler Particle Analyzer),

Dantec Dynamics (Phase Doppler Anemometer), and Artium (also denoted as Phase Doppler Interferometer) offer turn-key products comprising all required hardware and software.

In its simplest configuration, LDA consists of four components: a (stationary) laser, a (moving) scattering object, a (stationary) detector (photodiode or photomultiplier), and a unit for signal evaluation (signal processor). The two-beam LDA configuration has established as standard [219] where the light emitted by a continuous wave single-mode laser (argon-ion gas lasers or solid-state diode lasers are frequently used [209]) is split into two beams by a beam splitter before both laser beams are focused (overlapped) by a lens to form the probe volume in which the droplets scatter the laser light (Figure 5.4). The technique requires that there is a single droplet only inside the probe volume at a given time since otherwise measurement errors falsify the results [208].

To determine the droplet velocity, exact knowledge about the dimensions of the probe volume and the fringe pattern is required. With that, the velocity can be calculated by the frequency of the light-intensity fluctuations scattered by a droplet crossing the probe volume. The detected burst signal is proportional to the velocity magnitude of the droplet (more precisely: its velocity component perpendicular to the fringe pattern) [209, 219]. Another way to explain the underlying principle is based on the fact that the laser light experiences a frequency shift when it is scattered on a moving droplet [208]. The frequency shift between the original laser wavelength and the wavelength of the scattered light is called Doppler shift (see Doppler effect, e.g., [148]) and is proportional to the velocity of the droplet. Thus, the scattered light from a droplet crossing the probe volume consists of two (different) Doppler shifted frequencies that are superimposed on the detector and create a beat frequency (due to their small frequency difference) [219]. For typical flows, this frequency lies in the MHz range whereby it is easy to measure by conventional photo detectors [209].

In the simple two-beam LDA configuration, the flow-direction of a droplet cannot be determined (directional ambiguity) because identical frequencies in the signal fluctuation are measured, regardless of whether a droplet crosses the fringe pattern perpendicularly from bottom to top or vice versa [219]. Thus, one of both laser beams is frequency shifted using for instance a diffraction grating or a Bragg cell [209], before both beams are intersected by a lens. By that, the (interference) fringe pattern generated in the probe volume becomes unsteady (i.e., it moves with or against the flow-direction of the droplet). Thereby, the detector receives a higher frequency Doppler burst when a droplet crosses the probe volume against the movement-direction of the fringe pattern (and vice versa) [208, 219].

To determine droplet sizes simultaneously with the droplet velocity, a second detector is required that enables employing the geometrical fact that the optical path length of the light scattered on a droplet in the probe volume is different for two observers at different spatial positions [220]. Thus, two (stationary) photo detectors receive the light scattered by a droplet with a certain time delay depending on their angular position [221]. Both signals carry identical Doppler frequencies (corresponding to the droplet velocity), but due to the time delay of the detection, a phase shift can be observed when comparing the respective signal bursts obtained by each photo detector [221]. Durst and Zaré showed that the phase shift depends linearly on the droplet diameter [222]. For infinitesimally small droplets, the phase shift is zero and the bigger the diameter of a (spherical) droplet, the bigger its induced phase shift.

As the droplet size increases, the phase difference becomes so large that it can no longer be clearly determined from the periodic signal whether the signal is shifted by one phase (i.e.,  $2\pi$ ) or more. This

is called  $2\pi$ -ambiguity, where the measured phase difference can be assigned to more than one droplet size [221]. Multiple methods are available to overcome this issue, e.g., a pure software-related solution determining the time shift between both detector signals, and multiple hardware-related solutions using three or more detectors [209]. Combining the conventional two-detector PDA with a planar PDA in a single optical receiver, one obtains a dual-mode PDA (or simply Dual PDA, Figure 5.4) [209]. This configuration is capable of measuring two independent droplet-sizes of one and the same droplet simultaneously to detecting two droplet-velocity components [221]. By comparing both measured droplet sizes with each other, the dual PDA is able to detect non-sphericity of droplets accurately, which is not possible with three or less detectors [223]. In the spherical validation, a droplet is rejected from the results if the difference between both measured droplet sizes is greater than a certain threshold, i.e., when the droplet shape deviates too much from sphericity [223].

Besides spherical validation, multiple other validation criteria are applied when processing the raw data (e.g., signal-to-noise, level ratio, coincidence, amplitude, and transit-time validation [209, 224]), before they are considered trustworthy [209]. However, if the adjustable parameters (e.g., laser beam power, amplification level of the photomultipliers, and signal gain [225]) are not chosen carefully, results may be validated but still be physically wrong (e.g., the determined droplet diameter may alter by a factor of two when parameters are selected inappropriately [225]).

Further potential for biasing the measurement of droplet sizes is related to the choice of the refractive index [226]. In reactive systems, e.g., spray flames, the droplet temperature may vary in a wide range up to the boiling point (e.g.,  $78.3^{\circ}\text{C}$  for ethanol [133]). Since the individual droplet temperature cannot be determined at the time of the PDA measurements, the user must select a single refractive index (each, for the liquid phase and the surrounding gas phase) in the software. Nevertheless, since the refractive index of the liquid is directly employed for the calculation of the droplet size (more precisely: when calculating the setup-specific phase factors [221]), it is obvious that deviations from the real physical droplet diameter might occur in flames. Therefore, an error estimation for the results presented in this work is provided in the appendix (chapter A1).

As LDA/PDA is a counting technique, a certain minimum number of samples (also called “counts”) at each measurement position is mandatory for obtaining statistically meaningful data that individually depends on the investigated flow [220]. Most studies, though, report at least 1000 counts per position [88, 101, 110, 211] while others use 40000 counts and more [111, 223]. The technique is limited to a maximum droplet flux (below  $10^{13} / \text{m}^2 \text{ s}$ ) where the measured data results from superimposed signals caused by multiple droplets that are crossing the probe volume simultaneously [227]. Extremely high droplet density may further lead to low signal-to-noise ratios due to light absorption of the surrounding droplets [228]. However, such high droplet flux is considered unrealistically high for practical applications [227]. Another limitation is that spherically shaped droplets are required [228], which is why measurements, e.g., on two-fluid nozzles, provide reliable data only above the zone of the primary spray break-up.

From the acquired results of each single droplet, statistics like mean value, standard deviation, span, spherical validation rate, number mean diameter (D10), area mean diameter (D20), and Sauter mean diameter (D32) can be calculated, while software solutions – like Dantec’s BSA Flow Software – provide fully automated determination of numbers that involve the size of the probe volume, e.g., droplet concentrations (droplets /  $\text{cm}^3$ ) and volumetric droplet flux ( $\text{cm}^3 / \text{cm}^2 \text{ s}$ ) [221]. However, even though these algorithms include correction functions (e.g., Dantec’s *Probe Volume Correction* (PVC)

[221]), special care should be taken when interpreting these numbers since it is known that, for instance, the Gaussian beam effect and the slit effect may imply uncertainties around 30% [101].

The final results are commonly plotted as axial profiles (e.g., Figure 5.16), radial profiles (e.g., Figure 5.26), but also depicted as two-dimensional interpolated maps (e.g., Figure 5.10). At each measurement position, the individual result of each validated sample data can be used to create histograms (e.g., Figure 5.14). The most significant parameters and settings for data acquisition and post processing of the results presented in this thesis are documented in the respective Experimental sections (chapter 5.2.2). In addition, all parameters used are included in the digital raw data (cf., chapter A3.3.2).

### 2.2.5 Multi-pulse RGB shadowgraphy for Particle Tracking Velocimetry

Multi-pulse Red-Green-Blue (RGB) Illumination is an optical technique developed at the IVG [13, 95], whereby the flow field is illuminated with a three-color high-power LED and droplet velocities are determined by subsequent Particle Tracking Velocimetry (PTV) [229].

RGB-PTV enables *in situ* imaging measurements of the droplet movement within short time intervals ( $<1 \mu\text{s}$ ) for instance for the characterization of two-fluid atomizer nozzles [96] or for determining liquid flow velocities in a water tank using seeding particles [95]. RGB illumination can be used for (in-cylinder) spray visualization and flow-velocity determination by analyzing the spray-front propagation of gasoline direct-injection sprays [96, 97]. Using Particle Image Velocimetry algorithms for post processing, similar techniques enable the investigation of 3D-velocity fields using single line-of-sight detection [230] as well as tomographic reconstruction [231]. So far, there are no commercial providers offering this technology as a turn-key application with all required hardware and software.

For RGB-PTV a (spray) droplet is illuminated by a sequence of (short) light pulses of three different colors. All pulses (red, green, and blue) are released within the exposure time of a single photo taken with a consumer digital single lens reflex (DSLR) camera [95]. The LED pulse-train is triggered by the consumer camera. When taking a photo, a signal is provided via the camera's flash trigger to a pulse-delay generator that generates separate trigger pulses with precise pulse widths and time delays for the LED driver [96]. For operating the LED's, a driver circuit is used that is capable of generating pulses down to 250 ns [232, 233]. The LED driver is supplied with voltage by a laboratory power supply and generates short current pulses that overdrive the three-color high-power LED (e.g., [234]) causing it to emit pulses higher than 75 W [95].

The pulse widths should be as short as possible to "freeze" the movement of the droplet on the image. On the other hand, the pulse widths should be as long as possible to provide sufficient signal that the highest possible contrast is created on the image. The time delay between the pulses should be long enough so that the droplets are not superimposed on the image and short enough so that the algorithm used in post-processing can correctly "connect" the shadows of a droplet to a trace.

The arrangement of camera and illumination source can be designed differently. In their study, Menser et al. [95] show that laser diodes can be used as an alternative to LEDs that illuminate the measurement volume from the side as a light sheet. This illumination has the advantage that only those droplets are illuminated that are located within the (thin) laser sheet, whereby less complex post processing is required. Nevertheless, for many applications like for the droplet sizes investigated in the present thesis (around  $15 \mu\text{m}$ ), side illumination causes low-contrast images (cf., section on Mie

scattering provided in chapter 2.2.3) [95]. Even if the laser diodes are replaced with a (high-power) LED, problems with the elimination of out-of-focus shadows in the post processing were reported when utilized in side-illumination leading to lower particle-tracking capabilities [95]. For these reasons, the shadowgraphic arrangement (Figure 6.3) has proven to be suitable for applications, where the camera is oriented towards the LED to detect droplet shadows (Figure 2.5a) [95, 96]. This arrangement is also known as diffuse back-illumination (DBI) [97]) and is similar, for instance, to the concept of Particle Shadow Velocimetry (PSV) introduced by Estevadeordal et al. [235].

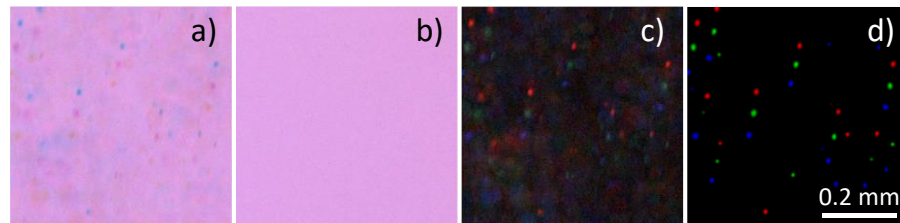


Figure 2.5: Close-up view of spray droplets originating from a downwards oriented two-fluid nozzle. (a) Raw shadowgraph illuminated with an RGB pulse train of a high-power LED, (b) background image, (c) color-inverted image, i.e. (c) = (b)-(a), (d) processed image.

Since the image post processing for RGB-PTV is performed in Matlab, the following paragraph is not formulated in a general manner. Instead, valuable insights into the first fully-automated workflow developed at the IVG are presented (for details on the Matlab script, see chapter 6.2.2 and Table A4.6). The image files need to be converted from their raw format (e.g., the proprietary Nikon Electronic Format “NEF”) to a lossless file format readable by Matlab [236]. For that, the software DCRaw [237] is used following the guidelines by [236, 238]. While preserving the original sensor data (i.e., no gamma correction, no color management, no white balance), demosaicing the Bayer-filtered images [239] is performed before converting them to 16-bit TIFF files. In the next step, the images are color inverted (Figure 2.5c), i.e., a background image (Figure 2.5b) is subtracted from the measurement image (Figure 2.5a). For further background correction, a median filter (Matlab function: medfilt2) and a morphological maximum filter (Matlab function: imopen [95]) is applied. Subsequently, the spectral overlap of the three color channels of the DSLR camera sensor is corrected (color cross-talk [240, 241]) according to Menser et al. [96]. After normalizing each color channel, intensity values below a certain threshold are set to zero. For further contour shaping and to further increase the droplet shadow intensities (Figure 2.6), a Gaussian mask correlation is applied [242].

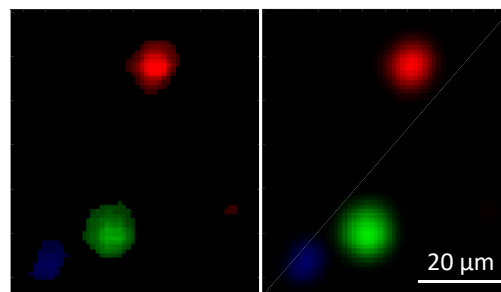


Figure 2.6: Background-filtered droplet shadows before (left) and after (right) Gaussian mask correlation.

The resulting images of each color channel are converted into binary images. By connected-component detection (Matlab function: bwconncomp), the center of each shadow is located and passed over to a particle-tracking algorithm (here: SimpleTracker [243]) as a list of  $x,y$ -coordinates. The PTV algorithm connects the three color channels of each droplet shadow to a “particle track” [244], so

that the spatial distance between the center points of each droplet can be calculated using simple trigonometry. By employing the time delay between the LED pulses used in the experiment, the velocity (magnitude and direction) of each section of the particle track (red–green, green–blue, and red–blue) of each droplet can be obtained. Therefore, RGB-PTV is also capable of detecting droplet acceleration using either a single RGB pulse train or a series of two (i.e., RGBRGB) or more consecutive pulse trains [96].

By evaluating a series of full-frame images, statistically meaningful (in-plane) velocity distributions can be determined (e.g., Figure 6.7). The most significant parameters and settings for data acquisition and post processing of the results presented in this thesis are documented in the respective experimental sections (chapter 6.2.2). In addition, all parameters used are provided together with the digital raw data (chapter A3.4.2).

### 3 Lab-scale premixed gas burner for nanoparticle synthesis

#### 3.1 Porous-bronze flat-flame burner

The investigated gas burner aims to generate a laminar one-dimensional premixed flat flame that is stabilized on a porous bronze matrix. This concept has been successfully used for more than twenty years at IVG-RF for nanoparticle synthesis in low-pressure flames [33]. The burner design investigated in this thesis provides simple operation due to less complex cooling compared to its predecessor versions [33, 34, 245, 246] and enables easy replacement of the porous bronze matrix as well as simple exchange of burners between the reactors, as all connectors have been standardized. Figure 3.1 shows a photo of the flat flame burner frequently used by the laser diagnostics group (Thomas Dreier) and the nanoparticle synthesis group (Hartmut Wiggers).



Figure 3.1: Photo of the flat flame burner after several hours of operation. Even though the matrix structure is not affected, precursor residuals can partially clog the porous bronze requiring replacement of the burner matrix. The modular design of the burner enables easy cleaning or replacement of the porous bronze. Figure 3.2 provides details of the burner design.

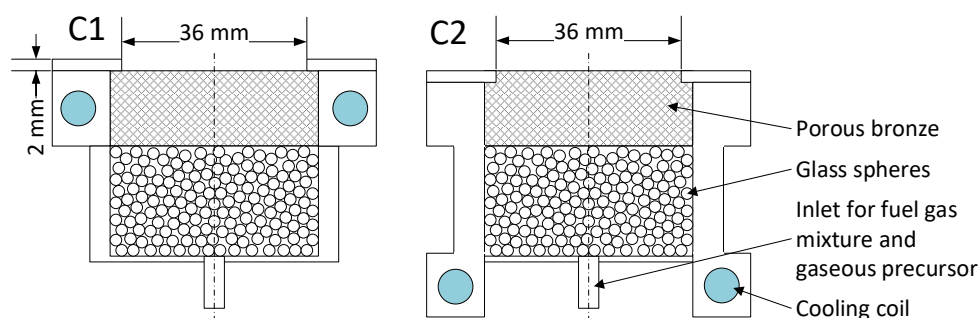


Figure 3.2: Hardware configuration C1 and C2 of the flat flame burner utilized in this thesis with 12 mm total height of the porous bronze matrix. In configuration C2, the cooling coil is located 70 mm below the burner surface.

The flat-flame burner uses a 36-mm diameter porous bronze [180] comparable to the modified McKenna burner introduced by Campbell et al. [247]. Together with the imposed mass-flow rates, the production rate of the flat flame burner is in the order of a few grams of nanoparticles per hour, which is high enough to perform detailed particle analysis, but low enough to avoid blocking of probe-sampling nozzles and window fouling [248]. The burner can be operated in a pressure range from atmospheric pressure down to a few millibar with either methane or hydrogen. It is suitable for precursors that have a high vapor pressure such as hexamethyldisiloxane, iron pentacarbonyl, and tungsten hexafluoride. Hence, the burner provides an ideal environment for investigating the fundamentals of

flame-based nanoparticle synthesis (chapter 2.1). Versatile nanoparticle diagnostics have been utilized on this burner in recent works [60, 248-251] via molecular-beam sampling:

- Particle growth by measuring number-based particle mass distribution by particle mass spectrometry (PMS) at different heights above the burner (HAB)
- Mass-based distribution of charged nanoparticles by application of a quartz crystal microbalance (QCM)
- Charging probability and deposition-rate of nanoparticle fractions by combining PMS and QCM
- Identification of decomposition products of various precursors and the intermediate species by time-of-flight mass spectrometry (TOF-MS).

The burner has also been used for the ongoing development of *in situ* optical diagnostics like multiline NO-LIF thermometry (chapter 2.2.2), multiline SiO-LIF thermometry (where intermediate species naturally occurring during silicon-containing precursor decomposition are used for imaging temperature measurements), as well as a combination of LIF and Rayleigh scattering for measuring absolute gas-phase concentrations of silicon monoxide [22, 61, 166, 252, 253].

To provide constant synthesis conditions and to prevent the matrix from melting (i.e., losing integrity of its porous structure), the flat flame burner needs active cooling. Figure 3.2 illustrates both cooling configurations investigated in this work:

1. Configuration C1: A single cooling coil surrounding the porous bronze
2. Configuration C2: A passive cooling body around and below the porous bronze that is cooled by a cooling coil located 70 mm below the porous bronze

In the more recent burner configuration C2, the surface of the porous plug and the mounting plate are flush, allowing full optical access from the side to the burner surface. In addition, the position of the cooling coil was moved 70 mm below the porous bronze in configuration C2 aiming to reduce the radial temperature gradient discussed in Ref. [248]. For practical reasons, a homogeneous cooling with simultaneous uniform gas supply is not feasible and it is known that in the outer area of the matrix, the flame deviates from its one-dimensional structure [254]. As shown by Kluge et al. [60], two-dimensional gas temperature fields exhibit a radial variation in planes perpendicular to the burner surface. Therefore, the assumption of temperature and species concentration being independent of the radial position of the burner needs to be investigated.

Consequently, the influence of the operating conditions and both cooling configurations on the surface-temperature distribution of the flat flame burner was analyzed by pyrometric imaging (chapter 3.3.1). Using multiline NO-LIF thermometry, the gas-phase temperature of the burner is characterized *in situ* during operation with and without iron pentacarbonyl and tungsten hexafluoride as precursor (chapter 3.3.2). To investigate the effect of both cooling designs on the gas-phase temperature, radial profiles of the matrix temperature and the gas-phase temperature in close vicinity of the burner are compared in chapter 3.3.2.

## 3.2 Experimental

### 3.2.1 IR pyrometry

The flat flame burner (Figure 3.2) was installed inside a low-pressure flame reactor operated at 30 mbar. The cylindrical, stainless steel reactor chamber has an inner diameter of 100 mm. Four quartz windows provide optical access to the burner from the side (further details are provided in Ref. [255]). At the upper part of the reactor, a T-pierce was installed to extract the exhaust gases from the side allowing to install a window (W1) at the top of the reactor chamber to provide optical access from above as indicated in Figure 3.3.

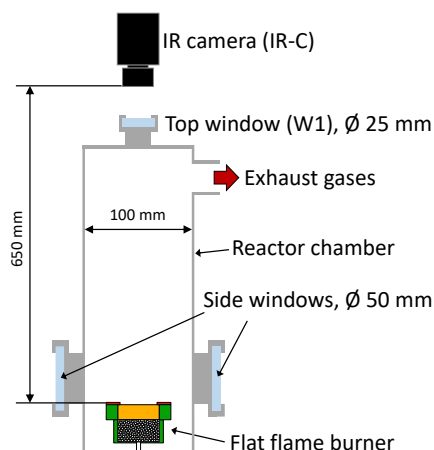


Figure 3.3: Side view of the experimental setup of the thermographic camera installed at a low-pressure flame reactor commonly used at the IVG for nanoparticle synthesis. For clarity, only two side windows are shown.

An IR camera (IR-C, cf., Table 3.1) was installed facing the burner surface at a distance of 650 mm. The interchangeable camera lens made of germanium has a focal length of 30 mm ( $f_{\#} = 1$ ) and projects the measurement object on an uncooled microbolometer focal plane array (FPA) detector ( $640 \times 480$  pixels) that is thermally stabilized by a Peltier element [150]. The resulting 16-bit images are stored on a secure digital (SD) memory card in the proprietary file format *IRB* and were evaluated with the software *IRBIS 3 plus*. Further details that simplify the reproducibility of the results presented in chapter 3.3 are given in the appendix (chapter A3.1.1). The operating parameters used for the experiment can be found in Table 3.3 in chapter 3.3.

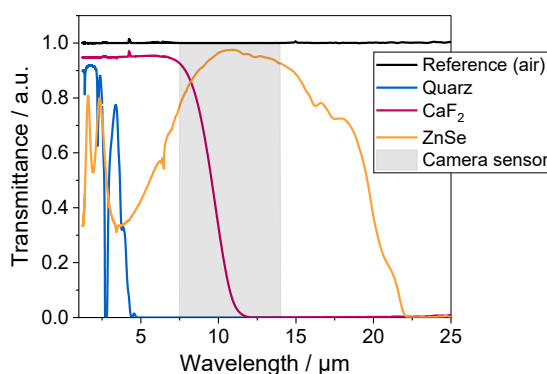


Figure 3.4: Transmittance of different window materials between 1.25–25  $\mu\text{m}$  measured with an IR spectrometer. The spectral detection range of the micro bolometer sensor of the utilized IR camera is indicated in gray.

Using an IR spectrometer (IR-S), the transmittance of different window materials was measured to identify a suitable window (W1) for the thermographic imaging. The detected transmission curves

(Figure 3.4) show that neither the fused silica (quartz) nor the calcium fluoride window are suitable. Instead, the zinc-selenide window that shows an average transmittance of 92% over the entire detection spectrum of the camera (7.5–14  $\mu\text{m}$ ) was found to be best suited for this application. Table 3.1 provides an overview of the utilized measurement equipment.

Table 3.1: Equipment used for IR thermography and for analyzing the transmittance of the reactor window (W1). All hardware identifiers (e.g., C1) are only valid in the context of IR thermometry.

Identi-	Vendor	Product	Serial number
IR-C	InfraTec	VarioCAM hr	336116
IR-S	Bruker	FT-IR spectrometer Vertex 80	1543

### 3.2.2 Multiline NO-LIF thermometry

The flat flame burners (C1 and C2, cf., Figure 3.2) were each installed inside a low-pressure flame reactor operated at 30 mbar that were equipped with molecular beam sampling and different measurement tools for nanoparticle analysis as described by Kluge et al. [250]. For iron-oxide synthesis, C1 was installed in a flame reactor (R1) with a particle mass spectrometer (PMS) and a quartz-crystal microbalance (QCM), while for tungsten-oxide synthesis C2 was installed in a flame reactor (R2) adapted to a time-of-flight mass spectrometer (TOF-MS). The described combinations are summarized in Table 3.4 and the setup for multiline NO-LIF thermometry is shown in Figure 3.5.

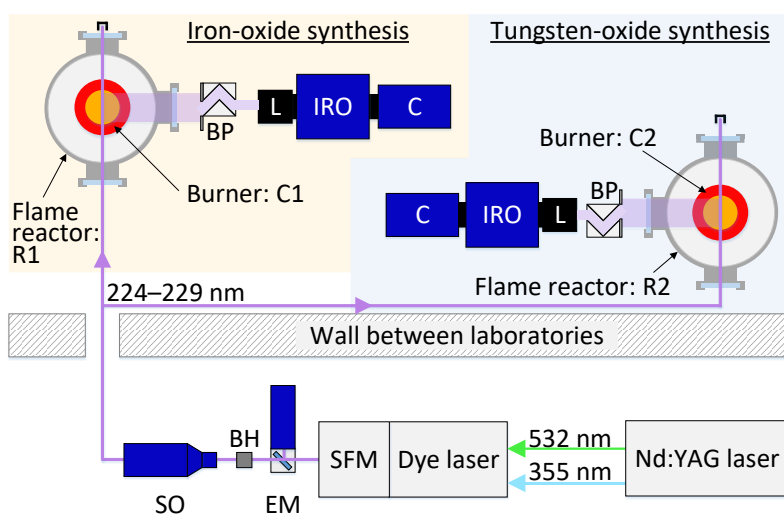


Figure 3.5: Top view of the setup for multiline NO-LIF thermometry at iron-oxide synthesis and tungsten-oxide synthesis. Following the direction of the laser beam, the utilized components are: sum-frequency mixing (SFM), energy monitor (EM), beam homogenizer (BH), sheetforming optics (SO), bandpass filter (BP), UV camera lens (L), intensified relay optics (IRO), and CCD camera (C). All major components are specified in Table 3.2. For better clarity, computer (PC), pulse/delay generator (PD), signal-interrupter box (IB), and mirrors are not indicated. A separate sketch showing the wiring is provided in the appendix (chapter A2).

For *in situ* temperature imaging with multiline NO-LIF thermometry, the second harmonic (532 nm) of a Nd:YAG laser (Table 3.2) pulsed with 10 Hz was used to pump a dye laser operated with DCM (4-(Dicyanomethylene)-2-methyl-6-(4-dimethylaminostyryl)-4H-pyran) in ethanol [167]. By sum frequency mixing (SFM), the resulting dye laser fundamental (peak efficiency at 627 nm) was overlapped with the third harmonic (355 nm) of the Nd:YAG laser in a BBO crystal ( $\beta\text{-BaB}_2\text{O}_4$ ), resulting in an UV laser beam tunable between 224 and 229 nm. While the Nd:YAG laser was controlled manually using the remote control, the dye laser was controlled with a computer (PC) and the software *Sirah control*

(Sirah Lasertechnik GmbH). The laser frequency was calibrated by comparing a measured NO-LIF spectrum with a simulated spectrum using the Matlab scripts *Extract Spectra from LIF Scan* and *Vergleich Sim Exp* (Table A4.3 in the appendix). A LaVision energy monitor (EM) measured the pulse-to-pulse laser intensity for image correction in the post processing. To remove hot spots from the laser intensity profile, a beam homogenizer (BH) was used [180, 256]. Using a LaVision beam expander (sheet-forming optics, SO), a thin (1 mm) laser sheet with 50 mm height was generated. The laser sheet was guided vertically through each respective flame reactor with its lower end aligned right above the burner surface. The resulting NO-LIF signal was detected perpendicular to the laser sheet plane after being spectrally filtered by a four-fold reflection bandpass filter (BP) [176], whose transmission curve was measured using an UV spectrometer (UV-S) and being plotted together with a typical NO-LIF emission spectrum in Figure 3.6.

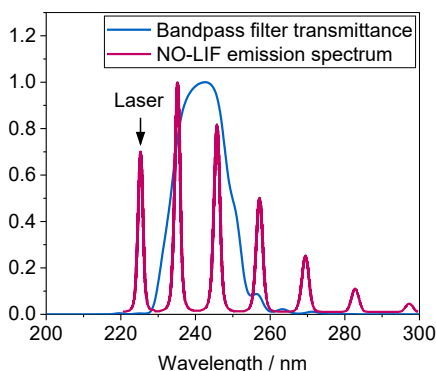


Figure 3.6: Measured normalized transmittance of the utilized dielectric reflection bandpass filter (BP) and typical NO-LIF emission spectrum when exciting the NO molecules at the indicated laser position (arrow) following Ref. [176].

The filtered signal was captured by a  $f = 105$  mm UV camera lens (L). At 50 ns intensifier gate-width, the intensified relay optics (IRO) amplified the signal and focused it on the charge-coupled device (CCD) sensor of the camera (C). The intensified camera was controlled together with the energy monitor by the software *DaVis 7.2* (LaVision). An in-house designed signal-interrupter box (IB) was used to suspend image acquisition during dye-laser scan (details provided in the appendix in chapter A2). For the measurements during iron-oxide synthesis, a laser system from 2013 was used (LS-2013) and 25 images were acquired on each wavelength position between  $44406\text{--}44422\text{ cm}^{-1}$  with  $0.1\text{ cm}^{-1}$  step width. For the tungsten-oxide synthesis a laser system from 2010 was utilized (LS-2010) and 50 images were recorded on each wavelength position between  $44408\text{--}44422\text{ cm}^{-1}$  with  $0.1\text{ cm}^{-1}$  step width. The resulting 12-bit images were stored on the computer as *IMX* files (proprietary file format by LaVision) using an in-house code (*Disk grab*, cf. chapter A4.2). Beside image acquisition, the *Disk grab* macro was used for post processing the time averaged image series using LIFSim [185]. Further details that simplify the reproducibility of the results presented in chapter 3.3.2 are given in the appendix (chapter A3.1.2). In both experiments, the operating parameters of *Flame A* were used (see Table 3.3 in chapter 3.3). The operation of the flame reactor was performed by Sebastian Kluge from the working group of Hartmut Wiggers (IVG). Table 3.2 provides an overview of the utilized measurement equipment.

Table 3.2: Equipment used for multiline NO-LIF thermometry and for analyzing the transmittance of the reflection bandpass filter (BP). All hardware identifiers (e.g., EM) are only valid in the context of multiline NO-LIF thermometry on the flat flame burner.

Identi-	Vendor	Product	Serial number
LS-2010	Spectra Physics	Nd:YAG laser Pro 230	4064PR
	Sirah Lasertechnik	Dye laser Cobra Stretch-SL	CSTR-LG-24, 10/01/04
	Sirah Lasertechnik	Sum frequency mixing unit	SFM-355, 10/01/07
LS-2013	Spectra Physics	Nd:YAG laser LAB-170-10H	4294L
	Sirah Lasertechnik	Dye laser Cobra Stretch	CBST-LG-24, 13/06/07
	Sirah Lasertechnik	Sum frequency mixing unit	SFM-355-N, 13/06/08
EM	LaVision	Energy Monitor	VZ09-0530
BH	SUSS MicroOptics	Beam homogenizer	N/A
SO	LaVision	Sheet and collimator optics	VZ09-0266, VZ09-
BP	Laser Optik	Bandpass 235–250 nm (FWHM)	N/A
L	Nikon	Camera lens UV-Nikkor ( $f = 105$ mm, $f_{\#} = 4.5$ )	200482
IRO	LaVision	Intensified relay optics	VC09-0053
C	LaVision	CCD camera Imager Intense	VC09-0058
PC	LaVision	Computer (Article: 1104001)	VP05-0084
PD	Stanford Research Sys-	Pulse/Delay generator DG535	08780
IB	IVG in-house design	Signal-interrupter box	N/A
UV-S	Horiba	UV spectrometer FL-1000	0220-0410

### 3.3 Results

#### 3.3.1 Pyrometric imaging of the porous plug

Even though the design of this burner was introduced and utilized for nanoparticle synthesis, the radial temperature gradient of either configuration has not been quantified yet. Hence, both burner configurations were investigated by thermographic imaging with two parameter sets each (Table 3.3). Parameter sets A and B were used in the thermographic imaging while only parameter set A was used for nanoparticle synthesis investigated by multiline NO-LIF thermometry (chapter 3.3.2).

Table 3.3: Operating parameters of the flat flame burner at 30 mbar.

Operating parameter set	H <sub>2</sub> / sccm	CH <sub>4</sub> / sccm	O <sub>2</sub> / sccm	Ar / sccm	$\phi$
A	400	0	400	600	0.5
B	700	0	900	300	0.39
C	700	100	800	300	0.375

This work does not aim to determine absolute temperatures of the burner surface since accurate measurements require exact knowledge about the emissivity of the surface and interfering light (e.g., flame chemiluminescence) [141]. Instead, the relative temperature distribution of its surface was investigated to gain insight in the cooling quality of both burner configurations. Therefore, the effects of selective emissivity and angle dependence of the thermal radiation (cf. chapter 2.2.1) are neglected. The porous bronze is assumed to consist of uni-sized, homogeneously distributed bronze spheres, whose surface texture is regarded as constant on average, so that the emissivity can be assumed constant at any point across the porous bronze in good approximation. Thus, the application

of the model of the graybody radiator is enabled that requires the determination of the emissivity, only (cf., chapter 2.2.1).

However, in the experiment, a direct determination of the emissivity of the porous bronze has not been possible. Since the IR camera is oriented vertically towards the burner surface (Figure 3.3), the camera detects both, its heat radiation and the radiation of the flame. Thus, the mounting ring that fixes the porous plug outside the luminous flame zone was selected for calibrating the emissivity. By comparing the measured temperature of the thermocouple installed in the mounting ring of C1 with the indicated temperature of the IR camera, the emissivity was iterated until both measured temperatures (thermocouple and IR camera) matched each other [257]. As soon as the burner has reached constant temperature during operation, the temperature difference between the outer edge of the porous bronze and the inner edge of the mounting ring can be assumed negligibly small. This allows the emissivity of the porous bronze to be approximated by the emissivity of the mounting ring ( $\varepsilon = 0.82$ ). The transmittance of the zinc-selenide reactor windows characterized in chapter 3.2.1 was used for correcting the IR images. However, various effects remain uncorrected (e.g., the emissivity of the flame and the reactor window), which is why the temperature values determined can only be used as a rough estimate of the true temperatures.

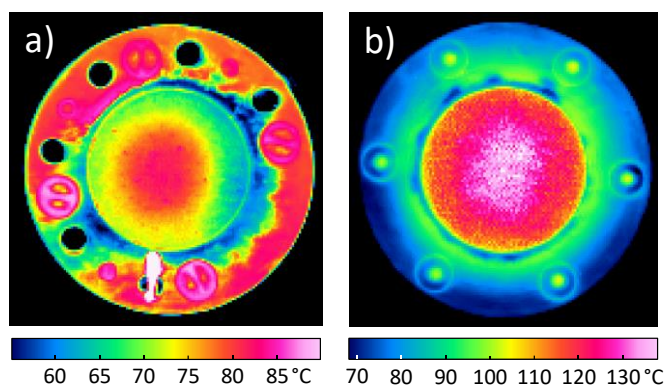


Figure 3.7: Thermograms of the porous matrix for configuration C1 (a) and C2 (b), both operated with parameter set B while cooled with 15°C water.

The comparison between both burner configurations C1 and C2 (Figure 3.7) shows that none of both provides a fully homogeneous temperature distribution across the porous bronze. Despite this, it can be seen that C2 provides a more homogeneous temperature distribution along the burner matrix that can be seen as radially symmetrical in good approximation. The surface temperature of the mounting ring stays lower at C2 compared to C1 but shows small colder zones (blue) close to the porous bronze that are surrounded by warmer regions (green) indicating non-uniform cooling. It is also noticeable that the mounting ring in configuration C1 is warmer on the outside than on the inside, while C2 shows exactly the opposite behavior. This, however, has not been further investigated, as the mounting ring is only of minor interest.

C1 shows an inhomogeneous temperature distribution that indicates the entry and exit of the cooling coil below the mounting ring (cold zone crossing the mounting ring at the bottom-left side in Figure 3.7). It can also be seen that in particular on the right half of the burner, the temperature is comparably low, spreading up to 5 mm across the burner matrix towards the center axis. In this region, the matrix temperature is approximately 25% lower than the measured temperature in the center of the matrix. Apart from that, the porous bronze can be subdivided into two co-annular regions. The outer ring-shaped zone extends from the edge of the porous bronze to about 15 mm inner diameter (again,

originating from the central axis of the burner), where lower temperatures are observed compared to the central zone. For C1, the highest temperature is found within the region of the innermost circular surface (with a diameter of about 15 mm). The temperature gradient across those two co-annular zones spreads about 12% relative to the measured peak temperature of 85°C (as discussed in chapter 3.2.1; again, these absolute temperatures need to be regarded as rough estimates).

The porous bronze plug of C2 can be subdivided into three co-annular regions. The lowest temperatures appear at the outer ring-shaped zone that extends from the edge of the porous bronze to a radius of 11 mm. The middle range starts at 11 mm radius and extends to a radius of about 5 mm, where higher temperatures are measured than in the outer co-annular ring. The highest overall temperatures are found in the area of the innermost circular surface within a radius of about 5 mm. The temperature gradient spreading across these three co-annular zones is about 16% of the measured peak temperature of 125°C. However, the temperature distribution across the porous plug of C2 is radially symmetric, which enables comparisons between experiments and computed fluid dynamic (CFD) simulations as well as off-axis probe sampling, e.g., for transmission electron microscopy (TEM) analysis of synthesized particles.

For both burners, the considerations regarding the homogeneity of the surface temperature are valid for both sets of operating parameters A and B. This is independent of the fact that the burners become hotter when operated with parameter set B due to the larger total fuel flow. The assumption that the inhomogeneity of the temperature distribution at C1 results from a non-optimal cooling design is confirmed by thermographic measurements in which the burner was operated without cooling (M04 & M06, not shown here, for averaged temperatures see Figure 3.8, setup 1). In this case, a homogeneous temperature distribution is obtained across the porous bronze of C1 but the surface temperature rises steadily (1.5 K/min for parameter set A, 4 K/min for parameter set B), wherefore the experiments had to be terminated to protect the burner components from thermal degradation after 40 min in case of parameter set A and after 20 min in case of parameter set B.

To compare the different burner configurations and operating parameters more quantitatively, the temperature values were extracted across a circular area spanning the entire diameter of the burner matrix (Figure 3.7). The average temperatures and corresponding standard deviations are summarized in Figure 3.8.

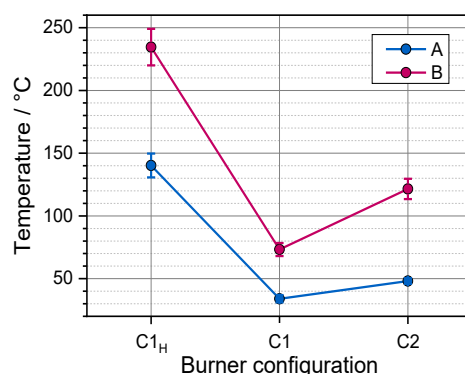


Figure 3.8: Mean temperatures and standard deviations across the porous bronze plug determined by thermographic imaging: C1 without cooling (C1<sub>H</sub>), C1 with cooling, and C2 with cooling. In each configuration, the burner was operated with operating parameter set A and B (compare listed raw data in Table A3.1 for details).

As expected, higher temperatures are measured in all three configurations at the operating parameter set B due to its higher fuel-gas flow rate. Both the highest and the lowest mean matrix temperatures were measured for C1 (compare C1<sub>H</sub> and C1 in Figure 3.8). Switching on the cooling of C1 reduces the surface temperature by 76% for operating parameter set A and 69% for operating parameter set B. If C1 is operated without cooling (C1<sub>H</sub>), the average surface temperature is 40% lower when operated with parameter set A instead of B. With cooling switched on (C1), the relative temperature difference between both operating points is 54%. Despite cooling, C2 shows a higher average surface temperature than C1 suggesting that the effective cooling performance is lower compared to C1. This observation coincides with the geometric arrangement of the cooling coil that is spatially more separated from the porous bronze in case of C2 compared to C1 (Figure 3.2). In case of parameter-set A, the mean surface temperature of the porous bronze is 41% higher for C2 than for C1, while at parameter-set B it is even 66% higher (compare C1 and C2 in Figure 3.8). However, for both parameter sets, C2 provides a more homogeneously distributed temperature across the porous bronze compared to C1 (Figure 3.7). In the following chapter, radial temperature profiles of the porous bronze are presented (Figure 3.13) and discussed in the context of the gas-phase temperature measurements on the flat flame burner.

### 3.3.2 Temperature imaging during nanoparticle synthesis

To investigate the gas-phase temperature of the flat flame burner during nanoparticle synthesis, multiline NO-LIF measurements were performed on an iron-doped flame (together with O. Feroughi) and on a tungsten-doped flame (together with R. Chrystie). The results were partially published in Refs. [60, 248] where the total height of the field of view was limited to 9 mm in maximum in case of the iron-doped flame since the studies focused on nanoparticle characterization by probing the flame at different HABs using a sampling nozzle. Based on these measurements, the authors discuss the spatial distribution of iron atom concentration and the influence of the precursor concentration on the flame temperature [60, 248]. In contrast, comparatively little information was available on the tungsten oxide material system synthesized from WF<sub>6</sub> as precursor when the measurements were performed in 2016. Consequently, multiline NO-LIF thermometry measurements were performed in the low-pressure flame reactor to investigate the influence of the tungsten hexafluoride precursor on the flame chemistry and the flame temperature.

Table 3.4: Hardware configuration and materials systems for the respective flame-based nanoparticle synthesis experiments characterized by NO-LIF thermometry. The operating conditions can be found in Table 3.3.

	Iron-oxide synthesis	Tungsten-oxide synthesis
Low-pressure flame reactor	Particle mass spectrometer (PMS) and quartz-crystal microbalance (QCM)	Time-of-flight mass spectrometer (TOF-MS)
Burner	C1	C2
Flame	A	A
Precursor	Iron pentacarbonyl (Fe(CO) <sub>5</sub> )	Tungsten hexafluoride (WF <sub>6</sub> )

However, neither temperature fields of the iron-doped flame with HABs greater than 9 mm nor any temperature fields of the tungsten-doped flame at all were presented, yet. Hence, additional *in situ* multiline NO-LIF measurements were performed for the iron-oxide synthesis flame across the maximum possible height of 25 mm. In the experiment, no larger HABs could be investigated, because the

field of view was limited at the lower end by the optical access to the reactor and at the upper end by the fixed position of the sampling nozzle. Nevertheless, the sampling nozzle is sufficiently far away from the burner so that its effect on the temperature field discussed by Kluge [248] can be neglected. This allows the investigation of the overall temperature distribution in the gas flow of the flat flame burner as well as its interpretation in the context of the temperature gradient across the porous bronze examined by pyrometric imaging. Moreover, a comparison of the temperature fields of the iron-doped and the tungsten-doped synthesis flame is enabled.

For the multiline NO-LIF measurements on the precursor-doped flat flames, the burners C1 and C2 were installed in the low-pressure flame reactors as depicted in Figure 3.5. Table 3.4 lists both setups with respect to burner, precursor system, and flame reactor (identified by the installed particle-measurement technology).

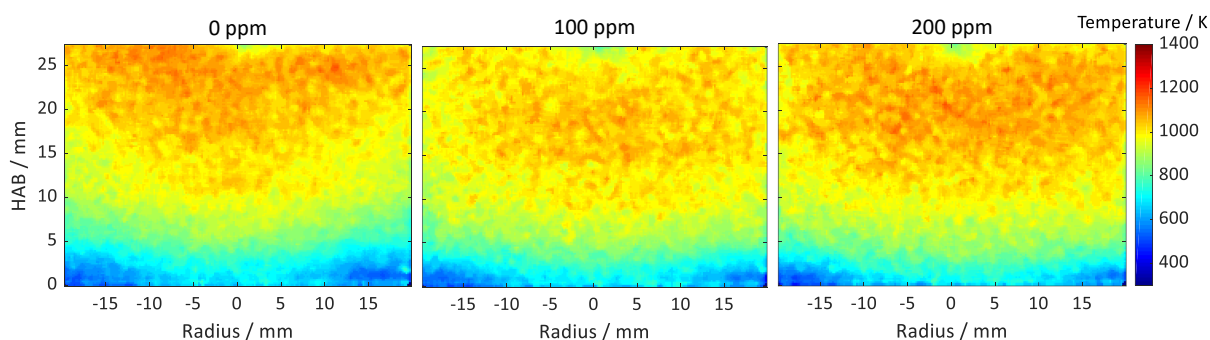


Figure 3.9: Temperature fields of Flame A with 0 ppm, 100 ppm, and 200 ppm iron pentacarbonyl. The respective burners and flame reactors are specified in Table 3.4.

All investigated precursor concentrations of the iron-doped flame (Figure 3.9) show a similar temperature distribution. At the top, locally reduced temperatures on the center axis are caused by the tip of the sampling nozzle. The temperature maps are axisymmetric and can be regarded as one-dimensional flames inside a radius of  $\pm 7$  mm around the axis. Within this range, temperature (and species concentrations) depend on the HAB only [258]. As depicted in the pyrometric images of the porous bronze plug of burner C1 (Figure 3.7a), this area correlates with the inner circular zone in which the highest mean matrix temperature is found (homogeneous temperature distribution within the inner 15 mm diameter). With increasing radial distance from the center, the gas-phase temperature right above the burner surface decreases, which coincides with the surface temperature gradient across the burner matrix that is  $12^{\circ}\text{C}$  (30%) cooler on the outside than on the inside (cf. Figure 3.13). Starting from a radius of  $\pm 10$  mm, cold zones ( $T < 500$  K) are clearly identifiable in all temperature fields that expand axially with increasing radius. Further downstream, these radial temperature gradients are still apparent and propagate axially over the entire height of 25 mm. Thus, a clear correlation between the radial temperature gradient in the flame and the temperature gradient along the surface of the porous bronze plug is evident that is not compensated within the observed height. From the temperature maps, no clear trend is found regarding the influence of the precursor concentration on the gas-phase temperature. Therefore, a quantitative comparison of the axial temperature profiles (Figure 3.12) is given later in this chapter.

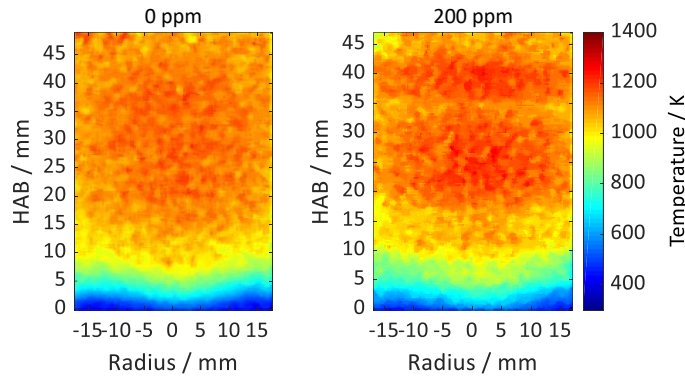


Figure 3.10: Temperature fields of Flame A with 0 ppm and 200 ppm tungsten hexafluoride. The respective burners and flame reactors are specified in Table 3.4.

The measurements in the tungsten-oxide flame were limited (by the sampling nozzle) to a maximum height of 50 mm. Similar to the iron-doped flames, the temperature fields are axisymmetric and can be regarded as a one-dimensional flames within a radius of  $\pm 5$  mm around the central axis (Figure 3.10). In the pyrometric images of the porous bronze plug of burnerC2 (Figure 3.7b), this area correlates with the zone in which the highest matrix temperature is measured (inner 10 mm in diameter). With increasing radial distance from the center, the averaged gas-phase temperature field right above the burner surface cannot be correlated with the postulated co-annular temperature zones (chapter 3.3) of the porous bronze of C2, unambiguously. Starting from a radius of 6 mm, cold areas ( $T < 500$  K) in the temperature fields (Figure 3.10) expand axially with increasing radii as observed in the iron-doped temperature field. Thus, although the temperature distribution of the porous bronze is more homogeneous in configuration C2, it is concluded that no significant improvement with respect to the radial temperature gradient in the gas-phase temperature field was achieved by the improved cooling configuration of C2 compared to C1.

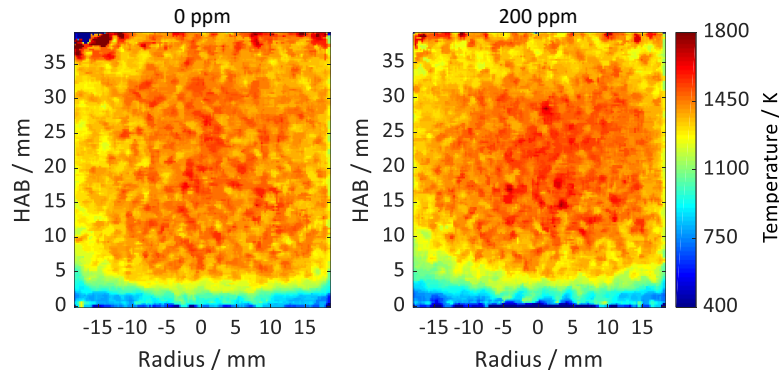


Figure 3.11: Temperature fields of Flame C with 0 ppm and 200 ppm tungsten hexafluoride. The respective burners and flame reactors are specified in Table 3.4.

In contrast to the temperature measurements on the tungsten-doped flame operated with parameter set A (Table 3.3), the field of view was limited to 40 mm by the sampling nozzle in the case of Flame C (Figure 3.11). Due to the increased amount of fuel gas (additional 100 sccm methane) and the reduced Argon flow rate, 400 K higher peak temperatures were measured and the cold flame zone ( $T < 500$  K) is reduced in height down to 1 mm. The temperature map indicates a temperature drop beyond 30 mm HAB in the precursor-doped case while for the undoped flame, the temperature is constant around 1450 K between 5 mm HAB and the upper end of the field of view. Similarly to Flame A, Flame C can be regarded as one-dimensional only within the inner  $\pm 5$  mm radius. For 200 ppm, the

temperature field is not axisymmetric and stronger radial temperature gradients compared to the undoped flame are observable.

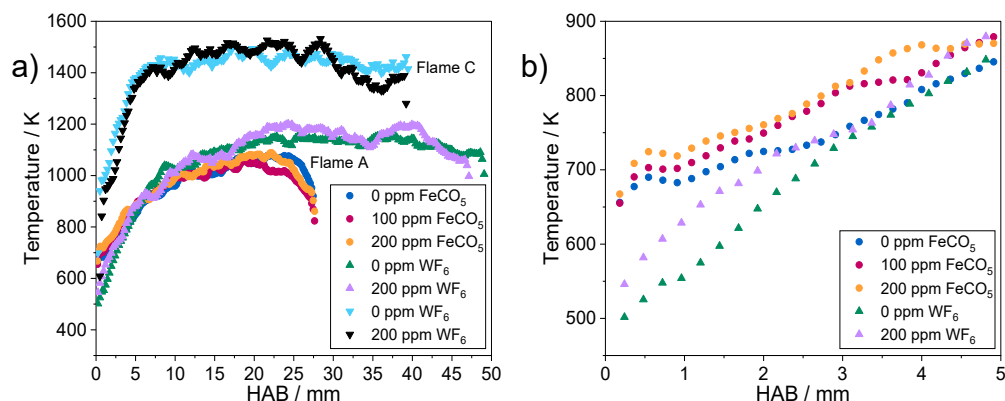


Figure 3.12: Axial temperature profiles of the iron pentacarbonyl and tungsten hexafluoride flames. The profiles were extracted  $\pm 1.5$  mm around the centerline from the temperature maps depicted in Figure 3.9, Figure 3.10, and Figure 3.11. To illustrate the precursor-concentration dependence of the temperature observed in Flame A, an enlarged section of the first 5 mm HAB of (a) is shown in (b).

The mentioned temperature difference between Flame A and Flame C becomes particularly clear when analyzing the axial temperature profiles (Figure 3.12a). While Flame A doped with iron pentacarbonyl reaches a mean temperature around 1050 K, doping with tungsten hexafluoride causes a 90 K higher temperature around 1140 K. For Flame A, the temperature exceeds 1000 K between 8 and 10 mm HAB for the undoped flames as well as for the iron-doped and the tungsten-doped flame. The observable temperature drop at the end of each profile is due to the sampling nozzle. The peak temperatures of Flame A were measured at 200 ppm precursor concentration for both precursors and differ by 112 K since 1201 K were measured in the tungsten-doped flame and 1089 K peak temperature were determined in the iron-doped flame. For Flame A, a similar trend is found for all temperature profiles and no clear dependency of the precursor concentration on the mean temperature is observable for any of both precursors. However, on the first 5 mm above the burner it is indicated that higher precursor concentrations correlate with slightly higher temperatures (Figure 3.12b).

Besides overall higher peak temperatures, Flame C shows a steeper temperature increase reaching flame temperatures above 1400 K within 6 mm HAB. Like in Flame A, the highest temperature is found for 200 ppm tungsten hexafluoride doping, too. With 1531 K, a 330 K higher peak temperature is measured in Flame C compared to the pure hydrogen/oxygen flame. After the peak temperature is reached at 28 mm HAB, the temperature drops below 1350 K at 34 mm HAB. Since this temperature drop is not observed in the undoped case, it is not associated with the sampling nozzle. A similar temperature drop is observed in Flame A doped with tungsten hexafluoride right after the peak temperature of 1201 K is reached at 40 mm HAB, it drops to 1058 K at 46 mm HAB while the undoped profile remains constant around 1090 K between 40 and 46 mm HAB. Due to these observations it is concluded that the iron-doped flame may still be affected by the sampling nozzle (despite its distance of 25 mm) whereby the measured peak temperature might be lower than in an undisturbed flow. However, it is still expected that the peak temperature of the iron-doped flame will remain below the peak temperature of the tungsten-doped flame.

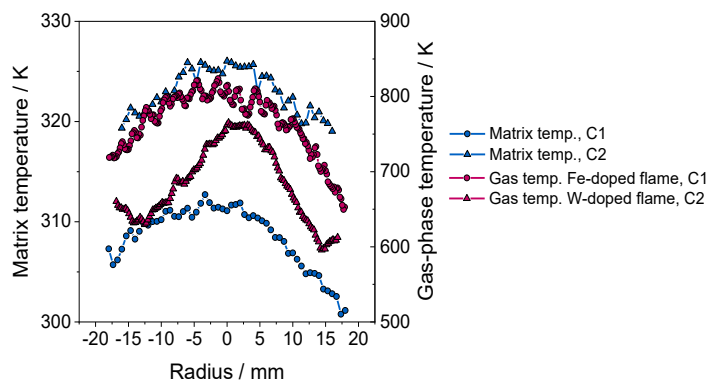


Figure 3.13: Radial temperature profiles of the porous bronze extracted from thermographic imaging (chapter 3.3) as well as gas-phase temperature profiles of the iron-doped and tungsten-doped flame spatially averaged between 0–5 mm HAB. All measurements were performed with Flame A. For the gas-phase temperature measurements, 200 ppm precursor were added.

To enable a comparison between gas-phase temperature in the close vicinity of the burner matrix and the surface temperature of the porous bronze plug, radial profiles of the gas-phase temperature were extracted from the *in situ* temperature fields shown in Figure 3.9 and Figure 3.10 and averaged over the first 5 mm HAB. As apparent in Figure 3.13, both flames and thereby both burners show similar deviations between center temperature and outer-rim temperature. At 18 mm radius, the gas-phase temperature is 174 K (21%) lower for C1 and 169 K (22%) lower for C2 compared to the temperature on the centerline. Similarly, when looking at the radial temperature profiles of the porous bronze plug, higher temperatures are apparent in the center as opposed to the edges for both burner configurations C1 and C2 as well as for both operating points. For C1, 12 K (30%) lower temperatures were found at the edge of the matrix compared to the center temperature when operated with parameter set A while at parameter set B, up to 16 K (18%) lower temperatures were measured in the outer region compared to the center. On the other hand, for C2, 7 K (13%) lower temperatures were found in the outer zone compared to the center when operated with parameter set A while the difference in surface temperature reaches 36 K (26%) when operated with parameter set B. Hence, a clear correlation between radial temperature distribution of the porous bronze and the gas-phase temperature is evident.

### 3.4 Outlook

Based on the present results, deviations in the temperature fields cannot clearly be assigned to the variation of the precursor or the respective burner cooling configuration. In future investigations-, imaging gas-phase temperature measurements should be performed under identical synthesis conditions in which only the burner configuration is varied. The accuracy of the surface temperature measurements can be improved by using multiple thermocouples installed at multiple locations in the mounting ring and inside the porous bronze. Alternatively, thermographic phosphors could be used for the determination of the absolute temperature of the porous bronze behind the flame [71, 141]. Moreover, spatially resolved gas-phase velocity measurements should be performed, e.g., by flow-tagging [92, 259] or PIV (chapter 2.2.3), to investigate the influence of vortices and backflows inside the burner chamber on the flame and the resulting temperature field.

## 4 Pilot-scale non-premixed gas burner for nanoparticle synthesis

### 4.1 Concentric multi-tube gas burner

The pilot-scale gas burner investigated in this chapter was developed with a pilot-scale flame reactor in a joint venture between IVG, IUTA (Duisburg), and Evonik (Hanau) in 2007 and 2008. Together with a hot wall reactor and a plasma reactor, they form the core of the IUTA technology center for gas-borne nanoparticle production on the pilot scale [68]. The idea behind the pilot facility, launched in November 2008, is to explore the up-scaling steps (chapter 2.1) required to transfer established lab-scale processes with production rates of few grams per hour to the kilogram scale as required for commercial applications [67, 260].

The IUTA flame reactor consist of a 1.1 m long stainless-steel cylindrical tube, equipped with an inner quartz tube (called “inliner”) with an inner diameter of 89 mm to guide the gas flow smoothly along twelve optical ports (three ports each at four levels) and to reduce the thermal load on the reactor wall. Figure 4.1 shows a sketch of the flame reactor and photos of the pilot-scale gas burner. For a better overview, the sketch of the flame reactor (Figure 4.1a) shows only the upper section with its lateral optical ports for the first two viewing levels. Further details can be found in chapter 4.2.2 in the context of the experimental setup.

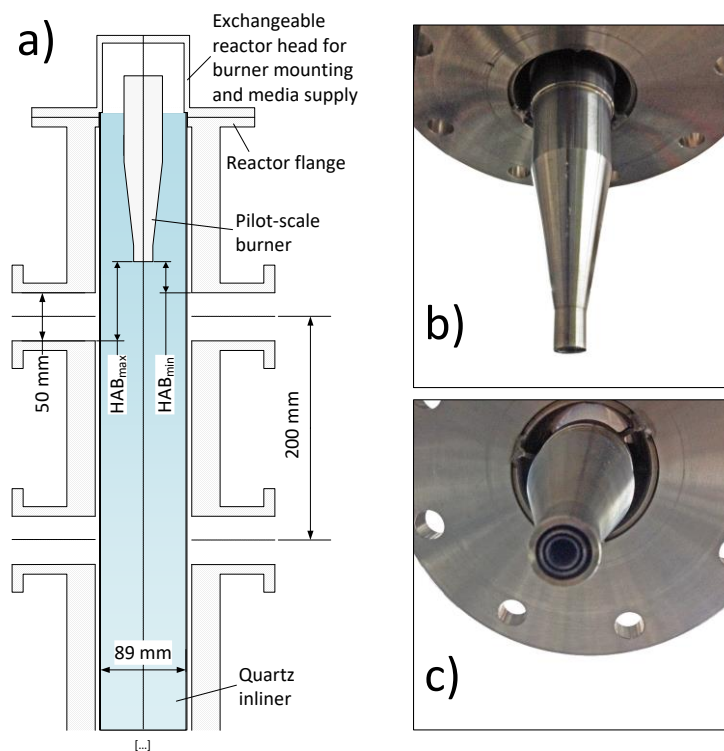


Figure 4.1: Sketch (a) of the upper part of the IUTA flame reactor and photos (b) & (c) of the pilot-scale gas burner. For clarity, only the lateral optical ports at the two heights closest to the nozzle exit are displayed in (a).

The concentric burner nozzle assembly is installed vacuum-tightly facing upside-down at the upper end of the reactor mounted in an exchangeable reactor head. Due to the design, the burner surface does not extend to the upper edge of the top optical port. Hence, the flow of the burner can be investigated *in situ* between  $HAB_{\min} = 5 \text{ mm}$  and  $HAB_{\max} = 55 \text{ mm}$  (cf. Figure 4.1a). The burner consists of three co-annular tubes in a nozzle-shaped arrangement (Figure 4.2) where the gaseous fuel and

the vapor-phase nanoparticle precursor is provided through the central tube of the burner and the combustion air is fed through the outermost annular gap. Between these two flows, a separating gas flow (nitrogen) is injected that allows for modifying the flame geometry and the flame lift-off. An additional coflow is provided to cool the quartz inliner and to shield the flame from unwanted recirculation and interfering side-flows to ensure well-defined boundary conditions for CFD simulations. Figure 4.2 provides details of the burner and its flow channels.

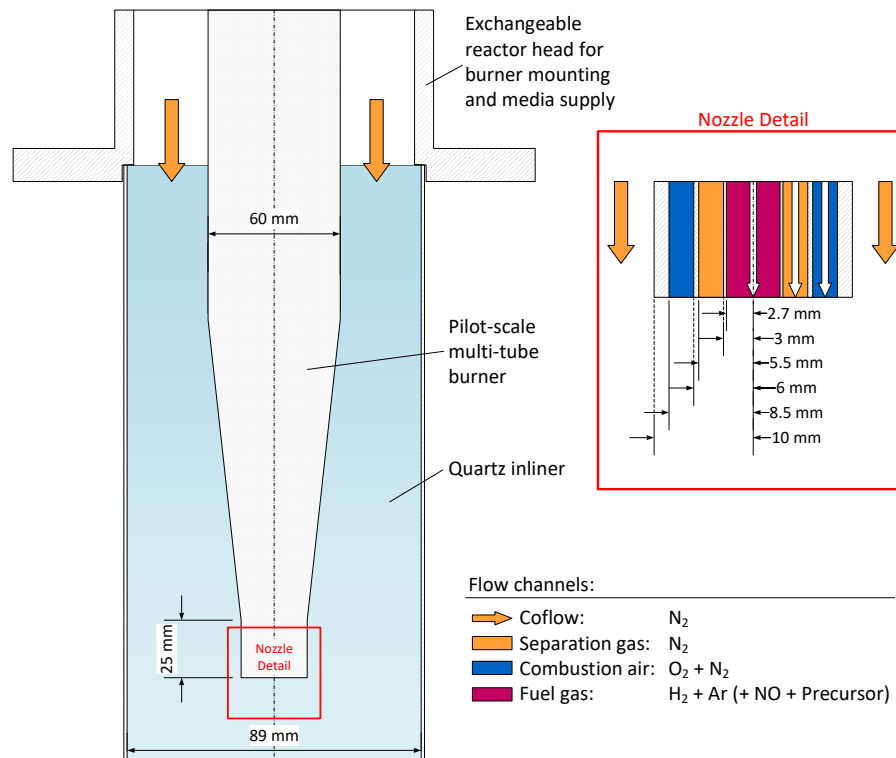


Figure 4.2: Sketch of the IUTA pilot-scale gas burner showing nozzle dimensions and flow channels.

Since commissioning of the IUTA gas burner in January 2010, studies to determine suitable operating parameters as well as measurements of *in situ* iron concentrations and gas-phase temperatures with and without iron pentacarbonyl precursor have been performed [167]. The experimental data was utilized to validate a gas-phase reaction mechanism for the formation of iron oxide nanoparticles from elementary iron particles and iron clusters [60, 167]. In addition, the effects of spatial flame (i.e., temperature) fluctuations during a multiline NO-LIF wavelength scan in the mildly turbulent flame of the IUTA gas burner was quantified in the absence of precursor [22, 170].

To enable CFD simulations of the pilot-scale gas burner, measurements of gas-phase velocities are required as boundary conditions. Therefore, a study of the non-reacting (cold) gas flow of the burner using particle image velocimetry is presented (chapter 4.3.1). Additionally, *in situ* temperature measurements were performed inside the IUTA flame reactor on a flame doped with titanium isopropoxide (TTIP). For that, the multiline NO-LIF thermometry setup utilized in past works [22, 61, 180, 253] was extended by two dye cuvettes and two additional cameras to enable correcting the laser-fluence attenuation of the laser sheet by absorption (e.g., by particle deposition on the reactor windows) during the measurement. The developed workflow as well as a proof-of-principle measurement under real process conditions is presented in chapter 4.3.2.

## 4.2 Experiment

### 4.2.1 Particle Image Velocimetry

For gas-phase velocity measurements, the IUTA gas burner was installed together with the reactor head (Figure 4.1 and Figure 4.2) in a nozzle test rig at the IVG preserving the downwards-oriented arrangement. The nozzle test rig consists of twelve aluminium profiles (ITEM GmbH) that have been connected to a framework with the form of a rectangular cuboid with a base area of  $910 \times 910 \text{ mm}^2$  and a height of 1600 mm. All gases listed in Table 4.3 were replaced by pressurized air. Four mass flow controllers (MFC) were used to meter the coflow (MFC1) and the flows through the combustion-gas channel (MFC2), the separation-gas channel (MFC3), and the fuel-gas channel (MFC4) that are indicated in Figure 4.2. Seeding droplets were generated using an aerosol generator (AG) and added either to the combustion-gas channel or to the coflow (for each result, the seeded channel is specified in the respective figure description). A minimum of 26 slm (i.e., 0.3 bar seeder operating pressure) was required to generate a fine DEHS aerosol. A bypass and a manual valve (V) were used to control the seeding density. All tubes were connected to the reactor head that provides the interface for the media supply of the IUTA gas burner. The downwards-oriented flow originating from the nozzle was shielded by a quartz inliner and pumped off from the lower side of the quartz tube providing a similar environment as inside the IUTA flame reactor in good approximation. The spatially overlapped second harmonics (532 nm) of two pulsed Nd:YAG lasers (also called PIV laser, PL) were extended to a laser sheet using LaVision sheet-forming optics (SO). The laser sheet ( $120 \times 1 \text{ mm}^2$ ) was adjusted centrally below the nozzle of the burner. To reduce reflections on the quartz inliner, the inner side of the glass tube was matted using black spray paint except for the areas where the laser sheet crossed the inliner as well as the field of view between camera and laser sheet. The light scattered on the seeding droplets was detected perpendicular to the laser sheet plane through a band-pass filter (BP) with a center wavelength of 532 nm and a full width half maximum of 10 nm. A 50 mm lens (L) was used for imaging the signal on a LaVision scientific complementary metal-oxide semiconductor (sCMOS [261, 262]) camera. The camera (C) is working in global shutter mode where all pixels are exposed simultaneously [263]. Figure 4.3 shows the experimental setup utilized for PIV measurements on IUTA pilot-scale burners.

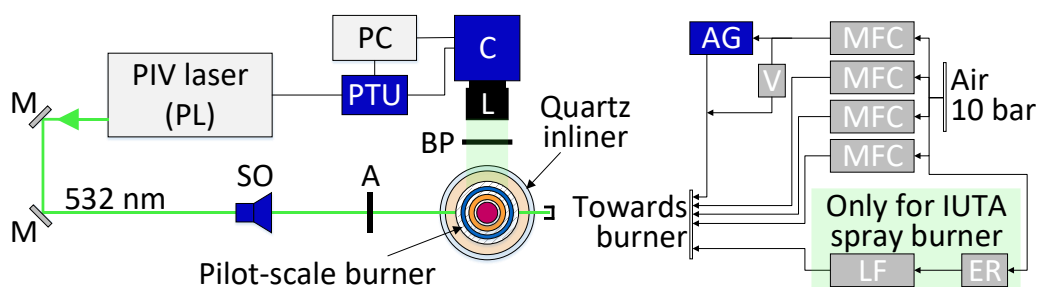


Figure 4.3: Top view of the PIV setup installed at the nozzle test rig at the IVG. Following the direction of the laser beam, the utilized components are: mirrors (M), sheet-forming optics (SO), aperture (A), bandpass filter (BP), camera lens (L), sCMOS camera (C), programmable timing unit (PTU), and computer (PC). For burner operation, pressurized air was metered with mass flow controllers (MFC) and provided through the media supply interface of the exchangeable reactor head (Figure 4.2) to the pilot-scale burner. The aerosol generator (AG) could be bypassed by a manual valve (V) to adjust the seeding density. For the IUTA spray burner (chapter 6.1), ethanol was dosed through a liquid-flow meter (LF) from a pressurized ethanol reservoir (ER). All major components are specified in Table 4.1.

The camera and the overall triggering were controlled by a computer (PC) and a programmable timing unit (PTU) via *DaVis 8.1.4*, while the laser was controlled partly by its remote control and partly by the LaVision software. In the experiment, the flow rates of each flow channel were varied (one at a time) and different parameter sets utilized by IUTA for nanoparticle synthesis were examined resulting in a total of 72 measurements (Table A3.4). The major results are discussed in chapter 4.3.1. For each measurement, 200 double-frame images were recorded that were evaluated using the *PIV package of DaVis 8.4*. In the post processing, the background noise was reduced by applying a subtract-time filter (i.e., a sliding-background filter) on the image series [264]. Second, the vector field was calculated by cross correlation in multi-pass iterations of decreasing-size interrogation areas from  $64 \times 64$  to  $32 \times 32$  pixels with shape adaption at 50% overlap between the interrogation areas [265]. Here, the options for uncertainty calculation [206], image correction, and high-accuracy mode for final passes (with B-spline 6 reconstruction) were selected [264]. Subsequently, vectors with a peak ratio smaller than 1.5 were deleted and a four-pass regional median filter was applied without smoothing [264]. Finally, the vector fields were calculated (mean value and root mean square). Further details that simplify the reproducibility of the result presented in chapter 4.3.1 are given in the appendix (chapter A3.2.1). An overview of the utilized equipment is provided in Table 4.1.

Table 4.1: Equipment used for gas-phase velocity measurements by PIV. All hardware identifiers (e.g., AG) are valid in the context of PIV on the IUTA pilot-scale gas burner (Figure 4.2) and spray burner (Figure 6.1).

Identi-	Vendor	Product	Serial number
MFC1	MKS Instruments	Mass flow controller 300 slm N <sub>2</sub>	G565640G20
MFC2	MKS Instruments	Mass flow controller 50 slm Ar	G562390G20
MFC3	MKS Instruments	Mass flow controller 25 slm Ar	G484832G20
MFC4	MKS Instruments	Mass flow controller 50 slm H <sub>2</sub>	G562391G20
LF	Brooks	Quantim Liquid Flow Meter	01B40491239
AG	LaVision	Aerosol generator	VZ09-0683
PL	Litron Lasers	Nd:YAG laser Nano L135-15	LM1636
SO	LaVision	Sheet-forming optics	VZ09-0265
BP	LaVision	Bandpass filter 532 nm	VZ09-0663
L	Nikon	Camera lens AF Nikkor ( $f = 50$ mm, $f_{\#} = 1.8$ )	2130056
C	LaVision	Camera sCMOS	VC12-0226
PTU	LaVision	Programmable timing unit V9.0	VZ12-0697
PC	LaVision	Computer	VP09-0068

#### 4.2.2 Multiline NO-LIF thermometry

For *in situ* temperature imaging with multiline NO-LIF thermometry, the IUTA gas burner (Figure 4.1 and Figure 4.2) was installed inside the pilot-scale flame reactor operated at 900 mbar. The second harmonic of a Nd:YAG laser (532 nm) was used to pump a dye laser operated with DCM in Ethanol. The required UV radiation for NO excitation between 224 and 229 nm was generated by sum-frequency mixing (SFM, cf., Table 4.2) of the dye laser radiation (around 615 nm) and the third harmonic of the Nd:YAG laser (355 nm). The Nd:YAG laser (La1) was controlled manually using the remote control and the dye laser (La2) was controlled with a computer (PC) and the software *NarrowScan Laser control* (Radiant Dyes GmbH). The spectral dye laser offset of  $14 \text{ cm}^{-1}$  was determined by comparing a measured NO-LIF spectrum with a simulated spectrum using the Matlab scripts *Extract Spectra from*

*LIF Scan and Vergleich Sim Exp* (Table A4.3). Energy monitor (EM), beam homogenizer (BH), sheet-forming optics (SO), and bandpass filter (BP) were used as described in chapter 3.2.2. The filtered NO-LIF signal was captured by a 100 mm UV camera lens (L1). At 50 ns gate-width, the intensified relay optics (IRO) amplified the signal and focused it on the charge-coupled device (CCD) sensor of the camera (C). The intensified camera was controlled together with the energy monitor by the software *DaVis 7.2* (LaVision GmbH). An in-house designed signal-interrupter box (IB) was used to suspend image acquisition during dye-laser scan (details provided in the appendix in chapter A2). For the measurements during TiO<sub>2</sub> nanoparticle synthesis, 20 images were acquired on each wavelength position between 44407–44422 cm<sup>-1</sup> with 0.1 cm<sup>-1</sup> step width.

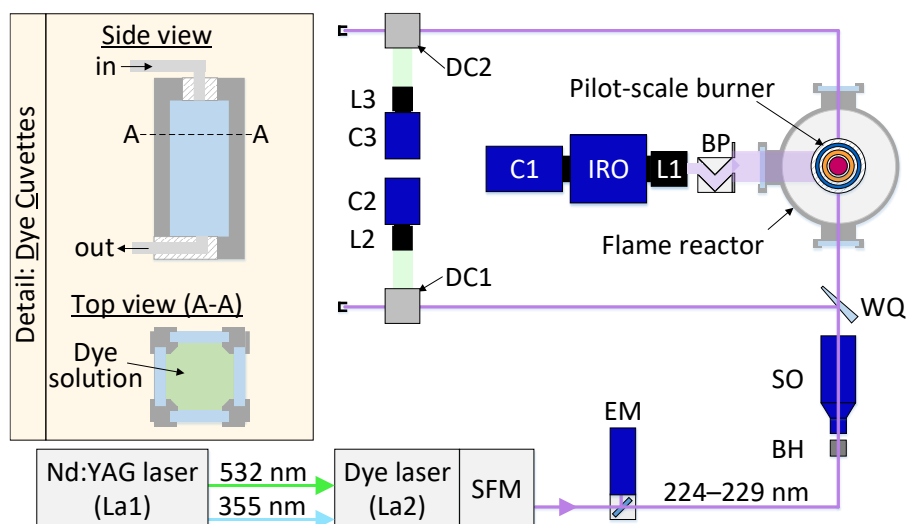


Figure 4.4: Top view of the multiline NO-LIF setup installed at the IUTA flame reactor. Following the direction of the laser beam, the utilized components are: sum-frequency mixing (SFM), energy monitor (EM), beam homogenizer (BH), sheet-forming optics (SO), quartz wedge (WQ), bandpass filter (BP), UV camera lens (L1), intensified relay optics (IRO), and CCD camera (C1). Furthermore, the dye cuvette (DC1/2) and the CCD camera (C2/3) with its respective lens (L2/3) used for laser-sheet correction. On the left, details of the dye cuvettes are shown indicating the inlet and outlet of the liquid dye solution. All major components are specified in Table 4.2. For better clarity, computer (PC), pulse/delay generator (PD), signal-interrupter box (IB), and mirrors are not indicated. A table documenting the wiring is provided in the appendix (chapter A2).

The setup depicted in Figure 4.4 shows an enhancement of the conventional setup for multiline NO-LIF thermometry (as shown for instance in Figure 3.5) that enables the correction of the spatial laser-sheet intensity distribution. Therefore, uranine (disodium fluorescein) was dissolved in water (around 1 mg/l) continuously pumped through two dye cuvettes (DC1/2). The cuvettes were equipped with quartz windows (94 × 34 mm<sup>2</sup>) allowing the laser sheet to pass the cuvette at full height (50 mm). The anti-reflex coating for UV (220–350 nm) and VIS (400–700 nm) enabled maximum transmittance of the UV laser sheet and the emitted green fluorescence radiation. Perpendicular to the laser-sheet plane, two camera lenses (L2/3) collected the fluorescence signal of the dye solution imaging it on the CCD sensors of two LaVision E-Lite cameras (C2/3).

For image acquisition of all three cameras (C1–C3), the *DaVis* macro *DiskGrab* (chapter 3.2.2) was modified. In the modified version (*DiskGrabAcq\_1.2.CL*, see chapter A4.2 in the appendix for details), averaged images for each of the three cameras are computed before storing the single-shot images to the computer whereby image acquisition rates around 10 Hz are enabled. The resulting 14-bit *IMX* files (proprietary file format by LaVision) images were averaged for each spectral measurement position and post processed in two steps. First, the Matlab code *Absorptionskorrektur* (Table A4.3) was

applied that was developed in the present thesis and is described together with the proof-of-principle measurement presented in chapter 4.3.2. In a second step, the laser sheet-corrected results (i.e., the output produced by the Matlab code *Absorptionskorrektur*) are evaluated in LIFSim [185] to derive a two-dimensional temperature map. Further details that simplify the reproducibility of the result are given in the appendix (chapter A3.2.2). An overview of the utilized measurement equipment is provided in Table 4.2. In the experiment, TiO<sub>2</sub> nanoparticles were produced from titanium tetraisopropoxide (TTIP) precursor added through the central channel of the IUTA gas burner (Figure 4.2) using operation-parameter set 2 documented in Table 4.3 in chapter 4.3.1. The operation of the flame reactor was performed by Mathias Spree and co-workers from the department of Tim Hülser (IUTA).

Table 4.2: Equipment used for multiline NO-LIF thermometry. All hardware identifiers (e.g., EM) are valid in the context of multiline NO-LIF thermometry on the IUTA pilot-scale gas burner (Figure 4.2) and spray burner (Figure 6.1).

Identi-	Vendor	Product	Serial number
La1	Continuum Electro-Optics	Nd:YAG laser PL8010	6800
La2	Radiant Dyes	Dye laser NarrowScan D	1334 03/10
EM	LaVision	Energy Monitor	VZ05-0500
BH	SUSS MicroOptics	Beam homogenizer	N/A
SO	LaVision	Sheet and collimator optics	VZ09-0267, VZ09-
BP	Laser Optik	Bandpass 235–250 nm (FWHM)	N/A
L1	LaVision	UV camera lens ( $f = 100$ mm, $f_{\#} = 2.8$ )	N/A
IRO	LaVision	Intensified relay optics	VC09-0177
C1	LaVision	CCD camera Imager ProX	VC09-0171
PC	LaVision	Computer (Article: 1104038)	VP09-0092
PD	Stanford Research Sys-	Pulse/Delay generator DG535	18452
IB	IVG	Signal-interrupter box	N/A
L2	Computar	Camera lens ( $f = 25$ mm, $f_{\#} = 1.4$ )	N/A
C2	LaVision	CCD camera E-Lite	VC09-0227
L3	Computar	Camera lens ( $f = 25$ mm, $f_{\#} = 1.4$ )	N/A
C3	LaVision	CCD camera E-Lite	VC15-0285

## 4.3 Results

### 4.3.1 Gas-phase velocity measurements under non-reacting conditions

The non-reacting gas flow of the IUTA gas burner was investigated by PIV outside the flame reactor (chapter 4.2.1). Due to aspiration of the nozzle-injected air from the lower end of the quartz tube, the experiments are regarded as close to the real conditions in the flame reactor. The operating parameters are summarized in Table 4.3. For the PIV measurements, all gas flows were replaced by compressed air. Since the velocity range of PIV is limited by the selected time delay ( $dt$ ) between both laser pulses (chapter 2.2.3), the surrounding coflow or the inner nozzle flow (combustion-air flow) were seeded individually with appropriate choices of  $dt$ . Accordingly, in the results presented below, the area in which no physically meaningful velocities could be determined is masked, i.e., when the  $dt$  was optimized for the fast flow, the area dominated by the slow flow is masked and vice versa.

Table 4.3: Operating parameters used at the IUTA for nanoparticle synthesis with the pilot-scale gas burner at 900 mbar. For the PIV measurements outside the flame reactor, all gas flows were replaced by compressed air and the nozzle was operated at atmospheric pressure. All flow rates are given in slm.

Parameter set	Coflow	Combustion air	Separation gas	Fuel gas
	N <sub>2</sub> or air	O <sub>2</sub> + N <sub>2</sub>	N <sub>2</sub>	H <sub>2</sub> + Ar
1	200	28	2.1	12.6
2	200	28	2.1	15.4
3	200	28	4.2	21.0
4	200	28	4.2	23.5

For each measurement, 200 double-frame images were recorded and evaluated as described in chapter 3.3.1. The color-coding represents the calculated velocity magnitude  $u_{\text{mag}}$  and the definition of the 0 mm HAB mark refers to the position of the exit plane of the burner. Figure 4.5 shows the resulting averaged velocity fields of parameter sets 1, 2, and 3.

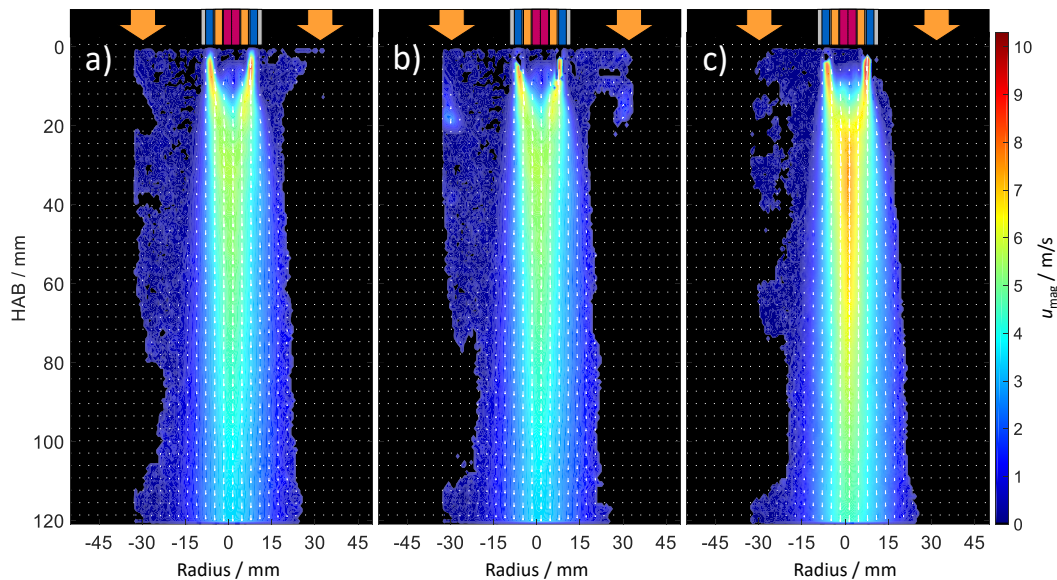


Figure 4.5: Averaged velocity fields for (a) operating parameter set 1, (b) parameter set 2 and (c) parameter set 3. For clarity, the gas burner nozzle as well as the surrounding coflow is depicted schematically (cf., Figure 4.2) and only every fourth velocity vector is plotted. Areas in which the standard deviation is more than 5% are masked.

Since only the combustion air could be seeded with DEHS droplets for the PIV measurements, there is an u-shaped area along the vertical central axis close to the nozzle where no velocities could be measured because the seeding density was too low. For all three operating parameter sets, the highest velocities were measured between 0–10 mm HAB centrally below the annular gap through which the combustion air exits the burner nozzle. Below that, the annular flow of the combustion air can no longer be distinguished from the separation and fuel-gas flow (in the following, the proportion of the flow making the significant contribution to the total flow velocity is referred to as primary flow field). This primary flow field with gas-phase velocities in the range of 4–8 m/s tapers with increasing HAB. In contrast, the outer zone of the primary flow field (with velocities between 2–3 m/s) evolves as a cone-shaped flow in all three velocity fields that increases in diameter with increasing HAB. For example, the flow field at 20 mm HAB has a diameter of 20 mm while at 120 mm HAB, the diameter increased to more than 40 mm. The flow near the nozzle exit shows slightly higher velocities on the

right than on the left side (this observation is discussed later in this chapter in the section about the variation of the separation-gas flow rate). As expected, the length of the primary flow field and its total velocity increases with increasing separation-gas flow and fuel-gas flow (the latter increase from left to right in Figure 4.5). It is noticeable that in Figure 4.5c the velocity magnitude increases from 6 m/s (at 20 mm HAB) to 7.5 m/s (at 32 mm HAB) along the centerline of the primary flow field. In contrast, in (a) and (b) the velocity decreases with increasing HAB, as intuitively expected. The reason for this is a 44% higher mass flow of the inner two channels of the burner (fuel gas and separation gas) in (c) compared to (b). Since the inner two mass flows are not seeded (see chapter 4.2.1), their velocity cannot be determined on the first 20 mm HAB, i.e., until the seeding particles mix with all inner gas flows.

In the PIV results shown in Figure 4.5, no direct information about the influence of the surrounding coflow can be extracted due to the selected  $dt$  between both YAG lasers ( $40 \mu\text{s}$ ) that was optimized for resolving the fast (inner) nozzle flow. Hence, separate measurements were performed investigating the coflow at different mass flow rates. Since operating parameter set 4 (Table 4.3) is favored by IUTA based on their experience in nanoparticle synthesis, all studies shown in the following are based on these flow rates. In order to investigate the effect of particular gas flows on the overall flow field, only one parameter was varied at a time, while all other parameters were kept constant.

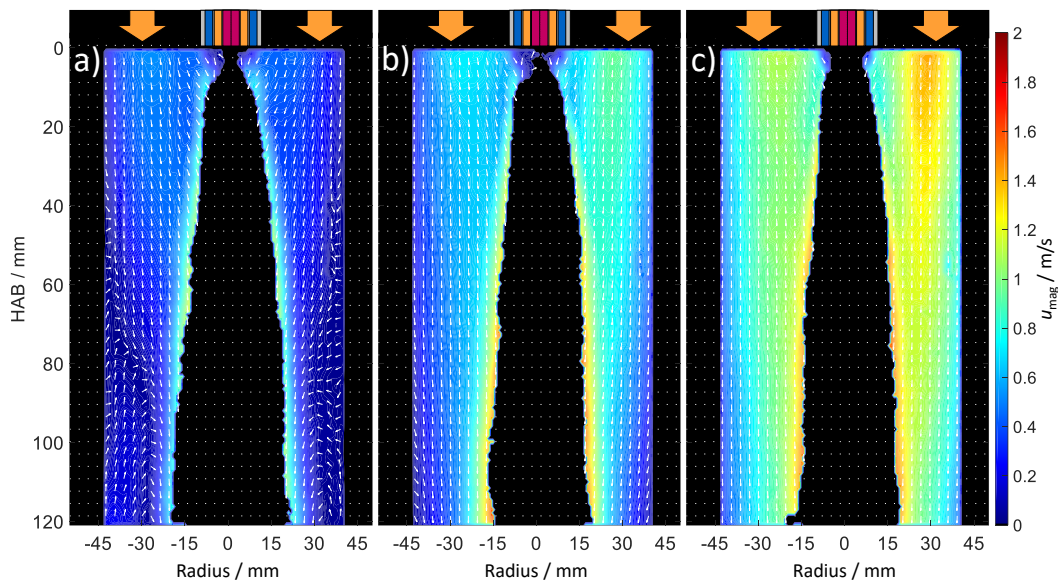


Figure 4.6: Averaged velocity fields for operating parameter set 4 increasing the coflow from (a) 100 slm to (b) 200 slm to (c) 300 slm. For clarity, the gas burner nozzle as well as the surrounding coflow is depicted schematically (cf., Figure 4.2) and only every fourth velocity vector is plotted (scaled to uniform length). Areas in which the standard deviation is more than 5% are masked.

Figure 4.6 shows the resulting velocity fields of the coflow. For these measurements, the temporal separation between both laser pulses was set to  $400 \mu\text{s}$  to enable measuring the coflow velocities in the range of 0.1–1.5 m/s with sufficient resolution. Therefore, the central area below the nozzle is masked as no physically meaningful velocities could be extracted. In the case of 100 slm coflow, slightly higher inflow velocities were found on the left than on the right side and a upwards-oriented counterflow is apparent that hits the downwards propagating coflow at 80 mm HAB. Both flows merge and are drawn inwards by the high momentum of the central nozzle flow. Furthermore, the counterflow has an upstream effect on the coflow as already at 30 mm HAB the coflow vectors close

to the quartz inliner are deflected inwards towards the centerline axis. Already at 150 slm coflow (M26, not shown here), the counterflow is not directly visible anymore but can be recognized indirectly by those vectors close to the quartz inliner that start deviating from their straight-downwards orientation to an inwardly inclined direction at 70 mm HAB. Also, for 150 slm coflow, only, an axial symmetrical velocity distribution is observed. For 200 slm coflow (Figure 4.6b), an inclination of the velocity vectors towards the central nozzle flow can be observed beginning 100 mm HAB downwards. It is concluded that the region of the first 100 mm HAB in which most of the precursor is converted (compare results from Fe-LIF measurements at the IUTA gas burner during synthesis of iron-oxide nanoparticles in Ref. [167]) is free from recirculation zones and counterflows. However, only higher coflow rates (e.g., 250 slm (not shown here) or 300 slm, (Figure 4.6c) do not show any indication for a counterflow within the observed 120 mm HAB and effectively keep the field of view free from recirculation. In order to investigate the influence of the coflow on the nozzle flow, measurements with identical parameter variation were carried out (not shown here), whereby the  $dt$  was optimized for the nozzle flow (40  $\mu$ s) and the combustion-gas channel was seeded DEHS droplets. Here, no effect was observed of the varied coflow rates between 100–300 slm on the nozzle flow, neither with regard to its radial nor with regard to its axial expansion. The results suggest testing 250 or 300 slm coflow rates at the next nanoparticles synthesis with the pilot-scale gas burner in the flame reactor at IUTA and check for reduced window fouling and improved nanoparticle quality.

The design of the IUTA gas burner allows the adjustment of the axial distance between the flame and the burner surface by varying the separation-gas mass flow fed through the annular gap located in between the (innermost) fuel-gas channel, and the (outermost) combustion-gas supply (Figure 4.2). To study the influence of the separation-gas flow on the flow field, PIV measurements were performed on parameter set 4 (Table 4.3) varying the separation-gas flow rate between 3–15 slm. As the flow rates of the separation-gas flow were too low for seeding with the installed seeder (chapter 4.2.1), the combustion-gas channel was seeded instead.

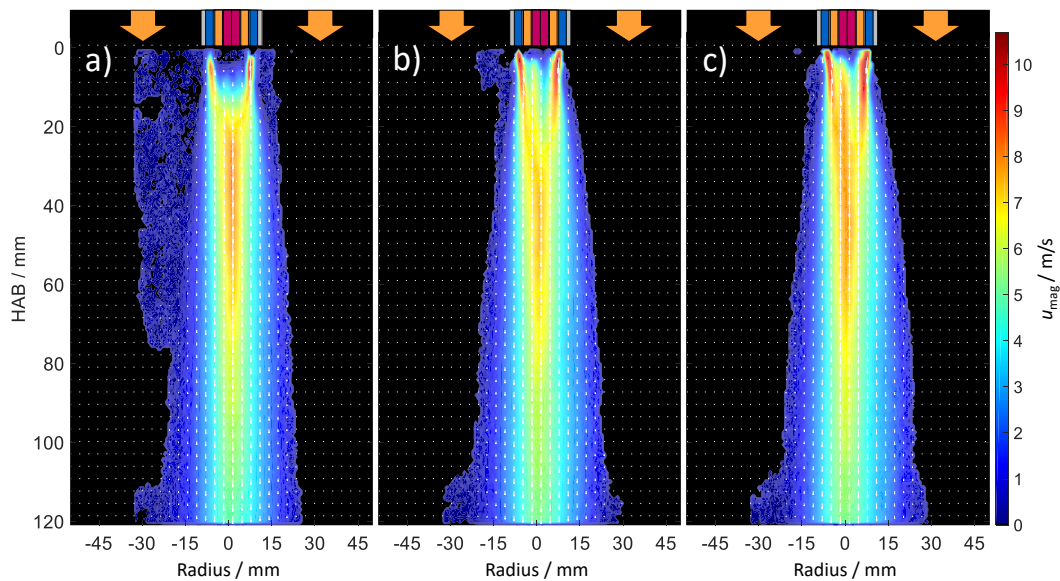


Figure 4.7: Averaged velocity fields for operating parameter set 4 varying the separation gas flow from (a) 4.2 slm to (b) 11.2 slm to (c) 15 slm. For clarity, the gas burner nozzle as well as the surrounding coflow is depicted schematically (cf., Figure 4.2) and only every fourth velocity vector is plotted. Areas in which the standard deviation is more than 5% are masked.

Figure 4.7 shows the evaluated flow fields of the most favored operation point for nanoparticle synthesis at the IUTA with 4.2 slm separation gas flow (a). In addition, another operation point well-rated by IUTA for nanoparticle synthesis with 11.2 slm separation gas flow (b), and the operation point with the highest separation gas flow rate investigated (15 slm, c) is presented. In Figure 4.7a, it can be seen that within a diameter of the innermost 8 mm, velocity vectors can only be calculated at minimum 8 mm HAB as the seeding density is too low at smaller HABs in this area. Nevertheless, the outflow from the separation-gas channel can clearly be identified by chronologically examining the evolution of the flow field within these inner 8 mm in diameter in Figure 4.7a–c. Here, an asymmetrical outflow is apparent that increases in velocity with increasing separation-gas flow rate mainly penetrating the left-hand side of the primary flow field (for a detailed view see region B in Figure 4.8 a–c). At 4.2 slm separation-gas flow, the air exiting the (innermost) fuel-gas channel dominates the primary flow field, as observable when looking at the centerline of the flow field of more than 8 m/s flow velocity between 25–50 mm HAB in Figure 4.7 a. The unambiguous allocation of this flow as “fuel-gas-channel flow” follows from the measurement data M38–M43 (not shown here), in which the fuel-gas flow rate is varied, exclusively. At 11.2 slm separation-gas flow (Figure 4.7b), 0.5 m/s lower peak velocity is found in the primary flow field along the centerline. In addition, the region of the primary flow field of velocities higher than 7 m/s is shifted (along the centerline) from 20 mm to 30 mm HAB. At the same time, the region below the (outermost) combustion-gas channel (with velocities higher than 8 m/s) increases spatially with increasing separation-gas mass flow, even though all other mass flows are kept constant (for a detailed view see region A in Figure 4.8). At 15 slm separation-gas flow, this trend continues (compare region A in Figure 4.8b and c). At the same time, the separation-gas flow forms a region with velocities above 7 m/s in region B (Figure 4.8c).

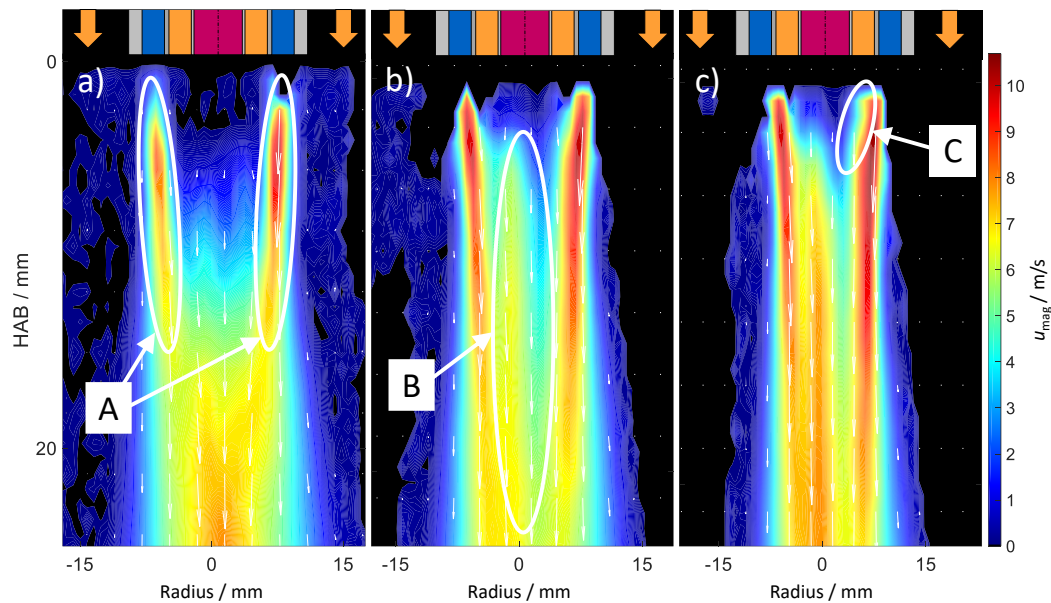


Figure 4.8: Enlarged view of Figure 4.7 into the near field of the IUTA gas burner nozzle. Region A marks the seeded flow emanating from the combustion-gas channel, region B marks the area in which the unseeded separation-gas flow and fuel-gas flow interact, and region C marks the area in which separation-gas and combustion-gas interact. The names of the regions are valid for all three subplots (a–c) although only one region is indicated per subplot for a better overview. For clarity, the gas burner nozzle as well as the surrounding coflow is depicted schematically (cf., Figure 4.2) and only every fourth velocity vector is plotted. Areas in which the standard deviation is more than 5% are masked.

Furthermore, as already observed in the velocity fields of operating parameter sets 1–3 (Figure 4.5), the flow exiting the combustion-gas channel (region A in Figure 4.8) shows higher velocities on the right side than on the left side of the nozzle for all investigated mass flows. Supported by the growing shoulder observable in region C in Figure 4.8 a–c, these observations suggest that the separation-gas flow and the combustion-gas flow merge on the right-hand side of the flow field close to the nozzle (especially noticeable in region C in Figure 4.8c. This also explains why the gas flow emanating from the combustion-gas channel (region A) shows higher velocities on the right side than on the left side in all measurements. Hence, the study of the separation-gas flow provides, in addition to the mass-flow corresponding velocity magnitudes, first insights into the interaction of the individual gas flows emanating from the burner that should be investigated more detailed in subsequent studies.

Although the IUTA gas burner has been thoroughly cleaned before being examined by PIV, it cannot be excluded that precursor or particle deposits may still be present inside the narrow annular gaps of the burner that cannot be removed by manual cleaning. However, even if assuming a completely clean burner, small irreversible changes in the widths of the co-annular gaps of the burner could have occurred for instance by thermal expansion of the burner during nanoparticle synthesis that explains the observed asymmetries in the flow field. Even though the behavior of the flame and the controllability of the distance between flame and burner surface cannot be directly assessed in this study, the results prove that the flow field can be significantly influenced by varying the mass flow of the separation-gas channel. The obtained results now enable the definition of boundary conditions for CFD simulations of the pilot-scale gas burner and studies under reactive operating conditions. A complete overview of all available measurement data is given in Table A3.4 in the Appendix.

#### 4.3.2 Temperature imaging with laser sheet correction during nanoparticle synthesis

Imaging gas-phase temperature measurements have already been performed before in the IUTA flame reactor [22]. However, the operating parameters applied in these previous investigations deviate significantly from the parameters used in the study presented in this chapter. For the previous flow field characterization, iron pentacarbonyl ( $\text{Fe}(\text{CO})_5$ ) precursor and 100 mbar reactor pressure was used while in the present study titanium isopropoxide (TTIP), 900 mbar, and higher mass flows were utilized. Hence, *in situ* characterization of the temperature field under these conditions is required. While the characterization of the non-reacting flow field was performed outside the flame reactor on a nozzle test rig at the IVG, the proof-of-principle temperature measurement with laser sheet correction presented in the following was performed inside the flame reactor during synthesis of titanium-dioxide nanoparticles at the IUTA. Therefore, the IUTA gas burner was operated with parameter set 2 (Table 4.3) and the gaseous precursor was fed together with nitric oxide required for NO-LIF thermometry through the central fuel gas channel. During the first tests, it was found that the quartz inliner strongly distorts the laser sheet, so that no physically meaningful mapping of the fluorescence images of both dye cuvettes was possible. It was not possible to mount the burner and the quartz inliner perfectly concentrically and reproducibly in the reactor chamber. Therefore, beam distortion could not be minimized (by hitting the inliner at  $90^\circ$ ) when measuring in the center plane of the flame. Therefore, a shortened quartz inliner was used for all experiments at the flame reactor in the IUTA that begins at the lower edge of the uppermost optical port (see  $\text{HAB}_{\text{max}}$ -marker in Figure 4.1) and thus does not interfere with the laser light sheet. Thus, both dye cuvettes provide the spatial distribution of the laser sheet energy entering and exiting the flame reactor (Figure 4.4) enabling the

intensity correction of the LIF images taken during the multiline NO-LIF measurements caused by light absorption due to particle deposition on the reactor windows during synthesis (window fouling).

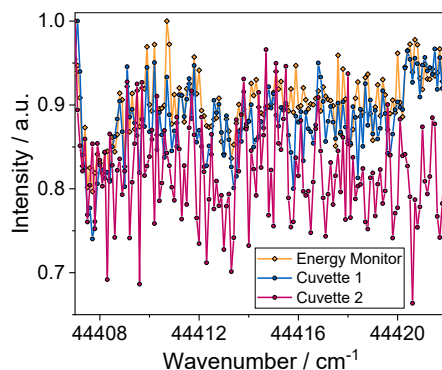


Figure 4.9: Measured laser intensities during a multiline NO-LIF scan with the energy monitor and spatially averaged fluorescence intensities of the laser sheet measured before entering the flame reactor (cuvette 1) and after leaving the reactor (cuvette 2). Each data point is averaged from 20 laser shots per wavelength position.

With this approach, data was obtained from the cuvette fluorescence that can be used as comparison to the laser-energy values measured simultaneously by the energy monitor (Figure 4.4). As depicted in Figure 4.9, the comparison of the laser intensities before entering the flame reactor shows similar trends for both measuring devices. When the signal increases at the energy monitor, an intensity increase is also observed with cuvette 1 and vice versa. Generally, the scaled intensity values of cuvette 1 are lower than the values of the energy monitor that can be explained by the difference in the detection technique. While the energy monitor measures the energy of the UV laser beam with an attenuated photodiode, the fluorescence signal measured in cuvette 1 (by a camera) is integrated over the height of the laser sheet after the laser beam has passed several additional optical components, such as the multi-lens array of the beam homogenizer, the sheet-forming optics, the beam splitter in front of the reactor, and the cuvette entrance window. However, at some wavelength positions, opposing trends are noticeable as also found in the comparison of the signal of cuvette 2 with cuvette 1 that could not be further investigated within the scope of the present thesis. Therefore, detailed suggestions are provided in the outlook (chapter 4.4) that identify and prioritize the most relevant next steps required for subsequent work.

Since both E-Lite cameras (Figure 4.4) capture the full height of the laser sheet fluorescence in each respective cuvette, the setup does not only provide a single correction factor per wavelength position but enables line-by-line correction of the NO-LIF images along the entire laser sheet height. Consequently, for the evaluation of the data derived from both E-lite cameras and for correcting the corresponding NO-LIF images, a Matlab code has been developed (“Absorptionskorrektur.m”, Table A4.3). In post processing, the single-shot images are averaged for each wavelength position and a rectangular region of interest (ROI) showing the fluorescence signals of the dye cuvettes is defined manually in the images. Each horizontal pixel line within this ROI is binned to a single value, resulting in a single intensity profile per cuvette as exemplarily shown in Figure 4.10 for an arbitrary laser shot taken during a NO-LIF scan in a precursor-free flame.

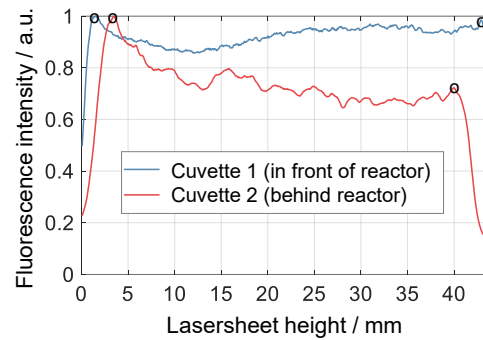


Figure 4.10: Intensity profiles of both dye cuvettes at an arbitrary moment during a NO-LIF scan before entering (cuvette 1) and after exiting (cuvette 2) the IUTA flame reactor operated with a precursor-free flame. The marked peaks define the upper and lower (spatial) limits of the laser sheet.

The height of the respective region of interest is selected for each cuvette image based on the height of the laser sheet so that the upper and lower limits of the ROI correspond to the peaks marked in Figure 4.10. It is apparent that the resulting lengths of the extracted intensity vectors differ from each other. This is due to exceeding the maximum working distance (max. 2000 mm [266, 267]) of the sheet forming optics (Figure 4.4) that could not be avoided in the experiment. To compensate for the different heights of the laser sheet in both cuvettes, the longer vector is mapped to the shorter one in the next post-processing step enabling the calculation of a correction vector (per spectral position) that quantifies the attenuation of the laser sheet when crossing the flame reactor. In this calculation, the flame reactor is abstracted as a black box, where it cannot be distinguished whether the attenuation of the laser sheet was caused by particle deposits on the reactor window, species-specific laser absorption (e.g., gas-phase intermediate species), particles, or other effects. Of course, the emitted NO fluorescence itself experiences attenuation on its way from the flame to the NO-LIF camera (not least due to the deposition of particles on the window in front of the camera), but this part was not further investigated in the present.

The correction vector then needs to be applied to the images detected by the LIF camera. A rectangular region of interest is selected from the LIF images based on cases with significant NO-LIF signal. Therefore, an interactive dialog for image selection is provided in the Matlab code. The selected width of the ROI is arbitrary, but the height must be limited to the area showing maximum NO LIF. After the correction vector from the cuvette measurements has been mapped to the height of the cropped NO-LIF images, it is multiplied for each wavelength position of the NO-LIF scan line by line with the NO-LIF image. Since the NO-LIF images are cropped, it is required to write the energy monitor value corresponding to each NO-LIF image into pixel (1,1) (equal to pixel (0,0) in DaVis). The corrected LIF images are exported to the IMX file format (using the “writeimx” command provided in LaVision’s “readimx 2.0” toolbox) and afterwards evaluated using DaVis and LIFSim as described in chapter 3.2.2.

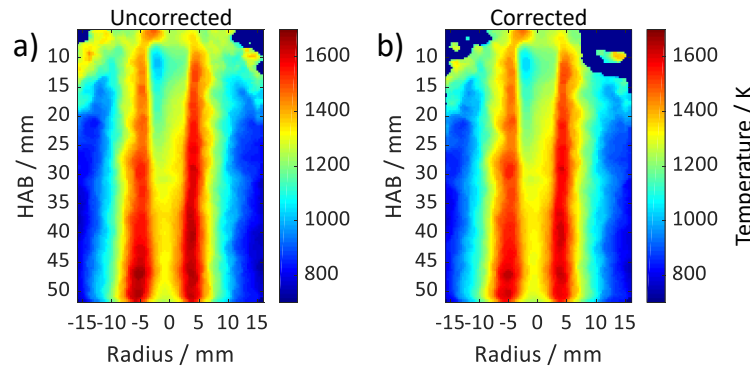


Figure 4.11: Temperature field of the synthesis flame (parameter set 2, Table 4.3) doped with 230 ppm TTIP before (a) and after (b) applying the correction for the laser fluence variation within the laser sheet.

In Figure 4.11, the proof-of-principle measurement of the laser sheet correction on a TTIP-doped flame is presented. Despite the elongated axial expansion of the hot flame zone, no visible flame chemiluminescence was observed through the second-highest optical access of the IUTA flame reactor (located 200 mm further below, cf. Figure 4.1). Hence, all investigations were limited to the uppermost optical port. Along the centerline, a distinctive cooler zone is apparent that was also observed in the temperature fields measured by Feroughi et al. [167, 170]. Due to the higher mass flows in comparison to the parameters investigated by Feroughi et al., this central zone extends axially beyond the lower limit of the optical port, showing temperatures between 1100 and 1300 K. For the flames examined by Feroughi et al. as well as for the flame investigated in this work, the cooler zone in the center is surrounded by hotter zones (here: 1400–1650 K) located on a radius between  $\pm 3$ –7 mm. These hotter zones extend from 9 mm HAB downwards beyond the field of view. Thereby, they enlarge radially from 2–5 mm indicating to merge into a single hot zone uniting at the center axis in further axial distance as recognizable in the flames of Feroughi et al., too. There, the hot zones of the flames merge between 20–30 mm HAB depending on the operating conditions.

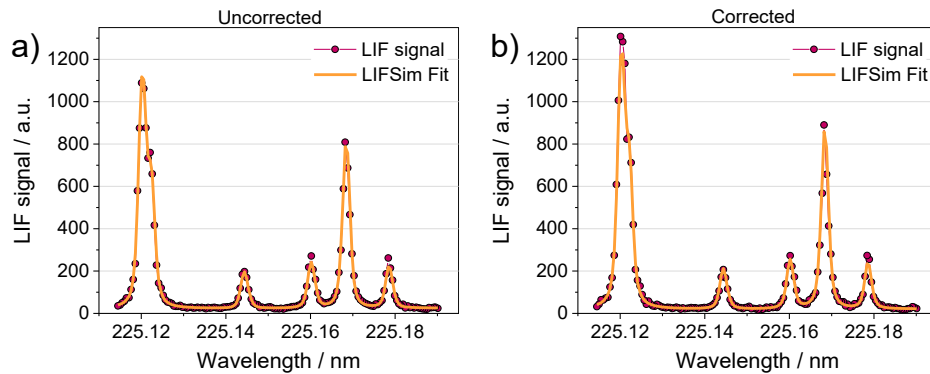


Figure 4.12: Excitation spectra and corresponding LIFSim fits (a) before and (b) after applying the laser sheet correction.

Further striking features of the temperature field are located in the upper left and right corners of the temperature maps shown in Figure 4.11, where temperatures around 1300 K are found. Similar zones can be identified in all temperature fields investigated by Feroughi et al. [167, 170] where they extend up to more than 40 mm HAB while in Figure 4.11 they can be found up to 20 mm HAB, only. It is assumed that the size difference of these zones is caused by the different operating pressures (100–200 mbar in the work by Feroughi, 900 mbar in the flame presented here) since a reduction in spatial expansion is observed when comparing the 200 mbar temperature field with the 100 mbar

temperature fields [167]. However, further investigations are required for verification. One possible explanation for these findings is the presence of recirculation zones in the upper section of the flame reactor. Although these were not observed in the PIV measurements presented in the previous chapter, a difference in the flow that leads to recirculation zones cannot be excluded since the LIF measurement of the TTIP-doped flame was carried out with a shortened quartz inliner inside the flame reactor. Especially in the area of the slow surrounding coflow (around 1 m/s, Figure 4.6), recirculation zones may be present in the reactor, e.g., caused by geometric disturbance of the upper edge of the optical ports or by thermal buoyancy.

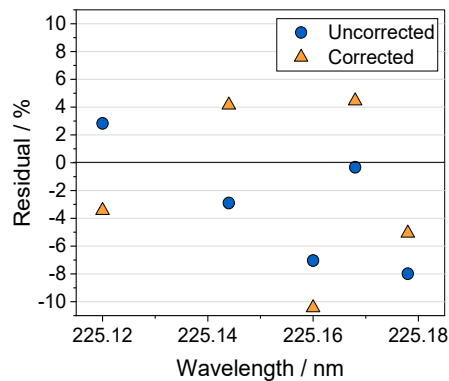


Figure 4.13: Residuals of the LIFSim fit averaged for each peak before and after applying the correction for the laser fluence variation within the laser sheet.

The comparison of experimental spectra and their corresponding fits (Figure 4.12) show the influence of the laser sheet correction. The total signal intensity rises for all peaks, e.g., by 20% for the peak at 225.12 nm and 10% for the peak at 225.168 nm while the other peaks are affected less significantly, e.g., 5% for the peak at 225.144 nm, 0.6% for the peak at 225.16 nm, and 4.5% for the peak at 225.178 nm. Since this affects the ratio of the peaks, the fits result in (slightly) different temperatures, e.g., 1303 K for the uncorrected spectrum (Figure 4.12a) and 1317 K for the corrected spectrum (Figure 4.12b). Moreover, for the fits shown in Figure 4.12, the averaged residuals between the excitation spectrum and the fit, range between +3% and -8% for the uncorrected case and +4% and -10% for the corrected case (Figure 4.13). In total, the mean value of the residual decreases from -3% in the uncorrected case to -2% after laser sheet correction indicating that the laser sheet correction improves the quality of the fit and thereby the evaluated temperature. A statistical evaluation of the residuals of all spectra of an image series would be useful to quantify the influence of laser sheet correction more detailed (see Outlook in chapter 4.4), but could not be performed in the context of this work, since LIFSim stores only five spectra per evaluation (instead of storing the spectra of each pixel).

In the corrected temperature field, the regions where the LIFSim evaluation failed are slightly larger (see upper left and upper right corners). Moreover, the calculated temperatures in the hot zones (located on a radius between  $\pm 3$ –7 mm) are about 40–50 K (2.5–3%) lower in (b) whereas no significant differences are found in the rest of the temperature fields. For better comparison, axial profiles were extracted (Figure 4.14) that show identical trends and similar absolute temperatures. Between 8 and 15 mm HAB, the temperature is on average 15 K (1.2%) higher for the corrected profile while between 31 and 52 mm HAB, the corrected profile indicates 15 K (1%) lower temperatures on average. Due to strategic decisions of the IUTA management, the flame reactor needed to be equipped

with the pilot-scale spray burner (Figure 6.1) and it was not possible to perform further measurements at other operating parameters or precursor-free flames with the pilot-scale gas burner. Therefore, the effect of the laser sheet correction on the temperature field is further evaluated in the context of the results of the pilot-scale spray flame presented in chapter 6.

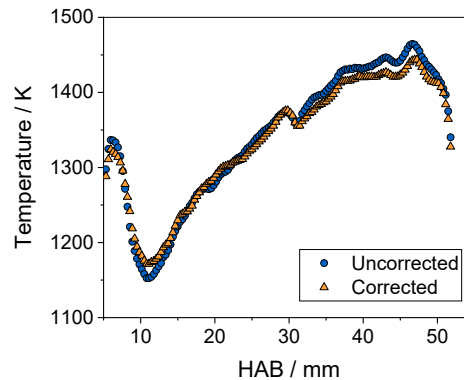


Figure 4.14: Axial temperature profiles with and without laser sheet correction extracted  $\pm 2$  mm around the centerline from the temperature fields depicted in Figure 4.11.

#### 4.4 Outlook

To further investigate the cause of the observed asymmetries in the primary flow field of the IUTA pilot-scale gas burner (Figure 4.8), PIV measurements were performed from two additional perspectives (not shown in this work, see list of measured data in Table A3.4 in the appendix). However, a final clarification of the origin of the observed flow asymmetry was not possible within the scope of this work. Hence, measurements of the individual exit velocities from the various gas inlets of the nozzle in absence of all other flows will enable further interpretation. Therefore, subsequent work should perform a parameter study utilizing seeders that allow seeding of lower volume flows (compare chapter 4.2.1).

The gas-phase velocity measurements suggest testing 250 and 300 slm coflow for nanoparticle synthesis with the IUTA flame reactor to reduce window fouling on the quartz inliner and for improving product quality (by decreasing the recirculation of nanoparticle-laden flows near the flame). Since up to 0.4 m/s (28%) higher coflow velocities were measured on the right side of the primary flow field than on the left side (Figure 4.6c), further experimental investigations are required to determine the origin of the observed asymmetry in the velocity field of the coflow, e.g., by analyzing the flow field inside the exchangeable reactor head (Figure 4.1) from where the coflow is emanating. Moreover, the results indicate the presence of a helical vortex in the coflow since for instance at 100 slm coflow, the average gas velocity is higher on the left side of the primary flow field while at 200–300 slm coflow, the velocity is higher on the right side. Here, stereo PIV measurements or tomographic imaging, where each flow channel is seeded with distinguishable tracers, would provide key insights.

The development of the laser sheet correction at the IUTA pilot-scale nanoparticle facility turned out to be ineffective, as parts of the setup had to be removed frequently due to project-relevant modifications on the flame reactor (the flame reactor is utilized for a number of projects that overlap in time). Moreover, the operation of the flame reactor requires considerable time and personnel effort so that the number of (test) measurements was limited. For the necessary improvements mentioned below, the experimental setup should be moved to a lab-scale reactor that offers single-person operation and easy accessible experimental boundary conditions. As a first step for improving the laser

sheet correction, the dye laser should be scanned spectrally (in the wavelength region required for multiline NO-LIF thermometry) while the reactor is operated without flame (but with cold NO) to analyze the trends of the laser intensity measured by the energy monitor and both dye cuvettes (compare Figure 4.9) more detailed. In this context, the implausibility of a decreasing correction factor (associated with decreasing window fouling during nanoparticle synthesis) needs to be addressed. Subsequently, the Matlab script should be optimized with regard to the determination of the areas in which the fluorescence of the laser sheet can be observed (ROI) on the three individual camera images (currently, the determination of the outer edges is critical). Automatic ROI-detection by a dynamic threshold or by a neural network algorithm will enhance reproducibility. Also, structuring the laser sheet (e.g., by placing a grating in the beam path of the laser sheet at the beginning of each measurement) has proven to be helpful in assigning the limits of the ROI in the post processing. Here, an improved grating design with adjustable upper and lower limits would help in limiting the height of the laser sheet to the region of homogeneous energy distribution (detectable by the fluorescence signal of the dye cuvettes). As the safety infrastructure of the IUTA flame reactor does not allow operation of the burner (i.e., the mass flow controllers) without flame (e.g., to enable NO-addition to the reactor without flame operation), these important development steps could not be sufficiently performed within the scope of the present work. However, it is expected that the suggestions mentioned above will significantly improve the quality of the laser sheet correction. Hereafter, further *in situ* characterization of the reacting flow of the gas burner inside the IUTA flame reactor should be performed, e.g., to determine temperature fields without precursor that provide additional valuable boundary conditions for future CFD simulations. In this context, precursor-doped temperature measurements with the operating parameters investigated by PIV (Table 4.3) would allow for comprehensive insights.

Future evaluation of the multiline NO-LIF thermometry data should be performed with the improved LIFSim version that is currently developed in Matlab. Thereby, statistical evaluation of the fit residuals of all pixels will be enabled that can be used to further quantify the fit quality as well as the influence of the laser sheet correction.

## 5 Lab-scale spray burner for nanoparticle synthesis

Sections of the following chapter are reprints from the publications:

**Schneider, F.**, Dreier, T., Schulz, C., *SpraySyn – Standard Burner for the Collaborative Investigation of Spray-Flame Synthesis of Nanoparticles: Droplet Velocity and Size of the Non-Reactive Ethanol Spray*, 9th European Combustion Meeting, 2019, Lisbon, Portugal

**Schneider, F.**, Suleiman, S., Menser, J., Borukhovich, E., Wlokas, I., Kempf, A., Wiggers, H., Schulz, C. *SpraySyn – A standardized burner configuration for nanoparticle synthesis in spray flames*. Rev. Sci. Instrum., 2019. 90(8): p. 085108; DOI: 10.1063/1.5090232; licensed under CC BY 4.0

**Schneider, F.**, Suleiman, S., Wlokas, I., Dreier, T., Wiggers, H., Schulz, C., *The SpraySyn standard burner enabling coordinated research on materials synthesis in spray flames*, 29. Deutscher Flammentag, 2019, Bochum, Germany

The respective parts are entirely based on my own experimental work. The final version of the respective publication was written together with the coauthors who also have contributed to structuring and wording of the article.

### 5.1 SpraySyn burner

Spray-flame synthesis (chapter 2.1) was first proposed by Sokolowski et al. for synthesizing alumina nanoparticles from finely sprayed aluminium acetylacetonate solutions [44] and has been extensively developed by Pratsinis, Mädler, and co-workers [29, 51, 268, 269]. In these works, spray-flame burners are presented where a liquid precursor solution is atomized by a two-fluid nozzle and ignited either by:

- Six [48] or eighteen [49] surrounding pilot flames
- A non-premixed methane/oxygen flame originating from two co-annular ring gaps [50]
- A premixed pilot flame originating from a single narrow (150–200  $\mu\text{m}$ ) co-annular ring gap [51-53], also used in a commercial apparatus

To link detailed experiments with numerical simulations, the latter burner concept has been optimized aiming to provide:

- A modular burner design that is easy to assemble and facilitates the exchange of spare parts to ensure operation under clean and reproducible conditions
- Alignment capability to generate symmetric flames
- Simulation-friendly geometry that prevents the time consuming simulation of the periphery of the flame (e.g., locally high gas velocities in the pilot flame) and that is well documented
- High flow rates to prevent the need for active cooling
- Shielding against the environment

In the burner version presented by Menser et al. in 2015 [54], the design was improved by three micrometer screws that, unlike other spray-flame burners [48, 270], enabled the alignment of the capillary for the fluid supply within the two-fluid nozzle to generate vertical and radial symmetrical spray flames [54]. Moreover, the pilot-flame gas mixture was no longer provided through a narrow ring gap but through a porous bronze matrix generating a round, flat pilot flame stabilized on top of

the porous bronze. With this burner, numerous investigations on spray-flame synthesis of tailored functionalized nanoparticles like titanium dioxide [271], iron oxide [272], and perovskites [273-275] have been performed.

However, since spray-flame synthesis covers multiple interdisciplinary challenges (chapter 2.1), most experimental investigations available in literature have focused on the characterization of the final material produced neglecting detailed studies of the process chain (solution stabilization, spray formation, precursor transition from liquid phase into gas phase, interaction of precursor with flame chemistry, and finally particle formation in a complex turbulent reacting flow field). In addition, only little progress was achieved so far in simulating these processes, since the overall process extends over several spatial and temporal scales and occurs in a complex two-phase reacting flow [26]. Examples like the Gülder [39], Santoro [38], McKenna [31], and Taran burner [276, 277], the Tsuji laminar burners [278], the TNF turbulent flames [58], ECN sprays [59], Sandia Flame D [57], and many more [30] successfully demonstrated that standardized experiments enable major progress in comprehensive, interdisciplinary research.

For these reasons, the latest iteration known as SpraySyn burner [7, 26, 279] has been developed to series maturity within the DFG priority program SPP1980 [280] and was introduced as a reference experiment [26]. By that, for the first time, a standardized experiment in the field of combustion-based nanoparticle synthesis has been established. At the end of 2017, in total 16 SpraySyn burners were distributed within the community providing an ideal environment for comprehensive experimental investigations as well as for the development and validation of models and simulation methods and thus enabling synergies in interdisciplinary research activities [26].

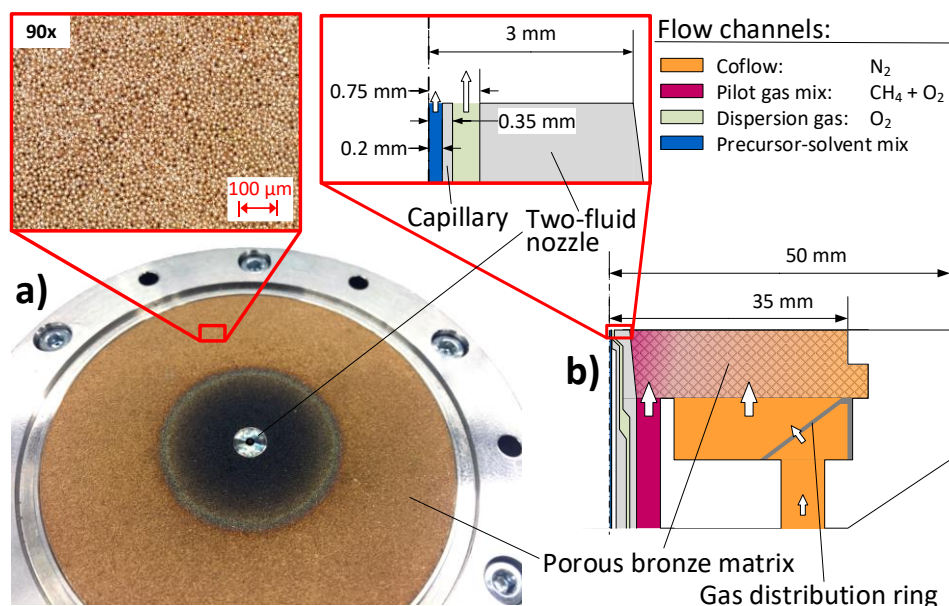


Figure 5.1: Photo of the SpraySyn burner (a) with a magnification of the surface of the porous bronze matrix and a sketch (b) providing all relevant geometries as well as all flow channels of the SpraySyn burner.

In the SpraySyn burner (Figure 5.1), nitrogen is fed as coflow through a single tube located below a gas distribution ring that is installed to distribute the gas flow below the porous plug homogeneously within an annular gap (orange) between 9.5 and 35 mm. The oxygen/methane pilot gases are pre-mixed in the supply line of the burner and exit through an annular gap (red) with an outer radius of 7.5 mm below the porous plug. Within the porous bronze there is no spatial separation between the

pilot gas mixture and the coflow allowing both flows to interact with each other along the 10 mm height of the porous plug. Thereby, the coflow is not only used to shield pilot and spray flame against the environment but to provide computationally convenient boundary conditions for CFD simulations. Finally, the ignited pilot gases form a round, flat pilot flame that is stabilized slightly above the porous bronze.

In the center of the burner, a two-fluid nozzle adjoins the porous plug at an outer radius of 3 mm. The central orifice of the nozzle has a radius of 0.75 mm, where a high-speed oxygen flow (detail of Figure 5.1 (b), green) atomizes a liquid solvent or precursor-solvent mix (blue) that is fed through a capillary on the centerline of the two-fluid nozzle. The capillary has an inner radius of 0.2 mm and an outer radius of 0.35 mm and ends right at the top of the two-fluid nozzle, i.e. the upper burner surface. In Table 5.1 all relevant dimensions for the gas and liquid flows are summarized.

Table 5.1: Overview of the relevant outlet radii of the gas and liquid flows of the SpraySyn burner in mm. All radii are given at the respective outlet cross-sections. In case of the capillary and the two-substance nozzle, the outlet cross-sections are located at the top of the burner; in case of the pilot gas mixture and coflow, the outlet cross-sections are located below the porous bronze plug (cf., Figure 5.1b). Reprinted with modified layout from Refs. [55, 56].

Name	Inner radius	Outer radius
Capillary	0.2	0.35
Two-fluid nozzle	0.75	3
Pilot gas mixture	4	7.5
Coflow	9.5	35

Since the SpraySyn burner is intended to provide a standardized research flame, first, a method needs to be developed that ensures equal burner operation and thus similar flames in every laboratory. Therefore standard operating conditions were defined (Table 5.2) and a consumer-camera-based flame characterization scheme for the quantitative assessment of the flame geometry such as flame length, diameter, tilt angle, and photometric distribution of visible chemiluminescence along the center axis of the flame was developed in the context of this thesis [26]. In chapter 5.3.1, details of the flame characterization are outlined and an exemplary benchmark of the reference flames (Figure 5.2) is shown.

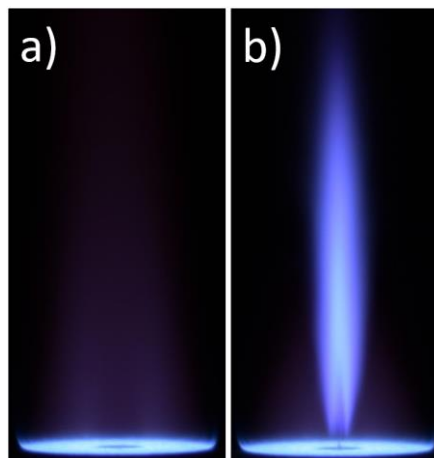


Figure 5.2: a) Pilot flame (PF1) and b) ethanol spray flame (SF1) taken with an exposure time of 1/13 s (ISO 100,  $f_{\#} = 1.8$ ). The flames were operated according to the parameters given in Table 5.2. Reprinted with modified layout from Refs. [55, 56].

For the SpraySyn burner, all relevant quantities such as gas-phase and liquid-phase velocities and temperatures as well as droplet diameters need to be determined to provide a comprehensive database for more in-depth investigations and, furthermore, to provide boundary conditions for CFD simulations. In this work, droplet velocities and sizes in the non-reacting sprays of ethanol, acetone, 1-butanol, and n-hexane (chapters 5.3.2 and 5.3.4) as well as in the ethanol spray flame are presented (chapters 5.3.3 and 5.3.4) and a characterization of the two-fluid nozzle is performed (chapter 5.3.5).

Table 5.2: Standard operating conditions of the SpraySyn burner for the non-reacting ethanol spray (S1), the pilot flame (PF1,  $\phi = 0.25$ ) and the ethanol spray flame (SF1). Reprinted with modified layout from Refs. [55, 56].

Flow channel	S1	PF1	SF1
Pilot O <sub>2</sub>	-	16 slm	16 slm
Pilot CH <sub>4</sub>	-	2 slm	2 slm
Coflow N <sub>2</sub>	120 slm	120 slm	120 slm
Dispersion O <sub>2</sub>	10 slm	-	10 slm
Liquid feed	2 ml/min	-	2 ml/min

## 5.2 Experiment

### 5.2.1 Standardized experiment for imaging flame characterization

To ensure operation of the flame under standard conditions and to rule out adverse effects of deteriorated burner parts (porous plate or capillary) an imaging-based characterization method is introduced using a DSLR consumer camera and a Matlab image post-processing algorithm. Together, they enable the user to benchmark own results with the reference flames PF1<sub>ref</sub> (Figure 5.2a) and SF1<sub>ref</sub> (Figure 5.2b) regarding flame height, diameter, tilt angle, and flame color. Table 5.3 describes the recommended equipment and settings for flame imaging measurements that form the basis of the comparison and generate the correct data format for post-processing. The use of other hardware as well as deviation from the suggested setup and post-processing may lead to different evaluation results that make the comparison of the investigated flame with the reference flame pointless.

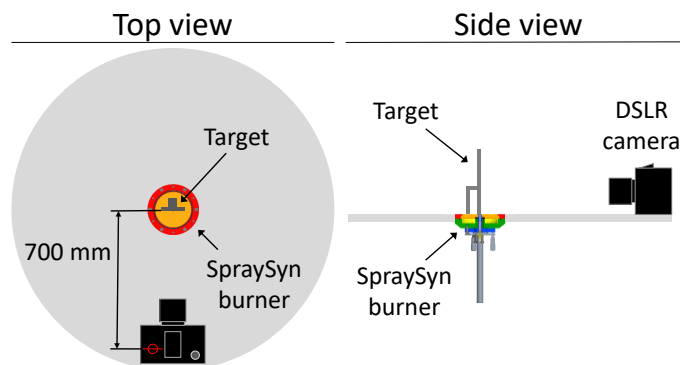


Figure 5.3: Optical arrangement for flame characterization. A detailed manual that guides through the process of image acquisition and post processing is available on [www.spraysyn.org](http://www.spraysyn.org). Reprinted from Ref. [26] licensed under CC BY 4.0.

A customized structured metal sheet (SpraySyn target, see [www.spraysyn.org](http://www.spraysyn.org)) is positioned upright and centrally on the SpraySyn burner facing the camera. The camera body is placed horizontally at the same level as the upper surface of the SpraySyn burner at a distance of 700 mm between the

camera chip and the front side of the target (Figure 5.3). For the flame characterization, a target image, background images, as well as about 50 images per flame (PF1 and SF1) are taken in a dark environment at the defined exposure times and  $f$ -stop settings given in Table 5.3. A detailed tutorial, the Matlab codes as well as the reference flame data for the flame benchmark can be downloaded from [www.spraysyn.org](http://www.spraysyn.org). The post processing is based on the RAW images that are converted to 16-bit TIFF files using DCRaw [237] to make them accessible in Matlab [236]. No gamma correction, color management, or white balancing is applied to the images. The TIFF images of the flame are checked for overexposure and the background is subtracted subsequently. If the flames are operated under the standard conditions (Table 5.2) and recorded with the given camera settings (Table 5.3), there should be no overexposed image in the series.

Table 5.3: List of hardware and camera settings. Use manual mode M only; automated image correction must be disabled, e.g., active D-lighting, HDR, special effects, etc. Reprinted with modified layout from Ref. [26] licensed under CC BY 4.0.

Camera	Nikon D5300 (Nikon item number VBA370AE, EAN 018208935543)
Lens	Nikon AF-S 50/1.8G Nikkor (Nikon item number JAA015DA, EAN 018208021994)
Resolution	24 megapixel, 14 bit
ISO	100
$f\#$	1.8
Exposure time	1/13 s

### 5.2.2 Phase Doppler Anemometry

The SpraySyn burner was operated with the parameters listed in Table 5.2. Four mass flow controllers (MFC) were used to meter coflow (MFC1), pilot flame fuel gas (MFC2), pilot flame oxidizing gas (MFC3), and dispersion gas (MFC4) for operation of the two-fluid nozzle. A syringe pump (SP) was used to meter the liquid volume flow. Droplet velocities and size distributions in the ethanol spray (S1) were measured using a commercial fiber-based dual phase-Doppler anemometry (PDA) system (Dantec Dynamics). Figure 5.4 shows the setup for *in situ* measurements on the SpraySyn burner using first order refraction of the droplets. It consists of two monochrome diode lasers operated at 20 mW with beams at 532 and 561 nm. Beam splitters divide each of both laser beams and a frequency shift is applied by a Bragg cell (B) to one of both beams of each color. The focusing-lens (L1) overlaps all four rays into an ellipsoidal probe volume, resulting in a moving interference pattern in the plane of intersection of each laser beam. Due to the applied frequency shift (i.e., the moving interference pattern), the directional ambiguity is removed, whereby the flow direction of the droplets can be clearly identified. By using two lasers, two velocity components  $u$  and  $v$  of the spray droplets (corresponding to the HAB-axis and the  $r$ -axis, respectively) can be measured simultaneously. Due to the 300 mm focal length of the focusing lens (L1) and the outer diameter of the SpraySyn burner (100 mm), a minimum height above the burner (HAB) of 10 mm can be probed in the presented configuration.

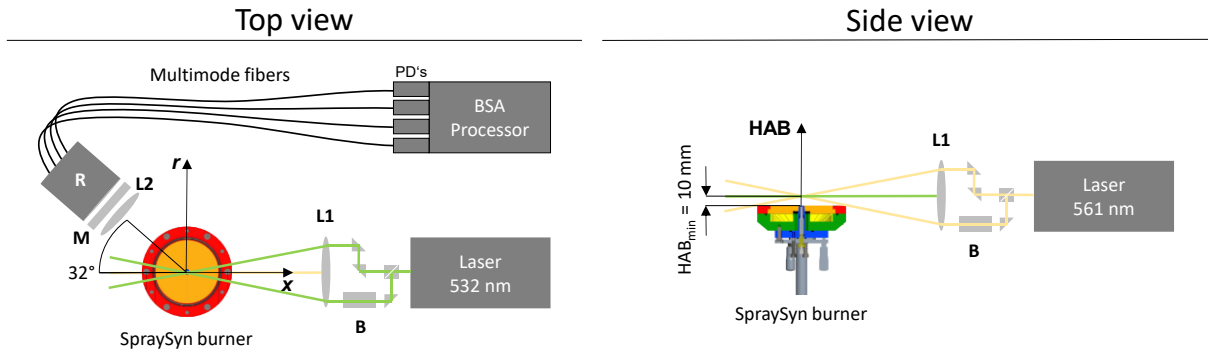


Figure 5.4: Fiber-based dual PDA setup applied to the SpraySyn burner indicating the axis definitions ( $x$ ,  $r$ ,  $HAB$ ). The top view shows the 532 nm laser, the optical receiver, the photo detectors (PD) and the BSA processor that are omitted in in the side view for better clarity. The side view shows the 561 nm laser and the minimal height above the burner ( $HAB$ ) accessible in this configuration (figure based on Ref. [56]).

An optical receiver (R) is collecting the scattered light induced by droplets crossing the measuring volume by a collimating-lens (L2) mounted in front of the receiver. The scattered light is separated through an exchangeable detection mask (M) into four channels corresponding to each of the four photo-detectors (PD) installed in the BSA processor. The combination of the applied mask and the four-detector setup enables the measurement of droplets in the range from 1–63  $\mu\text{m}$ . The light passing the mask is focused on an adjustable slit (50  $\mu\text{m}$ ) inside the receiver and then collimated for each channel by a segmented lens that couples the light into a multimode optical fiber where it is directed to the photo-detectors and processed by the burst spectrum analyzer (BSA processor), subsequently.

Table 5.4: Equipment used for droplet velocity and size measurements by PDA. All hardware identifiers (e.g., BSA) are only valid in the context of PDA on the SpraySyn burner.

Identi-	Vendor	Product	Serial number
MFC1	Bronkhorst	300 slm $\text{N}_2$ mass flow controller	W1721361F
MFC2	Bronkhorst	5 slm $\text{CH}_4$ mass flow controller	M17217137A
MFC3	Bronkhorst	20 slm $\text{O}_2$ mass flow controller	M17217137I
MFC4	Bronkhorst	20 slm $\text{O}_2$ mass flow controller	M17217137H
SP	Ayxisis	Syringe pump AP-SP04-db	18004
Laser	Dantec Dynamics	Laser Flow Explorer DPSS 300	0124
R	Dantec Dynamics	HiDense Probe / Receiver	9060X0421
BSA	Dantec Dynamics	Burst Spectrum Analyzer P600	9063N0531-213
PC	Dell	Computer	8VS25M2
T	Dantec Dynamics	Traverse	684

A computer (PC) was used to control the laser, the BSA processor, and a traverse (T) that was used to move the laser and the receiver simultaneously in all directions whereby spatial scanning of the flow field is enabled. The Dantec BSA Flow Software (v6.50) was used for all measurements that provides interfaces to control and monitor all devices and performs automated signal evaluation. Four validation criteria are applied to each signal burst. First, the burst detector filters out signals below a certain SNR threshold (set to 0 dB). The second validation criterium is based on the FFT spectrum of each burst where the dominant peak correlates with the frequency of the measured droplet. The spectral power of the highest peak in the spectrum needs to be four times higher than the second highest peak to accept the burst. By that, the effective peak ratio for the dual PDA measurements is two times higher compared to conventional PIV measurements. The third validation criterium is coincidence

filtering that checks for overlapping arrival times of the signals at both laser frequencies indicating light scattering from a single (i.e., the same) particle only. Finally, spherical validation is applied that compares the droplet sphericity calculated from each color channel. In our measurements, we accept a deviation of 30% from sphericity. Further details that simplify the reproducibility of the results presented in chapter 5.3.2–5.3.5 are given in the appendix (chapter A3.3.2). An overview of the utilized measurement equipment is provided in Table 5.4.

## 5.3 Results

### 5.3.1 Characterization of the SpraySyn reference flames

After taking photos of the pilot flame and the ethanol spray flame with the setup and parameters defined in chapter 5.2.1, the images are evaluated fully automated with the Matlab scripts provided at [www.spraysyn.org](http://www.spraysyn.org). Details of the processing steps are documented in the appendix in chapter A3.3.1. This unified procedure allows a quantitative comparison of the end-user operated flame with the reference flame, ensuring that the SpraySyn burner is operating correctly.

The flame evaluation can be split into two parts. In part one, the flame geometry is characterized. Therefore, all three color-channels of each image are summed up and radial intensity profiles are taken every two millimeters above the burner. A Gaussian fit is applied to each radial profile using a non-linear least-squares solver to determine the flame diameter by the FWHM of the Gaussian curve (Figure 5.5).

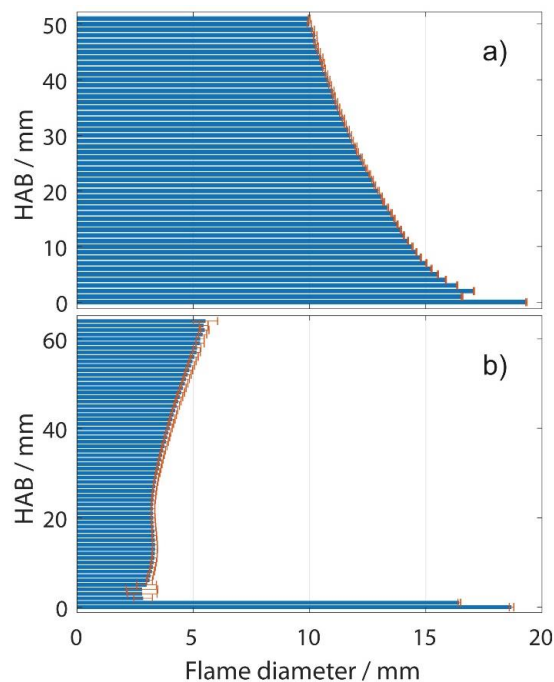


Figure 5.5: Average flame diameter depending on height above the burner (HAB) for (a) PF1<sub>ref</sub> and (b) SF1<sub>ref</sub>. The error bars show  $2\sigma$  of the results from 200 images for PF1<sub>ref</sub> and 300 images for SF1<sub>ref</sub> [26]. Reprinted from Ref. [26] licensed under CC BY 4.0.

The flame centerline is found by fitting a straight line through all peaks of the Gaussian profiles. Based on that, the flame height is calculated from the intensity distribution along the centerline for each image. The lower limit is preset to HAB = 0 and the upper limit, i.e., the flame height is preconfigured to an intensity threshold of 10% from the maximum counts along the centerline. Furthermore, the

tilt angle is calculated between the flame centerline and a vertical line originating from  $r = 0$  at  $HAB = 0$ . To keep the experiment simple, the tilt angle is evaluated from a single perspective only. To minimize the tilt angle, the user of the SpraySyn burner needs to align the capillary (Figure 5.1) centrally in the two-fluid nozzle with the micrometer screws first, then optimize the position of the capillary slightly during operation of the spray flame aiming to adjust it as vertical as possible. The position of the camera should be chosen so that the flame is photographed from the perspective, from which the user observes the greatest angle of inclination, i.e., the camera position is orthogonal to the largest tilt angle. For closer inspection, users can take pictures from one to two additional perspectives to ensure correct alignment. Figure 5.6 shows the evaluated height and tilt angle of the reference flames. The resulting flame geometries (height, diameters, and tilt angle) are summarized in the characterized flame images (Figure 5.7).

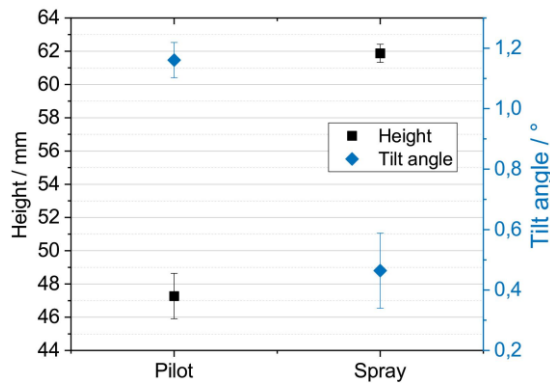


Figure 5.6: Averaged flame heights and flame tilt angles for  $PF1_{ref}$  and  $SF1_{ref}$ . The error bars show  $2\sigma$  of the results from 200 images for  $PF1_{ref}$  and 300 images for  $SF1_{ref}$  [26]. Reprinted from Ref. [26] licensed under CC BY 4.0.

In the second part of the flame characterization, the color information along the flame centerline is evaluated using the broadband flame chemiluminescence detected through the embedded Bayer filter of the DSLR camera. As the camera is part of the standardized experimental setup, the color profiles can directly be compared without further processing like color cross-talk correction [96]. Axial color profiles are taken along the flame centerline from the RGB images. The ratio of the blue and red color channel  $C_{br}$  is used to evaluate the proper color distribution of the flame.

In the final flame benchmark, the flame characteristics evaluated by each user of the SpraySyn burner are compared with the reference flames  $PF1_{ref}$  and  $SF1_{ref}$ . For that, the values of flame diameter and color ratio  $C_{br}$  are extracted at  $HAB = 10$  mm for  $PF1_{ref}$  and  $HAB = 20$  mm for  $SF1_{ref}$  that are known to be particularly sensitive to parameter variations for the respective flame. Figure 5.8 shows two example flame benchmarks, on the one hand for the pilot flame (a) and on the other hand for the ethanol spray flame (b).

In an ideal case, the deviation between the flame investigated (orange) and the reference flame (blue) would be zero for all four criteria (height, diameter, tilt angle and color ratio). In the given example, the height of the pilot flame (Figure 5.8a) matches the height of the reference flame almost perfectly. Also, the diameter of the pilot flame is only slightly larger compared to the reference flame, while the tilt angle is just within the specified tolerance of 5% (indicated by the blue error bars). The color ratio  $C_{br}$  of the investigated pilot flame is about 1.5% smaller compared to the reference flame, hence indicating that the investigated pilot flame emitted a slightly stronger red proportion in its broadband

chemiluminescence. In summary, the investigated pilot flame passes the benchmark successfully, that allows the user to perform the flame characterization of the ethanol spray flame.

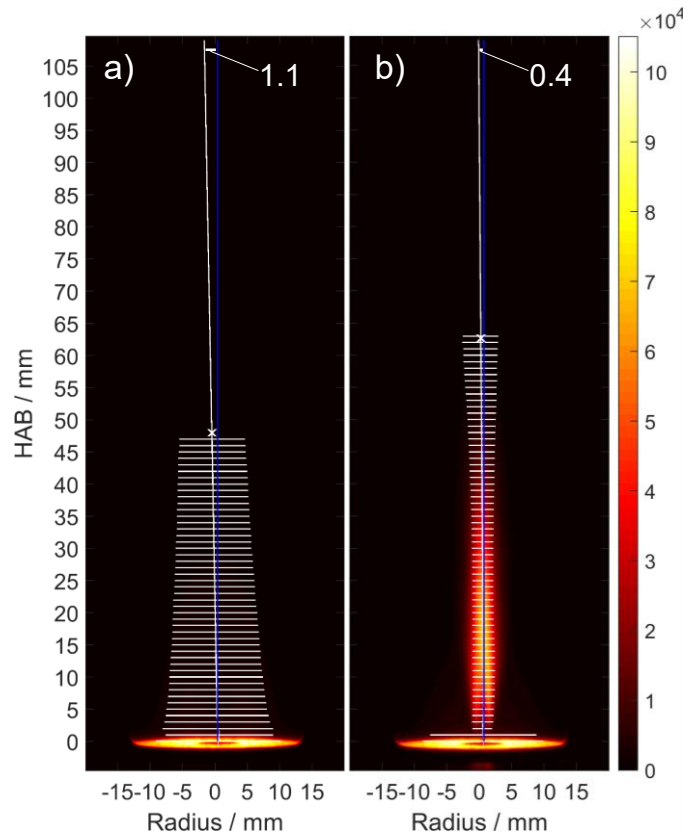


Figure 5.7: Characterized flame images for (a) PF1<sub>ref</sub> and (b) SF1<sub>ref</sub> showing the flame diameters (horizontal lines), the flame height (white x), and the flame tilt angle derived from the flame centerline (white) and the corresponding vertical line (blue) [26]. Reprinted from Ref. [26] licensed under CC BY 4.0.

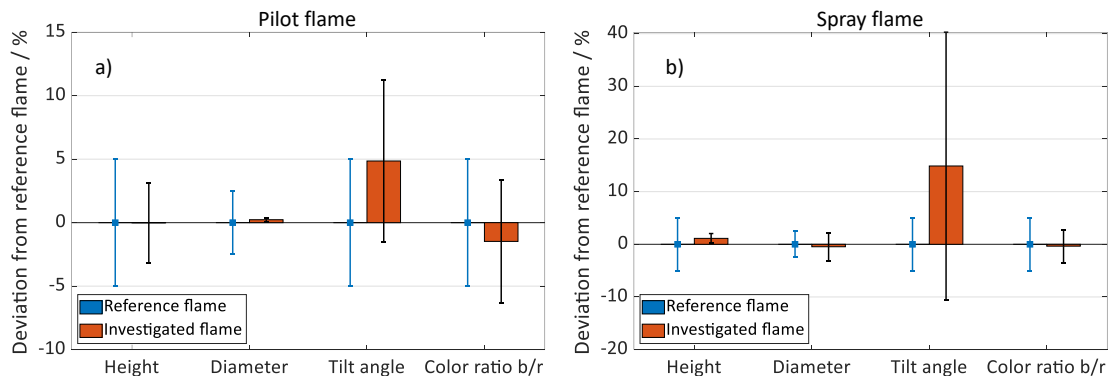


Figure 5.8: Example flame benchmark of the investigated flames PF1 (a) and SF1 (b) performed by a user of the SpraySyn burner. The error bars of the reference flame (blue) indicate the given tolerances within that a flame operated by the user should rank to pass the benchmark successfully. The orange bars illustrate the relative deviations of the investigated flame from the reference flame indicating the calculated standard deviations by the black error bars [26]. Reprinted with modified layout from Ref. [26] licensed under CC BY 4.0.

The flame benchmark of the ethanol spray flame (Figure 5.8b) shows that the investigated spray flame is about 1% higher than the reference flame. Regarding diameter and color ratio  $C_{br}$ , the investigated flame is slightly smaller and, again, slightly more red in contrast to the reference flame. Especially noticeable in this example is that the tilt angle is more than 12% greater compared to the reference flame. In this case, a readjustment of the capillary inside the nozzle of the SpraySyn burner is required

and a new flame characterization should be performed by the user to assure comparable burner operation with regard to the reference flames. This way, comparability between results from different laboratories is enabled.

Beside the presented figures (Figure 5.5–5.8), the provided Matlab codes export the results of the flame characterization and benchmark in mat-files to provide the user with all relevant results highlighting if benchmark criteria exceed the given tolerances. Table 5.5 summarizes the characterization results of the reference flames that are applied in the flame benchmark.

Table 5.5: Characterization results of the reference flames ([www.spraysyn.org](http://www.spraysyn.org)) for a SpraySyn burner operated without enclosure at an ambient temperature of  $22\pm 2^\circ\text{C}$  and atmospheric pressure ( $1015\pm 8$  mbar). The results are based on 200 images for PF1<sub>ref</sub> and 300 images for SF1<sub>ref</sub>. Diameter and color ratio are extracted at HAB = 10 mm for PF1<sub>ref</sub> and HAB = 20 mm for SF1<sub>ref</sub> [26]. Reprinted with modified layout from Ref. [26] licensed under CC BY 4.0.

	Height / mm	Diameter / mm	Tilt angle / °	Color ratio $C_{br}$
Reference flame PF1 <sub>ref</sub>	47.3	14.4	1.16	1.86
Reference flame SF1 <sub>ref</sub>	61.9	3.3	0.46	5.1
Tolerance / %	5	2.5	5	5

### 5.3.2 Droplet size and velocity measurements in non-reacting sprays

To assure correct burner operation, flame benchmarks of the pilot flame PF1 and the ethanol spray flame SF1 have been performed (Figure 5.9). Both, the investigated pilot and the ethanol spray flame meet the specified tolerances of the reference flames such that the burner operation is found to be adequately [55]. By that, the results of the measurements presented in the following are qualified to contribute to the database at [www.spraysyn.org](http://www.spraysyn.org) [280].

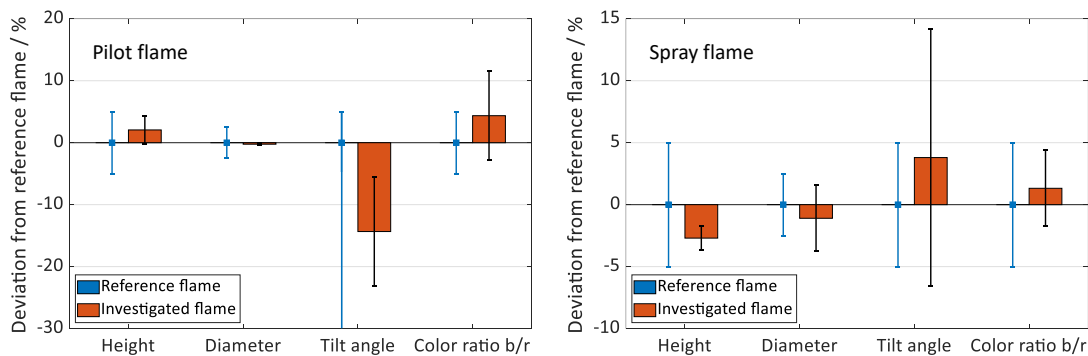


Figure 5.9: Successfully passed flame benchmarks of the investigated pilot flame (PF1) and spray flame (SF1, reprinted from Refs. [55, 56]).

To characterize the non-reacting sprays of different solvents as well as the ethanol spray flame SF1 (Table 5.2), measurements were performed with a Dual-Phase Doppler Anemometer (PDA, chapter 2.2.4). Since PDA is a pointwise measurement technique, the cold ethanol spray (S1) was scanned pointwise in vertical and horizontal planes. At each point, droplets were either counted for a fixed time slot of 10 s, or until a number count of 100,000 validated droplets was reached. A measurement range of  $6 \times 50 \text{ mm}^2$  was scanned in 1 mm steps in radial direction and 5 mm steps in axial direction. The interpolated velocity field of the spray operated with the parameters listed in Table 5.2 is shown in Figure 5.10 with the grid of physical measurement locations indicated by black dots.

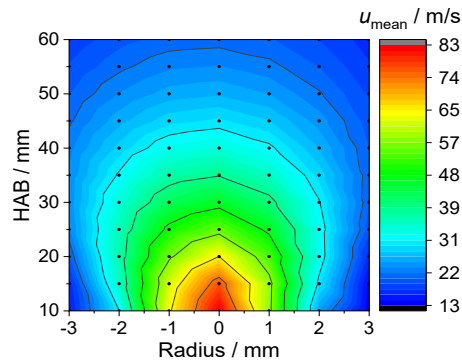


Figure 5.10: Interpolated axial component ( $u$ ) of the velocity field of the non-reacting ethanol spray (S1) scanned vertically at  $x = 0$ . The black dots indicate the measurement positions. Reprinted with modified layout from Ref. [55].

The highest droplet velocities were measured along the centerline of the burner and reach more than 83 m/s at 10 mm HAB. The velocity is radially symmetric and decreases to 60 m/s at a radius of 1 mm and 30 m/s at 2 mm radius. It can be seen that the droplets propagate angled towards greater radii with increasing height above the burner.

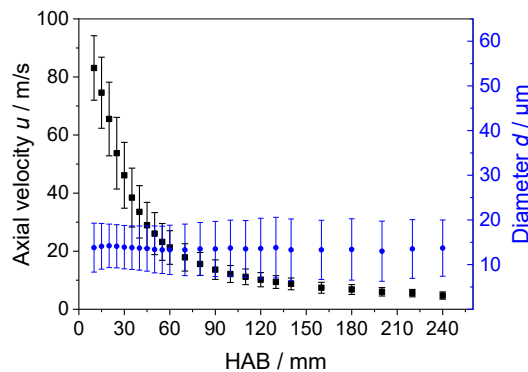


Figure 5.11: Axial droplet velocity  $u$  and median droplet diameter  $d$  along the centerline of the non-reacting ethanol spray (S1). The error bars indicate the standard deviation of the averaged velocity and diameter. Reprinted with modified layout from Ref. [55].

Figure 5.11 presents the averaged axial velocity and median droplet diameter and its respective standard deviations measured along the centerline of the burner. The mean droplet velocity decreases exponentially from 83 to 5 m/s over a vertical distance of 230 mm. The median of the droplet diameter varies slightly between 13 and 14.2  $\mu\text{m}$ . It needs to be considered, that the number of droplets measured at each position decreases exponentially with increasing HAB, which affects the calculated median. Thus, the median at 100 mm HAB is calculated from 5000 droplets only and at 200 mm HAB from 500 droplets only, while at 10 mm HAB the 100,000 droplet-count limit was attained within the chosen time slot of 10 s. An estimate of the theoretical evaporation time of a single, spherical ethanol droplet with a diameter of 14  $\mu\text{m}$  is about 28 ms assuming steady-state evaporation in a still atmosphere calculated according to Refs. [281, 282]. With an average velocity of 44 m/s a droplet needs 5.2 ms to travel between 10 and 240 mm HAB. According to the  $d^2$  law, the droplet evaporation increases quadratically with decreasing diameter. It should also be noted that the ethanol droplets in the continuously operated spray are in a local environment with high ethanol vapor concentrations, which inhibits the evaporation process. We thus may conclude, that for the non-reacting ethanol spray the mean droplet diameter can be assumed to be constant at 13.6  $\mu\text{m}$  along the HAB investigated here.

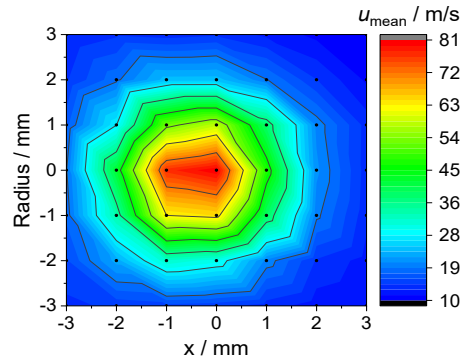


Figure 5.12: Interpolated velocity field of the axial velocity component  $u$  of the non-reacting ethanol spray (S1) scanned horizontally at 10 mm HAB. The black dots indicate the measurement positions. Reprinted with modified layout from Ref. [55].

Figure 5.12 shows the interpolated axial velocity field of a horizontal scan at 10 mm HAB. The spray center is shifted by  $x = -0.5$  mm relative to the alignment of the laser above the nozzle as the relative positioning of laser and nozzle to each other could not be aligned more precisely in the experiment. Regardless of the distortions caused by interpolation on the cartesian coordinate system, the central area is dominated by droplet velocities above 70 m/s.

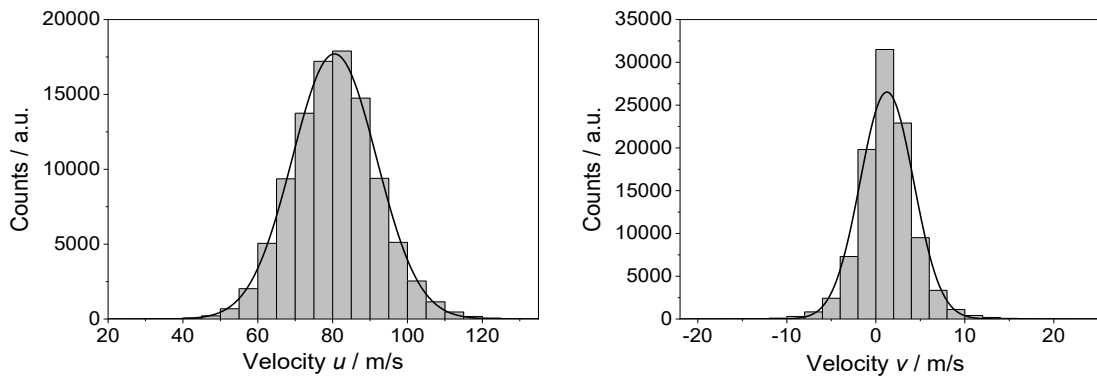


Figure 5.13: Velocity distributions of the non-reacting ethanol spray (S1) at the center axis at 10 mm HAB. The mean axial velocity (left) is 81 m/s (FWHM = 26.6 m/s) while the mean radial velocity (right) is 1.2 m/s (FWHM = 7.1 m/s). Reprinted with modified layout from Ref. [55].

At a radial distance of 3 mm, the droplet velocity has decreased to 10 m/s. Figure 5.13 indicates that the measured axial and radial velocities on the various HAB correspond to Gaussian distributions. The mean axial velocity  $u$  is about 83 m/s with a standard deviation of 11 m/s at 10 mm HAB and decreases to 8.8 m/s at 140 mm HAB with a standard deviation of 2 m/s. The mean radial velocity  $v$  is about 1.2 m/s with a standard deviation of 3 m/s at 10 mm HAB and converges to zero with a standard deviation of 1 m/s with increasing HAB.

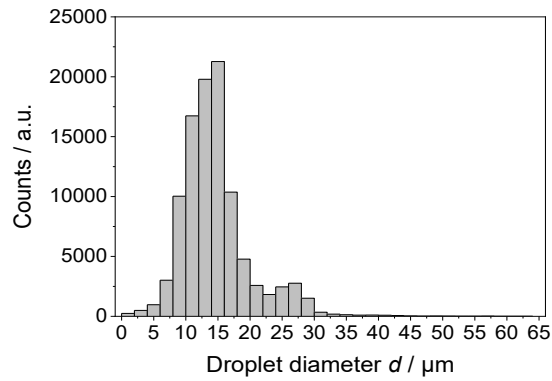


Figure 5.14: Droplet size distribution of the non-reacting ethanol spray (S1) at the center axis ( $x = r = 0$  mm) at 10 mm HAB. Reprinted with modified layout from Ref. [55].

Multiple horizontal scans at different HABs were taken showing that the spray widens and the mean droplet diameter becomes more homogeneous over the cross-section of the ethanol spray with increasing HAB. At each HAB, we found a bimodal droplet size distribution with peaks around 14 and 27  $\mu\text{m}$  (Figure 5.14). Moving from the centerline towards the edge of the spray the proportion of larger droplets increases. The same applies for increasing HAB along the centerline. Droplet LIF imaging (not shown here) suggests that this finding may be caused by the breakup of filaments that are ejected radially from the primary spray cone. To study the influence of the operating conditions on the resulting droplet sizes and velocities, parameter studies were performed that are presented here. For four different solvents (ethanol, 1-butanol, acetone, and n-hexane) the dispersion gas flow was varied (from 4–17 slm for ethanol and from 4–20 slm for the other three solvents) under non-reacting conditions. Since the distribution of the droplet velocities is Gaussian (Figure 5.13), the arithmetically averaged axial and radial velocities are plotted in the following graphs. In contrast, the droplet sizes show individual outliers or bimodal distributions (Figure 5.14), which is why the median drop diameter was chosen for being displayed in the following graphs. Figure 5.15 shows the count rate of sampled validated droplets of the ethanol spray measured along the centerline from 2–100 mm HAB. For the standard operating point S1 with 10 slm dispersion gas (Table 5.2), the highest count rate of all five investigated mass flows was measured with 16.2 kHz at HAB = 4 mm. The second highest count rate was measured for 13 slm dispersion gas with 12.7 kHz at HAB = 5 mm while the third highest count rate was measured for 7 slm with 11.9 kHz at HAB = 3 mm. Hence, a high-count rate can be considered as an indicator of fine droplet atomization.

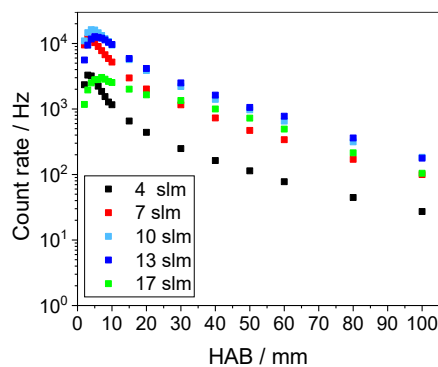


Figure 5.15: Droplet count rate along the centerline of the non-reacting ethanol spray.

Consequently, the measured data proves that 10 slm dispersion gas provides the finest atomization for ethanol by the two-fluid nozzle of the SpraySyn burner. With 13 and 17 slm dispersion gas, the

spray is no longer atomized continuously but pulsating with a regular frequency. The Venturi effect provides a hypothesis for the cause of this observation, i.e., part of the liquid in the uppermost section of the capillary is sucked-out by the high dispersion gas velocity and atomized, subsequently. Afterwards, it takes a fraction of a second for the syringe pump to completely fill-up the capillary again up to the outlet cross section where its sucked out again as recently discussed by Bieber et al. [213]. The frequency of the spray dropouts increases with increasing dispersion gas mass flow. However, the exact cause and further details were not further investigated in the context of the present work. It should be noted that 4 slm dispersion gas flow atomize the spray insufficiently fine and 17 slm cannot be evaluated as a stable operating point due to the high frequency of spray dropouts.

Regarding the axial droplet velocities, a clear trend is found, namely, the higher the dispersion gas flow, the higher the axial velocity (Figure 5.16 left). On the first millimeters after leaving the capillary the droplets accelerate as also observed by Stodt et al. in their PDA droplet velocity measurements [211]. Overall, peak velocities of 29.5 m/s at 4 slm dispersion gas flow, 78.1 m/s at 10 slm, and 136.6 m/s at 17 slm were measured in the ethanol spray. The respective velocity difference correlates with the mass flow difference, e.g. an increase in mass flow by 70% (from 10 to 17 slm) leads to an increase in the axial droplet velocity by 74.9%.

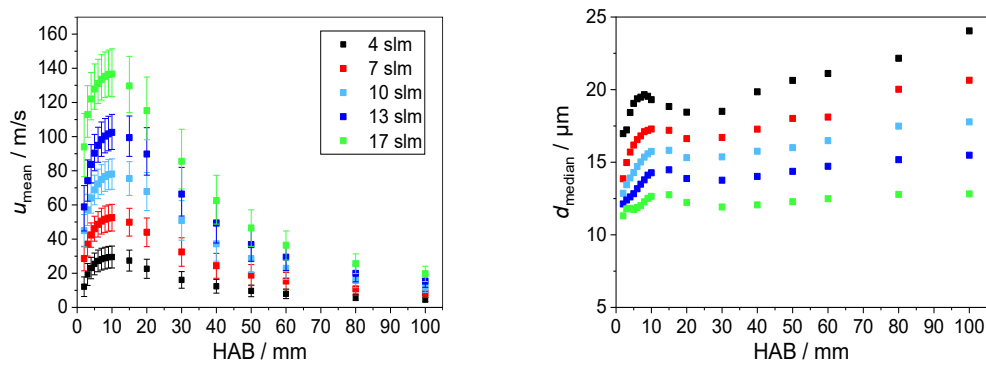


Figure 5.16: Averaged axial droplet velocity (left) and median of droplet diameter (right) of the non-reacting ethanol spray. The error bars indicate the respective standard deviations and the legend depicted in the left plot also applies to the right plot.

In comparison, the measured droplet diameters behave inversely proportional to the dispersion gas mass flow. The lower the mass flow, the larger the mean droplet diameter (Figure 5.16 right). This is a typical behavior of two-fluid nozzles as their atomization-fineness decisively depends on the dispersion gas mass flow and the corresponding velocity difference between gas and liquid phase [282, 283]. For all mass flows, the mean drop diameter increases on the first millimeters above the nozzle until a local maximum of the droplet diameter is reached at about 8–10 mm HAB. With further increasing HAB, the droplet diameter decreases until a local minimum is reached at 30 mm HAB. Subsequently, the droplet diameter increases monotonously with increasing HAB. From literature, it is well known that PDA measurements show non-monotonic variation in droplet size with increasing HAB along the centerline of a spray [284-288]. This change between ascending and descending trends allows the classification into three distinctive zones in which different effects must be considered when interpreting the measured droplet diameters.

In zone 1 ( $\text{HAB} < 10$  mm), the exclusion of non-spherical droplets [211] (e.g., filaments during primary spray breakup) lead to an inevitable bias in droplet-size statistics that shifts the droplet size distribution towards smaller droplets. With increasing HAB, droplet break-up becomes less and less and the

surface tension creates spherical droplets that are then passing the “spherical validation” of the PDA and shift the size distribution towards larger droplets. Furthermore, the increase in droplet diameter within the first 10 mm HAB can be explained by converging-diverging droplet trajectories [211] that lead to droplet collisions and ultimately to coalescence [287].

In zone 2 ( $10 < \text{HAB} < 30 \text{ mm}$ ), the mean droplet diameter decreases. From experiments on a burner with a similar two-fluid nozzle it is known that the spray is fully developed at  $\text{HAB} > 10 \text{ mm}$  [289]. A fully developed spray is characterized by the fact that the primary and secondary spray break-up are completed, for which the spherical validation rate of the PDA measurements can be used as an indicator. For all measurements of the non-reacting ethanol spray, the spherical validation rate is between 67.2 and 99.9%. The higher the dispersion gas mass flow, the higher the spherical validation rate. Apart from 4 slm dispersion gas flow (where 88.5% spherical validation at 10 mm HAB was measured), all spherical validation rates are above 95% starting from 10 mm HAB.

In zone 3 ( $\text{HAB} > 30 \text{ mm}$ ) an increase in droplet size is apparent in Figure 5.16 (right). However, it is assumed that the trend of decreasing droplet diameter observed in zone 2 will continue with increasing HAB in this regime, also. This hypothesis is based on findings by Heine et al. [289] and Aliseda et al. [287]: On the one hand, differential turbulent diffusion and the widening of the spray cone lead to a stronger decrease in the proportion of smaller droplets on the centerline with increasing HAB compared to the proportion of bigger droplets. On the other hand, the smaller droplets that remain on the centerline evaporate faster than the larger droplets (according to the  $d^2$ -law) and finally fall below the detection limit of the PDA (conventional PDAs can only detect droplets with a size of  $1 \mu\text{m}$  or more [290]). These arguments are supported by the measured droplet count rates that decrease strongly with increasing HAB (Figure 5.15), i.e. low count rates indicate that most (especially small) droplets are evaporated. As a result, the size distributions measured at  $\text{HAB} > 40 \text{ mm}$  are inevitably biased and shifted to larger droplets.

### 1-Butanol

Figure 5.17 shows the count rate of sampled validated droplets of the 1-butanol spray measured along the centerline from 2–100 mm HAB. For 13 slm dispersion gas, the highest count rate of all six investigated mass flows was measured with 14.3 kHz at  $\text{HAB} = 5 \text{ mm}$ . The second highest count rate was measured for the standard operating point S1 with 10 slm dispersion gas (see Table 5.2) with 14.2 kHz at  $\text{HAB} = 4 \text{ mm}$ . For butanol, the count rate is identical at 10 and 13 slm while it is in total 12.5% smaller compared to the count rate measured for ethanol. The lower count rate might be related to the viscosity of butanol, that is almost 2.5 times higher compared to ethanol (see Table 5.6).

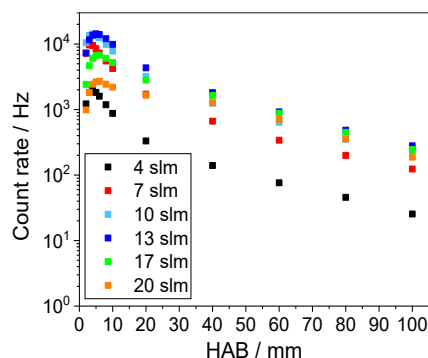


Figure 5.17: Droplet count rate along the centerline of the non-reacting 1-butanol spray.

It is evident, that for butanol 10 and 13 slm are both equivalently suitable for spray atomization. Regarding 7 slm, the third highest data-rate of all investigated dispersion gas flows was measured with 9.7 kHz at 3 mm HAB. In contrast to ethanol, the butanol count rate at 17 slm dispersion gas exceeds the count rate at 7 slm already at 8 mm HAB (while for ethanol the 7 slm count rate is not exceeded until 30 mm HAB). Further downstream, the 17 slm count rate approximates the values measured for 10 and 13 slm. Hence, a much wider field of suitable dispersion gas flows for spray atomization is found for butanol (7–17 slm) compared to ethanol (10–13 slm). It should be noted that 4 slm dispersion gas flow atomizes the spray insufficiently fine and 20 slm cannot be evaluated as a stable operating point due to the high frequency of spray dropouts.

Similar to the measured axial droplet velocities of ethanol, it can be stated that the higher the dispersion gas flow, the higher the axial velocity (Figure 5.16 left). Up to 10 mm HAB the droplets accelerate to their maximum axial velocity for each respective dispersion gas flow. Overall, peak velocities of 27.7 m/s at 4 slm dispersion gas flow, 75.5 m/s at 10 slm, and 155.9 m/s at 20 slm were measured in the butanol spray. Again, the respective velocity difference correlates with the mass flow difference, e.g. doubling mass flow from 10 to 20 slm leads to an increase in the axial droplet velocity by 106.5%.

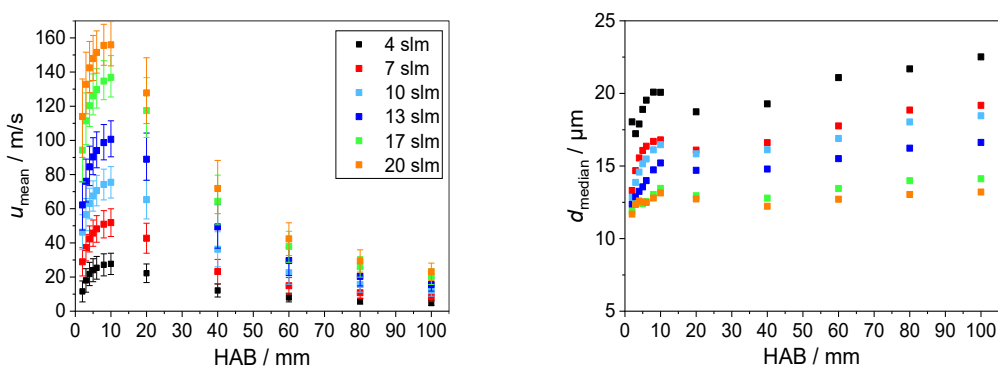


Figure 5.18: Averaged axial droplet velocity (left) and median of droplet diameter (right) of the non-reacting 1-butanol spray. The error bars indicate the respective standard deviations and the legend depicted in the left plot also applies to the right plot.

As observed for ethanol, the measured droplet diameters behave inversely proportional to the dispersion gas mass flow, i.e. the lower the mass flow, the larger the mean droplet diameter (Figure 5.18 right). Again, as discussed for ethanol, the ascending and descending trends in droplet diameter allow a classification into three distinctive zones where a competition of different (physical) phenomena leads to the droplet sizes ultimately measured by PDA.

In zone 1 ( $\text{HAB} < 10$  mm), the mean drop diameter increases on the first millimeters above the nozzle until a local maximum of the droplet diameter is reached for all mass flows at about 8–10 mm HAB. In zone 2 ( $10 < \text{HAB} < 40$  mm), the measured droplet diameter decreases until a local minimum is reached. For 4–13 slm, the local minimum median droplet diameter is found at 20 mm HAB while for the other two mass flow rates, the local minimum is found at 40 mm HAB. However, it should be noted that the difference in diameter between 20 and 40 mm HAB is smaller than  $0.5 \mu\text{m}$  which is why it is concluded that the local minimum in diameter is located around 30 mm HAB (for 4–13 slm dispersion gas flow rate), as found for ethanol. Subsequently, in zone 3 ( $\text{HAB} > 40$  mm), the droplet diameter increases with increasing HAB. In the context of the ethanol spray results below Figure 5.16, a detailed discussion about the driving forces for the observed fluctuations in mean droplet diameter is provided that is valid for the present results of the 1-butanol spray, too.

### Acetone

Figure 5.19 shows the count rate of sampled validated droplets of the acetone spray measured along the centerline from 2–100 mm HAB. For the standard operating point S1 with 10 slm dispersion gas (see Table 5.2), the highest count rate of all six investigated mass flows was measured with 17.7 kHz at HAB = 4 mm. The second highest count rate was measured for 13 slm dispersion gas with 14.1 kHz at 6 mm HAB and the third highest count rate is found for 7 slm dispersion gas with 13.1 kHz. This is comparable with the values measured for ethanol even though the viscosity of acetone is more than 3.5 times smaller than ethanol (in contrast, the surface tension of acetone is only 5% higher than the one of ethanol, see Table 5.6). However, if the acetone-droplet count rate is considered over the entire investigated HAB, only 10 and 13 slm are found to provide optimal spray atomization as all other mass flow rates lead to lower count rates. It should be mentioned that for acetone, spray pulsation already occurs at 10 slm dispersion gas flow (for details to spray pulsation, see discussion below Figure 5.15). Overall, 4, 17, and 20 slm mass flow rate are considered insufficient for fine spray atomization since comparably low count rates were measured.

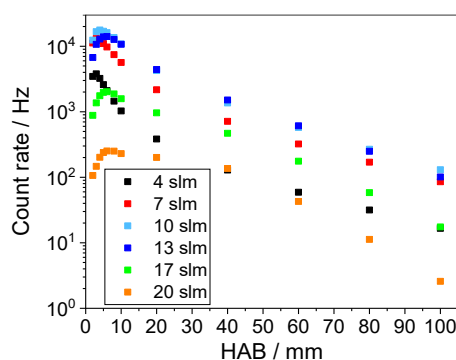


Figure 5.19: Droplet count rate along the centerline of the non-reacting acetone spray.

As also observed for ethanol and butanol, the measured axial droplet velocities of acetone follow the principle that the higher the dispersion gas flow, the higher the axial velocity (Figure 5.20 left). Except for 4 and 20 slm flow rate, the droplets accelerate up to 10 mm HAB to their maximum axial velocity. For the other two mass flows, the highest droplet velocity is already achieved at 8 mm HAB. Overall, peak velocities of 28.2 m/s at 4 slm dispersion gas flow, 76.5 m/s at 10 slm, and 152.4 m/s at 20 slm were measured in the acetone spray. As for the other two solvents, the respective velocity difference correlates with the mass flow difference, e.g. doubling mass flow from 10 to 20 slm leads to an increase in the axial droplet velocity by 97.8%.

As observed for ethanol and butanol, the measured acetone droplet diameters behave inversely proportional to the dispersion gas mass flow, i.e., the lower the mass flow, the larger the mean droplet diameter (Figure 5.20 right). Again, the ascending and descending trends in droplet diameter allow a classification into three distinctive zones (as discussed for ethanol and butanol) where a competition of different (physical) phenomena leads to the droplet sizes measured by PDA.

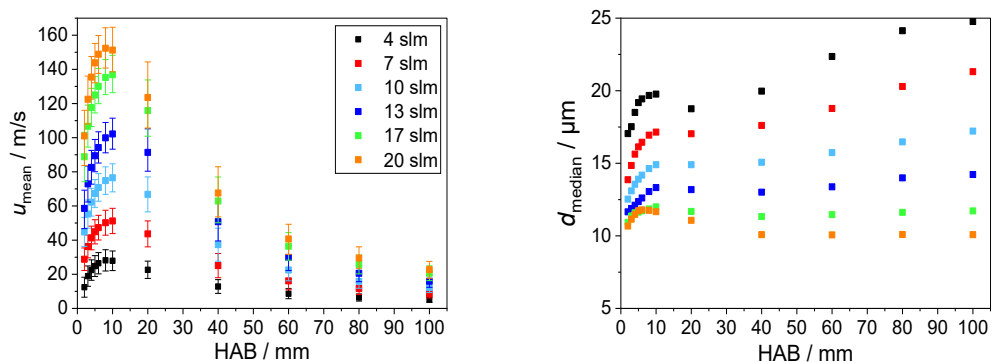


Figure 5.20: Averaged axial droplet velocity (left) and median of droplet diameter (right) of the non-reacting acetone spray. The error bars indicate the respective standard deviations and the legend depicted in the left plot also applies to the right plot.

In zone 1 (Figure 5.20,  $\text{HAB} < 10$  mm), the mean drop diameter increases on the first millimeters above the nozzle until a local maximum of the droplet diameter is reached for all mass flows (except for 20 slm) at about 8–10 mm HAB. For 20 slm dispersion gas, the local maximum is found closer to the nozzle at 6 mm HAB that is not observed for any other investigated solvent. In zone 2 ( $10 < \text{HAB} < 40$  mm), the measured droplet diameter decreases until a local minimum is reached. For 4–10 slm, the local minimum median droplet diameter is found at 20 mm HAB while for 13–20 slm mass flow rate, the local minimum is found at 40 mm HAB. Unlike ethanol and butanol, the median droplet diameter of acetone in zone 3 ( $\text{HAB} > 40$  mm) shows both ascending and descending trends. At 17 slm the droplet median diameter remains constant at  $11.5 \pm 0.2 \mu\text{m}$  from 20–100 mm HAB. At 20 slm dispersion gas flow it even decreases with increasing HAB from  $11.8 \mu\text{m}$  at 6 mm HAB to  $10.1 \mu\text{m}$  at 100 mm HAB. A reason, why no increase in diameter is observed for 17 and 20 slm mass flow is found when analyzing the droplet size distributions for these two dispersion gas flow rates. For instance, at 2 mm HAB and 20 slm dispersion gas mass flow drops are measured between 6 and  $15 \mu\text{m}$ , while at 4 slm dispersion gas (at the same HAB) the droplet size range spreads from 5– $30 \mu\text{m}$ . At 80 mm HAB, where predominantly small droplets already evaporated down to less than  $1 \mu\text{m}$  (detection limit), the (slower evaporating) large droplets that are generated at 4 slm, only, shift the entire measured size distribution towards larger droplets. In contrast, at 20 slm, no comparable large droplets existed at any HAB, so the measured mean droplet size is less biased at larger HABs. The histograms (not shown here) allow the conclusion that the atomization at 17 and 20 slm mass flow leads to a narrow size distribution of small acetone drops (around  $11 \mu\text{m}$ ), i.e., no larger droplets (around  $30 \mu\text{m}$ ) are formed by spray atomization that shift the statistics towards larger droplets (as observed for the lower dispersion gas flow rates in zone 3). Hence, for 4–13 slm mass flow rate, the droplet diameter increases with increasing HAB in zone 3 (Figure 5.20,  $\text{HAB} > 40$  mm) as discussed before in the context of the ethanol spray results below Figure 5.16.

### n-Hexane

Figure 5.21 shows the count rate of sampled validated droplets of the n-hexane spray measured along the centerline from 2–100 mm HAB. For the standard operating point S1 with 10 slm dispersion gas (see Table 5.2), the highest count rate of all six investigated mass flows was measured with 21.1 kHz at  $\text{HAB} = 4$  mm. The second highest count rate was measured for 7 slm dispersion gas with 16.5 kHz at 3 mm HAB and the third highest count rate is found for 13 slm dispersion gas with 11.3 kHz. Comparing all four examined solvents with each other, n-hexane shows the overall highest count rate

measured (21.1 kHz) that is 30% more compared to the overall second highest count rate measured for ethanol. In terms of physical properties, n-hexane has a dynamic viscosity comparable to acetone (about 3.5 times smaller than ethanol), but about 17% lower surface tension compared to ethanol and 21% lower compared to acetone (Table 5.6). Considering the hexane-droplet count rate over the entire investigated HAB, only 7 and 10 slm are found to provide optimal spray atomization as all other mass flow rates lead to lower count rates. At 13 slm a 46% lower count rate was found compared to 7 and 10 slm dispersion gas indicating insufficient spray atomization. Overall, 4, 17, and 20 slm mass flow rate are considered as insufficient for fine spray atomization (equally concluded for acetone) since comparably low count rates were measured for these dispersion gas flows.

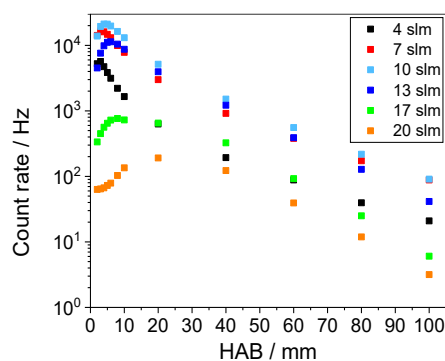


Figure 5.21: Droplet count rate along the centerline of the non-reacting n-hexane spray.

As with all other solvents, the higher the dispersion gas flow, the higher the axial velocity also applies for the hexane droplets (Figure 5.22 left). Except for 17 and 20 slm flow rate, the droplets accelerate up to 10 mm HAB to their maximum axial velocity before decreasing with increasing HAB. For 17 slm, the highest drop velocity is achieved at 8 mm HAB while for 20 slm the peak velocity is measured at 5 mm HAB. Overall, peak velocities of 29.6 m/s at 4 slm dispersion gas flow, 81.6 m/s at 10 slm, and 149.9 m/s at 20 slm were measured in the acetone spray. Compared to the other solvents, the hexane droplet velocity does not increase proportionally to the dispersion gas mass flow, e.g., doubling the mass flow from 10 to 20 slm leads to an increase in the axial droplet velocity by 83.7%. A possible explanation for that could be that the hexane droplets are deformed stronger than the droplets of the other solvents due to their on average 21% lower surface tension that may cause aerodynamically less-ideal shaped droplets.

It is found that the measured hexane droplet diameters behave inversely proportional to the dispersion gas mass flow as observed for all investigated solvents, i.e. the lower the mass flow, the larger the mean droplet diameter (Figure 5.22 right). The ascending and descending trends in droplet diameter allow a classification into three distinctive zones (as discussed for ethanol, butanol, and acetone) where a competition of different (physical) determinants leads to the droplet sizes ultimately measured by PDA.

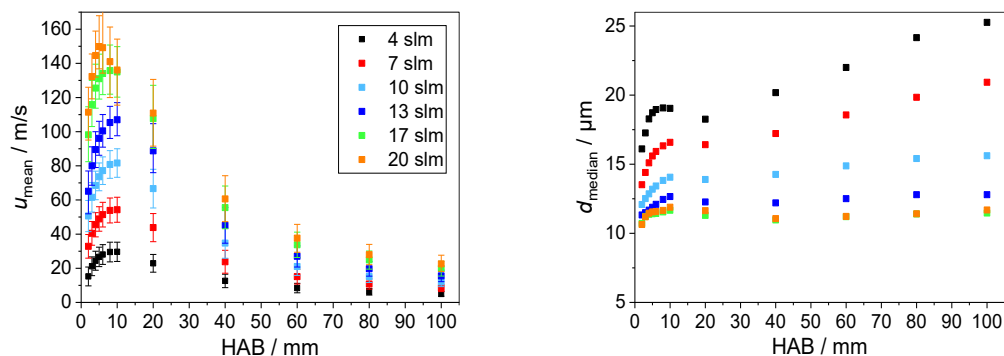


Figure 5.22: Averaged axial droplet velocity (left) and median of droplet diameter (right) of the non-reacting n-hexane spray (M65–M70). The error bars indicate the respective standard deviations and the legend depicted in the left plot also applies to the right plot.

In zone 1 (Figure 5.22,  $\text{HAB} < 10$  mm), the mean drop diameter increases on the first millimeters above the nozzle until a local maximum of the droplet diameter is reached for all mass flows at about 8–10 mm HAB. In zone 2 ( $10 < \text{HAB} < 40$  mm), the measured droplet diameter decreases until a local minimum is reached. For 4–13 slm, the local minimum median droplet diameter is found at 20 mm HAB while for the other two mass flow rates, the local minimum is found at 40 mm HAB. However, it should be noted that the difference in diameter between 20 and 40 mm HAB is smaller than  $0.5 \mu\text{m}$  which is why it is concluded that the local minimum in diameter is located around 30 mm HAB (for 4–13 slm dispersion gas flow rate), as observed for ethanol and butanol. Subsequently, in zone 3 ( $\text{HAB} > 40$  mm), the droplet diameter increases with increasing HAB. In the context of the ethanol spray results below Figure 5.16, a detailed discussion about the driving forces for the observed fluctuations in mean droplet diameter is provided that is valid for the present results of the n-hexane spray, too. Hence, despite the lower surface tension of hexane, the trend of fluctuating droplet sizes with increasing HAB is similar to ethanol and butanol for all investigated dispersion gas flows.

### 5.3.3 Droplet size and velocity measurements in the ethanol spray flame

For the ethanol spray flame (SF1), parameter studies have been performed measuring droplet velocities and sizes *in situ* along the centerline of the flame. At each point, droplets were either counted for a fixed time slot of 10 s or until a number count of 100,000 validated droplets was reached. The left side of Figure 5.23 presents the averaged axial droplet velocities measured along the centerline of the ethanol spray flame (SF1) using 4–16 slm dispersion gas flow. For all conditions, starting from  $\text{HAB} = 10$  mm, an increase in the velocity is observed leading to peak velocities between 49 and 158 m/s located at  $\text{HAB} = 20$  mm for 4–13 slm and  $\text{HAB} = 30$  mm for 16 slm dispersion gas flow. Within this distance, the velocity increase is found to be in the range of 7–10% for all conditions. With further increasing HAB, the droplet velocities are approaching each other.

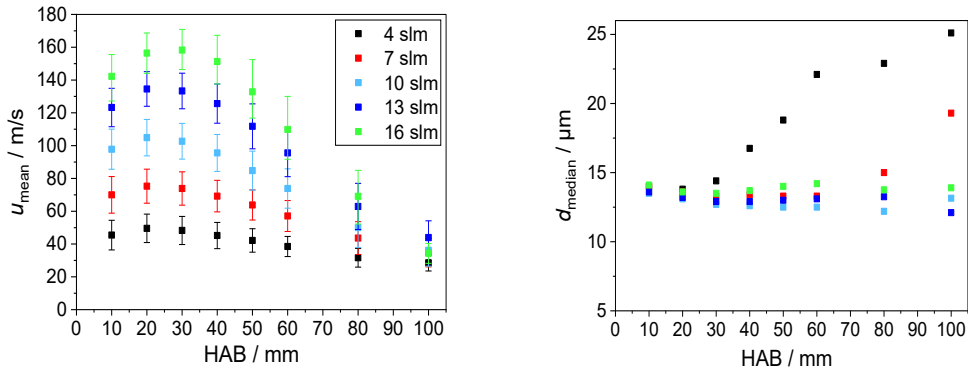


Figure 5.23: Averaged axial droplet velocities (left) and droplet median diameters (right) measured along the centerline of the ethanol spray flame (SF1) under variation of the dispersion gas flow. The legend depicted in the left plot also applies to the right plot and the error bars indicate the respective standard deviations. Reprinted with modified layout from Ref. [56].

In contrast, the droplet sizes show low sensitivity to the variation of the dispersion gas (Figure 5.23, right). We tend to find the smallest droplet diameter of  $12.8 \mu\text{m}$  averaged over the first 60 mm above the burner at 10 slm dispersion gas flow. For all other operating parameters, the averaged droplet size is  $0.5\text{--}1 \mu\text{m}$  higher. Our results are in good agreement with recent wide-angle light scattering (WALS) measurements from Münsterjohann et al. [114] that varied the dispersion gas flow from 8–12 slm and measured droplet size distributions at 40 mm height above the burner. For all conditions, the authors find mean droplet diameters around  $15 \mu\text{m}$  and well-matching size distributions spreading between 1 and  $30 \mu\text{m}$ .

For the 4 and 7 slm dispersion gas flow cases, an increase in droplet diameter with increasing HAB is observed in our measurements that is well known in literature [284, 286, 291]. For 4 slm the droplet diameter increase starts at 30 mm, while for 7 slm the increase begins at 80 mm HAB. For the other three cases, no increase was measured as there were hardly any droplets detected at  $\text{HAB} > 100 \text{ mm}$  within the used acquisition time (Figure 5.24). In literature, three physical mechanisms are stated that explain the increase in droplet diameter with increasing HAB [287]: Differential turbulent diffusion that causes small droplets to travel away from the center of the spray, coalescence that forms larger droplets by droplet collision, and evaporation that causes small droplets to evaporate faster than bigger droplets (according to the  $d^2$ -law) biasing the measured size distribution as soon as the small droplets fall below the lower detection limit. Regarding the homogeneity of the measured size distributions, the standard deviation at  $\text{HAB} = 10 \text{ mm}$  for 4 slm dispersion gas flow is found to be  $9.5 \mu\text{m}$  while at 16 slm it is  $2.6 \mu\text{m}$ , only. Hence, the higher the dispersion gas flow, the smaller the size distribution of the measured droplets.

All measurements along the centerline were performed up to  $\text{HAB} = 200 \text{ mm}$ . The measured number of droplets within the selected acquisition time of 10 s falls below 100 counts at  $\text{HAB} = 80 \text{ mm}$  for 4 and 17 slm dispersion gas flow and at  $\text{HAB} = 100 \text{ mm}$  for all conditions (Figure 5.24). Thus, the measured velocities and quantities in these cases are no longer based on a sufficient statistical basis. Due to that, the results of the velocity and droplet size measurements are shown up to 100 mm, only. The comparison of the measurements in the ethanol spray flame (SF1) with the measurements in the non-reacting case (chapter 5.3.2) shows that the data rate of measured droplets in the non-reacting case is significantly higher, indicating faster evaporation of the droplets by the heat of the flame. We conclude that the majority of droplets evaporate within the first 60 mm of the flame and only few droplets remain up to 100 mm distance from the burner.

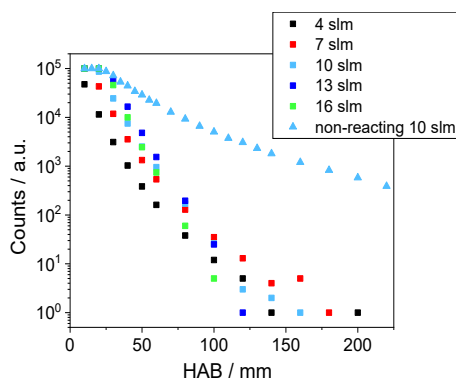


Figure 5.24: Measured droplet count numbers in the non-reacting ethanol spray (S1) and in the ethanol spray flame (SF1) for different dispersion gas flows. At each position, the droplets were either counted for a fixed time interval of 10 s or until a number count of 100,000 validated droplets was reached. Reprinted with modified layout from Ref. [56].

Further studies on the ethanol spray flame (SF1) were performed (not shown here, cf. Table A3.7 in the appendix) to determine, which operating parameters in addition to the dispersion gas affect the droplet velocities and sizes. The variation of the ethanol flow rate (M20, M27, and M28) shows higher axial velocities for lower ethanol flows, e.g., 107 m/s for 1 ml/min, 105 m/s for 2 ml/min, and 100 m/s for 4 ml/min (all at HAB = 20 mm), but no influence on the droplet size. When varying the pilot flame stoichiometry from  $\phi = 0.16$  (1.3 slm CH<sub>4</sub>, M26) to  $\phi = 0.25$  (2 slm CH<sub>4</sub>, M20), an increase of 9 m/s in the axial velocities averaged over the first 60 mm HAB was measured while the mean droplet diameter was found to be 0.5  $\mu\text{m}$  lower for higher methane flows along the first 60 mm HAB.

### 5.3.4 Comparison of reacting and non-reacting operation

To investigate the influence of the flame on droplet velocities and sizes, radial scans were performed in the non-reacting ethanol spray S1 and in the ethanol spray flame SF1 (Table 5.2). The radial profiles were acquired on three HABs derived from the results of axial scans along the centerline. In addition to other measurement results (count rate, droplet velocity, and size), the trend of spherical validation over HAB was used as an indicator to select significant HABs. With a spherical validation rate of more than 82%, 3 mm HAB was selected as the smallest distance to the burner for the radial scan (below 2 mm HAB, the massive increase in scattered light intensity indicates that the liquid cone has not yet completely disintegrated into droplets). The second significant HAB is 10 mm with a spherical validation of 95%. This is the smallest HAB at which the burning spray flame can be probed with the PDA (in the configuration shown in chapter 5.2.2) and thus the first HAB where measurements can be performed in both, the non-reacting spray and the burning flame. The third significant position is at HAB = 30 mm with a spherical validation rate of more than 98%. Although the trend of the spherical validation rate over HAB (not shown here) shows a further increasing spherical validation rate with increasing HAB, the count rate in the burning spray flame decreases strongly with increasing HAB. Hence, 30 mm HAB offers an optimum between high spherical validation and sufficiently high count-rate at the same time.

Since the diameter of the spray increases with increasing distance from the burner, the radial scans were performed at 3 mm HAB up to a radius of 3 mm, at 10 mm HAB up to 6 mm radius and at 30 mm HAB up to 10 mm radius. In order to keep the overall measurement time as short as possible, a larger step size was selected for larger HABs. However, as the measurements at 3 mm HAB are serving as

boundary conditions and the measurements at 10 and 30 mm are utilized for validation of CFD simulations, care was taken to ensure that the step size at each HAB is sufficiently fine with respect to the grid resolution utilized for simulations. Hence, at 3 mm HAB the selected step size is 0.1 mm, at 10 mm HAB it is 0.2 mm and at 30 mm HAB it is 0.5 mm. Figure 5.25 shows the count rate of sampled validated droplets of S1 and SF1 radially scanned across the center of the spray (flame) between  $\pm 10$  mm radius. The highest count rate was measured at 10 mm HAB in the center of ethanol spray flame SF1 with 60.7 kHz. It is particularly noticeable that the count rate is more than twice as high in the flame compared to the cold spray (26.2 kHz). This finding does not correlate with the axial drop velocity, which in both cases is 70 m/s (Figure 5.26). One possible explanation for the difference is that the center axis of the spray in the non-reacting case seems to shift spatially in comparison to the reactive case as indicated for instance in Figure 5.26 where the axial peak droplet velocity is shifted about 0.2 mm towards positive radii in the non-reacting case. Therefore, it cannot be excluded whether the cold spray has additionally moved towards (or away) from the PDA laser probe volume after the flame has been switched-off. This would result in the cold spray being sampled in a different vertical plane than the flame. Hence, an overall lower count rate would be acquired than theoretically possible. However, at 30 mm HAB, the count rate is found to be higher in the cold spray (12.7 kHz) than in the flame (8.4 kHz). This is consistent with the assumption that higher evaporation rates are expected in the flame than in the cold spray.

While the radial profile of the count rate of the droplets in the spray flame is radially congruent with the profile of the cold spray for 10 mm HAB (e.g., count rate  $> 1$  kHz within a radius of  $-2.5$ – $2.2$  mm), a radial constriction of the radial profile was measured in the cold spray S1 compared to SF1 at 30 mm HAB. Here, the radial expansion of the count rate profile of the spray flame is narrower compared to the cold spray, e.g., count rate  $> 1$  kHz for SF1 within a radius of  $-2.5$ – $1$  mm while for S1 within  $-4$ – $4$  mm radius. This can be explained by the fact that the spray density decreases with increasing radius (a lower spray density goes hand in hand with lower evaporation cooling), whereas the heat input of the pilot flame increases with increasing radius. Hence, this combination leads to particularly high evaporation rates in the outside surface of the spray, as evidenced by the droplet diameters in Figure 5.28 that increase with increasing radius. As discussed in chapter 5.3.2, evaporation has a greater effect on small droplets than on large ones, which is why the measured droplet size distribution (especially in the reactive case) is biased towards larger diameters.

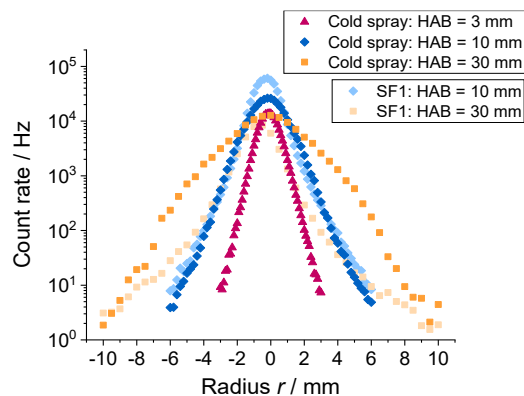


Figure 5.25: Droplet count rate over radius of the non-reacting ethanol spray S1 and the ethanol spray flame SF1.

Within the radius in which the count rate is  $> 100$  Hz, a sufficiently high statistical basis is reached that allows the comparison of average velocities and droplet diameters. Results based on fewer samples should be interpreted with caution. Figure 5.26 shows the average axial droplet velocity versus radius from the centerline. For clarity, the error bars (that show the width of the standard deviation) known from the axial scans shown in the previous chapters are not plotted in the graphs presented in this chapter. However, for comprehensive CFD simulations these data contain valuable information and should be incorporated in all subsequent work. In the non-reacting case, an increase in droplet velocity from 3 to 10 mm HAB can be seen, as already known from the axial scans. Also, in the non-reacting case, the peak velocity drops from 10 to 30 mm HAB while the mean droplet velocity increases in the spray flame from 10 to 30 mm HAB. The comparison of the velocity profiles at 10 mm HAB shows higher velocities beyond  $\pm 2$  mm radius in the reactive case than in the cold spray, e.g., the axial velocity at  $-2.2$  mm radius is more than 50% higher in the reactive case (36.8 m/s) than in the cold spray (23.1 m/s). This velocity difference is largely caused by the pilot flame. The high temperature of the pilot flame increases the gas velocity as shown by Martins et al. [292] that leads to droplet acceleration up to greater HABs compared to the non-reacting case. This finding is supported by droplet velocity measurements with and without pilot flame (not shown here, compare M45 and M46, Table A3.7 in the appendix). It is concluded that the further the droplets are away from the burner axis, the greater the influence of the pilot flame on the droplet velocity. At larger HABs (e.g., 30 mm HAB), the influence of the pilot flame becomes bigger for droplets located on the centerline of the flame, e.g., the axial droplet velocity at  $-0.5$  mm is 77% higher in the flame (75.1 m/s) than in the cold spray (39.6 m/s) while at  $-5$  mm radius the axial velocity is 27.4 m/s in the spray flame and 8.6 m/s in the cold spray. In addition to the pilot flame, the burning spray itself contributes to an increase in droplet velocity especially in the center of the flame. With regard to the radial expansion of the velocity profile, it is found that the larger the HAB, the flatter the radial gradients in both the reactive and the non-reacting case, which is also supported by gas-phase velocity measurements performed by Martins et al. [292, 293].

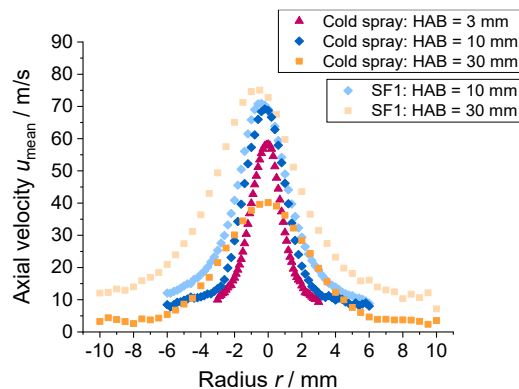


Figure 5.26: Averaged axial droplet velocity over radius of the non-reacting ethanol spray S1 and the ethanol spray flame SF1.

As expected, the axial droplet velocity is significantly higher than the radial velocity. Figure 5.27 shows that the highest radial velocity at 3 mm HAB was measured at 8 m/s. With increasing HAB, the radial velocity decreases. At 10 mm HAB, up to 4.7 m/s are measured while at 30 mm HAB the droplets reach maximum 2 m/s in radial direction. It is noticeable that the radial velocity increases at 10 mm HAB from the center up to a radius of  $\pm 1.5$  mm to 4.7 m/s, then passes a valley of 3.4 m/s until it increases again at  $\pm 4$ –5 mm radius to 4 m/s. This trend can only be found at 10 mm HAB in the non-

reacting case. For all other cases (including the reactive case) it is found that the radial velocity is close to zero in the center of the spray, then increases with increasing radius up to its respective maximum velocity, and finally decreases with increasing radius. In contrast to the findings for the axial velocities, there are no deviations in the radial droplet velocities between reactive and non-reacting case in the center of the spray (flame). However, with increasing radius, the influence of the pilot flame on the radial droplet velocity increases, e.g., at 10 mm HAB higher radial droplet velocities than in the cold spray are measured in the reactive case beginning from  $\pm 1$  mm radius. This trend can also be observed at 30 mm HAB, but here it is mainly prominent at negative radii, whereas at positive radii similar radial droplet velocities are found up to 5.5 mm radius.

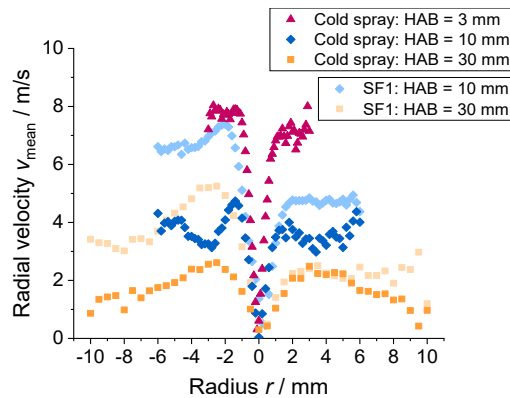


Figure 5.27: Averaged radial droplet velocity over radius of the non-reacting ethanol spray S1 and the ethanol spray flame SF1.

As observed for the axial droplet velocities, the radial gradients of the radial velocity flatten with increasing HAB. Furthermore, on all HABs, the measured velocity profiles are not perfectly axially symmetric. On the positive radii side in Figure 5.27, the measured peak radial droplet velocity is always slightly smaller than at negative radii. For the non-reacting case, the difference is largest at 3 mm HAB and decreases with increasing HAB, since the influence of the dispersion gas on the droplet velocity decreases with increasing HAB. For example, at 30 mm HAB only a negligibly small difference in radial velocity between positive and negative radii can be determined in the non-reacting case. In contrast, large asymmetries are observed in the radial velocity distribution in the reactive case. At 10 mm HAB, the average radial droplet velocity is around 7 m/s at negative radii, while a more than one-third lower radial velocity (4.5 m/s) was measured at positive radii. Similarly, at 30 mm HAB, radial velocities around 4 m/s are found on the left side, while velocities around 2 m/s are observable on the right side. Minimal differences in the positioning of the capillary could lead to asymmetries in the velocity field of the dispersion gas that could explain the differences in the radial droplet velocities. However, these asymmetries are only noticeable in the radial velocity component of the droplets and were neither detected by the Matlab flame characterization (i.e., the flame is found to be radially symmetric) or in the axial velocity components (that were measured simultaneously to the radial velocity). Hence, further investigations are required to clarify the origin of these asymmetries in radial velocities in SF1.

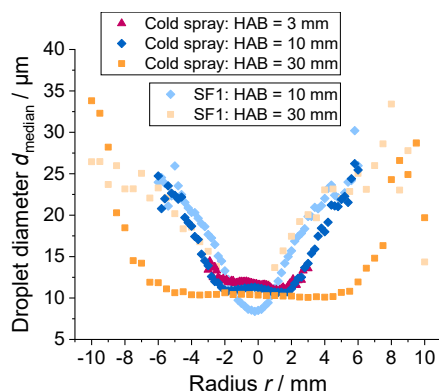


Figure 5.28: Median droplet diameter over radius of the non-reacting ethanol spray S1 and the ethanol spray flame SF1.

The plot of the droplet diameter over radius (Figure 5.28) clearly shows an increase of the diameter with increasing radius under both operating conditions (S1 and SF1) and for all HABs. Droplet diameters between  $11.6\ \mu\text{m}$  (HAB = 3 mm) and  $10.4\ \mu\text{m}$  (HAB = 30 mm) were measured along the centerline of the cold spray. In the spray flame, the overall smallest droplet median diameter was  $8.5\ \mu\text{m}$  (HAB = 10 mm), while the diameter at 30 mm HAB corresponds to the one measured in the non-reacting case. In the center of the cold spray, a plateau is present on all three investigated HABs that shows a constant drop diameter, e.g., at 3 mm HAB droplets around  $11.6\ \mu\text{m}$  are found between  $-2$ – $1.5$  mm while at HAB = 30 mm droplets around  $10.4\ \mu\text{m}$  are measured between  $-6$ – $5$  mm radius. The diameter of the plateau increases with increasing HAB. However, only a slight difference is found between HAB = 3 and 10 mm. It is remarkable that the diameter of the plateaus seems to be independent of the axial droplet velocity measured. Intuitively, it would be expected that the droplet diameter varies with different radii, i.e., with different axial (gas) velocities. For instance, at the center of the spray  $40\ \text{m/s}$  and a droplet diameter of  $10.4\ \mu\text{m}$  are measured while at 5 mm radius an axial droplet velocity of  $7.6\ \text{m/s}$  and a median droplet diameter of  $10.7\ \mu\text{m}$  is measured. Here, the median droplet diameter at the center is only 3% smaller while the mean axial droplet velocity is more than 5 times larger. Similar relationships apply for the other two HABs. Hence, the hypothesis is made that no significant secondary droplet break-up occurs in the cold spray above 3 mm HAB, because otherwise a more striking difference in droplet diameter at radii with lower axial (droplet) velocity would be expected. However, detailed knowledge of the surrounding gas-phase velocity and turbulence is required to isolate the dominant mechanisms of spray and droplet evolution at the various radii and HABs.

Outside the plateaus, the median droplet diameter increases as known in literature for comparable full-cone sprays [294-296]. One possible explanation for this is that larger droplets have a greater mass inertia than smaller ones. Hence, a large droplet is deflected less from its original trajectory (that it experiences at break-up) than a small one. Small drops that have experienced a similar momentum (and direction) at the primary spray break-up as bigger drops are more deflected towards the axial flow direction than large droplets when traveling through the (mostly axially oriented) flow field of the surrounding dispersion gas. This theory has already been proven experimentally for hollow-cone sprays, as shown in the well-elaborated figures presented by Refs. [216, 297]. Whether the same also applies to full-cone sprays such as those of the SpraySyn burner needs to be determined in subsequent work for example by PIV measurements of the gas- and liquid-phase.

In the spray flame, no comparable plateaus for the droplet diameters were found. For both examined HABs, an increase in droplet diameter with increasing radius is observed. The V-shaped profiles overlap largely, with a median diameter of 8.6  $\mu\text{m}$  being measured at the center of the spray flame SF1 at 10 mm HAB, while about 2  $\mu\text{m}$  larger droplet diameters were obtained at 30 mm HAB. In comparison, the drop sizes measured at 10 mm HAB in the center of the cold spray are about 2.5  $\mu\text{m}$  larger. The diameter plateau of the cold spray crosses the v-shaped diameter profile of the spray flame at  $-1.5$  and 1 mm radius at 11  $\mu\text{m}$  median droplet diameter. With increasing radius, the droplet sizes measured in the spray flame always remain larger than those measured in the cold spray until the median droplet diameters of the reacting and non-reacting case converge at  $\pm 5$  mm radius. At 30 mm HAB the difference in the diameter profiles of the cold spray and SF1 is similar. Although the droplet diameter is the same in both cases (10.5  $\mu\text{m}$ ) in the center of the spray, larger median droplet diameters are observed in the flame already at  $\pm 1$  mm radius. With increasing radius, a significant difference in diameter between both cases is observed, e.g., at  $\pm 5$  mm radius the median droplet diameter is twice as high in the spray flame (21  $\mu\text{m}$ ) compared to the cold spray. At  $\pm 9$  mm radius, the droplet diameters converge.

These results fit well to the study on the combustion behavior of the ethanol spray presented by Stodt et al. [211] where three combustion regimes of droplet groups (i.e., spray) are derived following the work of Chiu et al. [298]. For comparable gas–liquid ratios (GLR), Stodt et al. deduced external and internal group combustion up to 20 mm HAB, while single droplet combustion is expected at larger HABs. By that, the comparably small difference in droplet size measured at 10 mm between cold spray and spray flame can be attributed to external and internal group combustion, while the large difference in the radial profiles of the droplet diameters observed at HAB = 30 mm can be related to single droplet combustion. In this mode, every droplet within the spray burns, resulting in a significant increase in evaporation rate. Hence, small droplets fall below the detection limit of the PDA (see chapter 5.3.2) resulting in significantly larger median droplet diameters outside the center of the spray flame compared to the non-reacting ethanol spray at HAB = 30 mm. However, the observed approximation of droplet diameters at large radii on both HABs is considered vague as count rates below 10 Hz were measured on these radii, i.e. the results at these locations are based on 100 droplets or less.

### 5.3.5 Characterization of the two-fluid nozzle

*The dimensional analysis and the derivation of the equation presented in this chapter were performed by Irenäus Wlokas. The results are included in this thesis according to the joint publication [56] to ensure completeness of the chapter.*

Since the physical processes of atomization are still not fully understood, it is common practice to develop empirical equations to describe atomizer performance [282]. Therefore, droplet-size measurements on the non-reacting spray (S1) have been performed with solvents of different viscosity and surface tension. Since the lower 561 nm beam of the PDA laser (Figure 5.4a) is blocked by the mounting ring of the SpraySyn burner (Figure 5.1, red) at measuring heights below 10 mm, the mounting ring (and the porous bronze plate) had to be removed in order to measure a representative size distribution of droplets close to the spray break-up. Hence, in contrast to the measurements of the ethanol spray flame SF1 (Table 5.2), the non-reacting spray without coflow was investigated to characterize the burner nozzle. To ensure comparability with the ethanol spray S1, Droplet velocity and size

measurements with and without coflow were performed (M44, M45, see Table A3.7 in the appendix for more details). Thereby, we found a negligibly low influence of the coflow on the droplet velocity (0.5 m/s faster with 120 slm coflow compared to zero coflow) and no influence on the droplet size that qualifies also these measurements to contribute to the database [280].

In this study, four different solvents were investigated spanning a field in terms of surface tension, viscosity, and density (Table 5.6) that are found to be the most relevant properties of a liquid for atomization [282]. For the measurements on these non-reacting sprays, droplets were either counted for a fixed time slot of 60 s or until a number count of 100,000 validated droplets was reached.

Table 5.6: Investigated solvents atomized by the two-fluid nozzle varying the dispersion gas flow. The physical properties are given at 1013 mbar and 20°C. Reprinted with modified layout from Ref. [56].

Solvent	Density / kg/m <sup>3</sup>	Dynamic viscosity / kg/m s	Surface tension / kg/s <sup>2</sup>	Refractive index / –
Acetone	791	$3.27 \times 10^{-4}$	$2.33 \times 10^{-2}$	1.360
n-Hexane	660	$3.28 \times 10^{-4}$	$1.84 \times 10^{-2}$	1.377
Ethanol	790	$1.19 \times 10^{-3}$	$2.22 \times 10^{-2}$	1.359
1-Butanol	810	$2.93 \times 10^{-3}$	$2.46 \times 10^{-2}$	1.399

Each respective solvent was fed to the two-fluid nozzle of the SpraySyn Burner at 2 ml/min and atomized varying the dispersion gas (4, 7, 10, 13, 17, and 20 slm). From that, a mass-based gas/liquid flow ratio (GLR) is calculated with the respective density of the dispersion gas and the solvents. Furthermore, the Sauter mean diameter (SMD) is calculated in the Dantec BSA Flow Software according to Ref. [221] based on the measured spray-droplet diameters of the different solvents. The results of the PDA measurements form a characteristic diagram of the two-fluid nozzle of the SpraySyn burner (Figure 5.29). For all solvents investigated, the range smaller than 7 slm dispersion gas (GLR < 7.6) shows noticeably large SMDs (and wide size distributions) indicating inhomogeneous spray generation.

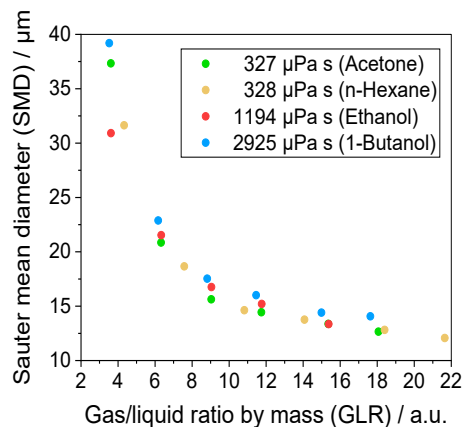


Figure 5.29: Characteristic nozzle curve of the two-fluid nozzle of the SpraySyn burner. Reprinted with modified layout from Ref. [56].

To study the influence of the surface tension on the droplet size, the comparison of acetone with n-hexane is suitable, since the former has a surface tension 26% larger than n-hexane with approximately the same dynamic viscosity. At 4 slm dispersion gas (GLR = 3.5–4.5) the influence of the surface tension on the SMD is significant (5.7 μm larger SMD for acetone compared to n-hexane). With 7 slm dispersion gas (GLR = 6.1–7.6), the acetone droplets are only 2 μm larger and asymptotically approach

the SMD of the hexane droplets with increasing gas/liquid ratio, i.e., the higher the amount of dispersion gas, the smaller the influence of the surface tension on the droplet size.

The influence of viscosity on the droplet size is apparent from the comparison of 1-butanol with acetone. Here we have a small difference in surface tension (5.5%), while the dynamic viscosity of 1-butanol is almost eight times higher than that of acetone. The droplet size of 1-butanol is on average 1.6  $\mu\text{m}$  larger than that of acetone across all gas/liquid ratios. In comparison, the SMD of the ethanol droplets ranges between the SMDs of 1-butanol and acetone at dispersion gas flows from 7–13 slm (GLR = 6.1–14.1) suggesting that the viscosity has a dominating influence on the resulting droplet size since the dynamic viscosity of ethanol ranges in between the viscosity of acetone and 1-butanol. Also, in this operating range the butanol droplets are on average 1  $\mu\text{m}$  larger than the ethanol droplets. Over all, we measured the lowest SMD of all examined solvents for ethanol at 4 slm dispersion gas (GLR = 3.5–4.5) contradicting the hypothesis of viscosity-dominated influence on droplet size. However, since we observe incomplete spray generation at this operating point that leads to a broad droplet size distribution and being outside the useful burner-operation regime (for nanoparticle synthesis), no further investigations have been carried out so far.

Looking at the entire measurement data set (Figure 5.29), it is noticeable that a characteristic feature of the atomizer is that at a certain GLR, the mean droplet size becomes nearly constant – in contrast to the strong dependence at lower gas-to-liquid ratios. The latter is the regime that should be avoided in nanoparticle synthesis because already small variations of the mass flow rates cause strong variations of the mean droplet diameter. The quite smooth characteristic of the atomizer enabled further investigation in terms of similarity, which is the usual procedure for characterization of spray nozzles [299, 300]. We postulate that the mean diameter and the standard deviation can be expressed as functions of geometric and process variables: capillary inner diameter  $d_0$ , gas-nozzle inner diameter  $d_i$  (i.e., the outer diameter of the capillary), and gas-nozzle outer diameter  $d_a$ , the liquid properties density  $\rho_L$ , viscosity  $\eta_L$ , and surface tension  $\sigma_L$ , the gas properties density  $\rho_G$ , viscosity  $\eta_G$ , the gas and liquid mass-flow rates  $\dot{m}_G$ ,  $\dot{m}_L$ , and the measured Sauter mean diameter SMD. The analysis of the problem by means of dimensional analysis results in a set of eight dimensionless groups. Further asymptotic considerations reveal that the dimensionless gas/liquid density ratio can be neglected, as well as the dimensionless viscosity ratio. Furthermore, the momentum of the injected liquid is small in respect to the momentum of the dispersion gas, such that the Reynolds number of the liquid is also neglected in further investigation. Finally, the characteristic of the SpraySyn-burner atomizer can be described as an implicit function of five dimensionless groups:

$$f = \left( \frac{d_i}{d_0}, \frac{d_a}{d_0}, \frac{\eta_L}{\sqrt{\rho_L d_0 \sigma_L}}, \frac{\dot{m}_G}{\dot{m}_L}, \frac{\text{SMD}}{d_0} \right) = 0 \quad 5.1$$

where the dimensionless expression  $\frac{\eta_L}{\sqrt{\rho_L d_0 \sigma_L}} \equiv \text{Oh}$  corresponds to the Ohnesorge number Oh (that requires most accurate knowledge of the materials properties) and  $\frac{\dot{m}_G}{\dot{m}_L} \equiv \text{GLR}$  is the gas-to-liquid ratio. The explicit formula for the Sauter mean diameter is then

$$\text{SMD} = d_0 \left( \frac{d_i d_a}{d_0^2} \right)^{b_1} \text{Oh}^{b_2} \text{GLR}^{b_3} \quad 5.2$$

In this form, the formula is unique for the investigated geometry, but simplifies the regression analysis for the exponents  $b_i$ . The final expression for the SMD of the SpraySyn burner two-fluid nozzle is then:

$$\text{SMD} = d_0 0.2874 \text{ Oh}^{0.084} \text{ GLR}^{-0.69} \quad 5.3$$

using the data measured at a distance of 2 mm from the nozzles exit (Figure 5.29) – a typical distance at which the simulation domain begins if the primary breakup of the spray is considered as “finished”. Presuming that the relative velocity of the droplets in the gas stream is already small at this distance, secondary breakup processes were neglected in the present investigation. However, secondary breakup via disruptive evaporation cannot be excluded in general, but it is strongly mixture- and temperature dependent and does not affect the early, cold spray. Also excluded in this model are thermal effects on the surface tension and viscosity presuming that the droplets enter the flame “cold” at a distance of 2 mm above the burner.

## 5.4 Outlook

The currently most important next step is the suppression of pulsation of the spray flame. Recent high-speed imaging of flame chemiluminescence and shadowgraphy have shown that the spray flame extinguishes and reignites sporadically instead of burning continuously and that the liquid is atomized unsteadily [213], which is consistent with the spray pulsation described in chapter 5.3.2. An optimized nozzle design presently being developed in Aachen as well as improved operating parameters (Duisburg) in which fuel (methane or hydrogen) is added to the dispersion gas are promising approaches. Subsequently, a new characterization of the reference spray flame using the Nikon DSLR camera is required and the resulting droplet sizes and velocities need to be updated. In addition, PDA measurements should be performed in precursor-doped flames.

The Matlab code for the uniform evaluation of the Nikon DSLR photos of the spray flame (chapter 5.3.1) should be further extended, e.g., by introducing an automatic image rotation to eliminate the influence of not perfectly horizontal camera (or burner) orientation on the evaluated tilt angle of the spray flame. Regarding the currently defined tolerances of the reference flames [26], iteration is required as soon as a reliable number of flame benchmarks have been reported back from other working groups. In this context, a study comparing several Nikon D5300 cameras regarding their photometric properties should be performed to quantify the deviation in their individual color-detection performance. Depending on the result, an automated camera calibration needs to be implemented in the Matlab codes.

Since SpraySyn ensures inter-comparability of scientific results, subsequent work should invest in the analysis of measurement data from different working groups that provide similar quantities, e.g., droplet sizes measured by PDA. Here, it is indispensable that all results are qualified by a successful flame benchmark. If necessary, further best-practice rules for burner operation must be specified (e.g., a strict definition of how far the capillary may protrude from the two-fluid nozzle) to allow a quantitative comparison of the results. Secondly, the results of different measuring techniques that provide for instance droplet diameters should be compared with each other, e.g., results from PDA and WALs (wide-angle light scattering). Besides enhancing process understanding of materials synthesis in spray flames, this step offers the possibility of improving current and developing future diagnostic measurement techniques.

## 6 Pilot-scale spray burner for nanoparticle synthesis

Results of this chapter are presented in the following Bachelor theses:

R. Zhou, *Bildgebende NO-LIF-Thermometrie mit Lichtschnittkorrektur in der Sprayflammen-Synthese von Eisenoxid-Nanopartikeln im Pilotmaßstab*, Bachelor thesis, University of Duisburg-Essen, 2018, supervisor: **F. Schneider**, examiners: C. Schulz, T. Dreier

Y. Zhang, *Optische Charakterisierung und Bestimmung von Geschwindigkeitsfeldern von Flüssigsprays mittels High-Speed Imaging, Particle Imaging und Particle Tracking Velocimetry*, Bachelor thesis, University of Duisburg-Essen, 2017, supervisor: **F. Schneider**, examiners: C. Schulz, T. Dreier

### 6.1 IUTA spray burner

The pilot-scale spray burner at IUTA consists of a combination of an in-house designed gas burner and a commercially available atomizer nozzle from BETE that is installed in the center of the gas burner. Its design is motivated by enabling production rates of nanoparticles in the two-fluid process on a kg/h scale using liquid fuels and precursors, since there are decisive restrictions regarding suitable precursors for pure gas-phase synthesis as well as significantly higher demands for the technical periphery regarding evaporation of the precursor and supply of the precursor vapor to the reactor (chapter 2.1). Although materials synthesis in a two-fluid environment is more complex compared to pure gas-phase processes, spray-flame synthesis shows clear advantages like less complex periphery, easy preparation of liquid fuel/precursor mixtures, lower costs precursors, and accessibility to almost all existing elements including salts that make it a promising approach for future materials synthesis on industrial scale [26]. At the end of 2011, stable burner operation was demonstrated outside the IUTA flame reactor, which was qualitatively characterized by color imaging using a DSLR camera while the operating parameters of an iso-propanol spray flame were varied. In the following, the infrastructure for operating the spray burner was improved (e.g., the peristaltic pump was replaced by more reproducible liquid metering with a pressurized reservoir and a mass flow controller).

The pilot-scale spray burner is mounted upside-down in a reactor head functioning as an interface to the media-supply infrastructure of the IUTA pilot plant. This allows the spray burner to be connected vacuum-tight to the IUTA flame reactor as shown in Figure 4.1a for the pilot-scale gas burner. The burner surface does not extend to the upper edge of the top optical port of the flame reactor. Hence, the flame can be optically investigated between  $HAB_{\min} = 15$  mm and  $HAB_{\max} = 65$  mm (c.f., Figure 4.1a). Like the pilot-scale gas burner (Figure 4.2), the gas flows of the IUTA spray burner are fed through co-annular gaps to the burner surface. Figure 6.1 provides the arrangement and all relevant geometries. A premixed methane/oxygen pilot-flame gas mixture is fed through the inner annular gap (red) and a nitrogen coflow is fed through the outer annular gap (orange). The latter is used as a shroud flow for shielding the pilot flame against unwanted recirculation and interfering side-flows as well as to provide well-defined boundary conditions for CFD simulations.

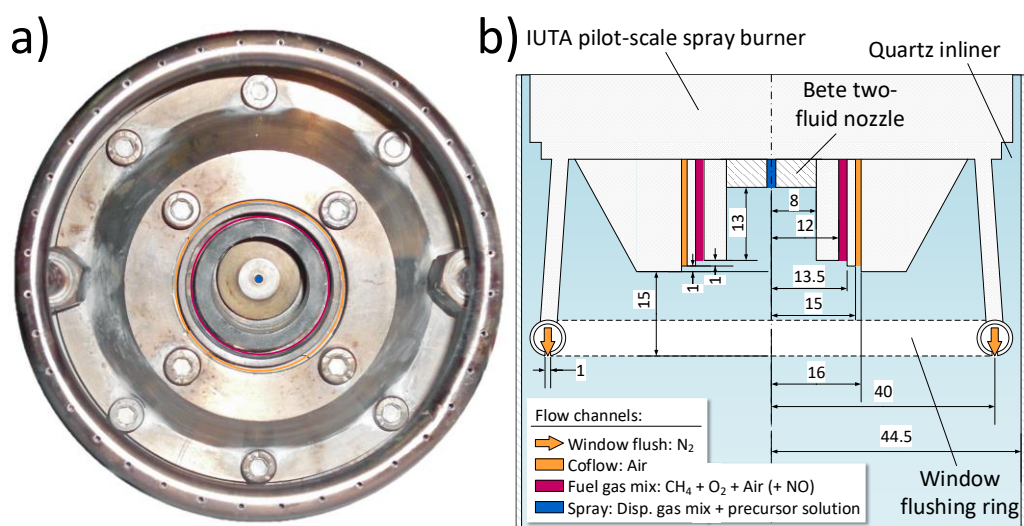


Figure 6.1: Photo (a, top-view) and sketch (b, side-view) of the pilot-scale spray burner. For better recognition, the co-annular gaps of the burner were highlighted in color on the photo. All dimensions are given in mm.

In the center of the burner, an internal-mixing two-fluid nozzle (BETE) is installed that consists of three core components:

1. A reservoir for the solvent or precursor-solvent mixture (liquid feed),
2. A chamber where the liquid is atomized (atomization chamber),
3. Six circularly distributed holes through which dispersion gas is fed into the chamber to atomize the liquid (air feed).

The cross-section of the spray nozzle shown in Figure 6.2a illustrates the arrangement of these components. The liquid is fed to an atomization chamber from a liquid reservoir, while dispersion gas enters the atomization chamber through six holes at high velocity. By that, the liquid is atomized by the dispersion gas and pushed through the air-cap nozzle orifice as a fine spray.

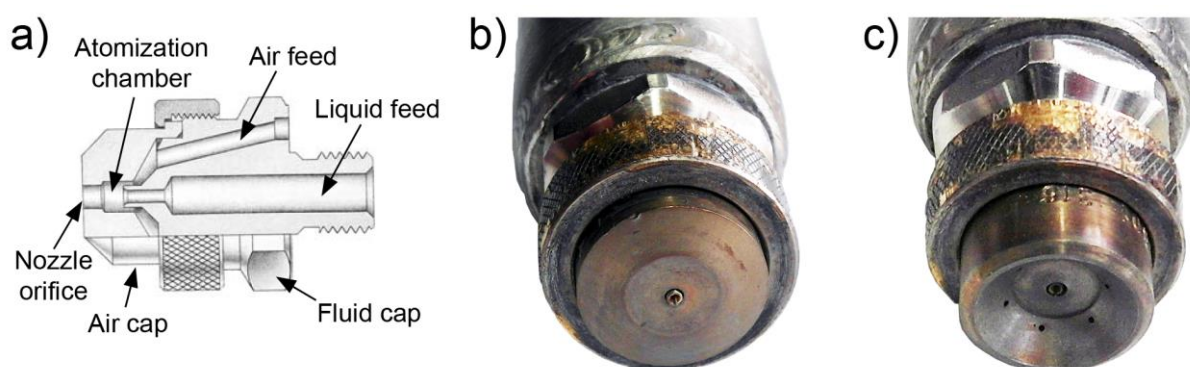


Figure 6.2: a) Sketch of the BETE two-fluid nozzle with internal mixing [301]; b) Photo of the two-fluid nozzle with installed air cap showing the needle in the center of the nozzle orifice; c) Photo of the two-fluid nozzle without air cap showing the inside of the upper half of the atomization chamber and the dispersion gas inlets.

The outlet of the liquid reservoir can be blocked by a needle that on the one hand serves as a plug to prevent unintentional leakage of the liquid from the reservoir, and on the other hand, to mechanically remove contaminations from the nozzle orifice of the air cap. The axial position of the needle is adjustable pneumatically. When the nozzle is in operation, the needle is retracted into the liquid reservoir. The two-fluid nozzle is specified in Table 6.1 and is meant to provide very fine atomization, a full-

cone spray pattern with a narrow spray angle of 17–22°, as well as the lowest flow available for nozzles in the portfolio of the manufacturer [302].

Table 6.1: Specification of the two-fluid nozzle (BETE Deutschland GmbH) used in the IUTA pilot-scale burner.

Model	¼" XA
Body style	00
Spray set-up number	SR 050
Fluid cap	FC 7 (Material spec. acc. to AISI 316)
Air cap	AC 1201
Hardware assembly	D (needle for both, clean-out and shut-off)
Dispersion-gas pressure range	0.7–4 bar
Liquid volume flow range	0.5–2.2 l/h
Max. liquid viscosity	200 mPa s

To characterize the flow of the IUTA pilot-scale spray burner and to enable CFD simulations, the reacting and non-reacting flow is investigated in the following. Therefore, measurements of the gas-phase velocity and the velocity of the spray droplets are performed under non-reacting conditions (chapter 6.3.1) using PIV. Since these results provide validation data for droplet velocities determined by multi-pulse RGB shadowgraphy (chapter 2.2.5), the spray was investigated using the technique presented in Refs. [95, 96] in the context of the present thesis. Additionally, the gas-phase temperature was measured *in situ* (during iron-oxide nanoparticle synthesis) inside the IUTA flame reactor (Figure 4.1) using multiline NO-LIF thermometry. The laser-sheet correction introduced in chapter 4 is discussed in the context of the spray-flame temperature studied at multiple operation-parameter sets (chapter 6.3.2). Furthermore, Fe-LIF measurements are performed to investigate the decomposition of iron(III) nitrate in a (spray) flame (chapter 6.3.3) that is mandatory for the development of a reaction mechanism of this precursor.

## 6.2 Experiment

### 6.2.1 Particle Image Velocimetry

The PIV measurements were performed outside the IUTA flame reactor under non-reacting conditions in a nozzle test rig at the IVG. The experimental setup is shown in Figure 4.3 and the utilized equipment is specified in Table 4.1. In the following, only the differences between the experiment on the IUTA gas burner (chapter 4.2.1) and the IUTA spray burner are pointed out: Four mass flow controllers (MFC) were used to meter pressurized air (Table 6.4) through the burners channels for coflow (MFC1), pilot-gas mix (MFC2), dispersion gas (MFC3), and window-flushing ring (MFC4) that are indicated in Figure 6.1. Ethanol was provided from a 500 ml reservoir (ER) where 1.5 bar overpressure (air) was applied to push the liquid to a liquid-flow meter (LF) to provide a controlled mass flow through the two-fluid nozzle. For PIV, fine DEHS droplets are added to the gas flow using the LaVision aerosol generator (AG) described in chapter 4.2.1. These droplets were added either to the combustion-gas channel, the coflow-channel, or the channel of the window-flushing ring (for each result, the seeded channel is specified in the respective figure caption) to observe not only the velocity but also the distribution of the respective gas flows in the burner chamber. In the experiment, the pilot-scale spray burner was operated with the parameters defined by IUTA (Table 6.4). Therefore, the measurements were performed with isolated operation of the individual channels (e.g., isolated operation of

the window-flushing ring as shown in Figure 6.5) as well as in simultaneous operation of all channels with and without spray. The latter was required since the gas-phase velocity could not be measured when the spray was operated. An overview about all acquired measurements is given in the appendix in Table A3.8 in the appendix. The major results are discussed in chapter 6.3.1. For each measurement, 300 double-frame images were recorded that were evaluated using the *PIV package* of *DaVis 8.1.4*.

## 6.2.2 Multi-pulse RGB shadowgraphy for Particle Tracking Velocimetry

For the droplet velocity measurements, the spray burner was installed together with the reactor head (Figure 4.1) in the nozzle test rig similar to that used for PIV measurements as described in chapter 6.2.1. The utilized mass flow controllers are shown in Figure 4.3 and specified in Table 6.3 while the operating parameters are listed in Table 6.4.

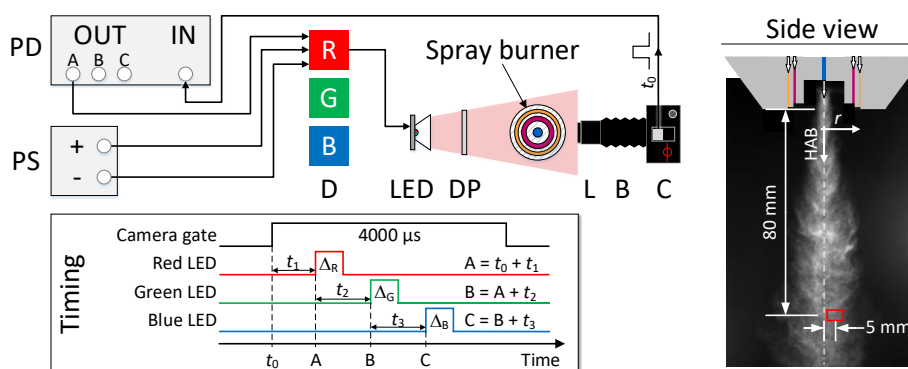


Figure 6.3: Top view of the setup for RGB-PTV in shadowgraphic arrangement showing the camera (C) that provides the initial trigger pulse ( $t_0$ ), the pulse/delay generator (PD), the laboratory power supply (PS), the LED drivers (D), the RGB-LED (LED), the diffuser plate (DP), the camera lens (L), and the bellows (B). For better clarity, wiring is only indicated for the red LED driver (the green and blue LED drivers are consequently connected to the other outputs (2 and 3) of the pulse/delay generator). On the right, the side view shows a photo of the investigated ethanol spray with a sketch of the IUTA spray burner nozzle indicating the location of the  $7 \times 4.6 \text{ mm}^2$  (full frame) measurement region (red box). On the lower left side, the RGB pulse-train is indicated that is placed within the exposure time of the acquired image (the minimum exposure time is limited by the camera flash synchronization limit, here  $1/250 \text{ s}$ ).

The optical setup for RGB-PTV is presented in Figure 6.3. A combination of red, green, and blue light-emitting diodes (RGB-LED [234]) was used for background illumination of the non-reacting ethanol spray through a diffuser plate (DP) made of Poly(methyl methacrylate) (PMMA). When the camera trigger is pressed, it provides the initial trigger ( $t_0$ ) to a delay generator (PD) that initiates the RGB pulse train (Figure 6.3). The LED drivers (Figure 6.4) that are fed with 20 V from a laboratory power supply (PS) were designed by Raphael Mansman and Jan Menser following the driver circuit presented by Willert et al. [232]. The required components are specified in Table 6.2. Further details about the LED driver are described by Menser et al. [95, 96].

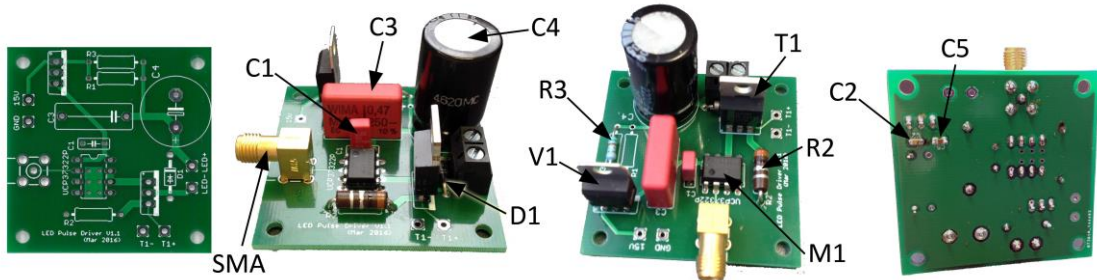


Figure 6.4: LED driver for generating high-power pulses down to 100 ns pulse width. On the left, the driver platine (D) is shown without components. This platine can easily be reproduced by submitting the Gerber files provided on the institute’s network storage drive to an electronics manufacturer like [www.itead.cc](http://www.itead.cc). All other images show the LED driver from multiple perspectives to identify all electronic components listed in Table 6.3.

To resolve single droplets by shadowgraphy imaging, high optical magnification was necessary. A DSLR camera (C) and a bellows (B) combined with a macro-reversed  $f = 50$  mm lens (L) was used reaching a magnification by a factor of 3.4. The resulting full-frame detection area was about  $7 \times 4.6$  mm<sup>2</sup> and the utilized LED pulse lengths ( $\Delta_{R/G/B}$ ) were 1  $\mu$ s each with a pulse separation of  $t_2 = t_3 = 5$   $\mu$ s. The minimum possible camera exposure time was confined by the camera’s flash synchronization limit of 1/250 s (i.e., 4 ms). Hence, blocking bright light from the field of view during the measurements was required.

Table 6.2: Electronic components utilized for the LED driver (D).

Component	Specification
C1	Film capacitor, 0.22 $\mu$ F, 50 V DC
C2, C5	Ceramic capacitor, 0.1 $\mu$ F, 50 V
C3	Film capacitor, 0.47 $\mu$ F, 250V DC
C4	Electrolytic capacitor, 2200 $\mu$ F, 35 V
D1	Schottky diode, SB260
R2	Resistor, 0.1 Ohm, 0.75 W $\pm$ 10%
R3	Resistor, 0.51 Ohm, 0.6 W $\pm$ 5%
T1	Transistor MOSFET IRFB3206
M1	Gate driver MOSFET UCC37322P
V1	Linear voltage regulator, type 78, e.g., STM L7809CV3
SMA	SMA female connector, e.g., BKL Electronic 0409071

For data evaluation, the 12-bit raw images stored by the camera were converted to the TIFF format using the software DCRaw [237] to make them accessible as de-mosaiced RGB images in Matlab [236]. Therefore, the applied parameters were “-T” to export the images to the TIFF file-format, “-4” to create linear 16-bit images without gamma correction, “-o 0” to not apply any color management, and “-r 1 1 1” to not apply any white balance. The general approach of further post processing and subsequent particle tracking is described in chapter 2.2.5. The utilized median filter was applied with a size of  $6 \times 6$  pixels and the morphological minimum filtering used a circular structuring element preserving elements larger than 10 pixels [95]. The threshold used for binarization of each individual color channel after normalization was iteratively determined and set to 0.3 (i.e., intensity values smaller than 0.3 were set to 0 while all other values were set to 1). For particle tracking with SimpleTracker (chapter 2.2.5), a maximum linking distance of 70 pixel (0.11 mm) was set to avoid that the algorithm connects tracks of different particles. Further details that simplify the reproducibility of

the result presented in chapter 6.3.1 are given in the appendix (chapter A3.4.2). An overview of the utilized equipment is provided in Table 6.3.

Table 6.3: Equipment used for droplet velocity measurements by RGB-PTV. All hardware identifiers (e.g., LF) are only valid in the context of RGB-PTV on the IUTA spray burner.

Identi-	Vendor	Product	Serial number
MFC1	MKS Instruments	Mass flow controller 300 slm N <sub>2</sub>	G565640G20
MFC2	MKS Instruments	Mass flow controller 50 slm Ar	G562390G20
MFC3	MKS Instruments	Mass flow controller 25 slm Ar	G484832G20
MFC4	MKS Instruments	Mass flow controller 50 slm H <sub>2</sub>	G562391G20
LF	Brooks	Liquid flow meter Quantim	01B40491239
C	Nikon	DSLR camera D90	N/A
PD	Highland Technology	Pulse/delay generator P400	355
PS	Hameg Instruments	Power supply HM8040	44983
D	IVG	LED pulse driver V1.1 (Mar 2016)	N/A
LED	LED Engin	RGB LED emitter	LZ4-00MC00
DP	BWF Kunststoffe	Diffusor plate (PMMA No. 11)	VR-1650-1, white
L	Nikon	Camera lens AF Nikkor ( $f_{\#} = 1.8$ )	2130056

### 6.2.3 Multiline NO-LIF thermometry and Fe-LIF

The experimental setup is described in chapter 4.2.2. The only difference compared to the multiline NO-LIF thermometry measurements performed on the IUTA gas burner (chapter 4) is that for each wavelength position, 30 (instead of 20) images were acquired to increase the signal-to-noise ratio in the precursor-doped spray flames. To measure the spatial distribution of iron atoms in the flame, the  $3p^63d^64s^2$  transition [123] excited at 225.15 nm (cf., Figure 6.18) was used. Therefore, no changes to the described setup were required.

## 6.3 Results

### 6.3.1 Gas-phase and droplet velocity measurements in the non-reacting ethanol spray

To provide first insights into the gas and liquid-phase velocity of the IUTA pilot-scale spray burner (Figure 6.1), the non-reacting flow was investigated at the nozzle test rig at IVG (Figure 4.3). The PIV measurements were performed with the setup described in chapter 6.2.1 and the operating parameters specified in Table 6.4. All measurements were performed with and without the shielding quartz inliner as well as with and without the window-flushing ring (disassembling required for data acquisition close to the burner mouth).

Table 6.4: Non-reacting operating conditions of the pilot-scale spray burner investigated with PIV and RGB-PTV at a nozzle test rig (Figure 4.3) at atmospheric pressure. The examined operating conditions correspond to flame 2 and 3 (Table 6.7) that are investigated inside the IUTA flame reactor in chapter 6.3.2 and 6.3.3.

Solvent	Dispersion gas	Pilot gas mix	Coflow	Window flushing
EtOH	Air	Air	Air	Air
g/h	slm	slm	slm	slm
500	18	28	90	40

Before data evaluation, the regions where reflections of the quartz inliner inhibit the detection of scattered light from the seeding particles as well as the upper part of the image where the nozzle is located were masked. Also, the regions in which no physically meaningful vectors could be determined were rejected in the post-processing (e.g., by uncertainty analysis [206, 207]). The presented time-averaged velocity fields are based on 300 double-frame images (one frame per laser pulse). The comparison of measurement data under identical operating conditions where either the channel of the coflow or the channel of the pilot-gas mixture was seeded, shows mutually covering velocity fields (compare for example the digital files of M5 with M8 or M15 with M13 (Table A3.8), not plotted in this manuscript). Thus, the determined velocity fields are independent of the choice of the seeded gas flow.

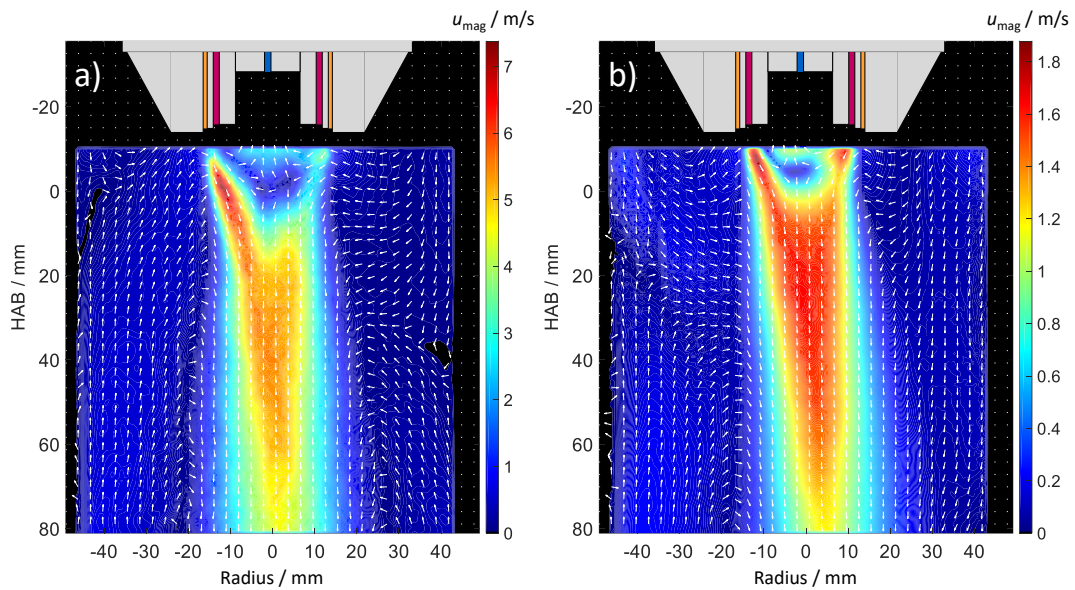


Figure 6.4: Gas-phase velocity measured for (a) isolated operation of the coflow and (b) isolated operation of the pilot gas channel. Seeding was added to the respective operated flow. Both measurements were performed with quartz tube and without window-flushing ring. For clarity, the spray burner is depicted schematically (cf., Figure 6.1) and only every fourth velocity vector is plotted (scaled to uniform length).

To measure the velocity fields of the individual gas flows, each flow of the spray burner was operated separately (i.e., in absence of all other flows) and seeded accordingly with DEHS droplets. However, since the given mass flow of 18 slm was too low to operate the seeder (see chapter 4.2.1 for details), the dispersion gas flow could not be measured isolated. Figure 6.4 shows the resulting velocity fields with isolated operation of the coflow channel (left) and the pilot-gas channel (right). For both measurements, the quartz tube was used to isolate the flows from interfering airflows in the laboratory. In all PIV results presented in this chapter, the color-coding represents the velocity magnitude  $u_{\text{mag}}$  while the normalized arrows indicate the flow direction. The definition of the 0 mm HAB mark refers to the position of the lower edge of the window-flushing ring (where the exit holes are located). For the velocity fields shown in Figure 6.4, the window-flushing ring was removed to allow measurements as close as possible to the nozzle outlet. However, even without the window-flushing ring, the laser sheet could not be positioned closer than 5 mm to the surface of the spray burner because there are four round-head screws (Figure 6.1a) that cause significant stray light.

In both velocity fields shown in Figure 6.4, the area right below the nozzle surrounded by the outflow of the respective annular gap indicates a recirculation zone on the first 10 mm (a) and 5 mm (b). Due

to the nozzle design, it is impossible to measure directly below the outlet of the annular gaps, as they are retreated 15 mm (Figure 6.1). However, this recirculation only appears when operating the respective gas flows alone (neighboring gas flows off). The effect is therefore not relevant for burner operation and not further investigated.

The measured velocity fields are not axisymmetric. In Figure 6.4a, the inflow velocity on the left side is 7.4 m/s while on the right side less than 4 m/s were measured. It is noticeable that the highest velocity on the left-hand side of the inflow does not occur directly below the burner ( $HAB = -10$  mm) but about five millimeters further downstream. On the right-hand side of the inflow, the velocity is first around 3.5 m/s, then drops between  $-5$  and  $2$  mm  $HAB$  to less than 2 m/s and then rises again adjoining the primary flow field (as known from chapter 4, the proportion of the flow making the significant contribution to the total flow velocity is referred to as primary flow). The reason for these observations could not be determined. It is assumed that the spray nozzle could not be aligned exactly vertically in the experiment since there was no crane available in the laboratory (together with the reactor head, the spray burner weighs about 50 kg). Also, Figure 6.1a shows that there are four brackets inside the annular gap of the coflow that are fixed by four round-head screws attached to the burner surface. These brackets are constructively required to fix the separation-wall between coflow and pilot gas mixture (Figure 6.1) to the main body of the burner. However, they cause significant swirls in the flow field that could explain the asymmetry between left and right side of the inflow. Both inflows merge at  $HAB = 5$  mm and form the straight downwards oriented primary flow field with 5.4 m/s average velocity that is slightly shifted to the right. With increasing  $HAB$ , a deceleration of the velocity can be observed. At  $HAB = 80$  mm still flow velocities of about 4.5 m/s (61% of the peak velocity at the inlet) are measured.

The primary flow induces a secondary flow inside the quartz tube that is asymmetric, too. On the left side, the secondary flow moves upwards towards the burner until reaching a downwards-oriented flow in the upper left corner at 17 mm  $HAB$ , deflecting the secondary flow towards the coflow inlet on the left side of the spray burner. On the right side of the primary flow, a secondary flow is moving towards the burner, too. However, already at 37 mm  $HAB$  it hits a downwards oriented counterflow. In the consequence, both streams are redirected towards the primary flow field on the centerline. Comparing the velocity magnitude of the secondary flows on both sides, it is apparent that the secondary flow on the left-hand side (0.65 m/s) is more than four times higher than on the right side (0.15 m/s) that explains the tilt of the primary flow field to the right side.

In Figure 6.4b, the gas flow originating from the fuel gas channel reaches 1.9 m/s maximum velocity. Overall, the velocity of the primary flow remains more than 75% of the maximum velocity up to 60 mm  $HAB$ . At 80 mm  $HAB$ , however, the velocity has dropped to 1.1 m/s (63%), which is comparable to (a). The flow field in (b) is more symmetrical compared to (a), however, on the right side of the inflow a comparable velocity dip is found around  $HAB = -2$  mm. While this sequence of a velocity decrease followed by a velocity increase is explained in (a) by a swirl caused by brackets in the coflow channel, no comparable element is found in the fuel gas channel. While the shape of the primary flow field and its tilt to the right side are similar to the velocity field of the coflow (Figure 6.4a), the angle of inclination is more pronounced. As observed in the flow field in Figure 6.4a), a secondary flow field is induced inside the quartz tube in (b), too. While in (a) both an upward as well as a downward oriented secondary flow encounter on the right side of the primary flow, a similar constellation can be observed in (b) on the left side. Here, the interface of both secondary flows adjoins between 12 and

32 mm HAB creating an inwards-oriented flow towards the primary flow field. In contrast to that, a downwards oriented secondary flow is apparent without any counterflow on the right side of the primary flow field of Figure 6.4b. This axial asymmetry of the surrounding secondary flows explains why the primary flow is shifted more to the right in (b) than in (a). Another remarkable feature of the flow field in (b) is an inwardly and upwardly oriented vortex that can be observed between  $HAB = -10$  and 7 mm on both sides of the inflow from the fuel gas channel. However, a concrete influence on the primary flow field cannot be derived on the basis of the available data. Here, PIV measurements from additional perspectives or CFD simulations are needed (maybe even in 3D) to quantify the effects of the vortices.

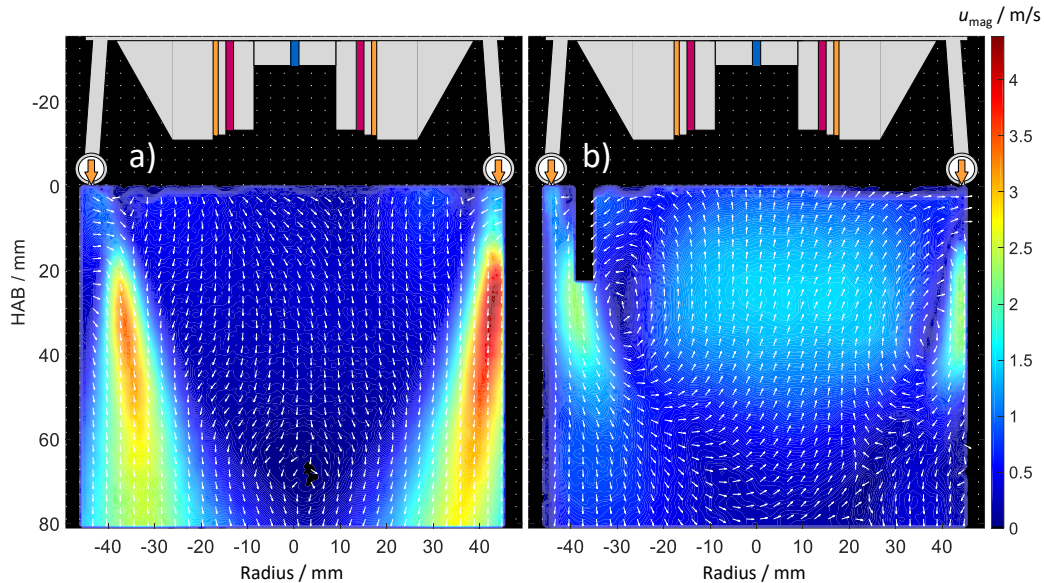


Figure 6.5: Gas-phase velocity measured for isolated operation of the window-flushing ring (a) without quartz inliner and (b) with quartz inliner (M12). Seeding was added to the window flushing flow. For clarity, the spray burner is depicted schematically (cf., Figure 6.1) and only every fourth velocity vector is plotted (scaled to uniform length).

Figure 6.5 shows the isolated operation of the window-flushing ring without quartz tube (a) and with quartz tube (b). The torus-shaped body itself is supplied with compressed air by two supply lines (Figure 6.1). The airflow leaves the window-flushing ring through 36 holes that are equidistantly placed on the torus-shaped body. For all experiments in which the window-flushing ring was installed, the laser sheet was aligned to cross centrally below the spray burner, i.e., to cut the central axis of the burner. It was not determined if any of the small holes of the torus-shaped body was positioned exactly above the laser sheet. Hence, axial symmetry is not to be expected in the results shown in Figure 6.5. Furthermore, it is pointed out that an inhomogeneous pressure drop is expected inside the torus-shaped body of the window-flushing ring, i.e., the exit velocity through the holes of the torus-shaped body that are close to the supply lines is expected to be higher than for the other holes. This pressure drop is due to constructional reasons and has not been further investigated in the context of the present thesis. Nevertheless, the measurements presented provide the best estimate of the velocity field below the window-flushing ring available yet.

The highest measured velocity was 4.4 m/s (Figure 6.5a). It was measured without the quartz tube 15 mm below the torus-shaped body on the right side of the velocity field. The raw images show that the laser sheet was not positioned exactly below one of the exit holes (neither on the left nor on the

right side), because no scattered light was captured from the seeding droplets closer than 15 mm to the torus-shaped body. This means that closer to the exit holes the maximum velocity is expected to be higher. An extrapolation based on a velocity profile extracted from the center of the stream on the right side of Figure 6.5a results in an estimated velocity of about 5.1 m/s right below the torus-shaped body. Overall, the primary flow induced by the window-flushing ring propagates mainly in axial direction while being slightly inclined towards the center axis of the burner.

When the quartz tube is present, the velocity of the primary flow is reduced by about 50%. The peak velocity is found to be 2.2 m/s and the velocity is 0.2 m/s higher (9%) on the left side than on the right side. Centrally below the window-flushing ring of the spray burner, an upwards-oriented secondary flow is induced. This secondary flow moves along the central axis towards the burner and forms vortices on the right and left side whose axis-of-rotation are perpendicular to the drawing plane. It is assumed that in three-dimensional space, both vortices form a single torus-shaped vortex with its center position at 30 mm HAB on the left side ( $r = -30$  mm) and 35 mm HAB on the right side ( $r = 37$  mm) of Figure 6.5b. Based on the results shown here (Figure 6.4 and Figure 6.5) and other results with and without quartz tube (e.g., M5 and M15, M8 and M23, M30 and M31, not plotted in this manuscript, see Table A3.8 in the appendix), the observed backflow and vortices are clearly related to the presence of the quartz tube. During synthesis, these vortices could lead to particle recirculation and unwanted particle growth. Moreover, whether the flow induced by the window-flushing ring effectively keeps the quartz inliner free of particle deposition during synthesis cannot be conclusively determined on the basis of the available data. Nevertheless, the velocity falls below 1 m/s between 45 and 50 mm HAB on the right side of Figure 6.5b, which is in the same order of magnitude as the secondary counterflow observed in Figure 6.4. Hence, it is concluded that the window-flushing flow is insufficient to keep the entire height of the top optical access of the IUTA flame reactor free from window fouling.

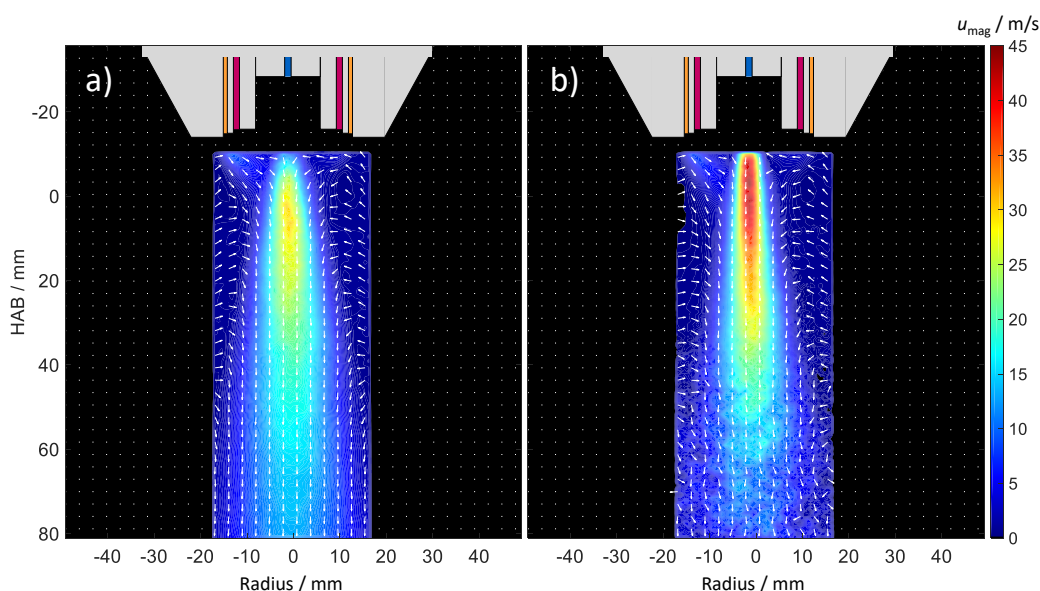


Figure 6.6: Simultaneous operation of all channels of the IUTA pilot-scale spray burner according to Table 6.4 (a) without ethanol spray and (b) with ethanol spray. In (a), the gas-phase velocity is measured (based on the DEHS seeding added to the pilot-gas channel) while in (b), the droplet velocity is measured where the PIV evaluation is based on the ethanol droplets instead of the DEHS seeding. Both measurements were performed with quartz tube and without window-flushing ring. For clarity, the spray burner is depicted schematically (cf., Figure 6.1) and only every fourth velocity vector is plotted (scaled to uniform length).

The velocity fields in which all channels of the spray burner are operated simultaneously with the mass flows specified in Table 6.4 are shown in Figure 6.6. The measurements were performed without window-flushing ring to measure as close as possible to the burner mouth. Figure 6.6a shows the primary gas flow centrally below the burner that reaches a peak velocity of 30.4 m/s. In the upper left area, the inflow through the coflow channel can be identified. Based on this data, the coflow velocity is found to be 1 m/s (13%) more than the results of Figure 6.4a show. Since all parameters were optimized with regard to the fast gas flow ( $> 10$  m/s) during measurement and evaluation of the data presented in Figure 6.6, the uncertainty of the evaluated velocity of slow flows is high. Hence, the velocity vectors of the slow flow should only be considered as rough estimates that indicate the direction of the secondary flow, predominantly, while the calculated velocity magnitude is biased. Also, for this reason, the velocity fields were masked with a rectangle that suppresses all data outside the width of the primary flow ( $\pm 16$  mm, see Figure 6.6a).

The primary flow of Figure 6.6a is axisymmetric in good approximation. With increasing HAB, the diameter of the downward-facing flow increases conically. While between  $HAB = -10$  and 50 mm an inwards-directed secondary flow is apparent on the left and right side of the primary flow field, the whole flow-field is downwards-oriented at  $HAB > 60$  mm. At 80 mm HAB, the gas-velocity is 13.4 m/s (44% of the peak velocity) on the centerline and 3.9 m/s at a radius of  $\pm 15$  mm.

Figure 6.6b shows the velocity field of the spray burner with the non-reacting ethanol spray. Since the droplets cause strong scattering of the laser light, the scattered light intensity of the DEHS oil droplets is exceeded by several orders of magnitude. Thus, the aperture of the PIV camera was decreased from 1.8 to 16 and the PIV evaluation was performed based on the ethanol droplets. In consequence, only the primary flow field could be evaluated, as there were too few ethanol droplets in the surrounding area to enable a profound evaluation of the secondary flow. The determined peak velocity of the ethanol spray is 45 m/s and the spray cone is narrower compared to the one of the airflow shown in Figure 6.6a. At 80 mm HAB, the droplet velocity has decreased to 14.5 m/s (32%). Table 6.5 lists all peak values of the measured gas and droplet velocities.

Table 6.5: Summary of measured peak velocities of the non-reacting flow field of the IUTA spray burner determined by PIV with and without the shielding quartz inliner. See Table A3.8 in the appendix for a complete overview of all relevant PIV results obtained at the spray burner.

Channel	Measured maximum velocity / m/s	
	without inliner	with inliner
Coflow	7.6	7.4
Pilot mix	2.5	1.9
Window flush	4.4	2.2
All channels without ethanol	33	30
Ethanol spray	48	45

The results of the PIV measurements of the non-reacting ethanol spray provide the opportunity to validate the LED-based measurement technique developed at the IVG [95, 96]. The technique enables the determination of droplet velocities illuminated with a pulse train of a RGB LED based on single particle tracking velocimetry (PTV). In my examinations, RGB-PTV was applied for the first time to a pilot-scale spray burner. For this, I worked on the advancement of the post-processing initiated by Jan Menser and developed a Matlab script that performs all required processing steps from the raw image to the determination of the final droplet-velocity distribution (Table A4.6).

With the setup described in chapter 6.2.2, the ethanol spray of the spray burner was investigated without any optical magnification, first. However, the droplet clouds were too dense for single particle tracking and the alternative method to determine the spray front propagation demonstrated by Menser on a gasoline direct-injection spray for an internal combustion engine [96] could not be applied because the spray burner is operated continuously. Therefore, by installing a bellows between camera and lens, optical magnification by a factor of 3.4 was achieved. Nevertheless, the spray close to the nozzle was still too dense to track individual particles, which necessitates to move the measurement region further downstream to  $HAB = 80$  mm.

To correlate the red, green, and blue (RGB) shadows of the individual droplets (Figure 2.5), a license-free particle-tracking algorithm (SimpleTracker) is utilized in the Matlab evaluation. SimpleTracker requires the specification of a value for the so-called maximum linking distance between each RGB shadow corresponding to its droplet trajectory. This value needs to be adapted according to the distance of the RGB-shadows on the images that depend on the time step between the individual LED pulses. The latter was optimized in the experiment to cover a droplet-velocity range between zero and 30 m/s according to the results known from PIV. If the time step would be too large, the tracking algorithm would no longer be able to assign the corresponding droplet-shadows on the image to a physically reasonable trajectory. Therefore, this time step must be as small as possible but on the other hand large enough so that low-speed droplets are not superimposed on the image. Accordingly, the value for the maximum linking distance must be as low as possible, too, to avoid the tracking algorithm skipping from one droplet trajectory to another. Another solution to assure correct droplet-to-trajectory assignment would be to further reduce the density of the investigated spray, i.e. move the field of view further downstream to less-dense regions. However, for measurements at HABs larger than 85 mm, no PIV data is available for comparison, so the compromise was chosen to set the maximum linking distance to 70 pixel (0.11 mm), which results in a maximum detectable velocity limit of 22.7 m/s. Figure 6.7 shows the distribution of the evaluated velocity magnitude of more than twelve thousand single droplets at 80 mm HAB.

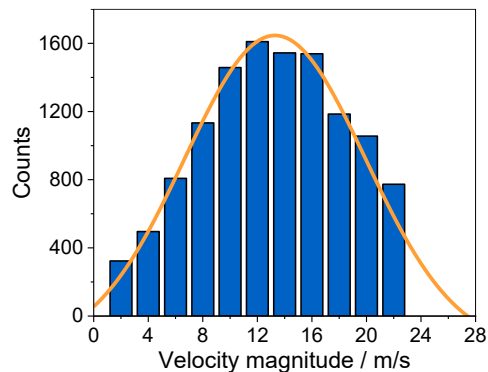


Figure 6.7: Droplet velocity distribution determined by RGB-PTV from more than 12,000 single droplets at  $HAB = 80$  mm. The pilot-scale spray burner was operated according to the parameters in Table 6.4. The mean velocity is 13.3 m/s with a standard deviation of 6.6 m/s according to the Gaussian fit.

With RGB-PTV, a mean droplet velocity of 13.3 m/s is found. This result can be compared with the PIV results discussed on the preceding pages. In Table 6.6, the mean velocities are summarized derived from both measurement techniques. The difference between the measured velocities is 1.2 m/s that corresponds to an 8.3% higher droplet velocity measured with PIV. However, since the velocity distri-

bution shown in Figure 6.7 is truncated on the right side due to shortcomings of the utilized particle-tracking algorithm SimpleTracker, the mean velocity derived by the Gaussian fit is biased and shifted to lower values. It is expected that a more sophisticated tracking algorithm optimized for the present application provides a complete velocity distribution, leading to an overall higher mean droplet velocity. Thus, the results of RGB-PTV are considered validated.

Table 6.6: Comparison of the spatially averaged droplet velocities measured by PIV and RGB-PTV. The listed PIV results are spatially averaged according to the field of view investigated by RGB-PTV.

PIV	RGB-PTV	$\Delta v$	$\Delta v_{rel}$
14.5 m/s	13.3 m/s	1.2 m/s	8.3%

### 6.3.2 Temperature imaging with laser sheet correction during nanoparticle synthesis

One of IUTA's current research goals is to produce nanoparticulate iron oxide on the pilot scale with ferromagnetic or superparamagnetic properties and narrow particle-size distribution. While more recent investigations within the SpraySyn project SPP1980 indicate that the final particle-size distribution depends on droplet disruptions caused by micro explosions [303-305], it is currently insufficiently known by which process quantity the proportion of the ferromagnetic phases of iron oxide can be controlled. Based on currently unpublished results, IUTA suggested a set of operating parameters where the oxygen content in the dispersion gas flow is varied (Table 6.7) to study the effect on the proportion of the magnetic phase, i.e., magnetite ( $\text{Fe}_3\text{O}_4$ ) and maghemite ( $\gamma\text{-Fe}_2\text{O}_3$ ), and to reduce the amount of the anti-ferromagnetic hematite ( $\alpha\text{-Fe}_2\text{O}_3$ ). For a better understanding of how chemical routes can be guided by external means favoring desired nanoparticle composition, *in situ* optical diagnostics of temperature and species concentrations can provide valuable data for validating CFD simulations including chemical kinetics and particle formation mechanisms.

Table 6.7: Operating conditions of the IUTA spray burner investigated with multiline NO-LIF thermometry and Fe-LIF at 900 mbar in the IUTA flame reactor. The examined parameters can be grouped into three flames (F1–F3, each with and without precursor) with decreasing oxygen content in the dispersion gas flow.

Spray				Pilot flame				Coflow	Window flushing	Flame
Solvent	Precursor	Dispersion gas		Tracer	Fuel gas	Oxidant				
EtOH g/h	Fe(NO <sub>3</sub> ) mol	N <sub>2</sub> slm	O <sub>2</sub> slm	NO in Ar slm	CH <sub>4</sub> slm	Air slm	O <sub>2</sub> slm	Air slm	N <sub>2</sub> slm	-
500	-	6	12	1	3	20	4	90	100	1
500	-	10	8	1	3	20	4	90	40	2
500	-	18	-	1	3	20	4	90	40	3
500	0.5	6	12	1	3	20	4	90	100	1
500	0.5	10	8	1	3	20	4	90	40	2
500	0.5	18	-	1	3	20	4	90	40	3

The listed flames were investigated using multiline NO-LIF thermometry as well as Fe-LIF for measuring qualitative iron concentrations. As described in chapter 4.3.2 for the IUTA gas burner, the IUTA spray burner could also not be positioned in the reactor concentrically with the quartz inliner. Hence,

the laser sheet could either be guided centrally through the quartz inliner or be guided centrally underneath the spray nozzle. For this reason, again the shortened quartz inliner that begins at the lower edge of the uppermost optical access was used in all experiments below. The laser sheet intensity correction by using two dye cuvettes introduced in chapter 4 was also applied for the LIF measurements on the spray burner. Due to the large number of successful measurements, an analysis of the influence of the laser sheet correction on the resulting temperature field is enabled. To this end, multiline NO-LIF thermometry measurements were evaluated with and without laser sheet correction and to quantify the effect on the retrieved temperature fields. Figure 6.8 shows an example of NO-LIF excitation in the A-X(0,0) band before (a) and after (b) laser sheet correction. At the time of this recording, the reactor windows were already covered by particle deposition.

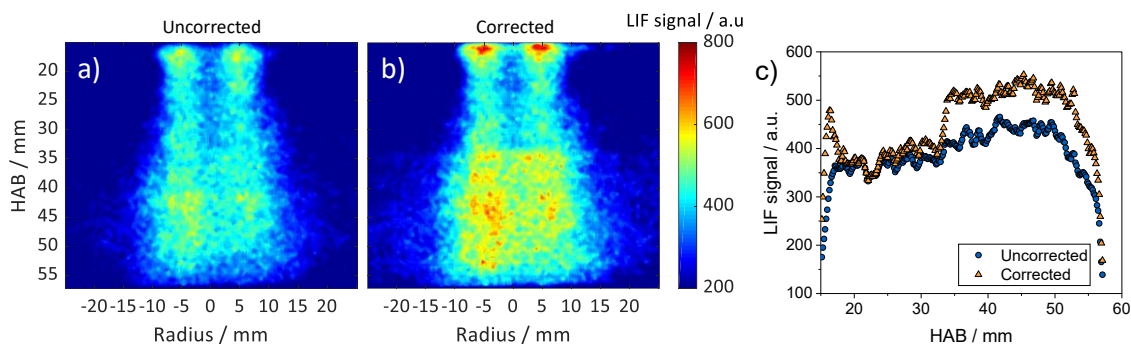


Figure 6.8: NO-LIF signal at  $44,420.9\text{ cm}^{-1}$  (NO A-X(0,0) transitions  $Q_1$ ,  $P_{21}(29.5)$ , and  $R_2(25.5)$  [176]) averaged over 30 single shot images (a) before and (b) after applying the algorithm for laser sheet correction. Axial profiles averaged  $\pm 2\text{ mm}$  around the centerline are shown in (c).

From Figure 6.8 it can be seen that the vertical area between  $\text{HAB} = 18$  and  $33\text{ mm}$  has been corrected less than the rest of the image. This implies that there is less window fouling in this area than in the rest of the window (remember that the laser sheet correction is not single-pixel based but row wise). A correlation to photos showing the window fouling during synthesis exactly at the time of the recording of the NO-LIF signal was not possible with the used setup. However, this observation can be explained by the type of window flushing that is installed at the reactor windows of the IUTA flame reactor. A flow of nitrogen is fed to the reactor through the window flange from the top of the window and hits mainly a single spot on the window, since no additional elements are installed to distribute the window-flushing flow more homogeneously. From observations during the experiments at the IUTA (and from other experiments at the IVG) it is known that this construction mainly reduces particle deposition in the upper third of the window and does neither affect the uppermost millimeters nor the lower half of the window, which coincides with the profiles shown in Figure 6.8c that indicate an almost clean window between 3 and 18 mm (to convert from the HAB scale to the dimensions of the window, the distance of the burner from the upper edge of the window ( $\text{HAB}_{\min} = 15\text{ mm}$ , cf., chapter 6.1 and Figure 4.1) must be subtracted). Several NO-LIF images were examined at different wavelength positions and from different measurements to check for plausibility. Since the signal obtained from the reference cuvette does also not show any comparable features, it is concluded that the calculated correction vectors for each wavelength position are plausible. Suggestions for improving the experimental setup are given in the outlook (section 6.4). Subsequent to the laser sheet correction based on the calculated correction vectors, the temperature field was evaluated using LIFSim. In Figure 6.9, the result (b) is compared with the temperature field determined from the same measurement but without (a) applying the laser sheet correction.

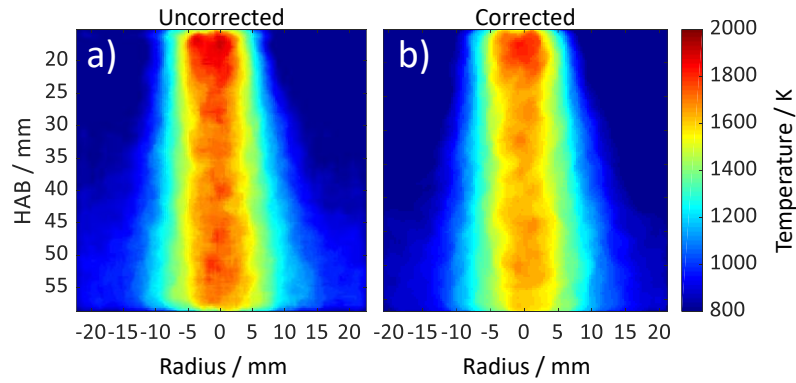


Figure 6.9: Temperature fields of the undoped ethanol spray flame 2 evaluated (a) without correction and (b) after laser sheet correction.

The evaluated temperature fields show a high similarity with regard to the overall temperature distribution. In both temperature fields, the temperature range over 1200 K extends over a diameter of 20 mm along the whole height of the image. In the upper part of the images, the region of temperatures higher 1200 K is narrower than in the lower region, which is consistent with the radially expanding flow with increasing HAB known from the PIV results (Figure 6.6). For a quantitative comparison, axial temperature profiles along the central axis are plotted in Figure 6.10. For all profile plots presented in the following, data was binned  $\pm 1$  mm around the centerline.

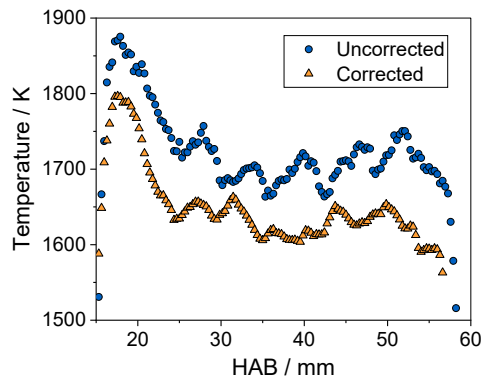


Figure 6.10: Axial temperature profiles taken along the central axis of the undoped ethanol spray flame 2 before and after applying the algorithm for laser sheet correction.

The temperature profile without laser sheet correction (blue circles) shows a 50–100 K higher temperature. The maximum temperature of the corrected profile (orange triangles) is with 1800 K in total 75 K (4%) lower than without laser sheet correction. However, since no single-shot images could be acquired in the experiments, a quantification of regions with different temperature accuracy as presented by Feroughi et al. for the pilot-scale gas burner [170] could not be performed. Hence, it remains unclear whether the discussed temperature difference of 4% lies within the measurement uncertainty. Nevertheless, it can be assumed that the highest measurement accuracy ( $\pm 1.5\%$ ) found by Feroughi et al. for the gas burner along the flame centerline also applies for the spray flame which is why the temperature difference shown in Figure 6.10 is regarded as a result of the laser-sheet correction. In both profiles, the peak temperature is found at 18 mm HAB followed by a downwards-oriented trend towards a local minimum of 1723 K (uncorrected) and 1632 K (corrected) located at 24 mm HAB. The subsequent oscillatory behavior between 25 and 55 mm HAB cannot be physically explained, yet. In general, a smoother trend would be expected for the time-averaged profiles. Since

the corrected profile shows less pronounced features compared to the uncorrected one (and no comparable temperature fluctuations are known from CFD simulations of similar flames), the laser sheet correction is found plausible, even though the question which temperature profile approximates the real process temperature closer cannot be finally determined without comparative results obtained by an independent *in situ* temperature-measurement technique. Consequently, all results presented in this chapter were evaluated with the algorithm for laser sheet correction before the final temperature field was determined using LIFSIm. The results discussed in the following show the comparison with and without iron(III) nitrate precursor for each of the three investigated flames (Table 6.7).

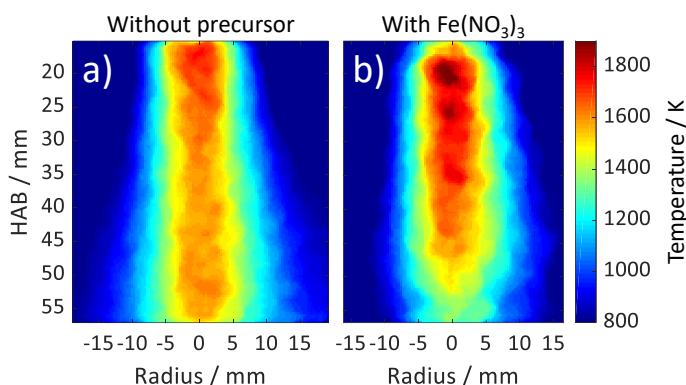


Figure 6.11: Temperature fields of spray flame 1 (Table 6.7) without precursor (a) and with  $\text{Fe}(\text{NO}_3)_3$  as precursor (b).

The highest amount of oxygen in the dispersion gas (66%) is provided in flame 1 where the gas mixture used for spray atomization consists of 12 slm oxygen and 6 slm nitrogen. Figure 6.11 shows the temperature fields of the flame without (a) and with iron(III) nitrate precursor (b). In the precursor-doped case, particles deposited quickly on the reactor windows after adding precursor to the flame, which is why the mass flow of the window flushing was increased to 100 slm nitrogen instead of the commonly used 40 slm. However, it was not possible to keep the windows free of particles. Hence, a low signal to noise ratio due to window fouling was achieved especially on the upper and lower 5 mm of Figure 6.11 (b), i.e., the measured temperatures in these regions should be interpreted with care. The maximum temperatures are reached near the nozzle both with and without precursor.

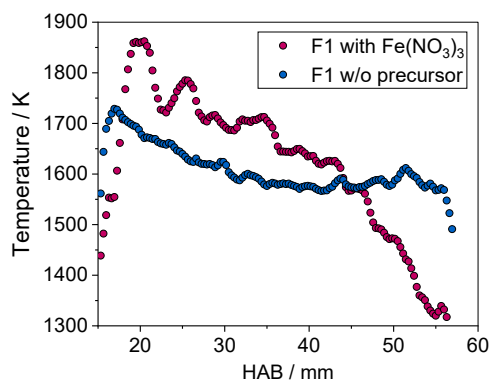


Figure 6.12: Axial temperature profiles of spray flame 1 with and without iron(III) nitrate as precursor.

The hot zone above 1200 K is 2 mm wider in diameter at the precursor-doped flame compared to the precursor-free flame due to the higher overall temperature. Beyond 50 mm HAB, a constriction is apparent in (b) where the hot zone ( $> 1200$  K) is reduced to 9 mm in diameter. This has not been observed in any other measurement and might be related to the 2.5 times higher window-flush flow

compared to flame 2 and 3. However, this is contradicted by the fact that no comparable effect can be identified in the precursor-free flame and thus requires further investigation.

From the axial temperature profiles of flame 1 shown in Figure 6.12 it is found that the peak temperature of the precursor-doped flame is 130 K hotter than the one of the precursor-free flame. One possible explanation for this temperature increase compared to the un-doped case are catalytic cycles of radical recombination occurring during precursor decomposition in the flame that are well known for transition metals like Fe [306]. At 20 mm HAB, a peak temperature of 1860 K is measured for the iron-doped flame. With increasing HAB, the temperature drops and crosses the temperature profile of the undoped flame at 45 mm HAB and 1600 K. Within the whole investigated height of the precursor-doped flame, a temperature drop of 560 K is measured. For the precursor-free flame, the maximum temperature reaches 1728 K located 3 mm closer to the burner mouth compared to the precursor-doped flame. Within 25 mm downstream, the temperature drops to 1575 K and forms a plateau with a mean temperature of 1600 K that extends to the lower end of the field of view.

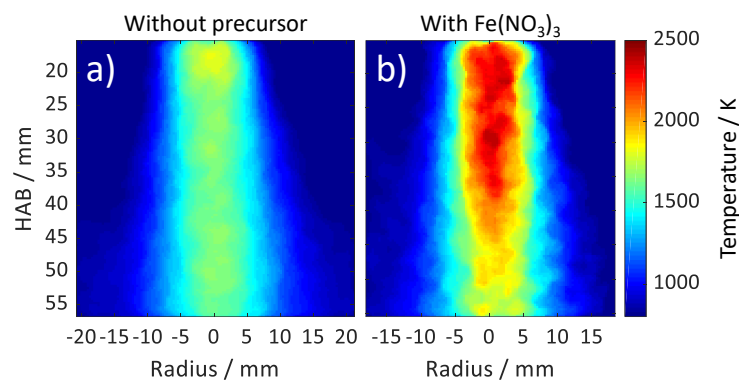


Figure 6.13: Temperature fields of spray flame 2 (Table 6.7) without precursor (a) and with Fe(NO<sub>3</sub>)<sub>3</sub> as precursor (b).

In flame 2 (Figure 6.13) the dispersion gas consists of 8 slm oxygen and 10 slm nitrogen, i.e., the oxygen content in the dispersion gas is 44%. Compared to flame 1, 22% less oxygen is provided to the reaction zone through the dispersion gas channel and an overall 60% lower mass flow rate is fed through the window-flushing ring of the spray burner. Both temperature fields show similar shapes regarding the spatial temperature distribution. Compared to flame 1, the ethanol flame in Figure 6.13a is less than 50 K hotter while the precursor-doped flame is more than 425 K hotter.

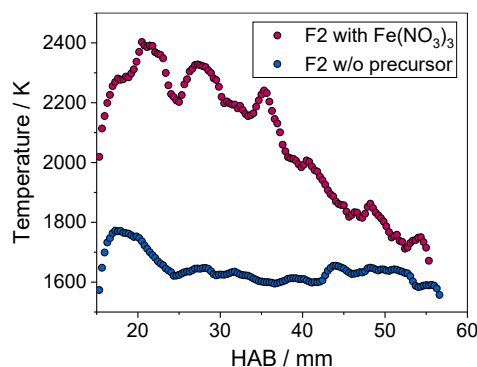


Figure 6.14: Axial temperature profiles of spray flame 2 with and without iron(III) nitrate as precursor.

Overall, a similar trend as in flame 1 can be observed with regard to the axial temperature profiles along the flame centerline (Figure 6.14): The maximum temperatures are reached at 20 mm HAB for

the iron-doped flame with 2400 K and at 17 mm HAB for the undoped flame (1770 K). Thus, the axial difference between both peak temperatures is again 3 mm. Moreover, a steep temperature drop is characteristic for the axial profile of the precursor-doped flame where a difference of 730 K is measured between 20 mm HAB and the end of the field of view at 55 mm HAB. In contrast, the axial profile of the undoped flame shows a temperature decrease of 150 K (from 1770 to 1620 K) between 17 and 24 mm HAB. Further downstream, a plateau with a mean temperature of 1620 K is apparent. Unlike flame 1, the two temperature profiles do not cross within the measuring range but approach a minimum difference of 80 K at 55 mm HAB indicating that the two temperature profiles cross within 60 and 70 mm HAB.

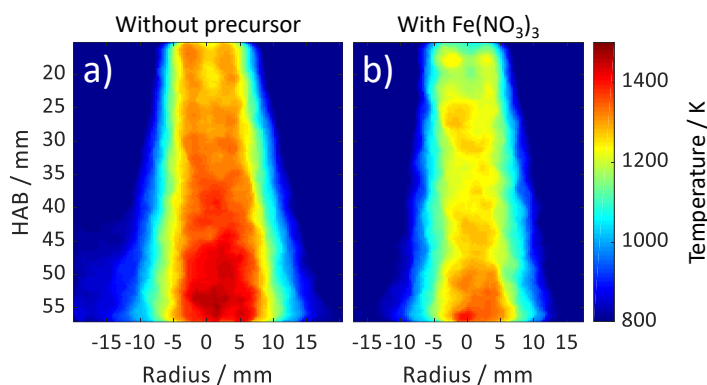


Figure 6.15: Temperature fields of spray flame 3 (Table 6.7) without precursor (a) and with  $\text{Fe}(\text{NO}_3)_3$  as precursor (b).

In flame 3, the dispersion gas consists exclusively of  $\text{N}_2$ . Hence, all oxygen required for the iron-oxide nanoparticle synthesis needs to be taken from the combustion air supply for the pilot flame (mix of 20 slm air and 4 slm oxygen) and from the coflow (90 slm air). Figure 6.15 shows the temperature field of flame 3 without (a) and with iron-nitrate precursor (b) that differs in many aspects from flame 1 and 2. The hot zone ( $> 1200$  K) of the undoped temperature field expands conically with increasing HAB while for the precursor-doped flame this conical shape is less pronounced. In flame 3, the hot zone above 1200 K is several millimeters wider in diameter in the precursor-free case compared to the iron-doped case. In contrast to the other flames, the undoped flame is hotter than the precursor-doped flame and the temperature increases with increasing HAB (Figure 6.16).

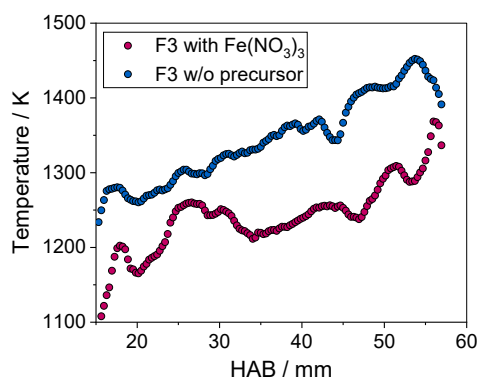


Figure 6.16: Axial temperature profiles of spray flame 3 with and without iron(III) nitrate as precursor.

Both temperature profiles follow a similar trend. In each case, the temperature difference between the undoped and the precursor-doped flame is 100 K on average and the highest temperature is found at 53 mm HAB. Here, a maximum of 1450 K is measured in the undoped flame and a maximum of 1370 K is measured in the iron-doped case at 56 mm HAB. It is assumed that the absolute maximum

temperature of flame 3 is beyond the accessible field of view through the uppermost optical port but above the second highest optical port (note that no flame chemiluminescence of any investigated flame discussed in this thesis was observed through the second highest optical port of the IUTA flame reactor).

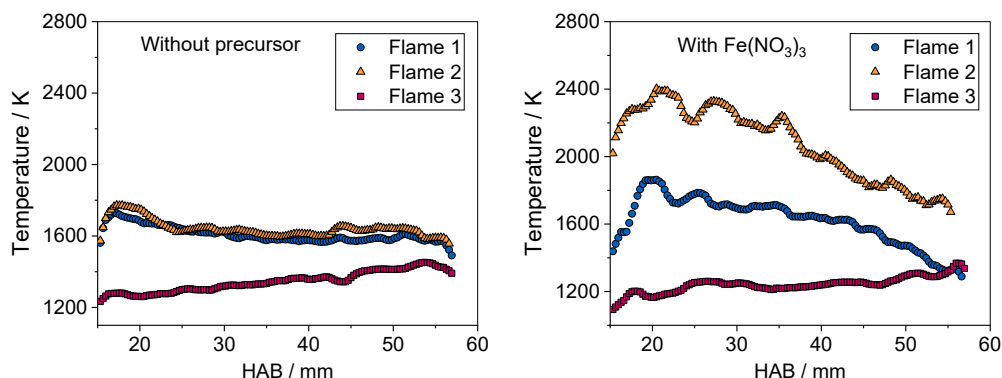


Figure 6.17: Axial temperature profiles of the undoped (left) and precursor-doped flames (right).

To better compare the temperature profiles of the undoped and precursor-doped flames with each other, all have been collected in respective graphs in Figure 6.17. With and without precursor, flame 2 reaches the highest temperatures of all three flames while the overall lowest temperature is measured in flame 3. While the lowest temperature corresponds to the case in which the dispersion gas flow is nitrogen only, the highest temperature is found in the case of 44% oxygen in the dispersion gas flow and therewith not in the case of the highest oxygen amount (66%) as expected intuitively. For the pure ethanol spray flames, it can be seen that the temperature difference between flame 1 and 2 is low pointing to the conclusion that flame 1 and 2 are stoichiometric or oxygen-rich spray flames. However, for more in-depth analysis, CFD simulations are required. For the precursor-doped flames, the temperature profile of flame 1 is located between flame 2 and flame 3 with approximately equal temperature differences to both flames, e.g., at 30 mm HAB, a temperature difference of 450 K to flame 3 and 520 K to flame 2 is found. A possible explanation for this is that the radical recombination described by Linteris et al. [306] is favored at the given oxygen/precursor ratio in flame 2 so that higher temperatures are achieved compared to either higher (flame 1) as well as lower (flame 3) oxygen/precursor ratios. This also indicates that the oxygen content in the dispersion gas plays a significant role in the decomposition of the iron(III) nitrate precursor. From Fe-LIF measurements on a premixed, flat  $\text{H}_2/\text{O}_2$  low-pressure flame (30 mbar) with iron pentacarbonyl ( $\text{Fe}(\text{CO})_5$ ) precursor and corresponding CFD simulations it is known that the iron pentacarbonyl precursor decomposes instantaneously after exiting the burner and forms iron atoms [22, 248]. Within the first millimeters downstream of the burner, homogeneous nucleation of the iron atoms takes place and the first FeO molecules are formed in parallel [60, 167]. As they pass the flame front, the nuclei and FeO molecules disintegrate again until a second nucleation process takes place further downstream enabling the formation of iron-oxide nanoparticles [60]. The subsequent particle growth is based on the agglomeration of iron dimers and iron oxide molecules [123]. In these investigations, addition of iron pentacarbonyl precursor to the flame is correlated with an increase in flame temperature [307], similar to the presented findings on the iron-nitrate doped spray flames.

### 6.3.3 Relative iron concentration during nanoparticle synthesis from iron(III) nitrate

To clarify, whether the iron(III) nitrate precursor investigated in this thesis decomposes in the flame into iron atoms as known for iron pentacarbonyl [60], Fe-LIF measurements were performed *in situ* during nanoparticle synthesis for all three spray flames (Table 6.7). Figure 6.18 shows a simulated NO-LIF spectrum (orange line) fitted to a measured spectrum (maple red symbols). The latter is acquired by scanning the dye laser spectrally over the twelve electronic transitions of the NO molecule in the A–X(0,0) band ( $44407\text{--}44422\text{ cm}^{-1}$ , described in detail in Refs. [22, 176, 181]) during operation of the IUTA flame reactor with the iron-doped spray flame and detecting the spectrally integrated fluorescence signal with the intensified camera (Figure 4.4). Since some transitions cannot be spectrally resolved due to the spectral width of the laser line and the selected step size of the scan, the resulting excitation spectrum shows five characteristic peaks that are utilized for deriving the respective least-squares-fit temperature. Additionally, at about  $225.15\text{ nm}$  ( $44415\text{ cm}^{-1}$ ) the iron-atom line is visible (see black arrow in Figure 6.18) described in detail by Hecht et al. [123].

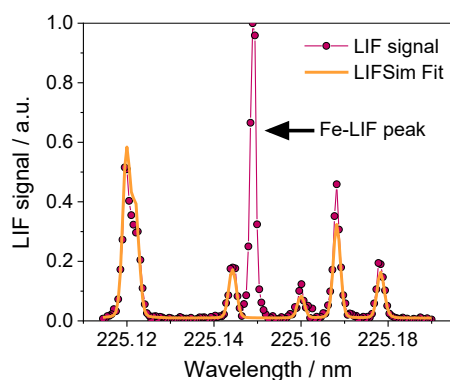


Figure 6.18: NO-LIF spectrum of flame 2 doped with  $\text{Fe}(\text{NO}_3)_3$  showing the iron-atom line ( $3p^63d^64s^2$ -transition [123]) excited at  $225.15\text{ nm}$ .

While the NO-LIF signal – due to the fact that this species is added to the fresh gases – is present, almost everywhere in the flame within the field of view (Figure 6.8), the – reactively generated – Fe-LIF signal is limited to a narrow elongated area centrally below the nozzle (Figure 6.19). This can be explained by the fact that NO is added through the annular gap of the pilot flame gases, while the iron-containing precursor is sprayed centrally into the pilot flame below the burner (compare Figure 6.1).

The results of the Fe-LIF measurements show that  $\text{Fe}(\text{NO}_3)_3$  decomposes to elemental iron in all investigated flames. As depicted in Figure 6.19, the iron atoms are located in the center of the spray flame, comparable to the findings for  $\text{Fe}(\text{CO})_5$  as precursor presented by Feroughi et al. [167]. Among all three flames, the iron-atom distribution of flame 2 is located closest to the burner mouth. An increase of the oxygen content in the dispersion gas from 44% (flame 2) to 66% (flame 1) extends the zone in which iron atoms occur in the axial direction (it should be noted that the window-flushing flow is increased from flame 2 to flame 1 from 40 slm to 100 slm, too). In flame 3 (dispersion gas consists exclusively of nitrogen), the iron-atom distribution extends over the entire measuring range. It is concluded, that the conversion of the iron atoms occurs faster if the dispersion gas is enriched with oxygen, however, certain oxygen/precursor ratios are more preferred with regard to the iron oxidation. Therefore, no clear relation was found between the variation of the oxygen content in the dispersion gas flow and the proportion of magnetite ( $\text{Fe}_3\text{O}_4$ ), maghemite ( $\gamma\text{-Fe}_2\text{O}_3$ ), and hematite ( $\alpha\text{-Fe}_2\text{O}_3$ ) in the final product.

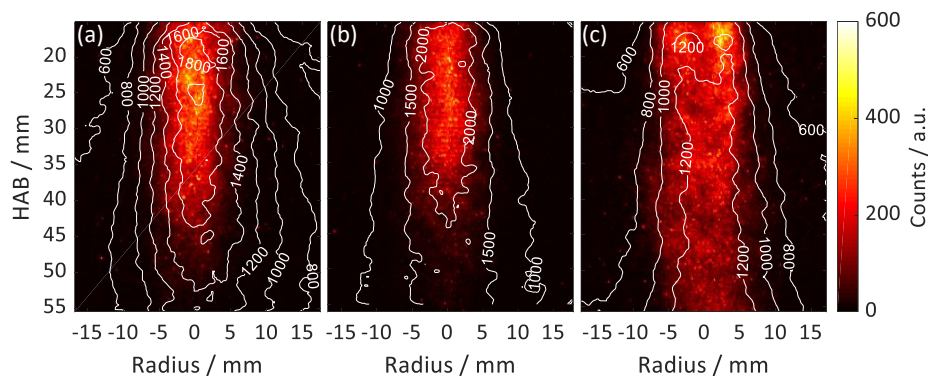


Figure 6.19: Averaged iron atom distributions during synthesis of iron-oxide nanoparticles from iron(III) nitrate dissolved in ethanol. The relative Fe concentration is color-coded while the corresponding temperature is indicated (in Kelvin) by the white iso-lines. The spray burner was operated with decreasing O<sub>2</sub> fraction in the dispersion gas (from left to right): Spray flame 1 with 66% O<sub>2</sub> in the dispersion gas (a), spray flame 2 with 44% O<sub>2</sub> in the dispersion gas (b), and spray flame 3 without O<sub>2</sub> in the dispersion gas (c).

However, a recent study of iron-oxide synthesis from iron(III) nitrate in (ethanol) spray flames shows results, where the hematite/maghemite ratio is tuned by the amount of oxygen in the flame [308]. The authors state that a reduction of oxygen in the flame zone shifts the phase ratio towards maghemite while oxygen-rich conditions shift the ratio towards hematite. Nevertheless, since for all pure-alcohol solvents investigated by Sorvali et al., both phases remain present in notable proportions, it is assumed that the overall oxygen amount in the spray flames investigated in this thesis was too high for all three parameter sets (Table 6.7) to see an effect on the phase ratio in the final product. Thus, further investigations are suggested in the outlook (chapter 6.4).

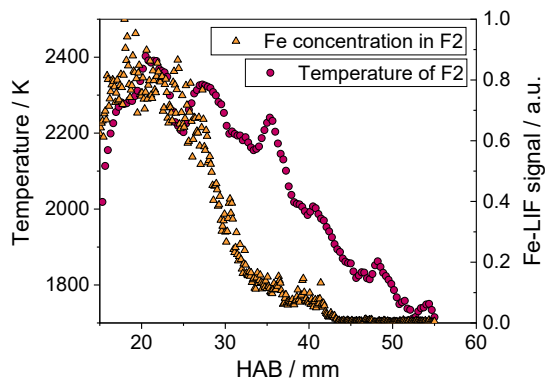
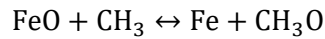
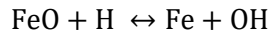
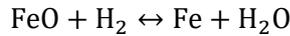


Figure 6.20: Axial profiles of the gas-phase temperature and the relative iron-atom concentration along the centerline of flame 2.

In order to investigate the correlation between the decomposition of the precursor and the measured temperature, an axial profile of the iron-atom distribution was extracted from the Fe-LIF image of flame 2 and plotted together with the corresponding axial temperature profile in Figure 6.20. Both profiles follow a similar trend. Iron atoms were mainly found up to HAB = 32 mm. About 2 mm behind the highest iron-atom concentration, the maximum temperature is reached. With increasing distance to the burner, the concentration of iron atoms decreases followed by a much shallower decrease of the temperature profile, indicating that exothermic chemical reactions are interlinked to the precursor conversion. Since the initial research question aimed at whether the iron(III) nitrate precursor decomposes to atomic iron, no further evaluations were performed and no quantification of the iron-atom concentration was required. Subsequently, instantaneous precursor decomposition after droplet evaporation is suggested according to Nanjajah et al. [309]:



As proposed in their mechanism for the  $\text{Fe}(\text{CO})_5$  precursor decomposition [310], iron-atoms are formed by reduction of FeO, e.g.,



Together with the iron sub-mechanism by Feroughi et al. [167] and the ethanol sub-mechanism by Olm et al. [311], these findings enable CFD simulations of iron-oxide particle formation in spray flames using iron(III) nitrate precursor.

## 6.4 Outlook

Since the gas-phase velocity could not be measured with the utilized setup when the burner was operated with the ethanol spray, additional PIV measurements with fluorescing seeding particles should be performed. To clarify whether helical flows are present and to which extent recirculation and vortices facilitate particle recirculation during synthesis, further measurements should be performed. Therefore, PIV measurements from additional perspectives (e.g., additional positions from the side, measurements from below the spray burner, or tomographic PIV) and CFD simulations are required. Moreover, since it was found that for the isolated operation of the window-flushing ring that the mass flow is insufficiently high to keep the total height of the uppermost optical access of the IUTA flame reactor free of particle deposition during synthesis, CFD simulations should be performed to study window fouling on the quartz inliner for different geometries. Whether an increase of the window-flushing mass flow (however, consider the influence on the particle synthesis) or whether higher (and more uniformly distributed) outlet velocities can be achieved by an optimized geometry of the window-flushing ring should be checked experimentally in parallel.

Since shortcomings in the currently implemented particle tracking algorithm (SimpleTracker) utilized in the image post-processing led to a truncated velocity distribution, SimpleTracker should be replaced in a first step by one of the more advanced algorithms discussed and compared for instance in Refs. [244, 312-314]. In a second step, the performance of the code should be investigated to enable faster post-processing of the images (currently, almost three hours processing time are required for each 12 MPx image). In the experiment, a higher optical magnification would enable measuring closer to the burner where the spray is denser.

The presented setup for laser sheet correction during NO-LIF measurements does not allow for assigning photos that show the window fouling during the synthesis to the laser sheet-fluorescence measurements of the dye cuvettes. Hence, the calculated correction vectors at each wavelength position could not be investigated in more detail with regard to plausibility. Future work should extend the present setup (chapter 3.3.2) by two photo cameras that take one photo each of the entrance and exit windows at each wavelength position of the laser during the scan. That way, the calculated correction vectors can be evaluated more in detail and the Matlab code can be further improved. However, it should be noted that a stronger or weaker apparent window fouling in the visible wavelength range does not allow direct conclusions on the laser sheet intensity without an investigation

of the spectroscopic properties of the window-contaminating particles. Independent of these suggestions, an improved window flushing system should be developed and installed at the IUTA flame reactor. To determine the regions in the temperature fields of the spray flame where different measurement accuracies are present, the effect of fluctuations on the time-averaged temperature fields should be quantified following the procedure presented by Feroughi et al. for the pilot-scale gas burner [170]. Moreover, it is emphasized that the question, which of the temperature profiles shown in Figure 6.10 approximates closer to the real process temperature cannot be finally assessed without comparative results obtained by another *in situ* temperature-measurement technique, e.g., by Raman scattering [21].

Based on the finding of iron atoms in the spray flame doped with iron(III) nitrate, large-eddy simulations of iron-oxide nanoparticle synthesis should be performed following the approach presented by Rittler et al. [315]. In future project phases, the experimental setup should be extended to enable quantitative concentration measurements, e.g., by measuring the effective fluorescence lifetime [316] or by generating a saturation curve for the measured LIF-signal intensities [317]. These measurements should be performed on optimized operating conditions of the spray flame considering the recent findings by Sorvali et al. [308]. The achieved results will significantly contribute to the understanding of phase-pure iron-oxide nanoparticle synthesis and can be used for further development and validation of CFD simulations of iron-oxide nanoparticle synthesis in spray flames.

## 7 Conclusions

Although flame-based nanoparticle synthesis has been successfully investigated for more than two decades and exceptional progress has been achieved in producing nanoparticles with narrow size distribution and selected materials properties, still great research potential exists, e.g.:

- In understanding the reaction mechanisms occurring between precursor decomposition and the formation of first nuclei from which the nanoparticles are formed
- In accessing the complex sub-processes of (spray-) flame synthesis of tailored nanoparticles and materials compositions experimentally and numerically
- For increasing the nanoparticle production rate from laboratory scale to pilot scale while maintaining the desired materials properties
- Towards detailed CFD simulations of nanoparticle synthesis covering all steps of (spray-) flame synthesis.

Therefore, in this work, optical *in situ* diagnostics have been applied to characterize lab-scale and pilot-scale gas and spray burners used for nanoparticle synthesis. For a lab-scale flat-flame gas burner (Figure 3.1), zones of inhomogeneous surface-temperature distributions along the porous bronze were quantified by thermographic imaging for two cooling configurations. With multiline NO-LIF thermometry, spatially resolved temperature fields were measured during the synthesis of iron-oxide and tungsten-oxide nanoparticles. A slight temperature increase with increasing precursor concentration was found within the first 5 mm height above the burner and a clear correlation between the radial temperature distribution of the porous bronze and the gas-phase temperature was observed. These results extend the range of boundary conditions used so far for CFD simulations and showed that a (simulation-aided) development of improved cooling designs is required. Since the presented two-dimensional temperature fields of the iron-doped and tungsten-doped flames complement one another with the findings on nanoparticle formation and growth presented in Refs. [60, 248], the results contribute to future development of kinetic models as well as reaction mechanisms required for more-detailed process understanding of tailored nanoparticle synthesis from the gas-phase.

For a pilot-scale gas burner (Figure 4.2), gas-phase velocity measurements have been performed by PIV in the non-reacting (cold) flow. Peak velocities of 12 m/s were measured and it was found that the flow through the central fuel-gas channel is hardly affected by flow emanating from the surrounding (separation-gas) channel for mass flows below 15 slm. The results show asymmetries and recirculation zones for coflow rates below 250 slm that may affect the final materials produced. Multiple operating parameters have been investigated whereby a broad range of boundary conditions was acquired enabling CFD simulations of the pilot-scale gas burner. To correct for laser-sheet absorption due to particle deposition on the optical ports of the IUTA flame reactor, a setup that enhances the conventional multiline NO-LIF thermometry [22, 61, 180, 253] by two dye cuvettes and two additional cameras has been developed together with a corresponding Matlab evaluation. During synthesis of titania particles, a proof-of-principle temperature measurement was successfully demonstrated and the influence of the laser-sheet-attenuation correction on the temperature field was discussed, however, only a minor effect on the final temperature was found. The temperature measurement enables validating future CFD simulations of nanoparticle synthesis with the pilot-scale burner. Based on these results, operating conditions can be optimized and an improved burner geometry can be developed that are major steps towards higher production rates.

For a lab-scale spray burner (SpraySyn burner, cf., Figure 5.1), a standardized optical flame benchmark has been developed that ensures correct burner operation across laboratories [26]. Therewith, the required basis for comparing experimental and numerical results from various research groups with one another is established, which yields great potential for major research progress in the field of materials synthesis in spray flames. To characterize the flow of the SpraySyn burner, droplet size and velocity measurements using Phase Doppler Anemometry have been performed for four different solvents. Together with the results acquired in the ethanol spray flame, these detailed investigations provided the fundamentally required boundary conditions that have enabled CFD simulations of the SpraySyn burner [293]. Since the benchmarks of the investigated flames match the specified tolerances of the reference flames, all results of the PDA measurements presented in this work are qualified as representative contribution to the SpraySyn database [280]. Thus, the achieved valuable key quantities provide a first step towards a comprehensive characterization of the SpraySyn burner aiming for a deeper understanding of tailored nanoparticle synthesis in spray flames.

For a pilot-scale spray burner (Figure 6.1), numerous gas-phase and liquid-phase velocity fields have been derived for non-reacting (cold) operation using PIV. Without spray, a peak gas-phase velocity of 30.4 m/s was measured while at operation with ethanol spray, a peak droplet velocity of 45 m/s was found. From isolated operation of the flow emanating from the window-flushing ring, it is concluded that the investigated mass flow is insufficient to prevent particle deposition on the quartz inliner around the uppermost optical access of the IUTA flame reactor during synthesis. The PIV results provide important boundary conditions that have enabled CFD simulations of the non-reacting flow of the IUTA spray burner as well as iron-oxide synthesis from iron pentacarbonyl [315, 318]. Additionally, droplet velocities were measured by a LED-based shadowgraphic technique and particle-tracking velocimetry (RGB-PTV) that were for the first time validated by the PIV results. During iron-oxide particle synthesis from iron(III) nitrate, temperature fields were measured *in situ* using multiline NO-LIF thermometry and the correction for spatial variation in laser-sheet attenuation. For the spray flame, 75 K (4%) lower peak temperatures were found along the flame centerline compared to the uncorrected measurements. For validation, additional *in situ* measurements with another suitable optical measurement technique (cf., Table 2.1) are required. However, the results show an influence of the oxygen content in the dispersion gas on the temperature and the iron-atom distribution measured with Fe-LIF. At 44% oxygen in the dispersion gas, iron atoms were found least far away from the burner (only up to HAB = 32 mm) and the highest flame temperatures were measured reaching up to 2400 K. Since the results show that iron(III) nitrate decomposes into iron atoms as known for iron pentacarbonyl [60], a reaction mechanism for  $\text{Fe}(\text{NO}_3)_3$  can be developed. Hence, the achieved results provide a decisive step towards the fundamental understanding and comprehensive simulation of iron-oxide nanoparticle synthesis in spray flames.

This work has contributed to an advancement of optical *in situ* diagnostics in the field of gas-phase synthesis of functional nanoparticles and provides a database for the optimization of cooling designs, burner designs, and operating conditions, thus further advancing up-scaling of tailored nanoparticle synthesis. The developed standardized flame benchmark is expected to lead to rapid progress in the investigation of spray-flame synthesis across laboratories. The experimental results provided the boundary conditions required for enabling CFD simulations of lab-scale and pilot-scale (spray) burners and supported the development of a reaction mechanism.

## References

- [1] M.C. Roco, *Building Foundational Knowledge and Infrastructure for Nanotechnology: 2000– 2030, Nanotechnology: Delivering on the Promise Volume 1*. ACS Publications (2016) 39-52.
- [2] A.L. Porter, J. Youtie, *Where does nanotechnology belong in the map of science?*. *Nature Nanotechnology* 4 (2009) 534-536.
- [3] Bundesministerium für Bildung und Forschung, *nano.DE-Report 2013*. BMBF, Bonn (2014).
- [4] K. Wegner, S. Pratsinis, M. Köhler, *Winnacker - Kuchler: Chemische Technik: Prozesse und Produkte, Band 2: Neue Technologien*. 1<sup>st</sup> ed., Wiley-VCH, Weinheim (2004).
- [5] F.J. Heiligtag, M. Niederberger, *The fascinating world of nanoparticle research*. *Materials Today* 16 (2013) 262-271.
- [6] W.J. Stark, P.R. Stoessel, W. Wohlleben, A. Hafner, *Industrial applications of nanoparticles*. *Chemical Society Reviews* 44 (2015) 5793-5805.
- [7] C. Schulz, T. Dreier, M. Fikri, H. Wiggers, *Gas-phase synthesis of functional nanomaterials: Challenges to kinetics, diagnostics, and process development*. *Proceedings of the Combustion Institute* 37 (2018) 83-108.
- [8] C. Bréchnignac, P. Houdy, M. Lahmani (editors), *Nanomaterials and nanochemistry*. 1<sup>st</sup> ed., Springer, Berlin (2007).
- [9] A. Lorke, M. Winterer, R. Schmechel, C. Schulz, *Nanoparticles from the Gasphase: Formation, Structure, Properties*. 1<sup>st</sup> ed., Springer, Heidelberg (2012).
- [10] P. Sela, S. Peukert, J. Herzler, M. Fikri, C. Schulz, *Shock-tube study of the decomposition of tetramethylsilane using gas chromatography and high-repetition-rate time-of-flight mass spectrometry*. *Physical Chemistry Chemical Physics* 20 (2018) 10686-10696.
- [11] S. Peukert, J. Herzler, M. Fikri, C. Schulz, *High-Temperature Rate Constants for H+ Tetramethylsilane and H+ Silane and Implications about Structure – Activity Relationships for Silanes*. *International Journal of Chemical Kinetics* 50 (2018) 57-72.
- [12] A.M. Ferris, A.J. Susa, D.F. Davidson, R.K.J.C. Hanson, *High-temperature laminar flame speed measurements in a shock tube*. *Combustion and Flame* 205 (2019) 241-252.
- [13] C. Weise, J. Menser, S. Kaiser, A. Kempf, I. Wlokas, *Numerical investigation of the process steps in a spray flame reactor for nanoparticle synthesis*. *Proceedings of the Combustion Institute* 35 (2015) 2259-2266.
- [14] H. Kronemayer, P. Ifeacho, C. Hecht, T. Dreier, H. Wiggers, C. Schulz, *Gas-temperature imaging in a low-pressure flame reactor for nano-particle synthesis with multi-line NO-LIF thermometry*. *Applied Physics B* 88 (2007) 373-377.
- [15] A. Gupta, P. Ifeacho, C. Schulz, H. Wiggers, *Synthesis of tailored WO<sub>3</sub> and WO<sub>x</sub> (2.9 < x < 3) nanoparticles by adjusting the combustion conditions in a H<sub>2</sub>/O<sub>2</sub>/Ar premixed flame reactor*. *Proceedings of the Combustion Institute* 33 (2011) 1883-1890.
- [16] J. Wei, Y. Ren, Y. Zhang, B. Shi, S. Li, *Effects of temperature-time history on the flame synthesis of nanoparticles in a swirl-stabilized tubular burner with two feeding modes*. *Journal of Aerosol Science* 133 (2019) 72-82.
- [17] A.C. Eckbreth, *Laser Diagnostics for Combustion, Temperature, and Species*. 1<sup>st</sup> ed., Abacus Press, Kent (1988).
- [18] D. Nabagło, T. Kurek, K. Wojdan, *Combustion Process Analysis and Diagnostic Using Optical Flame Scanners in Front-Fired Pulverized Coal Boiler*. *Journal of Energy Resources Technology* 140 (2018) 072003.
- [19] F. Hartmann, S. Buhl, F. Gleiss, P. Barth, M. Schild, S.A. Kaiser, C. Hasse, *Spatially resolved experimental and numerical investigation of the flow through the intake port of an internal combustion engine*. *Oil Gas Science Technology* 71 (2016) 2.
- [20] K. Kohse-Höinghaus, R.S. Barlow, M. Aldén, J. Wolfrum, *Combustion at the focus: laser diagnostics and control*. *Proceedings of the Combustion Institute* 30 (2005) 89-123.
- [21] T. Dreier, C. Schulz, *Laser-based diagnostics in the gas-phase synthesis of inorganic nanoparticles*. *Powder Technol.* 287 (2016) 226–238.

- [22] O.M. Feroughi, *Laserinduzierte Fluoreszenz zur abbildenden In-situ-Messung der Gastemperatur, Eisen- und Siliziumoxidkonzentration in Nanopartikelsynthesereaktoren*. Cuvillier, Göttingen, Germany (2016).
- [23] P. Roth, *Particle synthesis in flames*. Proceedings of the Combustion Institute 31 (2007) 1773-1788.
- [24] H. Wiggers, M. Fikri, I. Wlokas, P. Roth, C. Schulz, *Nanoparticles from the Gasphase: Synthesis of tailored nanoparticles in flames: Chemical kinetics, in-situ diagnostics, numerical simulation, and process development*, Springer-Verlag Berlin Heidelberg (2012) 3-48.
- [25] F. Fang, J. Kennedy, E. Manikandan, J. Futter, A. Markwitz, *Morphology and characterization of TiO<sub>2</sub> nanoparticles synthesized by arc discharge*. Chemical Physics Letters 521 (2012) 86-90.
- [26] F. Schneider, S. Suleiman, J. Menser, E. Borukhovich, I. Wlokas, A. Kempf, H. Wiggers, C. Schulz, *SpraySyn – A standardized burner configuration for nanoparticle synthesis in spray flames*. Review of Scientific Instruments 90(8) (2019) 085108.
- [27] C.D. Rosebrock, N. Riefler, T. Wriedt, L. Mädler, S.D. Tse, *Disruptive burning of precursor/solvent droplets in flame-spray synthesis of nanoparticles*. AIChE Journal 59 (2013) 4553-4566.
- [28] S.K. Friedlander, *Smoke, dust, and haze – Fundamentals of Aerosol Dynamics*. 2<sup>nd</sup> ed., Oxford University Press, Oxford (2000).
- [29] W.Y. Teoh, R. Amal, L. Mädler, *Flame spray pyrolysis: An enabling technology for nanoparticles design and fabrication*. Nanoscale 2 (2010) 1324–1347.
- [30] S. Li, Y. Ren, P. Biswas, S.D. Tse, *Flame aerosol synthesis of nanostructured materials and functional devices: Processing, modeling, and diagnostics*. Progress in Energy and Combustion Science 55 (2016) 1–59.
- [31] D.W. Senser, J.S. Morse, V.A. Cundy, *Construction and novel application of a flat flame burner facility to study hazardous waste combustion*. Review of Scientific Instruments 56 (1985) 1279–1284.
- [32] S. Prucker, W. Meier, W. Stricker, *A flat flame burner as calibration source for combustion research: Temperatures and species concentrations of premixed H<sub>2</sub>/air flames*. Review of Scientific Instruments 65 (1994) 2908-2911.
- [33] D. Lindackers, M. Strecker, P. Roth, C. Janzen, S.E. Pratsinis, *Formation and Growth of SiO<sub>2</sub> Particles in Low Pressure H<sub>2</sub>/O<sub>2</sub>/Ar Flames Doped with SiH<sub>4</sub>*. Combustion Science Technology 123 (1997) 287-315.
- [34] See [www.flatflame.com](http://www.flatflame.com) (accessed February 14, 2019) for information about Flat Flame Burners from Holthuis & Associates.
- [35] R. Barlow, R. Dibble, J.-Y. Chen, R. Lucht, *Effect of Damköhler number on superequilibrium OH concentration in turbulent nonpremixed jet flames*. 27<sup>th</sup> Aerospace Sciences Meeting (1990), Reno, USA.
- [36] R.D. Hancock, K.E. Bertagnolli, R.P. Lucht, *Nitrogen and hydrogen CARS temperature measurements in a hydrogen/air flame using a near-adiabatic flat-flame burner*. Combustion and Flame 109 (1997) 323-331.
- [37] M. Wooldridge, P. Torek, M. Donovan, D. Hall, T. Miller, T. Palmer, C. Schrock, *An experimental investigation of gas-phase combustion synthesis of SiO<sub>2</sub> nanoparticles using a multi-element diffusion flame burner*. Combustion and Flame 131 (2002) 98-109.
- [38] R.J. Santoro, H.G. Semerjian, R.A. Dobbins, *Soot particle measurements in diffusion flames*. Combustion and Flame 51 (1983) 203–218.
- [39] D.R. Snelling, K.A. Thomson, G.J. Smallwood, Ö.L. Gülder, *Two-dimensional imaging of soot volume fraction in laminar diffusion flames*. Applied Optics 38 (1999) 2478.
- [40] M.S. Wooldridge, *Gas-phase combustion synthesis of particles*, Progress in Energy Combustion Science 24 (1998) 63-87.
- [41] D. DuFaux, R. Axelbaum, *Nanoscale unagglomerated nonoxide particles from a sodium coflow flame*. Combustion and Flame 100 (1995) 350-358.
- [42] S.E. Pratsinis, W. Zhu, S. Vemury, *The role of gas mixing in flame synthesis of titania powders*. Powder Technology 86 (1996) 87-93.
- [43] K. Wegner, S.E. Pratsinis, *Scale-up of nanoparticle synthesis in diffusion flame reactors*. Chemical Engineering Science 58 (2003) 4581-4589.

- [44] M. Sokolowski, A. Sokolowska, A. Michalski, B. Gokieli, *The “in-flame-reaction” method for Al<sub>2</sub>O<sub>3</sub> aerosol formation*. Journal of Aerosol Science 8 (1977) 219-230.
- [45] J. Tikkanen, K. Gross, C. Berndt, V. Pitkänen, J. Keskinen, S. Raghu, M. Rajala, J. Karthikeyan, *Characteristics of the liquid flame spray process*. Surface Coatings Technology 90 (1997) 210-216.
- [46] J. Karthikeyan, C. Berndt, J. Tikkanen, J. Wang, A. King, H. Herman, *Nanomaterial powders and deposits prepared by flame spray processing of liquid precursors*. Nanostructured Materials 8 (1997) 61-74.
- [47] J. Mäkelä, S. Hellstén, J. Silvonen, M. Vippola, E. Levänen, T. Mäntylä, *Collection of liquid flame spray generated TiO<sub>2</sub> nanoparticles on stainless steel surface*. Materials Letters 60 (2006) 530-534.
- [48] L. Mädler, H. Kammler, R. Mueller, S.E. Pratsinis, *Controlled synthesis of nanostructured particles by flame spray pyrolysis*. Journal of Aerosol Science 33 (2002) 369-389.
- [49] T. Tani, L. Mädler, S.E. Pratsinis, *Homogeneous ZnO nanoparticles by flame spray pyrolysis*. Journal of Nanoparticle Research 4 (2002) 337-343.
- [50] R. Mueller, L. Mädler, S.E. Pratsinis, *Nanoparticle synthesis at high production rates by flame spray pyrolysis*, Chemical Engineering Science 58 (2003) 1969-1976.
- [51] L. Mädler, W.J. Stark, S.E. Pratsinis, *Flame-made Ceria Nanoparticles*. Journal of Materials Research 17 (2002) 1356–1362.
- [52] L. Mädler, W.J. Stark, S.E. Pratsinis, *Simultaneous deposition of Au nanoparticles during flame synthesis of TiO<sub>2</sub> and SiO<sub>2</sub>*, Journal of Materials Research 18 (2003) 115-120.
- [53] Tethis (editor), *NanoPowder Nozzle npn*. Product Catalog from Tethis S.p.A., Milan, Italy (2016).
- [54] J. Menser, S. Kluge, H. Wiggers, T. Dreier, C. Schulz, *Approach to standardize a spray-flame nanoparticle synthesis burner*. 7<sup>th</sup> European Combustion Meeting (2015), Budapest, Hungary.
- [55] F. Schneider, T. Dreier, C. Schulz, *SpraySyn – Standard Burner for the Collaborative Investigation of Spray-Flame Synthesis of Nanoparticles: Droplet Velocity and Size of the Non-Reactive Ethanol Spray*. 9<sup>th</sup> European Combustion Meeting (2019), Lisbon, Portugal.
- [56] F. Schneider, S. Suleiman, I. Wlokas, T. Dreier, H. Wiggers, C. Schulz, *The SpraySyn standard burner enabling coordinated research on materials synthesis in spray flames*. 29. Deutscher Flammentag (2019), Bochum, Germany.
- [57] R. Barlow, J. Frank, *Effects of turbulence on species mass fractions in methane/air jet flames*. Symposium (International) on Combustion 27 (1998) 1087-1095.
- [58] See [www.tnfworkshop.org](http://www.tnfworkshop.org) (accessed February 28, 2020) for information about standardized flames of the International Workshop on Measurement and Computation of Turbulent Flames.
- [59] See <https://ecn.sandia.gov> (accessed February 28, 2020) for information about standardized experiments of the Engine Combustion Network.
- [60] S. Kluge, L. Deng, O. Feroughi, F. Schneider, M. Poliak, A. Fomin, V. Tsionsky, S. Cheskis, I. Wlokas, I. Rahinov, T. Dreier, A. Kempf, H. Wiggers, C. Schulz, *Initial reaction steps during flame synthesis of iron-oxide nanoparticles*. CrystEngComm 17 (2015) 6930–6939.
- [61] R.S. Chrystie, O.M. Feroughi, T. Dreier, C. Schulz, *SiO multi-line laser-induced fluorescence for quantitative temperature imaging in flame-synthesis of nanoparticles*. Applied Physics B 123 (2017) 104.
- [62] K. Hembram, D. Sivaprakasam, T. Rao, K. Wegner, *Large-scale manufacture of ZnO nanorods by flame spray pyrolysis*. Journal of Nanoparticle Research 15 (2013) 1461.
- [63] M. Frenklach, A. Mebel, *On the mechanism of soot nucleation*. Physical Chemistry Chemical Physics 22(9) (2020), 5314-5331.
- [64] R. Koirala, S.E. Pratsinis, A. Baiker, *Synthesis of catalytic materials in flames: opportunities and challenges*. Chemical Society Reviews 45 (2016) 3053-3068.
- [65] M. Sadakata, Y. Xu, A. Harano, *A systematic approach for the design of aerosol reactors*. Powder Technology 88 (1996) 261-266.
- [66] A.J. Gröhn, S.E. Pratsinis, A. Sánchez-Ferrer, R. Mezzenga, K. Wegner, *Scale-up of nanoparticle synthesis by flame spray pyrolysis: the high-temperature particle residence time*. Industrial Engineering Chemistry Research 53 (2014) 10734-10742.
- [67] T. Bolsmann, *Winzige Teile – riesige Hoffnung*. NRZ, Zeitungsverlag Niederrhein, Duisburg (2008-11-26).

- [68] T. Hülser, S.M. Schnurre, H. Wiggers, C. Schulz, *Gas-phase synthesis of nanoscale silicon as an economical route towards sustainable energy technology*, KONA Powder Particle Journal 29 (2011) 191-207.
- [69] S. Mahmoud, G. Nathan, P. Medwell, B. Dally, Z. Alwahabi, *Simultaneous planar measurements of temperature and soot volume fraction in a turbulent non-premixed jet flame*, Proceedings of the Combustion Institute 35 (2015) 1931-1938.
- [70] R. Mansmann, T. Terheiden, P. Schmidt, J. Menser, T. Dreier, T. Endres, C. Schulz, *LIISim: a modular signal processing toolbox for laser-induced incandescence measurements*. Applied Physics B 124 (2018) 69.
- [71] M. Aldén, A. Omrane, M. Richter, G. Särner, *Thermographic phosphors for thermometry: a survey of combustion applications*. Progress in Energy Combustion Science 37 (2011) 422-461.
- [72] C. Tropea, *Optical particle characterization in flows*. Annual Review of Fluid Mechanics 43 (2011) 399-426.
- [73] T.D. Fansler, S.E. Parrish, *Spray measurement technology: a review*. Measurement Science and Technology 26 (2015) 012002.
- [74] C. Liu, L. Xu, *Laser absorption spectroscopy for combustion diagnosis in reactive flows: A review*. Applied Spectroscopy Reviews 54 (2019) 1-44.
- [75] T. Dreier, B. Lange, J. Wolfrum, M. Zahn, F. Behrendt, J. Warnatz, *Comparison of CARS Measurements and Calculations of the Structure of Laminar Methane-Air Counterflow Diffusion Flames*. Berichte der Bunsengesellschaft für Physikalische Chemie 90 (1986) 1010-1015.
- [76] F. Vestin, M. Afzelius, P.-E. Bengtsson, *Development of rotational CARS for combustion diagnostics using a polarization approach*. Proceedings of the Combustion Institute 31 (2007) 833-840.
- [77] S. Roy, J.R. Gord, A.K. Patnaik, *Recent advances in coherent anti-Stokes Raman scattering spectroscopy: Fundamental developments and applications in reacting flows*. Progress in Energy Combustion Science 36 (2010) 280-306.
- [78] W.G. Bessler, C. Schulz, *Quantitative multi-line NO-LIF temperature imaging*. Applied Physics B 78 (2004) 519-533.
- [79] C. Hecht, A. Abdali, T. Dreier, C. Schulz, *Gas-temperature imaging in a microwave-plasma nanoparticle-synthesis reactor using multi-line NO-LIF thermometry*. Zeitschrift für Physikalische Chemie 225 (2011) 1225-1235.
- [80] R.L. Gordon, A.R. Masri, E.J.C. Mastorakos, *Simultaneous Rayleigh temperature, OH- and CH<sub>2</sub>O-LIF imaging of methane jets in a vitiated coflow*. Combustion and Flame 155 (2008) 181-195.
- [81] D. Müller, R. Pagel, A. Burkert, V. Wagner, W. Paa, *Two-dimensional temperature measurements in particle loaded technical flames by filtered Rayleigh scattering*. Applied Optics 53 (2014) 1750-1758.
- [82] X. Zhou, X. Liu, J.B. Jeffries, R. Hanson, *Development of a sensor for temperature and water concentration in combustion gases using a single tunable diode laser*. Measurement Science Technology 14 (2003) 1459.
- [83] E. Bryner, K. Busa, J. McDaniel, C. Goynes, G. Diskin, *Spatially resolved temperature and water vapor concentration distributions in a flat flame burner by tunable diode laser absorption tomography*. 49<sup>th</sup> AIAA Aerospace Sciences Meeting including the New Horizons Forum and Aerospace Exposition (2011). Orlando, USA.
- [84] H.-N. Yang, B. Yang, X.-S. Cai, C. Hecht, T. Dreier, C. Schulz, *Three-Dimensional (3-D) Temperature Measurement in a Low Pressure Flame Reactor Using Multiplexed Tunable Diode Laser Absorption Spectroscopy (TDLAS)*. Lasers in Engineering 31 (2015) 285-297.
- [85] R.B. Miles, W.R. Lempert, J.N. Forkey, *Laser rayleigh scattering*. Measurement Science Technology 12 (2001) R33.
- [86] M. Boguszko, G.S. Elliott, *On the use of filtered Rayleigh scattering for measurements in compressible flows and thermal fields*. Experiments in Fluids 38 (2005) 33-49.
- [87] U. Doll, G. Stockhausen, C. Willert, *Pressure, temperature, and three-component velocity fields by filtered Rayleigh scattering velocimetry*. Optics letters 42 (2017) 3773-3776.

- [88] C. Edwards, R. Rudoff, *Structure of a swirl-stabilized spray flame by imaging, laser doppler velocimetry, and phase doppler anemometry*. Symposium (International) on Combustion (1991) 1353-1359.
- [89] R.K. Abdrakhmanov, B. Boyarshinov, S.Y. Fedorov, *Investigation of the local parameters of a cellular propane/butane/air flame*. International Journal of Heat Mass Transfer 109 (2017) 1172-1180.
- [90] L. Ribarov, J. Wehrmeyer, R. Pitz, R.A. Yetter, *Hydroxyl tagging velocimetry (HTV) in experimental air flows*. Applied Physics B 74 (2002) 175-183.
- [91] S. Wissel, G. Grünefeld, *Flow-field measurements of liquid and gaseous phases in the ultra-dense region of diesel sprays*, Applied Physics B 83 (2006) 181.
- [92] M.A. André, P.M. Bardet, R.A. Burns, P.M. Danehy. *Comparison of Simultaneous PIV and Hydroxyl Tagging Velocimetry in Low Velocity Flows*. 18<sup>th</sup> International Symposium on Applications of Laser and Imaging Techniques to Fluid Mechanics (2016), Lisbon, Portugal.
- [93] R. Adrian, *Particle-imaging techniques for experimental fluid mechanics*. Annual Review of Fluid Mechanics 23 (1991) 261-304.
- [94] J. Westerweel, G.E. Elsinga, R.J. Adrian, *Particle image velocimetry for complex and turbulent flows*. Annual Review of Fluid Mechanics 45 (2013) 409-436.
- [95] J. Menser, T. Dreier, S. Kaiser, C. Schulz, *Multi-pulse RGB illumination and detection for particle tracking velocimetry*. 7<sup>th</sup> European Combustion Meeting (2015), Budapest, Hungary.
- [96] J. Menser, F. Schneider, T. Dreier, S.A. Kaiser, *Multi-pulse shadowgraphic RGB illumination and detection for flow tracking*, Experiments in Fluids 59 (2018) 373.
- [97] C. Geschwindner, P. Kranz, C. Welch, M. Schmidt, B. Böhm, S.A. Kaiser, J. De la Morena, *Analysis of the interaction of Spray G and in-cylinder flow in two optical engines for late gasoline direct injection*. International Journal of Engine Research 21 (2020) 169-184.
- [98] D. Nguyen, D. Honnery, J. Soria, *Measuring evaporation of micro-fuel droplets using magnified DIH and DPIV*. Experiments in fluids 50 (2011) 949-959.
- [99] D. Honnery, D. Nguyen, J. Soria, *Microdroplet evaporation under increasing temperature conditions: Experiments and modelling*. Fuel 105 (2013) 247-257.
- [100] Y. Chen, D.R. Guildenbecher, K.N. Hoffmeister, M.A. Cooper, H.L. Stauffacher, M.S. Oliver, E.B. Washburn, *Study of aluminum particle combustion in solid propellant plumes using digital in-line holography and imaging pyrometry*. Combustion and Flame 182 (2017) 225-237.
- [101] C.T. Chong, S. Hochgreb, *Spray combustion characteristics of palm biodiesel*. Combustion Science Technology 184 (2012) 1093-1107.
- [102] H.C. Rodrigues, M.J. Tummers, E.H. van Veen, D.J. Roekaerts, *Spray flame structure in conventional and hot-diluted combustion regime*, Combustion and Flame 162 (2015) 759-773.
- [103] C. Presser, G. Papadopoulos, J.F. Widmann, *PIV measurements of water mist transport in a homogeneous turbulent flow past an obstacle*, Fire safety journal 41 (2006) 580-604.
- [104] B.P. Husted, P. Petersson, I. Lund, G. Holmstedt, *Comparison of PIV and PDA droplet velocity measurement techniques on two high-pressure water mist nozzles*, Fire safety journal 44 (2009) 1030-1045.
- [105] D. Hofeldt, R.K. Hanson, *Instantaneous imaging of particle size and spatial distribution in two-phase flows*. Applied Optics 30 (1991) 4936-4948.
- [106] Y. Hardalupas, S. Sahu, A.M. Taylor, K. Zarogoulidis, *Simultaneous planar measurement of droplet velocity and size with gas phase velocities in a spray by combined ILIDS and PIV techniques*. Experiments in Fluids 49 (2010) 417-434.
- [107] J. Hayashi, H. Watanabe, R. Kurose, F. Akamatsu, *Effects of fuel droplet size on soot formation in spray flames formed in a laminar counterflow*. Combustion and Flame 158 (2011) 2559-2568.
- [108] F. Meierhofer, M. Hodapp, L. Achelis, L. Buss, D. Noriler, H. Meier, U. Fritsching, *Investigation of atomization concepts for large-scale flame spray pyrolysis (FSP)*. Materialwissenschaft und Werkstofftechnik 45 (2014) 765-778.
- [109] C. Abram, M. Mezhericher, F. Beyrau, H.A. Stone, Y. Ju, *Flame synthesis of nanophosphors using sub-micron aerosols*. Proceedings of the Combustion Institute 37 (2019) 1231-1239.
- [110] R. Hedef, B. Lenze, *Effects of co-and counter-swirl on the droplet characteristics in a spray flame*. Chemical Engineering Processing: Process Intensification 47 (2008) 2209-2217.

- [111] A. Verdier, J.M. Santiago, A. Vandiel, S. Saengkaew, G. Cabot, G. Grehan, B. Renou, *Experimental study of local flame structures and fuel droplet properties of a spray jet flame*. Proceedings of the Combustion Institute 36 (2017) 2595-2602.
- [112] H. Oltmann, J. Reimann, S. Will, *Wide-angle light scattering (WALS) for soot aggregate characterization*. Combustion and Flame 157 (2010) 516-522.
- [113] H. Oltmann, J. Reimann, S. Will, *Single-shot measurement of soot aggregate sizes by wide-angle light scattering (WALS)*. Applied Physics B 106 (2012) 171-183.
- [114] B. Münsterjohann, S. Aßmann, F.J.T. Huber, S. Will, *Spray and Particle Characterization of a Spray Flame Synthesis Process using Wide-Angle Light Scattering (WALS)*. 9<sup>th</sup> European Combustion Meeting (2019), Lisbon, Portugal.
- [115] I. Rahinov, A. Goldman, S. Cheskis, *Intracavity laser absorption spectroscopy and cavity ring-down spectroscopy in low-pressure flames*. Applied Physics B 81 (2005) 143-149.
- [116] G.S. Humphries, I.S. Burns, M. Lengden, *Application of continuous-wave cavity ring-down spectroscopy to laminar flames*. IEEE Photonics Journal 8 (2016) 1-10.
- [117] D.K. Ottesen, D.A. Stephenson, *Fourier transform infrared (FTIR) measurements in sooting flames*. International conference on Fourier Transform Infrared Spectroscopy SPIE Vol. 289 (1981) 223-225.
- [118] O.I. Arabi-Katbi, S.E. Pratsinis, P.W. Morrison Jr, C.M.J.C. Megaridis, *Monitoring the flame synthesis of TiO<sub>2</sub> particles by in-situ FTIR spectroscopy and thermophoretic sampling*. Combustion and Flame 124 (2001) 560-572.
- [119] B. Paul, A. Datta, *FTIR characterization of soot precursor nano-particles from different heights of an isooctane/air premixed flame*. International Journal of Advances in Engineering Sciences Applied Mathematics 6 (2014) 97-105.
- [120] V.M. Baev, T. Latz, P.E. Toschek, *Laser intracavity absorption spectroscopy*. Applied Physics B 69 (1999) 171-202.
- [121] I. Rahinov, A. Fomin, M. Poliak, S. Cheskis, *Absorption electronic spectrum of gaseous FeO: in situ detection with intracavity laser absorption spectroscopy in a nanoparticle-generating flame reactor*. Applied Physics B 117 (2014) 317-323.
- [122] P. Fjodorow, O. Hellmig, V.M. Baev, *A broadband Tm/Ho-doped fiber laser tunable from 1.8 to 2.09 μm for intracavity absorption spectroscopy*. Applied Physics B 124 (2018) 62.
- [123] C. Hecht, H. Kronemayer, T. Dreier, H. Wiggers, C. Schulz, *Imaging measurements of atomic iron concentration with laser-induced fluorescence in a nanoparticle synthesis flame reactor*. Applied Physics B 94 (2008) 119.
- [124] M. Bass, E.W.v. Stryland, D.R. Williams, W.L. Wolfe, *Handbook of Optics – Volume I: Fundamentals, Techniques, & Design*. 2<sup>nd</sup> ed., McGraw-Hill, New York (1995).
- [125] M. Bass, E.W.v. Stryland, D.R. Williams, W.L. Wolfe (editors), *Handbook of Optics – Volume II: Devices, Measurements, & Properties*. 2<sup>nd</sup> ed., McGraw-Hill, New York (1995).
- [126] M. Bass, J.M. Enoch, E.W.v. Stryland, W.L. Wolfe (editors), *Handbook of Optics – Volume III: Classical, Vision, & X-Ray Optics*. 2<sup>nd</sup> ed., McGraw-Hill, New York (2000).
- [127] W. Demtröder, *Experimentalphysik Vol. 2 – Elektrizität und Optik*. 4<sup>th</sup> ed., Springer, Berlin (2006).
- [128] H. Haken, H.C. Wolf, *Atom- und Quantenphysik*. 7<sup>th</sup> ed., Springer, Berlin (2001).
- [129] D. Meschede (editor), *Gerthsen Physik*. 23<sup>rd</sup> ed., Springer, Berlin (2006).
- [130] G. Klages, H.A. Stuart, *Kurzes Lehrbuch der Physik*. 19<sup>th</sup> ed., Springer, Dordrecht (2009).
- [131] H. Haken, H.C. Wolf, *Molekülphysik und Quantenchemie*. 5<sup>th</sup> ed., Springer, Berlin (2006).
- [132] J.R. Albani, *Principles and Applications of Fluorescence Spectroscopy*. 1<sup>st</sup> ed., Blackwell Science, Oxford (2007).
- [133] P. Atkins, J.d. Paula, *Atkins' Physical Chemistry*. 8<sup>th</sup> ed., Oxford University Press, Oxford (2006).
- [134] W. Demtröder, *Laserspektroskopie*. 5<sup>th</sup> ed., Springer, Berlin (2007).
- [135] H. Niedrig (editor), *Bergmann, Schaefer: Lehrbuch der Experimentalphysik – Band 3: Optik*. 10<sup>th</sup> ed., Walter de Gruyter, Berlin (2004).
- [136] J. Eichler, H.J. Eichler, *Laser – Bauformen, Strahlführung, Anwendungen*. 7<sup>th</sup> ed., Springer, Berlin (2010).

- [137] J. Beránek, M. Hugenschmidt, U. Keller, G. Marowky, K. Rohlena, W. Schulz, W. Seelig, P. Simon, U. Sowada, S. Szatmári, J. Uhlenbusch, W. Viöl, R. Wester, *Laser Physics and Applications – Subvolume B: Laser Physics – Part 1 (Landolt-Börnstein)*. 1<sup>st</sup> ed., Springer, Berlin (2007).
- [138] R. Beigang, A. Bruns, E. Gornik, H.-J. Hoffmann, R. Iffländer, K.A. Janulewicz, M.J. Kelley, J. Limpert, G.R. Neil, P.V. Nickles, W. Sandner, A. Tünnermann, H. Wenzel, *Laser Physics and Applications – Subvolume B: Laser Systems – Part 2 (Landolt-Börnstein)*. 1<sup>st</sup> ed., Springer, Berlin (2008).
- [139] J.D. Vincent, S.E. Hodges, J. Vampola, M. Stegall, G. Pierce, *Fundamentals of Infrared and Visible Detector Operation and Testing*. 2<sup>nd</sup> ed., Wiley, Hoboken (2016).
- [140] G.A. Reider, *Photonik - Eine Einführung in die Grundlagen*. 2<sup>nd</sup> ed., Springer, Wien (2005).
- [141] J. Brübach, C. Pflitsch, A. Dreizler, B. Atakan, *On surface temperature measurements with thermographic phosphors: A review*. Progress in Energy Combustion Science 39 (2013) 37-60.
- [142] E. Ring, K. Ammer, *Infrared thermal imaging in medicine*. Physiological measurement 33 (2012) R33.
- [143] B. Lahiri, S. Bagavathiappan, T. Jayakumar, J. Philip, *Medical applications of infrared thermography: A review*. Infrared Physics Technology 55 (2012) 221-235.
- [144] A. Kylili, P.A. Fokaides, P. Christou, S.A. Kalogirou, *Infrared thermography (IRT) applications for building diagnostics: A review*. Applied Energy 134 (2014) 531-549.
- [145] F. Khodayar, S. Sojasi, X. Maldague, *Infrared thermography and NDT: 2050 horizon*. Quantitative InfraRed Thermography Journal 13 (2016) 210-231.
- [146] S. Soldan, G. Bonow, A. Kroll, *RoboGas<sup>Inspector</sup> – A mobile robotic system for remote leak sensing and localization in large industrial environments: Overview and first results*. IFAC Proceedings Volumes 45 (2012) 33-38.
- [147] J. Zalameda, T. Horvath, D. Tomek, A. Tietjen, D. Gibson, D. Mercer, E. Shea, B. Bush, S. Tack, J. Taylor, *Application of a Near Infrared Imaging System for Thermographic Imaging of the Space Shuttle During Hypersonic Re-Entry*. 48<sup>th</sup> AIAA Aerospace Sciences Meeting Including the New Horizons Forum and Aerospace Exposition (2010) Orlando, USA.
- [148] K. Lüders, G. von Oppen, *Bergmann, Schaefer: Lehrbuch der Experimentalphysik – Band 1: Mechanik, Akustik, Wärme*. 12<sup>th</sup> ed., Walter de Gruyter, Berlin (2008).
- [149] Verein Deutscher Ingenieure (VDI-GVC) (editor), *VDI-Wärmeatlas*. 10<sup>th</sup> ed., Springer, Berlin (2006).
- [150] InfraTec (editor), *VarioCAM high resolution Benutzerhandbuch (Stand November 2012)*. InfraTec GmbH, Dresden (2012).
- [151] A. Karim, J.Y. Andersson. *Infrared detectors: Advances, challenges and new technologies*. IOP Conference Series: Materials Science and Engineering (2013) 012001.
- [152] H. Czichos, M. Hennecke (editors), *Hütte - Das Ingenieurwissen*. 33<sup>rd</sup> ed., Springer, Berlin (2007).
- [153] F. Cverna (editor), *ASM ready reference: Thermal properties of metals*. 1<sup>st</sup> ed., ASM International, Russel Township, USA (2002).
- [154] H. Herwig, *Wärmeübertragung A-Z*. 1<sup>st</sup> ed., Springer, Berlin (2000).
- [155] D. May, *Transiente Methoden der Infrarot-Thermografie zur zerstörungsfreien Fehleranalytik in der mikroelektronischen Aufbau- und Verbindungstechnik*. Fakultät für Elektrotechnik und Informationstechnik, Technische Universität Chemnitz, Chemnitz, Germany (2015).
- [156] N. Bauer (editor), *Handbuch zur industriellen Bildverarbeitung: Qualitätssicherung in der Praxis*. 1<sup>st</sup> ed., Fraunhofer IRB Verlag, Stuttgart (2007).
- [157] D.A. Ramirez, J. Shao, M.M. Hayat, S. Krishna, *Midwave infrared quantum dot avalanche photodiode*. Applied Physics Letters 97 (2010) 221106.
- [158] S. Hellström, Z.-H. Chen, Y. Fu, M. Qiu, R. Soltanmoradi, Q. Wang, J. Andersson, *Increased photocurrent in quantum dot infrared photodetector by subwavelength hole array in metal thin film*. Applied Physics Letters 96 (2010) 231110.
- [159] A. Rogalski, *History of infrared detectors*. Opto-Electronics Review 20 (2012) 279-308.
- [160] H. Kronemayer, K. Omerbegovic, C. Schulz, *Quantification of the evaporative cooling in an ethanol spray created by a gasoline direct-injection system measured by multiline NO-LIF gas-temperature imaging*. Applied Optics 46 (2007) 8322-8327.

- [161] J.B. Bell, M.S. Day, J.F. Grcar, W.G. Bessler, C. Schulz, P. Glarborg, A.D. Jensen, *Detailed modeling and laser-induced fluorescence imaging of nitric oxide in a NH<sub>3</sub>-seeded non-premixed methane/air flame*. Proceedings of the Combustion Institute 29 (2002) 2195-2202.
- [162] T. Fujikawa, K. Fukui, Y. Hattori, K. Akihama, *2-D temperature measurements of unburned gas mixture in an engine by two-line excitation LIF technique*. SAE Technical Paper (2006) 2006-01-3336.
- [163] A.T. Hartlieb, B. Atakan, K.J.C. Kohse-Höinghaus, *Effects of a sampling quartz nozzle on the flame structure of a fuel-rich low-pressure propene flame*. Combustion and Flame 121 (2000) 610-624.
- [164] M. Röder, T. Dreier, C. Schulz, *Simultaneous measurement of localized heat-release with OH/CH<sub>2</sub>O-LIF imaging and spatially integrated OH\* chemiluminescence in turbulent swirl flames*. Proceedings of the Combustion Institute 34 (2013) 3549-3556.
- [165] T. Fuyuto, H. Kronemayer, B. Lewerich, W. Koban, K. Akihama, C. Schulz, *Laser-based temperature imaging close to surfaces with toluene and NO-LIF*. Journal of Physics: Conference Series 45(1) (2006) 69.
- [166] R.S. Chrystie, H. Janbazi, T. Dreier, H. Wiggers, I. Wlokas, C. Schulz, *Comparative study of flame-based SiO<sub>2</sub> nanoparticle synthesis from TMS and HMDSO: SiO-LIF concentration measurement and detailed simulation*. Proceedings of the Combustion Institute 37 (2019) 1221-1229.
- [167] O.M. Feroughi, S. Hardt, I. Wlokas, T. Hülser, H. Wiggers, T. Dreier, C. Schulz, *Laser-based in situ measurement and simulation of gas-phase temperature and iron atom concentration in a pilot-plant nanoparticle synthesis reactor*. Proceedings of the Combustion Institute 35 (2014) 2299-2306.
- [168] W.G. Bessler, F. Hildenbrand, C. Schulz, *Two-line laser-induced fluorescence imaging of vibrational temperatures in a NO-seeded flame*. Applied Optics 40 (2001) 748-756.
- [169] J.H. Moore, C.C. Davis, M.A. Coplan, S.C. Greer, *Building scientific apparatus*. 4<sup>th</sup> ed., Cambridge University Press, New York (2009).
- [170] O.M. Feroughi, H. Kronemayer, T. Dreier, C. Schulz, *Effect of fluctuations on time-averaged multi-line NO-LIF thermometry measurements of the gas-phase temperature*. Applied Physics B 120 (2015) 429-440.
- [171] A. Wodtke, L. Huwel, H. Schluter, G. Meijer, P. Andersen, H. Voges, *High-sensitivity detection of NO in a flame using a tunable ArF laser*. Optics Letters 13 (1988) 910-912.
- [172] C. Schulz, V. Sick, J. Heinze, W. Stricker, *Laser-induced-fluorescence detection of nitric oxide in high-pressure flames with A-X(0,2) excitation*. Applied Optics 36 (1997) 3227-3232.
- [173] C. Schulz, V. Sick, U.E. Meier, J. Heinze, W. Stricker, *Quantification of NO A-X(0,2) laser-induced fluorescence: Investigation of calibration and collisional influences in high-pressure flames*, Applied Optics 38 (1999) 1434-1443.
- [174] W.G. Bessler, C. Schulz, T. Lee, J.B. Jeffries, R.K. Hanson, *Laser-induced-fluorescence detection of nitric oxide in high-pressure flames with A-X(0,1) excitation*. Western States Section of the Combustion Institute, Spring Meeting, Second Joint Meeting of the US Sections (2001), Oakland, USA, paper number 2001-239.
- [175] R. Stocker, *Bestimmung verbrennungsrelevanter Größen in Flammen mit laseroptischen Verfahren*. Fakultät für Maschinenwesen, Technische Universität München, Munich, Germany (2004).
- [176] H. Kronemayer, *Laser-based temperature diagnostics in practical combustion systems*. Ruprecht-Karls-Universität Heidelberg, Heidelberg, Germany (2007).
- [177] W.G. Bessler, M. Hofmann, F. Zimmermann, G. Suck, J. Jakobs, S. Nicklitzsch, T. Lee, J. Wolfrum, C. Schulz, *Quantitative in-cylinder NO-LIF imaging in a realistic gasoline engine with spray-guided direct injection*. Proceedings of the Combustion Institute 30 (2005) 2667-2674.
- [178] A.C. Eckbreth, P.A. Bonczyk, J.F. Verdieck, *Laser Raman and Fluorescence Techniques for Practical Combustion Diagnostics*. Applied Spectroscopy Reviews 13(1) (1977) 15-164.
- [179] J.R. Lakowicz, *Principles of fluorescence spectroscopy*. 3<sup>rd</sup> ed., Springer, New York (2006).
- [180] C. Hecht, *Laserspektroskopische Charakterisierung von Reaktionsprozessen zur Gasphasensynthese von Nanopartikeln*. Institute for Combustion and Gas Dynamics – Reactive Fluids, University of Duisburg-Essen, Duisburg, Germany (2011).
- [181] W.G. Bessler, *Quantitative nitric oxide concentration and temperature imaging in flames over a wide pressure range with laser-induced fluorescence*. Ruprecht-Karls-Universität Heidelberg, Heidelberg, Germany (2003).

- [182] A.M.K.P. Taylor (editor), *Instrumentation for flows with combustion*. 1<sup>st</sup> ed., Academic Press, London (1993).
- [183] H. Kronemayer, W. Bessler, C. Schulz, *Gas-phase temperature measurements in evaporating sprays and spray flames based on NO multiline LIF*. Applied Physics B 81 (2005) 1071-1074.
- [184] W. Bessler, T. Lee, C. Schulz, J. Jeffries, R. Hanson, *Strategies for quantitative NO-concentration and temperature measurements by NO LIF in high pressure flames*. 3<sup>rd</sup> Joint Meeting of the US Sections of the Combustion Institute (2003), Chicago, USA.
- [185] W.G. Bessler, C. Schulz, V. Sick, J.W. Daily, *A versatile modeling tool for nitric oxide LIF spectra*. Proceedings of the Third Joint Meeting of the US sections of the Combustion Institute (2003), Chicago, USA.
- [186] L. Araneo, A. Coghe, F. Cozzi, A. Olivani, G. Solero, *Natural Gas Burners for Domestic and Industrial Appliances – Application of the Particle Image Velocimetry (PIV) Technique*. In: A. Schröder, C.E. Willert (editors), *Particle Image Velocimetry*. Topics in Applied Physics 112 (2008), 245-257.
- [187] C. Willert, G. Stockhausen, M. Voges, J. Klinner, R. Schodl, C. Hassa, B. Schürmans, F. Güthe, *Selected applications of planar imaging velocimetry in combustion test facilities*. In: A. Schröder, C.E. Willert (editors), *Particle Image Velocimetry*. Topics in Applied Physics 112 (2008), 283-309.
- [188] Y. Fukuchi, J. Sawada, M. Nakajima, Y. Murakumo, *Development of a new pressure measurement technique and PIV to validate CFD for the aerodynamics of full-scale vehicles*. SAE International Journal of Passenger Cars-Mechanical Systems 9 (2016) 808-816.
- [189] R. Konrath, R. Geisler, J. Agocs, H. Ehlers, F. Philipp, J. Quest, *High-speed PIV applied to wake of NASA CRM model at high Re-number sub- and transonic stall conditions*. CEAS Aeronautical Journal 9 (2018) 339-346.
- [190] S.T. Wereley, C.D. Meinhart, *Recent advances in micro-particle image velocimetry*. Annual Review of Fluid Mechanics 42 (2010) 557-576.
- [191] Q.-Q. Xiong, Z. Chen, S.-W. Li, Y.-D. Wang, J.-H. Xu, *Micro-PIV measurement and CFD simulation of flow field and swirling strength during droplet formation process in a coaxial microchannel*. Chemical Engineering Science 185 (2018) 157-167.
- [192] A. Schröder, C.E. Willert (editors), *Particle Image Velocimetry: New Developments and Recent Applications*. 1<sup>st</sup> ed., Springer, Berlin (2008).
- [193] M. Raffel, C.E. Willert, S.T. Wereley, J. Kompenhans, *Particle Image Velocimetry: A Practical Guide*. 2<sup>nd</sup> ed., Springer, Berlin (2007).
- [194] LaVision (editor), *Double-pulse Nd:YAG Product-Manual*. Manual No. 1003032 (February 9, 2016), LaVision GmbH, Goettingen, Germany (2016).
- [195] A. Voris, L. Riley, P. Puzinauskas, *Characterization of Flow Bench Engine Testing*. 68<sup>th</sup> Annual Meeting of the APS Division of Fluid Dynamics (2015), Boston, USA, L33.005.
- [196] L. Adrian, R.J. Adrian, J. Westerweel, *Particle Image Velocimetry*. 1<sup>st</sup> ed., Cambridge University Press, New York (2011).
- [197] R. Hain, T. Fuchs, L. Wein, T. Kluge, J. Seume, C.J. Kähler, *Stereoscopic PTV measurements in the housing/rotor cavity of a shrouded turbine rotor*. 13<sup>th</sup> International Symposium on Particle Image Velocimetry – ISPIV 2019 (2019), Munich, Germany.
- [198] I. Grant, *Particle Image Velocimetry: A Review*. Proceedings of the Institution of Mechanical Engineers, Part C: Journal of Mechanical Engineering Science 211 (1997) 55-76.
- [199] C. Engel, *Untersuchung der Laufradströmung in einem Radialventilator mittels Particle Image Velocimetry (PIV)*. Department of Mechanical Engineering, University of Duisburg-Essen, Duisburg, Germany (2007).
- [200] C. Kähler, B. Sammler, J. Kompenhans, *Generation and control of tracer particles for optical flow investigations in air*. Experiments in Fluids 33 (2002) 736-742.
- [201] LaVision (editor), *Aerosol Generator Product-Manual*. Manual No. 1003048 (October 7, 2015), LaVision GmbH, Goettingen, Germany (2015).
- [202] R.D. Keane, R.J. Adrian, *Theory of cross-correlation analysis of PIV images*. Applied Scientific Research 49 (1992) 191-215.
- [203] LaVision (editor), *FlowMaster Product-Manual*. Manual No. 1003005 (September 8, 2014), LaVision GmbH, Goettingen, Germany (2014).

- [204] J. Nogueira, A. Lecuona, P. Rodriguez, *Data validation, false vectors correction and derived magnitudes calculation on PIV data*. Measurement Science Technology 8 (1997) 1493.
- [205] C. Young, D. Johnson, E. Weckman, *A model-based validation framework for PIV and PTV*. Experiments in fluids 36 (2004) 23-35.
- [206] B. Wieneke, *PIV uncertainty quantification from correlation statistics*. Measurement Science Technology 26 (2015) 074002.
- [207] A. Sciacchitano, D.R. Neal, B.L. Smith, S.O. Warner, P.P. Vlachos, B. Wieneke, F. Scarano, *Collaborative framework for PIV uncertainty quantification: comparative assessment of methods*. Measurement Science Technology 26 (2015) 074004.
- [208] B. Ruck, *Laser Doppler Anemometry – A non-intrusive optical measuring technique for fluid velocity*. Particle & Particle Systems Characterization 4 (1987) 26-37.
- [209] H.-E. Albrecht, M. Borys, N. Damaschke, C. Tropea, *Laser Doppler and Phase Doppler Measurement Techniques*. 1<sup>st</sup> ed., Springer, Berlin (2003).
- [210] S. Bennett, J.L. Best, *Particle size and velocity discrimination in a sediment-laden turbulent flow using phase Doppler anemometry*. Journal of Fluids Engineering 117 (1995) 505-511.
- [211] M.F. Stodt, J. Kiefer, U. Fritsching, *Ethanol droplet formation, dynamics and combustion mode in the flame of the SpraySyn-nozzle*. Experiments in Fluids 60 (2019) 125.
- [212] A. Kourmatzis, P.X. Pham, A.R. Masri, *Air assisted atomization and spray density characterization of ethanol and a range of biodiesels*. Fuel 108 (2013) 758-770.
- [213] M. Bieber, R. Tischendorf, H.-J. Schmid, M. Reddemann, R. Kneer, *Influence of precursor concentration on spray and particle formation in flame spray pyrolysis*. 29<sup>th</sup> Conference on Liquid Atomization and Spray Systems (2019), Paris, France.
- [214] H.K. Suh, H.G. Roh, C.S. Lee, *Spray and Combustion Characteristics of Biodiesel/Diesel Blended Fuel in a Direct Injection Common-Rail Diesel Engine*. Journal of Engineering for Gas Turbines Power 130 (2008) 032807.
- [215] S. Soid, Z. Zainal, *Spray and combustion characterization for internal combustion engines using optical measuring techniques – A review*. Energy 36 (2011) 724-741.
- [216] M. Koegl, Y.N. Mishra, M. Storch, C. Conrad, E. Berrocal, S. Will, L. Zigan, *Analysis of ethanol and butanol direct-injection spark-ignition sprays using two-phase structured laser illumination planar imaging droplet sizing*. International Journal of Spray Combustion Dynamics 11 (2019) 1756827718772496.
- [217] W.D. Bachalo, C. Sipperley, G. Payne, *Aircraft Icing Research: Challenges in Cloud Simulation and Characterization*. 23<sup>rd</sup> Annual Conference on Liquid Atomization and Spray Systems (2011), Ventura, USA.
- [218] A.C. Heikkila, *Characterization of Marine Stratocumulus Clouds and Aerosol-Cloud Interactions During Oracles*. Department of Atmospheric Sciences, S.O.E.S.T, University of Hawai'i System at Mānoa, Honolulu, USA (2018).
- [219] Z. Zhang, *LDA Application Methods: Laser Doppler Anemometry for Fluid Dynamics*. 1<sup>st</sup> ed., Springer, Heidelberg (2010).
- [220] K. Bauckhage, *The Phase-Doppler-Difference-Method, a New Laser-Doppler Technique for Simultaneous Size and Velocity Measurements – Part 1: Description of the method*. Particle & Particle Systems Characterization 5 (1988) 16-22.
- [221] Dantec Dynamics (editor), *LDA and PDA Reference Manual*. 1<sup>st</sup> ed., Publication No. 9040U1312, Dantec Dynamics A/S, Skovlunde, Denmark (2011).
- [222] F. Durst, M. Zaré. *Laser Doppler measurements in two-phase flows*. LDA Symposium Copenhagen, Denmark (1975) 403–429.
- [223] N. Damaschke, G. Gouesbet, G. Gréhan, H. Mignon, C. Tropea, *Response of phase Doppler anemometer systems to nonspherical droplets*. Applied optics 37 (1998) 1752-1761.
- [224] Dantec Dynamics (editor), *BSA Flow Software User Guide*. Publication No. 9040U5747, Dantec Dynamics A/S, Skovlunde, Denmark (2016).
- [225] R. Kapulla, S.B. Najera, *Influence of user adjustable PDA-parameters on drop size measurements*. 13. Gala - Lasermethoden in der Strömungmesstechnik (2005), Cottbus, Germany.

- [226] J. Grohmann, *Experimentelle Untersuchungen zum Einfluss von Kohlenwasserstoffen auf das Verbrennungsverhalten drallstabilisierter Sprayflammen*. Fakultät für Luft- und Raumfahrttechnik und Geodäsie, University of Stuttgart, Stuttgart, Germany (2019).
- [227] C.F. Edwards, K. Marx, *Analysis of the Ideal Phase-Doppler System: Limitations Imposed by the Single-Particle Constraint*. *Atomization and Sprays* 2 (1991) 319-366.
- [228] A.M. Schmid, *Experimental characterization of the two phase flow of a modern, piezo activated hollow cone injector*. Departement Maschinenbau und Verfahrenstechnik, ETH Zurich, Zurich, Switzerland (2012).
- [229] A. Adamczyk, L. Rimai, *2-Dimensional particle tracking velocimetry (PTV): technique and image processing algorithms*. *Experiments in Fluids* 6 (1988) 373-380.
- [230] W.-H. Tien, P. Kartes, T. Yamasaki, D. Dabiri, *A color-coded backlighted defocusing digital particle image velocimetry system*. *Experiments in Fluids* 44 (2008) 1015-1026.
- [231] A.A. Aguirre-Pablo, M.K. Alarfaj, E.Q. Li, J.F. Hernández-Sánchez, S.T. Thoroddsen, *Tomographic particle image velocimetry using smartphones and colored shadows*. *Scientific Reports* 7 (2017) 1-18.
- [232] C. Willert, B. Stasicki, J. Klinner, S. Moessner, *Pulsed operation of high-power light emitting diodes for imaging flow velocimetry*. *Measurement Science Technology* 21 (2010) 075402.
- [233] C.E. Willert, D.M. Mitchell, J. Soria, *An assessment of high-power light-emitting diodes for high frame rate schlieren imaging*. *Experiments in Fluids* 53 (2012) 413-421.
- [234] LED Engin, RGB LED Emitter LZ4-00MC00, <http://www.ledengin.com/files/products/LZ4/LZ4-00MC00.pdf> (accessed February 2, 2020).
- [235] J. Estevadeordal, L. Goss, *PIV with LED: particle shadow velocimetry (PSV) technique*. 43<sup>rd</sup> AIAA Aerospace Sciences Meeting and Exhibit (2005), Reno, USA.
- [236] R. Summer, *Processing RAW Images in MATLAB*. University of California, Santa Cruz, USA (May 19, 2014).
- [237] D. Coffin, *DCRAW: Decoding raw digital photos in linux*. <https://www.dechifro.org/dcrawl/> (accessed March 25, 2020).
- [238] G. Luijk, *DCRAW Tutorial*. [http://www.guillermoluijk.com/tutorial/dcrawl/index\\_en.htm](http://www.guillermoluijk.com/tutorial/dcrawl/index_en.htm) (accessed February 15, 2020).
- [239] B.E. Bayer, *Color imaging array*. U.S. Patent US3971065A (March 5, 1976).
- [240] L. Goss, J. Estevadeordal, *Parametric characterization for particle-shadow velocimetry (PSV)*. 25<sup>th</sup> AIAA Aerodynamic Measurement Technology and Ground Testing Conference (2006), San Francisco, USA.
- [241] S. Pick, F.-O. Lehmann, *Stereoscopic PIV on multiple color-coded light sheets and its application to axial flow in flapping robotic insect wings*. *Experiments in Fluids* 47 (2009) 1009.
- [242] K. Takehara, T. Etoh, *A study on particle identification in PTV particle mask correlation method*. *Journal of Visualization* 1 (1999) 313-323.
- [243] J.-Y. Tinevez, *SimpleTracker*. <https://www.mathworks.com/matlabcentral/fileexchange/34040-simpletracker> (accessed April 3, 2016).
- [244] C. Manzo, M.F. Garcia-Parajo, *A review of progress in single particle tracking: from methods to biophysical insights*. *Reports on Progress in Physics* 78 (2015) 124601.
- [245] C.S. McEnally, L.D. Pfefferle, B. Atakan, K. Kohse-Höinghaus, *Studies of aromatic hydrocarbon formation mechanisms in flames: Progress towards closing the fuel gap*. *Progress in Energy and Combustion Science* 32 (2006) 247-294.
- [246] F.N. Egolfopoulos, N. Hansen, Y. Ju, K. Kohse-Höinghaus, C.K. Law, F. Qi, *Advances and challenges in laminar flame experiments and implications for combustion chemistry*. *Progress in Energy and Combustion Science* 43 (2014) 36-67.
- [247] M. Campbell, P. Schrader, A. Catalano, K. Johansson, G. Bohlin, N. Richards-Henderson, C. Kliewer, H. Michelsen, *A small porous-plug burner for studies of combustion chemistry and soot formation*. *Review of Scientific Instruments* 88 (2017) 125106.
- [248] S. Kluge, *Massenspektrometrische Untersuchung der Nanopartikelbildung in vorgemischten Niederdruckflammen*. Institute for Combustion and Gas Dynamics – Reactive Fluids, University of Duisburg-Essen, Duisburg, Germany (2016).

- [249] C. Weise, A. Faccinetto, S. Kluge, T. Kasper, H. Wiggers, C. Schulz, I. Wlokas, A. Kempf, *Buoyancy induced limits for nanoparticle synthesis experiments in horizontal premixed low-pressure flat-flame reactors*. Combustion Theory and Modelling 17 (2013) 504-521.
- [250] S. Kluge, H. Wiggers, C. Schulz, *Mass spectrometric analysis of clusters and nanoparticles during the gas-phase synthesis of tungsten oxide*. Proceedings of the Combustion Institute 36 (2017) 1037-1044.
- [251] J. Sellmann, I. Rahinov, S. Kluge, H. Jünger, A. Fomin, S. Cheskis, C. Schulz, H. Wiggers, A. Kempf, I. Wlokas, *Detailed simulation of iron oxide nanoparticle forming flames: Buoyancy and probe effects*. Proceedings of the Combustion Institute 37 (2018) 1241-1248.
- [252] R. Chrystie, F. Ebertz, T. Dreier, C. Schulz, *Strategy for determining absolute concentration levels of SiO in low pressure gas phase synthesis flames for silica nanoparticles*. Laser Applications to Chemical, Security and Environmental Analysis (LACSEA), Paper LW3C.6 (2018), Orlando, USA.
- [253] R.S. Chrystie, F.L. Ebertz, T. Dreier, C. Schulz, *Absolute SiO concentration imaging in low-pressure nanoparticle-synthesis flames via laser-induced fluorescence*. Applied Physics B 125 (2019) 29.
- [254] F. Migliorini, S. De Iulii, F. Cignoli, G. Zizak, *How "flat" is the rich premixed flame produced by your McKenna burner?*. Combustion and Flame 153 (2008) 384-393.
- [255] O.M. Feroughi, L. Deng, S. Kluge, T. Dreier, H. Wiggers, I. Wlokas, C. Schulz, *Experimental and numerical study of a HMDSO-seeded premixed laminar low-pressure flame for SiO<sub>2</sub> nanoparticle synthesis*. Proceedings of the Combustion Institute 36 (2017) 1045-1053.
- [256] S. Pfadler, F. Beyrau, M. Löffler, A. Leipertz, *Application of a beam homogenizer to planar laser diagnostics*. Optics Express 14 (2006) 10171-10180.
- [257] C. Tropea, A.L. Yarin (editors), *Springer Handbook of Experimental Fluid Mechanics*. 1<sup>st</sup> ed., Springer, Berlin (2007).
- [258] T. Kasper, *Molekularstrahlmassenspektrometrie zur Analytik in Flammen oxygenierter Brennstoffe*. Cuvillier, Göttingen, Germany (2007).
- [259] R.W. Pitz, J.A. Wehrmeyer, L.A. Ribarov, D.A. Oguss, F. Batliwala, P.A. DeBarber, S. Deusch, P.E. Dimotakis, *Unseeded molecular flow tagging in cold and hot flows using ozone and hydroxyl tagging velocimetry*. Measurement Science Technology 11 (2000) 1259.
- [260] T. Hülser, M. Spree, S. Schnurre, H. Wiggers, C. Schulz, *Gasphasensynthese von Silicium-Nanopartikeln im Technikumsmaßstab*. Chemie Ingenieur Technik 82 (2010) 1453-1454.
- [261] M. Bigas, E. Cabruja, J. Forest, J. Salvi, *Review of CMOS image sensors*. Microelectronics Journal 37 (2006) 433-451.
- [262] G. Holst, *sCMOS – Die eierlegende Wollmilchsau der Bildsensorik? Neue Joint-Venture Technologie ermöglicht eine Fülle von neuen wissenschaftlichen Kameraanwendungen*. Optik Photonik 4 (2009) 37-39.
- [263] LaVision (editor), *Imager sCMOS Product-Manual*. Manual No. 1006816 (March 17, 2016), LaVision GmbH, Goettingen, Germany (2016).
- [264] LaVision (editor), *FlowMaster Product-Manual for DaVis 8.4*. Manual No. 1003005 (January 20, 2017) LaVision GmbH, Goettingen, Germany (2017).
- [265] B. Wieneke, K. Pfeiffer, *Adaptive PIV with variable interrogation window size and shape*. 15<sup>th</sup> International Symposium on Applications of Laser Techniques to Fluid Mechanics (2010), Lisbon, Portugal.
- [266] LaVision (editor), *Sheet Optics (divergent) Product-Manual*. Manual No. 1003034 (May 4, 2010), LaVision GmbH, Goettingen, Germany (2010).
- [267] LaVision (editor), *Collimator Optics Product-Manual*. Manual No. 1004061 (March 12, 2010), LaVision GmbH, Goettingen, Germany (2010).
- [268] A. Camenzind, R. Strobel, S.E. Pratsinis, *Cubic or monoclinic Y<sub>2</sub>O<sub>3</sub>: Eu<sup>3+</sup> nanoparticles by one step flame spray pyrolysis*. Chemical Physics Letters 415 (2005) 193-197.
- [269] R. Strobel, S.E. Pratsinis, *Flame aerosol synthesis of smart nanostructured materials*. Journal of Materials Chemistry 17 (2007) 4743-4756.
- [270] J.D. Gounder, A. Kourmatzis, A.R. Masri, *Turbulent piloted dilute spray flames: Flow fields and droplet dynamics*. Combustion and Flame 159 (2012) 3372-3397.

- [271] S. Hardt, I. Wlokas, C. Schulz, H. Wiggers, *Impact of ambient pressure on titania nanoparticle formation during spray-flame synthesis*. Journal of Nanoscience and Nanotechnology 15 (2015) 9449-9456.
- [272] M. Hammad, S. Hardt, B. Mues, S. Salamon, J. Landers, I. Slabu, H. Wende, C. Schulz, H. Wiggers, *Gas-phase synthesis of iron oxide nanoparticles for improved magnetic hyperthermia performance*. Journal of Alloys and Compounds 824 (2020) 153814.
- [273] S. Angel, F. Schneider, W. Kaziur-Cegla, T. Schmidt, C. Schulz, H. Wiggers, *Spray-flame synthesis of  $LaMO_3$  ( $M = Mn, Fe, Co$ ) perovskite nanomaterials: Effect of spray droplet size and esterification on particle size distribution*. Proceedings of the Combustion Institute 38 (2020), accepted, in revision.
- [274] S. Angel, J. Neises, M. Dreyer, K. Friedel Ortega, M. Behrens, Y. Wang, H. Arandiyan, C. Schulz, H. Wiggers, *Spray-flame synthesis of  $La(Fe, Co)O_3$  nano-perovskites from metal nitrates*. AIChE Journal 66(1) (2020) e16748.
- [275] B. Alkan, D. Medina, J. Landers, M. Heidelmann, U. Hagemann, S. Salamon, C. Andronescu, H. Wende, C. Schulz, W. Schuhmann, *Spray-Flame-Prepared  $LaCo_{1-x}Fe_xO_3$  Perovskite Nanoparticles as Active OER Catalysts: Influence of Fe Content and Low-Temperature Heating*. ChemElectroChem 7 (2020) 1-12.
- [276] K. Müller-Dethlefs, A. Schlader, *The effect of steam on flame temperature, burning velocity and carbon formation in hydrocarbon flames*. Combustion and Flame 27 (1976) 205-215.
- [277] K. Müller-Dethlefs, M. Péalat, J.P. Taran, *Temperature and Hydrogen Concentration Measurements by CARS in an Ethylene-Air Bunsen Flame*. Berichte der Bunsen-Gesellschaft für physikalische Chemie 85 (1981) 803-807.
- [278] H. Tsuji, *Counterflow diffusion flames*. Progress in Energy and Combustion Science 8 (1982) 93-119.
- [279] A. Abdelsamie, D. Thévenin, *On the behavior of spray combustion in a turbulent spatially-evolving jet investigated by direct numerical simulation*. Proceedings of the Combustion Institute 37(3) (2019) 3373-3382.
- [280] See [www.spraysyn.org](http://www.spraysyn.org) for details on the SpraySyn burner, best-practice rules, operating parameters, and for the SPP1980, funded by the German Research Foundation, DFG (accessed March 1, 2020).
- [281] E.G. Lierke, *Wassertropfen in der Luft*. Tec5 Technical Note, Oberursel, Germany (June 2015).
- [282] A.H. Lefebvre, V.G. McDonell, *Atomization and Sprays*. 2<sup>nd</sup> ed., CRC Press, Boca Raton, USA (2017).
- [283] P.D. Hede, P. Bach, A.D. Jensen, *Two-fluid spray atomisation and pneumatic nozzles for fluid bed coating/agglomeration purposes: A review*. Chemical Engineering Science 63 (2008) 3821-3842.
- [284] W.-Q. Long, H. Ohtsuka, T. Obokata, *Characterization of conical spray flow for diesel engine by means of laser Doppler methods: PDA measurement of droplet size distribution*. JSME International Journal Series B Fluids Thermal Engineering 39(3) (1996) 554-561.
- [285] J. Lasheras, E. Villermaux, E. Hopfinger, *Break-up and atomization of a round water jet by a high-speed annular air jet*. Journal of Fluid Mechanics 357 (1998) 351-379.
- [286] C.M. Varga, J.C. Lasheras, E.J. Hopfinger, *Initial breakup of a small-diameter liquid jet by a high-speed gas stream*. Journal of Fluid Mechanics 497 (2003) 405-434.
- [287] A. Aliseda, E.J. Hopfinger, J.C. Lasheras, D. Kremer, A. Berchielli, E. Connolly, *Atomization of viscous and non-Newtonian liquids by a coaxial, high-speed gas jet. Experiments and droplet size modeling*. International Journal of Multiphase Flow 34 (2008) 161-175.
- [288] P. Thybo, L. Hovgaard, S.K. Andersen, J.S. Lindeløv, *Droplet size measurements for spray dryer scale-up*. Pharmaceutical Development Technology 13 (2008) 93-104.
- [289] M.C. Heine, S.E. Pratsinis, *Droplet and particle dynamics during flame spray synthesis of nanoparticles*. Industrial Engineering Chemistry Research 44 (2005) 6222-6232.
- [290] Dantec Dynamics (editor), *Schulungsmaterial zur Phase Doppler Anemometry*. Oral presentation at the Institute for Combustion and Gas Dynamics – Reactive Fluids on June 5, 2018 by K. Golgiyaz, Dantec Dynamics A/S, Denmark (2018).
- [291] J.C. Lasheras, E. Hopfinger, *Liquid jet instability and atomization in a coaxial gas stream*. Annual Review of Fluid Mechanics 32 (2000) 275-308.

- [292] F.J. Martins, A. Kronenburg, F. Beyrau, *PIV Measurements under Reacting and Non-Reacting Conditions at the Nozzle Outlet of the SPP1980 SpraySyn Burner*. 13<sup>th</sup> International Symposium on Particle Image Velocimetry – ISPIV 2019 (2019), Munich, Germany.
- [293] F.J. Martins, J. Kirchmann, A. Kronenburg, F. Beyrau, *Experimental Investigation of Axisymmetric, Turbulent, Annular Jets Discharged Through the Nozzle of the SPP1980 SpraySyn Burner Under Isothermal and Reacting Conditions*. *Experimental Thermal Fluid Science* 114 (2020) 110052.
- [294] J. Schmidt, H. Boye, *Influence of velocity and size of the droplets on the heat transfer in spray cooling*. *Chemical Engineering Technology: Industrial Chemistry-Plant Equipment-Process Engineering-Biotechnology* 24 (2001) 255-260.
- [295] J. Beck, A. Watkins, *On the development of a spray model based on drop-size moments*. *Proceedings of the Royal Society of London. Series A: Mathematical, Physical Engineering Sciences* 459 (2003) 1365-1394.
- [296] J. Beck, A. Watkins, *The simulation of fuel sprays using the moments of the drop number size distribution*. *International Journal of Engine Research* 5 (2004) 1-21.
- [297] J. Santolaya, L. Aisa, E. Calvo, I. García, J. Garcia, *Analysis by droplet size classes of the liquid flow structure in a pressure swirl hollow cone spray*. *Chemical Engineering Processing: Process Intensification* 49 (2010) 125-131.
- [298] H. Chiu, T. Liu, *Group combustion of liquid droplets*. *Combustion Science Technology* 17 (1977) 127-142.
- [299] J. Stichlmair, *Anwendung der Ähnlichkeitsgesetze bei vollständiger und partieller Ähnlichkeit*. *Chemie Ingenieur Technik* 63 (1991) 38-51.
- [300] A. Maurer, *Grundlagen und experimentelle Untersuchungen zum Zerstäuben von Druckfarben zur Farbdosierung bei Offsetfarbwerken*. Institute for Print and Media Technology, T.U. Chemnitz, Chemnitz, Germany (2003).
- [301] BETE (editor), *XA Low Flow Air Atomizing*. Product catalog for Air Atomizing Nozzle by BETE Deutschland GmbH, Bochum, Germany (2017) 72-78.
- [302] BETE (editor), *XA sr*. Product catalog for Air Atomizing Nozzle by BETE Deutschland GmbH, Bochum, Germany (2017) 105.
- [303] C.D. Rosebrock, T. Wriedt, L. Mädler, K. Wegner, *The role of microexplosions in flame spray synthesis for homogeneous nanopowders from low-cost metal precursors*. *AIChE Journal* 62 (2016) 381-391.
- [304] H. Li, C. Rosebrock, N. Riefler, T. Wriedt, L. Mädler, *Experimental investigation on microexplosion of single isolated burning droplets containing titanium tetraisopropoxide for nanoparticle production*. *Proceedings of the Combustion Institute* 36 (2017) 1011-1018.
- [305] H. Li, C.D. Rosebrock, Y. Wu, T. Wriedt, L. Mädler, *Single droplet combustion of precursor/solvent solutions for nanoparticle production: Optical diagnostics on single isolated burning droplets with micro-explosions*. *Proceedings of the Combustion Institute* 37 (2019) 1203-1211.
- [306] G.T. Linteris, M.D. Rumminger, V.I. Babushok, *Catalytic inhibition of laminar flames by transition metal compounds*. *Progress in Energy Combustion Science* 34 (2008) 288-329.
- [307] S. Staude, C. Hecht, I. Wlokas, C. Schulz, B. Atakan, *Experimental and numerical investigation of Fe(CO)<sub>5</sub> addition to a laminar premixed hydrogen/oxygen/argon flame*. *Zeitschrift für physikalische Chemie* 223 (2009) 639-649.
- [308] M. Sorvali, M. Nikka, P. Juuti, M. Honkanen, T. Salminen, L. Hyvärinen, J.M. Mäkelä, *Controlling the phase of iron oxide nanoparticles fabricated from iron(III) nitrate by liquid flame spray*. *International Journal of Ceramic Engineering Science* 1 (2019) 194-205.
- [309] M. Nanjaiah, H. Jünger, M.R. Lalanne, I. Rahinov, A. Kempf, I. Wlokas, *Detailed and Reduced Reaction Schemes for Iron Oxide Nanoparticle Synthesis Flames*. Oral presentation at the 17<sup>th</sup> International Conference on Numerical Combustion (2019), Aachen, Germany.
- [310] I. Wlokas, A. Faccinetto, B. Tribalet, C. Schulz, A. Kempf, *Mechanism of Iron Oxide Formation from Iron Pentacarbonyl-Doped Low-Pressure Hydrogen/Oxygen Flames*. *International Journal of Chemical Kinetics* 45 (2013) 487-498.

- [311] C. Olm, T. Varga, É. Valkó, S. Hartl, C. Hasse, T. Turányi, *Development of an ethanol combustion mechanism based on a hierarchical optimization approach*. International Journal of Chemical Kinetics 48 (2016) 423-441.
- [312] N. Chenouard, I. Smal, F. De Chaumont, M. Maška, I.F. Sbalzarini, Y. Gong, J. Cardinale, C. Carthel, S. Coraluppi, M. Winter, *Objective comparison of particle tracking methods*. Nature Methods 11 (2014) 281.
- [313] R.S. Wilson, L. Yang, A. Dun, A.M. Smyth, R.R. Duncan, C. Rickman, W. Lu, *Automated single particle detection and tracking for large microscopy datasets*. Royal Society Open Science 3 (2016) 160225.
- [314] H. Shen, L.J. Tauzin, R. Baiyasi, W. Wang, N. Moringo, B. Shuang, C.F. Landes, *Single particle tracking: from theory to biophysical applications*. Chemical Reviews 117 (2017) 7331-7376.
- [315] A. Rittler, I. Wlokas, A. Kempf, *Large Eddy Simulation of Iron-Oxide Nanoparticle Synthesis from Spray Flame Pyrolysis*. 8<sup>th</sup> European Combustion Meeting (2017), Dubrovnik, Croatia.
- [316] J. Tobai, T. Dreier, *Effective A-state fluorescence lifetime of formaldehyde in atmospheric pressure CH<sub>4</sub>/air flames*. Applied Physics B 74 (2002) 101-104.
- [317] J. Verdieck, P. Bonczyk, *Laser-induced saturated fluorescence investigations of CH, CN and NO in flames*. Symposium (International) on Combustion (1981) 1559-1566.
- [318] A. Rittler, *Large eddy simulation of nanoparticle synthesis from spray flames*. Institute for Combustion and Gas Dynamics – Reactive Fluids, University of Duisburg-Essen, Duisburg, Germany (2017).
- [319] M.M. Prenting, M.I.B. Dzulfida, T. Dreier, C. Schulz, *Characterization of tracers for two-color laser-induced fluorescence liquid-phase temperature imaging in sprays*. Experiments in Fluids 61(3) (2020) 77.

## Appendix

### A1 Influence of the refractive index on the PDA droplet-size measurement

To estimate the influence of the refractive index on the measured droplet size discussed in chapter 2.2.4, ethanol is chosen as medium because the ethanol spray flame SF1 is denoted as reference flame for the recently introduced SpraySyn standard burner for nanoparticle synthesis in flames [26]. To quantify the error, the measurement data of SF1 (Table 5.2) on the centerline of the burner (M20 in Table A3.7) at 10 mm HAB is used (Figure 5.23). The refractive index at room temperature (20°C) is 1.359 while at the evaporation temperature of ethanol at about 80°C it is 1.4. The difference between both refractive indices is therefore 0.041, i.e., the refractive index of ethanol is 3.02% higher at 80°C than at 20°C.

From Dantec's BSA Flow Software, the refractive-index-dependent phase factors  $U_{1,2}$  and  $V_{1,2}$  can be obtained for each corresponding detector pair of the dual PDA system utilized in this work (cf., Ref. [221]). Together with the phase difference (that is independent of the refractive index)

$$\Phi_{1,2} = 2\pi f \Delta t, \quad \text{A1.1}$$

where  $f$  is the laser frequency and  $\Delta t$  is the measured time difference between the wave fronts reaching the two detectors [221], a droplet diameter  $d$  can be calculated [290] using

$$d = \frac{\Phi_{1,2} / ^\circ}{U_{1,2} / ^\circ / \mu\text{m}}. \quad \text{A1.2}$$

Thus, an averaged droplet size of 15.19  $\mu\text{m}$  was calculated for 20°C, while 15.79  $\mu\text{m}$  was derived for 80°C resulting in a difference of 0.6  $\mu\text{m}$  (i.e., a 3.96% larger averaged droplet diameter is determined when using the refractive index of ethanol at 80°C instead of the one at 20°C). Since evaporation cooling is proven to have a measurable effect even in the ethanol spray flame, where droplet temperatures below 20°C were measured [319] and the individual droplet temperature is unknown at the time of measurement, the medium-specific refractive index at room temperature was used for all measurements. Furthermore, it should be noted that the dependence of the refractive index on the temperature of the surrounding gas phase (air/fuel mixture) is also neglected so that the refractive index of air at 20°C (1.0003) was used for all measurements. This procedure is well established in literature, as for instance reported by Grohmann, who also chose the refractive indices at room temperature for his PDA droplet size measurements in spray flames and estimates a maximum error of 6.5% [226].

### A2 Details of the experimental setup for multiline NO-LIF thermometry

To facilitate the reproducibility of the experimental setup for multiline NO-LIF thermometry, details of the technical arrangements are documented in this chapter specifically adapted to the hardware and software utilized for the measurements presented in this thesis. These and further guidelines and instructions were copied to the Institute's network drive (\\Arbeitsgruppen\Lasermesstechnik\Allgemeines\Multiline NO-LIF Thermometry).



- Anleitung 225nm-Erzeugung durch SFM\_fs2.pdf
- 2017-05-04\_Dye-Justage TIPPS.pdf

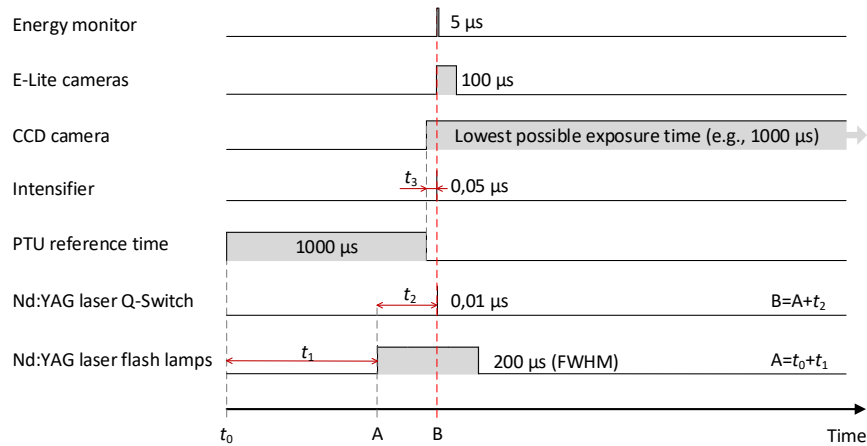


Figure A2.2: Signal flow for multiline NO-LIF thermometry measurements at the IUTA. Depending on the minimum possible reference time of the utilized programmable timing unit (PTU), the flash lamps of the Nd:YAG laser are triggered with a time delay  $t_1$  created by a pulse/delay generator. The laser's Q-switch is shifted by  $x_2$  to release a laser pulse at maximum intensity. The intensifier gate opens after a time delay  $x_3$  (at the time when the fluorescence signal is emitted) within the CCD camera gate. The same applies to the Energy Monitor and the E-lite cameras. Intensifier, Energy Monitor, and all cameras are operated at their individual lowest possible exposure time.

The signal interrupter depicted in Figure A2.1 is used for interrupting the image acquisition while scanning the dye laser. It is a custom-made device specially designed for each respective dye laser since some dye lasers provide a positive TTL signal when scanning while others provide a positive TTL signal when the stepper motor is inactive. For the setup at IUTA, a signal interrupter box was manufactured at the University's electronics workshop, where the input signal of the dye laser can be inverted by a toggle switch. This makes the signal interrupter universally applicable for all dye lasers utilized in this thesis, regardless of whether they provide a positive or a zero signal when the stepper motor is idle. The electrical layout is shown in Figure A2.3.

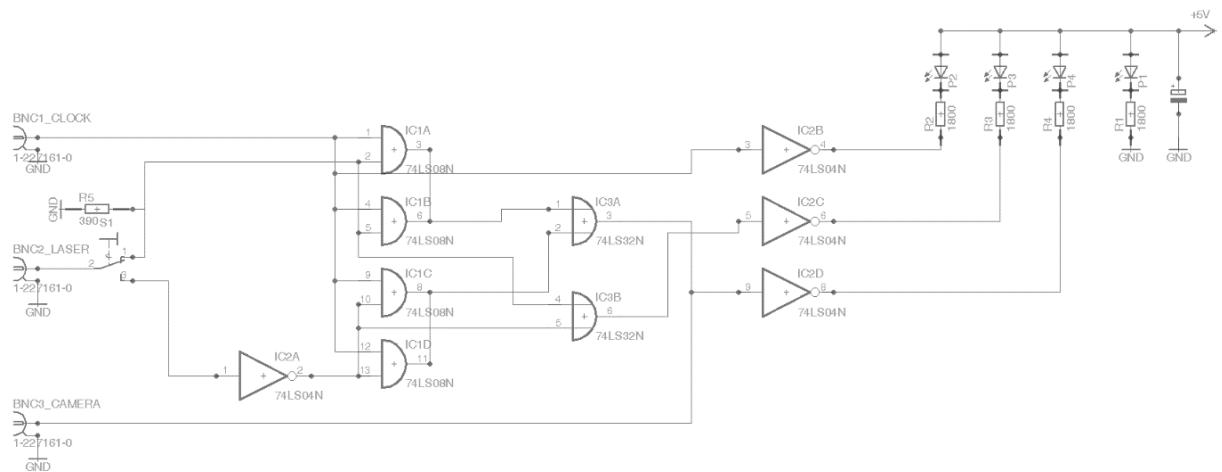


Figure A2.3: Electrical layout of the signal interrupter utilized for multiline NO-LIF thermometry measurements at the IUTA. Due to the toggle switch, the device can be used for both types of dye lasers, those providing a positive signal when the laser is scanning and vice versa.

## A3 Allocation of raw data and post processing to the presented figures

The explicit assignment of all presented figures to their raw data and applied post processing is provided in this chapter to enable reproducibility of the figures presented in this thesis as well as further figures for future publications.

For this purpose, a digital copy of all raw data and evaluations collected in the context of this PhD thesis was provided to the working group of Thomas Dreier on an external hard disc drive at the time of submission of this manuscript, in accordance with the *Leitlinie zum Umgang mit Forschungsdaten an der Universität Duisburg-Essen vom 14. Februar 2019*. The acquired raw data is documented in measurement-data protocols that contain all relevant parameters of the respective experiment. These protocols are attached to the respective measurement data folders. The assignment between the used folder structure and the chapters of this thesis is described in the file “PhD thesis and folder structure.pdf”. All figures presented in this work are collected in a single folder (see \\Florian\NETZ\Projekte\0\_Promotion\Dissertation\Abbildungen).

The overview tables presented in the following are based on these protocols and are intended to provide the reader of this thesis a link between the respective identification number (ID) of each measurement and the corresponding figure presented in this thesis. In these overview tables, only relevant results are listed (i.e., test measurements or measurements with bad quality are neglected). A complete list of all acquired raw data can be found in the respective digital measurement-data protocols together with additional comments and further details.

Please note that the respective measurement IDs (e.g., M11) require additional context like the applied optical diagnostics, the investigated burner, and/or the examined materials system to become unambiguous, e.g., PIV measurements at the pilot-scale gas burner: M11.

Apart from the explicit assignment of the raw data to the presented figures, the workflow is described in the following subchapters and details of the applied parameters are given to simplify reproducibility. For each processing step, only the file format that is read-in and the output file-format that is relevant for the next step is specified (often results are generated in additional file formats that are, however, not relevant for the next processing step). By that, for instance, the processing chain of LIFSim and the Matlab script “LIF\_PostProc\_TFeld.m” gets unambiguous: LIFSim reads-in IMX files and exports IMX files, while the mentioned Matlab script imports these IMX files and exports FIG files. For each program or script mentioned, this information is provided in the following according to the example: Script “LIF\_PostProc\_TFeld.m” (in: IMX; out: FIG). All software and scripts utilized in this work are documented in chapter A4.

### A3.1 Lab-scale gas burner

#### A3.1.1 IR thermography

The IR camera (InfraTec VarioCamHD) was manually controlled by using the respective hardware interface. The acquired image-series’ (Table A3.1) were stored on a secure digital (SD) memory card and manually copied to a computer for post processing. All images were evaluated using the InfraTec software IRBIS 3 plus (in: IRB; out: PNG). The parameters used are stored in the file “2019-12-18\_Correction.cdf” and can be imported by clicking on “Messen” and then on the small icon on the lower

right side of the box “Korr.-Gebiete”. In the following dialog (“Korrektur”) the file can be selected by clicking on “Laden” on the lower left side of the window. To reconstruct the used measurement regions, the file “2019-12-18\_Regions.mdf” can be imported by clicking on “Messen” and then on the small icon on the lower right side of the box “Messgebiete”. In the following dialog (“Messdefinitionen”) the file can be selected by clicking on “Laden” on the lower left side of the window. However, deviations were sometimes observed in the restored positions and sizes of the measurement regions. Therefore, please read the notes provided in “Thermography Workflow\_fs1.txt”. The extracted data (e.g., radial profiles or mean value and standard deviation) was subsequently processed in OriginPro 2017 and Origin 2018b (in: ASC; out: OPJU). The temperature maps were exported as bitmap files (PNG) and the final figures presented in this thesis were arranged in Microsoft PowerPoint 2016 (in: PNG; out: EMF).

Table A3.1: Relevant raw data acquired with infrared thermography. See Table 3.3 for further details on the operating parameters.

ID	Figure	Burner	Flame	Cooling with 15°C water
M03	Figure 3.7, Figure 3.8	C1	B	On
M04	Figure 3.8	C1	B	Off
M05	Figure 3.8, Figure 3.13	C1	A	On
M06	Figure 3.8	C1	A	Off
M07	Figure 3.8, Figure 3.13	C2	A	On
M08	Figure 3.7, Figure 3.8	C2	B	On

### A3.1.2 Multiline NO-LIF thermometry

The CCD camera and intensifier were controlled with DaVis 7.2.2 (LaVision) while image acquisition was performed by the DaVis macro DiskGrab (NOLIF\_20120903.CL). Details on the experimental setup are provided in chapter A2. The raw data (Table A3.2 and Table A3.3) was evaluated using LIFSim (in: IMX; out: IMX). The selected parameters were documented as screenshots of DiskGrab and stored together with the evaluated data. Subsequently, the evaluated data was processed with the Matlab scripts “LIF\_PostProc\_PlotSpectra.m” (in: DAT; out: FIG) and “LIF\_PostProc\_TFeld.m” (in: IMX; out: FIG). The final temperature maps presented in this thesis were created with the Matlab script “Vektorgrafik.m” (in: FIG; out: EMF) and were finally arranged in Microsoft PowerPoint 2016 (in: EMF; out: EMF). The final graphs were created with OriginPro 2017 and Origin 2018b (in: DAT; out: OPJ).

#### Iron-oxide synthesis

Table A3.2: Relevant raw data acquired with multiline NO-LIF thermometry in the flame of the flat flame burner installed inside a low-pressure flame reactor (cf., Table 3.4). The burner configuration C1 (Figure 3.2) was operated with parameter set A (Table 3.3) while precursor concentration and distance between burner and sampling nozzle (cf., chapter 3.3.2) were varied.

ID	Figure / publication	Sampling nozzle HAB / mm	Fe(CO) <sub>5</sub> concentration / ppm
M14	[60]	6	200
M16	-	4	200
M20	Figure 3.9, Figure 3.12, Figure 3.13	25	200
M21	[60]	6	0
M22	-	4	0

M24	Figure 3.9, Figure 3.12	25	0
M27	[60]	6	100
M29	-	4	100
M31	-	2	100
M32	Figure 3.9, Figure 3.12	25	100

### Tungsten-oxide synthesis

Table A3.3: Relevant raw data acquired with multiline NO-LIF thermometry in the flame of the flat flame burner installed inside a low-pressure flame reactor (cf., Table 3.4). The burner configuration C2 (Figure 3.2) was operated with parameter set A (Table 3.3) while precursor concentration and distance between burner and sampling nozzle (cf., chapter 3.3.2) were varied.

ID	Figure	Sampling nozzle HAB / mm	WF <sub>6</sub> concen- tration / ppm	Flame
M00	Figure 3.10, Figure 3.12	50	0	A
M04	Figure 3.10, Figure 3.12, Figure 3.13	50	200	A
M08	-	50	0	C
M10	Figure 3.11, Figure 3.12	40	0	C
M11	Figure 3.11, Figure 3.12	40	200	C

## A3.2 Pilot-scale gas burner

### A3.2.1 Particle Image Velocimetry

The PIV camera was controlled using DaVis 8.1.4 (see hardware configuration file “20170421\_Schneider\_PIV.set”). Image acquisition and evaluation (in: IM7; out: VC7) was also performed in DaVis 8.1.4 (for raw data see Table A3.4). All settings and parameters for data evaluation were stored in the file “2017-05-02 PIV Auswertug Scheider\_mit Uncertainty.xml”. The final velocity maps presented in this thesis were created with the Matlab script “PIV\_plot.m” (in: VC7; out: EMF) and were finally arranged in Microsoft PowerPoint 2016 (in: EMF; out: EMF).

Table A3.4: Relevant raw data acquired with particle image velocimetry in the non-reacting flow of the pilot-scale gas burner (Figure 4.2). For all measurements, the flow was shielded by a quartz inliner (Figure 4.3). Based on the operating parameter sets (Table 4.3), single operating parameters were varied in a wide range investigated from up to three different camera perspectives. The camera perspectives are specified in the digital files (since they are not relevant in the context of the present thesis). All gases were replaced by pressurized air and the seeded channel is indicated with an (S). For better clarity, the data is assigned into 15 groups and sorted accordingly. Moreover, in each group the parameters that are kept constant are written in gray letters.

Group	ID	Figure	Coflow slm	Combustion air channel slm	Separation gas chan- slm	Fuel gas slm	Perspec- tive
1	M01	Figure 4.5	200	28 (S)	2.1	12.6	1
	M44	-	200	28	2.1	12.6	2
	M59	-	200	28	2.1	12.6	3
2	M02	Figure 4.5	200	28 (S)	2.8	15.4	1
	M45	-	200	28	2.8	15.4	2
	M60	-	200	28	2.8	15.4	3
3	M03	Figure 4.5	200	28 (S)	4.2	21	1

	M46	-	200	28	4.2	21	2
	M61	-	200	28	4.2	21	3
4	M04	-	200	28 (S)	3	23.5	1
	M05	Figure 4.7, Figure 4.8	200	28	4.2	23.5	1
	M06	-	200	28	6	23.5	1
	M07	-	200	28	8	23.5	1
	M08	-	200	28	10	23.5	1
	M09	Figure 4.7, Figure 4.8	200	28	11.2	23.5	1
	M10	-	200	28	13	23.5	1
	M11	Figure 4.7, Figure 4.8	200	28	15	23.5	1
5	M12	-	100	28 (S)	4.2	23.5	1
	M13	-	150	28	4.2	23.5	1
	M14	-	250	28	4.2	23.5	1
	M15	-	300	28	4.2	23.5	1
6	M16	-	100	28 (S)	11.2	23.5	1
	M17	-	150	28	11.2	23.5	1
	M18	-	250	28	11.2	23.5	1
	M19	-	300	28	11.2	23.5	1
7	M20	-	100 (S)	28	4.2	23.5	1
	M21	-	150	28	4.2	23.5	1
	M22	-	200	28	4.2	23.5	1
	M23	-	250	28	4.2	23.5	1
	M24	-	300	28	4.2	23.5	1
8	M25	Figure 4.6	100 (S)	28	4.2	23.5	1
	M26	-	150	28	4.2	23.5	1
	M27	Figure 4.6	200	28	4.2	23.5	1
	M28	-	250	28	4.2	23.5	1
	M29	Figure 4.6	300	28	4.2	23.5	1
9	M30	-	200	30 (S)	4.2	23.5	1
	M31	-	200	32	4.2	23.5	1
	M32	-	200	34	4.2	23.5	1
	M33	-	200	36	4.2	23.5	1
10	M34	-	200	30 (S)	11.2	23.5	1
	M35	-	200	32	11.2	23.5	1
	M36	-	200	34	11.2	23.5	1
	M37	-	200	36	11.2	23.5	1
11	M38	-	200	28 (S)	4.2	10	1
	M39	-	200	28	4.2	15	1
	M40	-	200	28	4.2	20	1
	M41	-	200	28	4.2	25	1
	M42	-	200	28	4.2	30	1
	M43	-	200	28	4.2	35	1
12	M47	-	200	28 (S)	3	23.5	2
	M48	-	200	28	4.2	23.5	2
	M49	-	200	28	6	23.5	2
	M50	-	200	28	8	23.5	2
	M51	-	200	28	10	23.5	2

	M52	-	200	28	11.2	23.5	2
	M53	-	200	28	13	23.5	2
	M54	-	200	28	15	23.5	2
13	M55	-	100	28 (S)	4.2	23.5	2
	M56	-	150	28	4.2	23.5	2
	M57	-	250	28	4.2	23.5	2
	M58	-	300	28	4.2	23.5	2
14	M62	-	200	28 (S)	4.2	10	3
	M63	-	200	28	4.2	15	3
	M64	-	200	28	4.2	20	3
	M65	-	200	28	4.2	25	3
	M66	-	200	28	4.2	30	3
	M67	-	200	28	4.2	35	3
15	M68	-	200	28 (S)	4.2	23.5	3
	M69	-	200	30	4.2	23.5	3
	M70	-	200	32	4.2	23.5	3
	M71	-	200	34	4.2	23.5	3
	M72	-	200	36	4.2	23.5	3

### A3.2.2 Multiline NO-LIF thermometry

The CCD camera, the intensifier, and the E-lite cameras were controlled with DaVis 7.2 (see hardware configuration file “Hardware\_Setup\_2017-08-10\_ImagerProX\_und\_zwei\_Elite.set”) while image acquisition was performed by the DaVis macro DiskGrab (NOLIF\_20120903.CL). Details on the experimental setup are provided in chapter A2. The raw data (Table A3.5) was processed using the Matlab script “Absorptionskorrektur.m” (in: IMX; out: IMX) before evaluating the temperature fields with LIFSim (in: IMX; out: IMX). The selected parameters used for the Matlab processing were stored in the file “Results\_Abs\_korr.mat” that is stored together with the scripts output. The parameters for the LIFSim evaluation were documented as screenshots of DiskGrab and stored together with the evaluated data. Subsequently, the data was processed with the Matlab scripts “LIF\_PostProc\_PlotSpectra.m” (in: DAT; out: FIG) and “LIF\_PostProc\_TFeld.m” (in: IMX; out: FIG). The final temperature maps presented in this thesis were created with the Matlab script “Vektorgrafik.m” (in: FIG; out: EMF) and were finally arranged in Microsoft PowerPoint 2016 (in: EMF; out: EMF). The final graphs were created with OriginPro 2017 and Origin 2018b (in: DAT; out: OPJ).

Table A3.5: Relevant raw data acquired with multiline NO-LIF thermometry in the flame of the pilot-scale gas burner (Figure 4.2) operated inside the IUTA flame reactor (Figure 4.1). All gas flows listed are given in slm.

ID	Figure	Coflow	Combustion air			Separation gas		Fuel gas	
			N <sub>2</sub> slm	O <sub>2</sub> slm	N <sub>2</sub> slm	N <sub>2</sub> slm	H <sub>2</sub> slm	TTIP in Ar slm	NO in Ar slm
M02	-	200	24	4	2.8	6	5	4.2	
M04	Figure 4.9, Figure 4.11	200	24	4	2.8	6	5	4.2	

### A3.3 Lab-scale spray burner

#### A3.3.1 Imaging spray-flame characterization

The DSLR camera (Nikon D5300) was manually controlled using the respective hardware interface. The acquired image-series' (Table A3.6) were stored on a secure digital (SD) memory card and manually copied to a computer for post processing. All images were converted by DCRaw [237] (in: NEF; out: TIFF) using the Matlab script "SPP\_1\_RAW2TIFF.m" before evaluation with "SPP\_2\_CropImages.m" (in: TIFF; out: TIFF), "SPP\_3\_FlameGeometry.m" (in: TIFF; out: FIG), and "SPP\_4\_FlameBenchmark.m" (in: MAT; out: FIG and MAT). For each script, the selected parameters are stored as a MAT file together with the respective results. All scripts are provided together with a manual on [www.spraysyn.org](http://www.spraysyn.org). To create the MAT file of the reference flames, the script "SPP\_3\_1\_STANDARD\_Definition.m" was used after the data has been processed using the script "SPP\_3\_FlameGeometry.m".

Table A3.6: Relevant raw data acquired by imaging the flame of the SpraySyn burner (Figure 5.1) with a DSLR consumer camera. Only the data obtained using the standardized setup (Figure 5.3) is shown. Additional photos of the spray flame (ethanol, 1-butanol, acetone, and mix of ethanol with 2-ethyl-hexanoic acid) with methane and hydrogen admixture to the dispersion gas are available in the provided digital files (M44-M94; see digital measurement protocol). Data M35 and M38 were used for the following publications, figures, and tables (\*<sup>1</sup>): [26, 55, 56], Figure 5.2, Figure 5.5, Figure 5.6, Figure 5.7, Figure 5.8, and Table 5.5.

ID	Figure/ publication	Exposure time s	Pressure mbar	Pilot		Coflow N <sub>2</sub> slm	Dispersion gas O <sub>2</sub> slm	Liquid ml/min	Flame
				O <sub>2</sub> slm	CH <sub>4</sub> slm				
M35	* <sup>1</sup>	1/13	1019	16	2	120	-	-	PF1
M36	-	1/13	1010	16	2	120	-	-	PF1
M37	-	1/13	1010	16	2	120	10	-	PF1-D
M38	* <sup>1</sup>	1/13	1010	16	2	120	10	2	SF1
M39	-	1/13	940	16	2	120	-	-	PF1
M40	[26]	Various	940	16	2	120	10	2	SF1-Fe1
M41	[26], Figure 5.8	1/13	1010	16	2	120	-	-	PF1
M42	[26], Figure 5.8	1/13	1010	16	2	120	10	2	SF1
M43	[26]	Various	1010	16	2	120	10	2	SF1-EHA

#### A3.3.2 Phase Doppler Anemometry

The Dual-PDA system was controlled using Dantec's BSA Flow Software v6.5 that evaluated the acquired raw data (Table A3.7) fully automated. All parameters used for data acquisition are contained in the raw-data files (file type *LDA*). The data was exported from the BSA Flow software (in: *LDA*; out: *TXT*) to make it accessible for other software. Further processing was performed using the Matlab

script “PDA\_data\_eval.m” (in: TXT; out: TXT) and the exported results were plotted and further evaluated using predefined Origin templates (in: TXT; out: OPJ) as described in the manual “Postprocessing PDA-Daten\_fs07.pdf”.

Table A3.7: Relevant raw data acquired with Laser Doppler and Phase Doppler Anemometry on the SpraySyn burner (Figure 5.1). To make the individual studies easier to identify, the corresponding groups are highlighted alternately in white and light gray. The parameters that are kept constant between the individual measurements are written in gray letters.

ID	Figure/ publication	Pilot		Coflow N <sub>2</sub> slm	Disper- gas O <sub>2</sub> slm	Liquid	Liquid ml/min	Spray (flame)
		O <sub>2</sub> slm	CH <sub>4</sub> slm					
M16	-	-	-	120	10	Ethanol	2	S1
M17	[55], Figure 5.10, Figure 5.11	-	-	120	10	Ethanol	2	S1
M18	[55], Figure 5.12, Figure 5.13, Figure 5.14	-	-	120	10	Ethanol	2	S1
M19	-	16	2	120	10	Ethanol	2	SF1
M20	Figure 5.23, Figure 5.24	16	2	120	10	Ethanol	2	SF1
M21	-	16	2	120	10	Ethanol	2	SF1
M22	Figure 5.23, Figure 5.24	16	2	120	4	Ethanol	2	SF1
M23	Figure 5.23, Figure 5.24	16	2	120	7	Ethanol	2	SF1
M24	Figure 5.23, Figure 5.24	16	2	120	13	Ethanol	2	SF1
M25	Figure 5.23, Figure 5.24	16	2	120	16	Ethanol	2	SF1
M26	-	16	1.3	120	10	Ethanol	2	SF1
M27	-	16	2	120	10	Ethanol	1	SF1
M28	-	16	2	120	10	Ethanol	4	SF1
M29	-	16	2	120	10	Ethanol	2	SF1
M30	-	-	-	120	5	EHA/EtOH	2	S1-EHA
M31	-	-	-	120	6	EHA/EtOH	2	S1-EHA
M32	-	-	-	120	7	EHA/EtOH	2	S1-EHA
M33	-	-	-	120	8	EHA/EtOH	2	S1-EHA
M34	-	-	-	120	10	EHA/EtOH	2	S1-EHA
M35	[273]	16	2	120	5	EHA/EtOH	2	SF1-EHA
M36	[273]	16	2	120	6	EHA/EtOH	2	SF1-EHA
M37	[273]	16	2	120	7	EHA/EtOH	2	SF1-EHA
M38	[273]	16	2	120	8	EHA/EtOH	2	SF1-EHA
M39	-	16	2	120	10	EHA/EtOH	2	SF1-EHA
M40	-	-	-	-	10	Ethanol	2	S1
M41	-	-	-	-	10	Ethanol	2	S1
M42	-	-	-	-	10	Ethanol	2	S1
M43	-	-	-	-	10	Ethanol	2	S1

M44	-	-	-	-	10	Ethanol	2	S1
M45	-	-	-	120	10	Ethanol	2	S1
M46	-	16	2	120	10	Ethanol	2	SF1
M47	-	-	-	-	10	Ethanol	2	S1
M48	[56], Figure 5.15, Figure 5.16, Figure 5.29	-	-	-	10	Ethanol	2	S1
M49	[56], Figure 5.15, Figure 5.16, Figure 5.29	-	-	-	4	Ethanol	2	S1
M50	[56], Figure 5.15, Figure 5.16, Figure 5.29	-	-	-	7	Ethanol	2	S1
M51	[56], Figure 5.15, Figure 5.16, Figure 5.29	-	-	-	13	Ethanol	2	S1
M52	[56], Figure 5.15, Figure 5.16, Figure 5.29	-	-	-	17	Ethanol	2	S1
M53	[56], Figure 5.19, Figure 5.20, Figure 5.29	-	-	-	4	Acetone	2	S1
M54	[56], Figure 5.19, Figure 5.20, Figure 5.29	-	-	-	7	Acetone	2	S1
M55	[56], Figure 5.19, Figure 5.20, Figure 5.29	-	-	-	10	Acetone	2	S1
M56	[56], Figure 5.19, Figure 5.20, Figure 5.29	-	-	-	13	Acetone	2	S1
M57	[56], Figure 5.19, Figure 5.20, Figure 5.29	-	-	-	17	Acetone	2	S1
M58	[56], Figure 5.19, Figure 5.20, Figure 5.29	-	-	-	20	Acetone	2	S1
M59	[56], Figure 5.17, Figure 5.18, Figure 5.29	-	-	-	4	1-Butanol	2	S1
M60	[56], Figure 5.17, Figure 5.18, Figure 5.29	-	-	-	7	1-Butanol	2	S1
M61	[56], Figure 5.17, Figure 5.18, Figure 5.29	-	-	-	10	1-Butanol	2	S1
M62	[56], Figure 5.17, Figure 5.18, Figure 5.29	-	-	-	13	1-Butanol	2	S1
M63	[56], Figure 5.17, Figure 5.18, Figure 5.29	-	-	-	17	1-Butanol	2	S1
M64	[56], Figure 5.17, Figure 5.18, Figure 5.29	-	-	-	20	1-Butanol	2	S1
M65	[56], Figure 5.21, Figure 5.22, Figure 5.29	-	-	-	4	n-Hexane	2	S1
M66	[56], Figure 5.21, Figure 5.22, Figure 5.29	-	-	-	7	n-Hexane	2	S1
M67	[56], Figure 5.21, Figure 5.22, Figure 5.29	-	-	-	10	n-Hexane	2	S1
M68	[56], Figure 5.21, Figure 5.22, Figure 5.29	-	-	-	13	n-Hexane	2	S1
M69	[56], Figure 5.21, Figure 5.22, Figure 5.29	-	-	-	17	n-Hexane	2	S1
M70	[56], Figure 5.21, Figure 5.22, Figure 5.29	-	-	-	20	n-Hexane	2	S1
M71	Figure 5.25, Figure 5.26, Figure 5.27, Figure 5.28	-	-	-	10	Ethanol	2	S1

M72	Figure 5.25, Figure 5.26, Figure 5.27, Figure 5.28	16	2	120	10	Ethanol	2	SF1
-----	--	----	---	-----	----	---------	---	-----

## A3.4 Pilot-scale spray burner

### A3.4.1 Particle Image Velocimetry

The PIV camera was controlled using DaVis 8.1.4 (see hardware configuration file “2016-07-26\_Florian.set”). Image acquisition and evaluation (in: IM7; out: VC7) was also performed in DaVis 8.1.4 (for raw data see Table A3.8). All settings and parameters for data evaluation were stored in the file “2016-08-08\_PIV-Auswertung\_Schneider\_Zhang.xml”. The final velocity maps presented in this thesis were created with the Matlab script “PIV\_plot.m” (in: VC7; out: EMF) and were finally arranged in Microsoft PowerPoint 2016 (in: EMF; out: EMF).

Table A3.8: Relevant raw data acquired with particle image velocimetry in the non-reacting flow of the IUTA spray burner (Figure 6.1). The individual flow channels of the burner were operated with pressurized air according to the parameters listed in Table 6.4 while the seeded channel is indicated with an (S). For better clarity, the data is assigned into six groups and sorted accordingly. Moreover, in each group the parameters that are kept constant are written in gray letters.

Group	ID	Figure	Coflow	Pilot gas mix channel	Dispersion gas channel	Window flushing channel	Liquid (ethanol)	Window-flushing ring	Quartz inliner
1	M06	-	ON (S)	-	-	-	-	YES	NO
	M16	-	ON (S)	-	-	-	-	YES	YES
	M26	-	ON (S)	-	-	-	-	NO	NO
	M20	Figure 6.4	ON (S)	-	-	-	-	NO	YES
2	M07	-	-	ON (S)	-	-	-	YES	NO
	M14	-	-	ON (S)	-	-	-	YES	YES
	M24	-	-	ON (S)	-	-	-	NO	NO
	M22	Figure 6.4	-	ON (S)	-	-	-	NO	YES
3	M10	Figure 6.5	-	-	-	ON (S)	-	YES	NO
	M12	Figure 6.5	-	-	-	ON (S)	-	YES	YES
4	M27	-	ON (S)	ON	ON	-	-	NO	NO
	M28	-	ON	ON (S)	ON	-	-	NO	NO
	M19	-	ON (S)	ON	ON	-	-	NO	YES
	M21	Figure 2.4, Figure 6.6	ON	ON (S)	ON	-	-	NO	YES
5	M05	-	ON (S)	ON	ON	ON	-	YES	NO
	M08	-	ON	ON (S)	ON	ON	-	YES	NO
	M09	-	ON	ON	ON	ON (S)	-	YES	NO
	M15	-	ON (S)	ON	ON	ON	-	YES	YES
	M17	-	ON (S)	ON	ON	ON	-	YES	YES
	M13	-	ON	ON (S)	ON	ON	-	YES	YES
	M18	-	ON	ON (S)	ON	ON	-	YES	YES
	M11	-	ON	ON	ON	ON (S)	-	YES	YES

6	M30	-	ON (S)	ON	ON	-	ON	NO	NO
	M29	-	ON	ON (S)	ON	-	ON	NO	NO
	M31	Figure 6.6	ON (S)	ON	ON	-	ON	NO	YES
	M32	-	ON	ON (S)	ON	-	ON	NO	YES

#### A3.4.2 Multi-pulse RGB shadowgraphy for Particle Tracking Velocimetry

The DSLR camera (Nikon D90) was manually controlled using the respective hardware interface. The acquired image-series' (Table A3.9) were stored on a secure digital (SD) memory card and manually copied to a computer for post processing. All images were converted by DCRaw [237] (in: NEF; out: TIFF) using the Matlab script "RGB\_PTV\_0\_BKG\_Sub\_and\_Convert\_RAW\_to\_TIFF.m". Subsequently, the images were evaluated with the scripts "RGB\_PTV\_run\_ALL.m" (in: TIFF; out: MAT) and "Zusammenfassung\_Statistik.m" (in: MAT; out: MAT). Copies of the scripts are stored together with the results to provide all parameters used for the evaluation. The final graphs were created with Origin 2018b.

Table A3.9: Relevant raw data acquired with RGB-PTV in the non-reacting flow of the IUTA spray burner (Figure 6.1) operated with pressurized air according to the parameters listed in Table 6.4. The data of group 1 was acquired with lens front-to-front coupling of a 105 mm ( $f_{\#} = 2.8$ ) macro and a 50 mm lens ( $f_{\#} = 1.8$ ), while the data of group 2 was acquired with an inverted 50 mm lens ( $f_{\#} = 1.8$ ) and a bellows.

Group	ID	Figure	Aperture	Pulse length / $\mu\text{s}$			Pulse delays / $\mu\text{s}$		
				R	G	B	$t_1$	$t_2$	$t_3$
1	T30	-	8	2	2	2	20	20	20
	T33	-	6.3	2	2	2	20	10	10
	T35	-	2.8	2	2	2	20	10	10
	T36	-	4.5	2	2	2	20	10	10
	T39	-	6.3	2	2	2	20	15	15
	T43	-	2.8	1	1	1	20	15	15
	T44	-	4.5	1	1	1	20	15	15
	T45	-	6.3	1	1	1	20	15	15
	T49	-	4.5	1	1	1	20	5	5
2	T63	Figure 6.7	1.8	1	1	1	20	5	5
	T74	Figure 6.7	1.8	1	1	1	20	5	5
	T75	Figure 2.5, Figure 2.6, Figure 6.7	1.8	1	1	1	20	5	5
	T76	Figure 6.7	1.8	1	1	1	20	5	5
	T80	Figure 6.7	1.8	1	1	1	20	5	5

#### A3.4.3 Multiline NO-LIF-Thermometry

The workflow used for image acquisition and post processing is described in chapter A3.2.2. The raw data acquired on the pilot-scale spray burner is documented in Table A3.10.

Table A3.10: Relevant raw data acquired with multiline NO-LIF thermometry in the flame of the IUTA spray burner (Figure 6.1) operated inside the IUTA flame reactor (Figure 4.1). The parameters that are kept constant (compared to the previous line) are printed in gray. See Table 6.7 for further details of the operating parameters (e.g., the composition of the pilot flame).

ID	Figure	Spray				Pilot flame			Flame
		Solvent	Precursor	Dispersion gas		Fuel gas mix	Coflow	Window flushing	
		EtOH g/h	Fe(NO <sub>3</sub> ) mol	N <sub>2</sub> slm	O <sub>2</sub> slm	Various slm	Air slm	N <sub>2</sub> slm	-
M05	-	-	-	2	2	28	50	40	F0
M06	Figure 2.3	-	-	2	2	28	50	40	F0
M07	Figure 6.11, Figure 6.12, Figure 6.17	500	-	6	12	28	90	100	F1
M08	Figure 6.8, Figure 6.9, Figure 6.10, Figure 6.13, Figure 6.14, Figure 6.17	500	-	10	8	28	90	40	F2
M09	-	500	-	18	-	28	90	40	F3
M10	-	500	-	10	8	28	90	40	F2
M11	Figure 6.13, Figure 6.14, Figure 6.17, Figure 6.18, Figure 6.19, Figure 6.20	500	0.5	10	8	28	90	40	F2
M12	Figure 4.10, Figure 6.15, Figure 6.16, Figure 6.17	500	-	18	-	28	90	40	F3
M13	Figure 6.15, Figure 6.16, Figure 6.17, Figure 6.19	500	0.5	18	-	28	90	40	F3
M14	Figure 6.11, Figure 6.12, Figure 6.17, Figure 6.19	500	0.5	6	12	28	90	100	F1

## A4 List of utilized software

In this chapter, the software used for data acquisition and data evaluation is listed and a brief description is provided that specifies which software was used in which context. By that, reproducibility of the results presented in this work is simplified. A copy of all created scripts (including the utilized DiskGrab macro and LIFSim versions) was provided to the IVG on an external hard disk drive. Additional copies were stored on the Institute's network drive (\\Interna\IT\In-house software\Schneider) and on the University's Git server (<https://git.uni-due.de/>).

### A4.1 Proprietary software

- BSA Flow Software v6.50 (DantecDynamics): This software was used for data acquisition and evaluation of the LDA/PDA measurements (chapter 5.3.2–5.3.5).

- DaVis (LaVision): This software was used to control LaVision hardware (e.g., cameras, intensified relay optics, energy monitors) and other supported hardware (e.g., YAG lasers, dye lasers). Since multiple DaVis versions have been employed in the present thesis, a detailed overview is given in Table A4.1.
- IRBIS 3 plus (InfraTec): This software was used for evaluation of the thermographic images (chapter 3.3) recorded with the infrared camera from InfraTec.
- Matlab (MathWorks): This software was used for post processing and data evaluation of all results presented in this thesis (except the thermographic imaging). The individual scripts written in the context of the present thesis are listed and described in chapter A4.4.
- Origin (OriginLab): This software was used for creating graphs like Figure 6.17.

Table A4.1: Overview of the utilized DaVis releases.

Software	Used for
DaVis 6.2	Data evaluation of all presented multiline NO-LIF measurements with LIFSim (cf., chapter A4.3) using the DiskGrab macro (cf., chapter A4.2).
DaVis 7.2	Data acquisition of all multiline NO-LIF measurements using the DiskGrab macro (cf., chapter A4.2).
DaVis 8.1.4	Data acquisition of all PIV measurements.  Data evaluation of the PIV measurements performed on the pilot-scale spray burner (presented in chapter 6.3.1) using the <i>DaVis PIV package</i> .
DaVis 8.4	Data evaluation of the PIV measurements performed on the pilot-scale gas burner (presented in chapter 4.3.1) using the <i>DaVis PIV package</i> .

## A4.2 DiskGrab makro

DiskGrab is a DaVis macro written in DaVis command language (DaVis CL) to acquire the data for multiline NO-LIF thermometry fully automated in the structure required for data evaluation with LIFSim. The first version was written by Wolfgang Bessler in the year 2000 and has been further developed and modified since then. Besides the camera images, DiskGrab stores the measured value of the Energy Monitor in pixel 0,0 (top left of the LIF image), names the recorded images according to the required structure, and creates a measurement data log (protocol file) containing all necessary data for LIFSim post processing. It provides separate graphical user interfaces (GUI) for data acquisition and for providing parameters to the (command-line based) in-house software LIFSim.

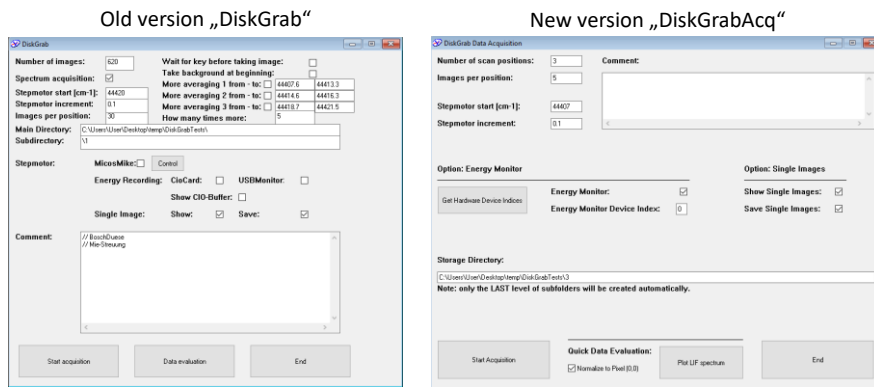


Figure A4.1: Old (left) and new (right) version of the DiskGrab macro introduced in 2018 specialized for data acquisition.

The experimental setup presented in Figure 4.4 made it necessary to modify the DiskGrab macro since images from three cameras needed to be recorded simultaneously. In the DiskGrab (version “NOLIF\_20120903.CL”) used for data acquisition in chapter 3.3.2, the macro can only compute averaged images for a single camera. To acquire images from all three cameras, the option “Save single images” needed to be switched-on permanently leading to a drop in acquisition rate from 10 to 3 Hz (most probably due to the limited performance of the “old” computer manufactured in 2009). Apart from that, DiskGrab (Figure A4.1 left) was not well suited for adapting to hardware modifications since the hardware selection, for instance of the energy monitor, is hidden in the code (without any guiding comments) and thereby not accessible without bigger effort.

DevIndex	DevName
0	Camera 1: Exposure time
1	Camera 1: II-Delay
2	Camera 1: II-Gate
3	Camera 1: II-Gain
4	Camera 2: Exposure time
5	Camera 3: Exposure time
6	Reference time 1
7	Laser power 1A
8	Recording:TriggerRate
9	Recording:RecordingRate
10	USB Energy Monitor 1, Channel 1

Figure A4.2: List displayed in DaVis when pressing the button „Get Hardware Device Indices“ enabling the user to identify the device indices of all hardware recognized by DaVis. To ensure acquisition of the signal detected by the energy monitor, the user has to enter the device index of the USB Energy Monitor (10) into the respective field provided in the GUI of the new DiskGrabAcq macro shown in Figure A4.1 on the right-hand side.

Hence, a condensed version of the DiskGrab macro was developed in the context of this thesis that is specialized for data acquisition (Figure A4.1 right). In the new version “DiskGrabAcq\_1.2”, bugs like the spatial mismatch between the displayed input fields of the GUI and the “true” positions of the input fields was removed and expired features like *MicosMike* or *CioCard* were removed since the addressed hardware is no longer available. A button for creating a list of all connected hardware and its respective device indices (Figure A4.2) was implemented, a field for entering the Energy Monitor’s device index was added to the GUI, and averaged images of all three cameras are automatically calculated. In this work, DiskGrab was employed as described in Table A4.2.

DiskGrabAcq is provided digitally via Git including a power point presentation that highlights the improvements compared to the previous version: <https://git.uni-due.de/IVG-RF/LaVision/DiskGrabAcq>

Table A4.2: Assignment of the DiskGrab macro versions to the measurements and evaluations performed in this thesis.

Macro version	Used for
NOLIF_20120903.CL	Data acquisition of the multiline NO-LIF measurements presented in chapter 3.3.2.  Data evaluation of all presented multiline NO-LIF measurements using DaVis 6.2 (cf., Table A4.1).
DiskGrabAcq_1.2.CL	Data acquisition of the multiline NO-LIF measurements presented in chapters 4.3.2, 6.3.2, and 6.3.3.

### A4.3 LIFSim

LIFSim [185] is a program used for the evaluation of temperature fields from multiline NO-LIF measurements. It was used as executable file (EXE file of version 3.17) together with the data files “NO-collision.dat” (April 17, 2003), “NO-lines.dat” (November 17, 2005), “NO-molecule.dat” (October 31, 2003), “no-partfunc.dat” (November 5, 2003), and “NO-quenching.dat” (November 20, 2001) in this thesis. The required parameters were handed over to LIFSim using the DaVis DiskGrab macro “NO-quenching.dat” (cf., Table A4.2).

To simulate NO spectra, LIFSim Desktop (EXE file of version 1.03) was used together with the data files “NO-collision.dat” (April 17, 2003), “NO-lines.dat” (November 5, 2003), “no-partfunc.dat” (January 10, 2014), and “NO-quenching.dat” (January 31, 2006).

### A4.4 Matlab codes

The Matlab scripts and functions listed in Table A4.3–Table A4.12 were developed by me during my PhD studies. In the header of each script, the minimum required Matlab version is specified (e.g., Matlab 2016a), the required input file-types are declared (e.g., DaVis IM7 files or TIFF bitmap images), and additionally required Matlab functions are indicated. These additional Matlab functions are not provided with the official Matlab release like for instance, user-created functions available on [www.mathworks.com](http://www.mathworks.com), self-written Matlab functions (Table A4.12), or Matlab functions from camera providers like LaVision (readIMX4Matlab; a package required for importing raw data acquired with DaVis (Table A4.1)).

Apart the isolated Matlab scripts, ready-to-use packages (zip-archives) of several Matlab scripts were provided on the institute’s network drive that help the user to get started with the script. These packages contain a manual, copies of the additionally required Matlab functions (subfolder “required m-files”), as well as sample data (subfolders “example input” and “example output”). All presented scripts include automated export of the major results.

For all scripts that were used to create figures depicted in this thesis, references to the corresponding figures are made. While the tables indicate the latest script version, it should be noted that figures may be evaluated with an older script version. An exact allocation of which figure was created with which script version is ensured by the “code-ID” (Table A4.12).

Table A4.3: Most relevant Matlab scripts developed for evaluation and data post processing of multiline NO-LIF thermometry measurements. For better overview, see the digitally provided flowcharts.

Script name	Used for
Absorptions_korrektur_fs31.m	Selecting the region of interest of each fluorescence signal from the dye cuvettes, selecting the region of interest from the NO-LIF signal inside the flame, and applying the laser sheet correction described in chapter 4.3.2.  Script used for Figure 4.11, Figure 6.9, Figure 6.11, Figure 6.13, and Figure 6.15.
LIF_PostProc_PlotSpectra_fs22.m	Plotting all five spectra (measured and fitted LIF spectrum) exported from LIFSim ("spectra.dat").
LIF_PostProc_TFeld_fs56.m	Plotting the temperature map exported from LIFSim ("temp.imx"), converting the pixel scale to a mm-scale, optional median filtering, as well as extraction and plot of radial and axial temperature profiles.  Script used for Figure 3.9, Figure 3.10, Figure 3.11, Figure 4.11, Figure 6.9, Figure 6.11, Figure 6.13, and Figure 6.15.
Extract_Spectra_from_LIF_Scan_fs21.m	Extracting spectra from multiline NO-LIF measurements; the positions in the image can be selected by mouse in an image showing clear NO-LIF signal and options for spatial averaging the spectra around a pre-selected region of interest around the selected position are provided.
Vergleich_Sim_Exp_fs02.m	Comparing a simulated with a measured NO-LIF spectrum (e.g., to determine the spectral dye laser offset).

Table A4.4: Matlab scripts developed for post processing Fe-LIF measurements.

Script name	Used for
FeLIF_plot_fs2.m	Plotting Fe-LIF images from IMX/IM7 files after optional median filtering, pixel to millimeter conversion, and extraction of axial and radial profiles.  Script used for Figure 6.19.
LIF_PostProc_TFeld_fs56_contour.m	Overlaying the Fe-LIF images (plotted with "FeLIF_plot.m") with contour lines of the corresponding temperature field (please note that this script does not provide any figure export, so that the final figure needs to be created with another script, e.g., "Vektorgrafik_fs02.m", cf., Table A4.11).  Script used for Figure 6.19.

Table A4.5: Matlab scripts developed for post processing PIV measurements after evaluation in DaVis (cf., Table A4.1).

Script name	Used for
ExtractLine _from_PIV_plot _fs1.m	Extracting velocity profiles from the DaVis export (IMX, IM7, VC7) after PIV evaluation with the DaVis PIV package.
PIV_plot_fs7.m	Plotting velocity fields from the DaVis export (IMX, IM7, VC7) after PIV evaluation with the DaVis PIV package.  Script used for Figure 4.5, Figure 4.6, Figure 4.7, Figure 4.8, Figure 6.4, Figure 6.5, and Figure 6.6.

Table A4.6: Most relevant Matlab scripts developed together with Jan Menser for evaluation and data post processing of RGB-PTV measurements. Details of the actions performed by the individual scripts are described in chapter 2.2.5 and 6.2.3.

Script name	Used for
RGB_PTV_0_BKG _Sub_and_Convert _RAW_to_TIFF _fs05.m	Converting raw images (NEF) to TIFF files including background subtraction. For raw decoding, the free software DCRaw [237] is called by the script.
RGB_PTV_1_Image _Postproc_fs17.m	Post processing the images covering all processing steps from background correction over color cross-talk correction to Gaussian mask correlation (using the “mask.m” function written by Jan Menser).
RGB_PTV_2_find _particles_fs13.m	Post processing the images covering all processing steps from binarization to particle localization.
RGB_PTV_3 _SimpleTrackerPTV _fs13.m	Post processing the images covering all processing steps from particle track determination using SimpleTracker [243] to calculation of the individual droplet velocities.
RGB_PTV_run_ALL _fs03.m	Evaluation of the data covering the whole processing beginning from the TIFF files to the final droplet velocities. The script was assembled from the three scripts listed above to enable automatized evaluation of multiple images.  Script used for Figure 6.7.
Zusammenfassung _Statistik_fs02.m	Merging the results obtained from the individual images into a single result (e.g., for determining the overall velocity distribution as well as statistics).  Script used for Figure 6.7.

Table A4.7: Most relevant Matlab scripts for evaluating images of an intensified camera connected to a spectrometer. The slit of the spectrometer was horizontally aligned to capture the radial intensity distribution (e.g., of flame chemiluminescence) and the scripts are designed to process the data of multiple HABs (located in separate subfolders) fully automated. For better overview, see the digitally provided flowchart.

Script name	Used for
Spek_IMX_1 _Kali_nm_fs12.m	Wavelength calibration of the camera images (this script processes a single folder, only).
Spek_IMX_2_extract _plot_fs15.m	Extracting spectra on multiple spatial positions of the image.
Spek_IMX_2a _uniform_yscale _fs03.m	Determination of a uniform intensity scale of the extracted spectra plots.
Spek_IMX_2b_plot _all_in_one_fs03.m	Merging all centerline spectra (e.g., for several HABs) into a 2D and a 3D line plot.
Spek_IMX_3_spatial _profile_fs09.m	Extracting radial profiles (emission intensity over radial position) for pre-defined spectral regions (e.g., SiO emission bands).
Spek_IMX_3a _uniform_fig _colorbar_fs02.m	Exporting all spectrally resolved images in a uniform color scale.
Spek_IMX_4 _interpolation _fs07.m	Merging all radial intensity profiles (e.g., for several HABs) into a 3D line plot and for generating an interpolated image (HAB over radial position) with a color-coded emission intensity.

Table A4.8: Matlab scripts for processing chemiluminescence images obtained at multiple HABs with a LaVision intensified CCD camera. For better overview, see the digitally provided flowchart.

Script name	Used for
ChemLum_1 _PostProc_fs26.m	Calculating averaged images and the corresponding (relative) standard deviation from single shot images of multiple HABs (located in separate subfolders) fully automated.
ChemLum_2_1 _mat_file _stitching_fs03.m	Sorting the 2D matrices of three different operating points into a single struct (Matlab data type) each for average, relative standard deviation, and absolute standard deviation.
ChemLum_2_2 _stitch_fs21.m	Generating concatenated images with a user defined overlap (in millimeters) between each HAB for three operating points as well as for creating the result plots.

Table A4.9: Matlab scripts for frequency analysis based on images obtained with a LaVision high-speed camera. For better overview, see the digitally provided flowchart.

Script name	Used for
HS_Frequ_Analysis_fs18.m	Performing 1D FFT analyses from three regions of interest (horizontal line, small image section, and sum of all pixels) of a high-speed image series including signal zero-padding and windowing.
HS_FFT_2D_fs05.m	Performing a 2D FFT analysis based single images.
HS_Wavelet_fs03.m	Performing a continuous wavelet analysis based on a high-speed image series. This code requires further development.

Table A4.10: Matlab scripts for performing the SpraySyn flame benchmark [26] and for creating the mat-files of the reference flames.

Script name	Used for
SPP_1_RAW2TIFF_fs07.m	<p>Converting the Nikon camera images from raw (NEF) to TIFF file format, identifying oversaturated pixels, and background subtraction.</p> <p>Script used for Figure 5.5, Figure 5.6, Figure 5.7, and Figure 5.8.</p>
SPP_2_CropImages_fs04.m	<p>Cropping all images to a region of interest defined by a target image and obtaining the pixel-mm-ratio.</p> <p>Script used for Figure 5.5, Figure 5.6, Figure 5.7, and Figure 5.8.</p>
SPP_3_FlameGeometry_fs24.m	<p>Characterizing the flame height, diameter, tilt angle, and color ratio.</p> <p>If every evaluated image shows the flame at different operating point, a parameter study is performed that enables for instance investigating the influence of the coflow on the pilot flame diameter.</p> <p>If multiple images from an identical operation point are evaluated, statistics are calculated for the final flame benchmark.</p> <p>Script used for Figure 5.5, Figure 5.6, Figure 5.7, and Figure 5.8.</p>
SPP_4_FlameBenchmark_fs05.m	<p>Benchmarking the investigated flame with the reference flame.</p> <p>Script used for Figure 5.5, Figure 5.6, Figure 5.7, and Figure 5.8.</p>
SPP_3_1_STANDARD_Definition_fs04.m	<p>Creating the mat-files of the reference flames provided on <a href="http://www.spraysyn.org">www.spraysyn.org</a> that are required for the flame benchmarks.</p> <p>While the four codes listed above are made publicly available (for each script, a protected function (p-code) and an editable input script were published that are used for parameter input and for calling the protected function), this script should not be made publicly available.</p> <p>Script used for defining the reference flames shown in Figure 5.8.</p>

Table A4.11: Alphabetically ordered Matlab scripts for various applications.

Script name	Used for
Black_Body	Calculating black body radiation and creating plots.
_Radiation_Planck _fs1.m	Script used for Figure 2.2.
Create_AVG_image _from_IMX_fs01.m	Calculating an averaged image from multiple IMX/IM7 files that may contain multiple frames (e.g., simultaneously acquired images from multiple cameras) and exporting it as a mat-file.
Create_Video_from _Bitmap_Images _fs03.m	Creating a video from multiple bitmap images of a single folder with a user defined frame rate. This script provides an option for skipping images for the sequence (e.g., take only every second image) and is not limited by the minimum frame rate (6 fps) of the Matlab function "WriteVideo".
Create_Video _from_IMX_fs05.m	Creating a video from multiple bitmap images of a single folder with a user defined frame rate. This script provides an option for skipping images for the sequence (e.g., take only every second image), enables pixel down-sampling, and is not limited by the minimum frame rate (6 fps) of the Matlab function "WriteVideo".
Crop_Multiple _Bitmap_Images _fs04.m	Cropping multiple images (identical image resolution required) to an identical region of interest (interactively selectable by mouse).
Export_IMX_as _Bitmap_fs16.m	Converting IMX/IM7 images to bitmap images with multiple options (e.g., axis conversion from pixel to millimeter, individual color map selection, and (vertical) image concatenation or blending).
Import_imx_Export _mat_file_fs02.m	Creating mat-files of each image series (IMX/IM7) located in separate subfolders.
PDA_data_eval _fs11.m	Evaluation and post processing of the results exported from Dantec's BSA flow software (cf., chapter A4.1).  Script used for all figures depicted in chapter 5.3.2–5.3.5.
Vektorgrafik_fs02.m	Importing finally processed figures (FIG) and applying cosmetically changes (e.g., font size, axis labels, or color scale) before exporting them as vector graphics (EPS, EMF) in publication-ready quality.  Script used for numerous figures in this thesis.

Table A4.12: Matlab functions (alphabetically ordered) frequently used in the Matlab scripts listed in Table A4.3–Table A4.11.

Function name	Used for
code_ID.m	Exporting a text file that documents the executed script name, version as well as date and time of code execution. By that, results exported by a Matlab script can easily assigned to a script version.
DCRAW_to_TIFF.m	Converting an unlimited number of raw images from a DSLR consumer camera (e.g., Nikon NEF format) using the software DCRaw [237].
fig_ticks_px_mm.m	Converting the pixel axis of a figure to a millimeter with multiple options (e.g., direction of the vertical axis, distance (in mm) between the individual ticks, and centering the ticks on the horizontal and/or vertical axis.
list_subfolders.m	Listing all subfolders of a folder selected via user dialog.
rformat.m	Obtaining the correct matrix orientation of an image (or an image series) by interactive comparison of the original image (IMX/IM7) with the imported image matrix (important since the image matrices imported in Matlab are mostly oriented differently than displayed in DaVis (Table A4.1)). This function is capable of obtaining the orientation of multiple (differently oriented) image frames.

## Publications

### Peer-reviewed journal articles

S. Angel, **F. Schneider**, W. Kaziur-Cegla, T. Schmidt, C. Schulz, H. Wiggers, *Spray-flame synthesis of  $LaMO_3$  ( $M = Mn, Fe, Co$ ) perovskite nanomaterials: effect of spray droplet size and esterification on particle size distribution*. Proceedings of the Combustion Institute 38 (2021), accepted, in revision.

**F. Schneider**, S. Suleiman, J. Menser, E. Borukhovich, I. Wlokas, A. Kempf, H. Wiggers, C. Schulz, *Spray-Syn – A standardized burner configuration for nanoparticle synthesis in spray flames*. Review of Scientific Instruments 90(8) (2019) 085108.

J. Menser, **F. Schneider**, T. Dreier, S. A. Kaiser, *Multi-pulse shadowgraphic RGB illumination and detection for flow tracking*. Experiments in Fluids 59 (2018) 90.

S. Kluge, L. Deng, O. Feroughi, **F. Schneider**, M. Poliak, A. Fomin, V. Tsionsky, S. Cheskis, I. Wlokas, I. Rahinov, T. Dreier, A. Kempf, H. Wiggers, C. Schulz, *Initial reaction steps during flame synthesis of iron-oxide nanoparticles*. Royal Society of Chemistry 17 (2015) 6930-6939.

### Conference proceedings

**F. Schneider**, S. Suleiman, I. Wlokas, T. Dreier, H. Wiggers, C. Schulz, *The SpraySyn standard burner enabling coordinated research on materials synthesis in spray flames*. 29. Deutscher Flammentag (2019), Bochum, Germany.

**F. Schneider**, T. Dreier, C. Schulz, *SpraySyn – Standard Burner for the Collaborative Investigation of Spray-Flame Synthesis of Nanoparticles: Droplet Velocity and Size of the Non-Reactive Ethanol Spray*. 9<sup>th</sup> European Combustion Meeting (2019), Lisbon, Portugal.

### Conference presentations

**F. Schneider**, T. Dreier, C. Schulz, *Experimental characterization of the flow field of the SpraySyn burner for coordinated research on materials synthesis in spray flames*. 2<sup>nd</sup> CENIDE Conference (2020), Bergisch Gladbach, Germany.

**F. Schneider**, S. Suleiman, I. Wlokas, T. Dreier, H. Wiggers, C. Schulz, *The SpraySyn standard burner enabling coordinated research on materials synthesis in spray flames*. 29. Deutscher Flammentag (2019), Bochum, Germany.

B. Alkan, **F. Schneider**, S. Suleiman, H. Wiggers, C. Schulz, *Spray-flame synthesis of function materials: Perovskite nanoparticles for oxygen evolution catalysis*. Gordon Conference on Laser Diagnostics in Combustion (2019), Les Diablerets, Switzerland.

**F. Schneider**, E. Borukhovich, H. Wiggers, T. Dreier, C. Schulz, *SpraySyn: A standardized burner configuration for coordinated studies on materials synthesis in spray flames*. 9<sup>th</sup> European Combustion Meeting (2019), Lisbon, Portugal.

**F. Schneider**, M. Prenting, T. Dreier, C. Schulz, *SpraySyn: A standardized burner configuration for coordinated studies on materials synthesis in spray flames*, CENIDE Jahresfeier (2018), Essen, Germany.

**F. Schneider**, R. Zhou, V. Letuzich, M. Spree, M. Prenting, E. Borukhovich, T. Helmig, A. Rittler, I. Wlokas, A. Kempf, S.-M. Schnurre, T. Hülser, T. Dreier, C. Schulz, *Iron Oxide Nanoparticle Synthesis in a Pilot-Plant Spray-Flame Synthesis Facility: Laser-Based Measurements and Simulation*, 37<sup>th</sup> International Symposium on Combustion (2018), Dublin, Ireland.

**F. Schneider**, S. Suleiman, M. Prenting, T. Dreier, C. Schulz, *The SpraySyn burner: A new standard burner for coordinated studies on materials synthesis in spray flames*, 37<sup>th</sup> International Symposium on Combustion (2018), Dublin, Ireland.

T. Dreier, **F. Schneider**, O. Feroughi, C. Schulz, *SiO laser-induced fluorescence imaging for quantitative concentration and temperature measurements*, Gordon Conference on Laser Diagnostics in Combustion (2015), Waterville Valley, USA.

**F. Schneider**, O. Feroughi, H. Kronemayer, T. Dreier, C. Schulz, *Effect of fluctuations on time-averaged multi-line NO-LIF thermometry measurements of the gas-phase temperature*, Gordon Conference on Laser Diagnostics in Combustion (2015), Waterville Valley, USA.

### Student supervision

Rui Zhou, *Bildgebende NO-LIF-Thermometrie mit Lichtschnittkorrektur in der Sprayflammen-Synthese von Eisenoxid-Nanopartikeln im Pilotmaßstab*, Bachelor thesis, University of Duisburg-Essen (2018), Duisburg, Germany.

Viktor Letuzich, *Test eines optischen Versuchsaufbaus für bildgebende NO-LIF Temperaturmessungen mit Absorptionskorrektur der Anregungsstrahlung an einem Flammensynthese-Reaktor im Pilotmaßstab*, Bachelor thesis, University of Duisburg-Essen (2018), Duisburg, Germany.

Yu Zhang, *Optische Charakterisierung und Bestimmung von Geschwindigkeitsfeldern von Flüssigsprays mittels High-Speed Imaging, Particle Imaging und Particle Tracking Velocimetry*, Bachelor thesis, University of Duisburg-Essen (2017), Duisburg, Germany.

# DuEPublico

Duisburg-Essen Publications online

UNIVERSITÄT  
DUISBURG  
ESSEN

*Offen im Denken*

ub | universitäts  
bibliothek

Diese Dissertation wird über DuEPublico, dem Dokumenten- und Publikationsserver der Universität Duisburg-Essen, zur Verfügung gestellt und liegt auch als Print-Version vor.

**DOI:** 10.17185/duepublico/72817

**URN:** urn:nbn:de:hbz:464-20201006-135349-0

Alle Rechte vorbehalten.